# A REDUCED-ORDER MODELING METHODOLOGY FOR THE MULTIDISCIPLINARY DESIGN AND ANALYSIS OF BOUNDARY LAYER INGESTION CONFIGURATIONS

A Thesis
Presented to
The Academic Faculty

by

Michael D. Bozeman Jr.

In Partial Fulfillment
of the Requirements for the Degree
Doctor of Philosophy in the
School of Aerospace Engineering

Georgia Institute of Technology
December 2019

# A REDUCED-ORDER MODELING METHODOLOGY FOR THE MULTIDISCIPLINARY DESIGN AND ANALYSIS OF BOUNDARY LAYER INGESTION CONFIGURATIONS

Approved by:


Professor Dimitri Mavris, Advisor
School of Aerospace Engineering
*Georgia Institute of Technology*

Dr. Marilyn Smith
School of Aerospace Engineering
*Georgia Institute of Technology*

Dr. Jimmy Tai
School of Aerospace Engineering
*Georgia Institute of Technology*

Dr. Irian Ordaz
Aeronautics Systems Analysis Branch
*NASA Langley Research Center*

Dr. Melissa Carter
Configuration Aerodynamics Branch
*NASA Langley Research Center*



Date Approved: November 1st 2019

*To Cheyenne Bozeman.*

*My wife, best friend, and better half.*

*This degree has been as hard on you as it has me. I have never met anyone as supportive and dedicated. You make me want to be better and can honestly say that I would not be the person I am today without you.*

# ACKNOWLEDGEMENTS

This thesis marks the end of a 10 year journey consisting of some of the best and worst times of my life. I never could have imagined that I would make it this far. Throughout this process, I discovered a love for learning and problem solving that I did not know existed. I have met some great people along the way that have helped to motivate and guide me through the process.

Dating back to my undergraduate time at Mississippi State University, Dr. Keith Koenig and Dr. David Thompson provided me with mentorship and motivation that lead to my ultimate decision to attend graduate school. I would like to thank Dr. Dimitri Mavris for giving me the opportunity to be part of the Aerospace Systems Design Laboratory (ASDL) and for his guidance and mentorship throughout my graduate career. I would like to express my gratitude to Dr. Jimmy Tai for meeting with me biweekly for the last four years and providing invaluable feedback and guidance. I would like to acknowledge Dr. Melissa Carter and Dr. Irian Ordaz of the NASA Langley Research Center for their mentorship and guidance throughout this process. Last but not least, I would like to acknowledge Dr. Marilyn Smith and Dr. Jonathan Gladin for taking the time out of their busy schedules to review my work and provide technical feedback. Without the people mentioned here, this accomplishment would not have been possible.

I have met a lot of great people and developed close friendships along the way. These relationships made the entire process more enjoyable and I will forever cherish the times we spent together. You know who you are. I would like to express thanks to my very close friend Brett Hiller for the endless conversations and continuous support. I would also like to thank my parents and siblings for their continous support and

encouragement.

Finally, I cannot overstate the gratitude that I have for my lovely wife Cheyenne. As anyone who has gone through this process knows, it is a roller coaster ride with the highest of highs, the lowest of lows, and some unexpected bumps and turns along the way. Cheyenne has been the only time invariant component in my life throughout this entire process. She stuck by my side with unwavering support. She comforted me at times and motivated me at others. This degree would not mean anything if she were not by my side to share it with me.

# TABLE OF CONTENTS

# LIST OF TABLES

# LIST OF FIGURES

# GLOSSARY

**AFC** Active Flow Control.

**AIP** Aerodynamic Interface Plane.

**AoA** Angle of Attack.

**BC** Boundary Condition.

**BLI** Boundary Layer Ingestion.

**BLI-Asym** Asymmetric Boundary Layer Ingestion.

**BLI-FA** Full-annular Boundary Layer Ingestion.

**CDISC** Constrained Direct Iterative Surface Curvature.

**CFD** Computational Fluid Dynamics.

**CRM** Common Research Model.

**DLR** German Aerospace Center.

**DOE** Design of Experiments.

**FEA** Finite Element Analysis.

**FOM** Full-Order Model.

**GE** General Electric.

**HWB** Hybrid Wing Body.

**IBLE** Integral Boundary Layer Equations.

**MDA** Multidisciplinary Analysis.

**MDAO** Multidisciplinary Analysis and Optimization.

**NASA** National Aeronautics and Space Administration.

**NPSS** Numerical Propulsion System Simulation.

**NURBS** Non-Uniform Rational Basis Spline.

**PAI** Propulsion Airframe Integration.

**PC** Parallel Compressor.

**POD** Proper Orthogonal Decomposition.

**RANS** Reynolds-Averaged Navier-Stokes.

**ROM** Reduced-Order Model.

**STARC-ABL** Single-Aisle Turboelectric Aircraft with Aft-Boundary Layer Ingestion.

**TCT** Tail-Cone Thruster.

**TeDP** Turboelectric Distributed Propulsion.

**TSFC** Thrust Specific Fuel Consumption.

**UHB** Ultra High Bypass.

$c$ Speed of sound.

$c_b$ Speed of sound at boundary.

$C_m$ Partial derivative of position of node $n$ w.r.t. displacement at node $m$.

$c_p$ Specific heat at constant pressure.

$c_{f,x}$ Axial skin friction coefficient.

$CP$ Pressure coefficient.

$D$ Drag.

$d$ Number of design variables.

$D_{fan}$ Fan diameter.

$DPCP$ Circumferential distortion for ARP1420 ring.

$DPCP_{avg,0}$ Average circumferential distortion for baseline configuration.

$DPCP_{avg}$ Average circumferential distortion at fan face.

$F$ Thrust.

$f$ Vector of regression function terms for kriging surrogate model.

$F_x$ Axial force.

$F_{x,0}$ Axial force for baseline configuration.

$FPR$ Fan Pressure Ratio, $FPR = \frac{P_{t,3}}{P_{t,2}}$.

$FPR_i$ Initial guess of fan pressure ratio.

$H_t$ Total enthalpy.

| | |
|---|---|
| $H_{t_b}$ | Total enthalpy at boundary. |
| $j$ | Degree of polynomial. |
| $\dot{m}$ | Mass flow rate. |
| $M$ | Number of POD modes. |
| $m$ | Number of primitive variables. |
| $\dot{m}_2$ | Mass flow rate at fan face. |
| $\dot{m}_3$ | Mass flow rate at fan exit. |
| $M_b$ | Mach number at boundary. |
| $N$ | Total dimension of CFD solution. |
| $n$ | Number of grid points. |
| $N_{corr}$ | Corrected fan speed. |
| $OBJ_i$ | $i^{th}$ objective function. |
| $P$ | Static pressure. |
| $P_2$ | Static pressure at fan face. |
| $P_\infty$ | Freestream static pressure. |
| $P_b$ | Static pressure at boundary. |
| $P_{req}$ | Power required. |
| $P_{t,18}$ | Total pressure at exit for cold stream. |
| $P_{t,2}$ | Total pressure at fan face. |
| $P_{t,3}$ | Total pressure at fan exit. |
| $P_{t,8}$ | Total pressure at exit for hot stream. |
| $P_{t,\infty}$ | Freestream total pressure. |
| $P_{t,avg_{low}}$ | Average of total pressure values below $P_{t,avg}$ for ARP1420 ring. |
| $P_{t,avg}$ | Average total pressure for ARP1420 ring. |
| $P_{t,b}$ | Total pressure at boundary. |
| $PR$ | Pressure recovery. |
| $PR_i$ | Initial guess of pressure recovery. |

| | |
|---|---|
| $Q$ | Number of low pressure regions for ARP1420 ring. |
| $R$ | Flux residual. |
| $r$ | Vector of error terms for kriging surrogate model. |
| $R^+$ | Outward propagating invariant. |
| $R^-$ | Inward propagating invariant. |
| $R^2$ | Coefficient of determination. |
| $r_n$ | Updated position of $n^{th}$ node. |
| $r_n^b$ | Position of $n^{th}$ node for baseline geometry. |
| $S$ | Number of snapshots. |
| $T$ | Static temperature. |
| $T_\infty$ | Freestream static temperature. |
| $T_b$ | Temperature at boundary. |
| $T_{t,18}$ | Total temperature at exit for cold stream. |
| $T_{t,2}$ | Total temperature at fan face. |
| $T_{t,3}$ | Total temperature at fan exit. |
| $T_{t,8}$ | Total temperature at exit for hot stream. |
| $T_{t,b}$ | Total temperature at boundary. |
| $TR$ | Throttle ratio. |
| $U$ | Orthogonal vector for $\widetilde{Y}\widetilde{Y}^T$. |
| $u$ | Velocity component in x-direction. |
| $U$ | Velocity in y-direction at boundary. |
| $u_\infty$ | Freestream velocity. |
| $U_b$ | Velocity magnitude at boundary. |
| $u_b$ | Velocity in x-direction at boundary. |
| $u_j$ | Jet velocity. |
| $u_w$ | Wake velocity. |
| $V$ | Orthogonal vector for $\widetilde{Y}^T\widetilde{Y}$. |

| | |
|---|---|
| $v$ | Velocity component in y-direction. |
| $W$ | Vector of primitive variables obtained from full-order model. |
| $w$ | Velocity component in z-direction. |
| $w_b$ | Velocity in z-direction at boundary. |
| $W_i$ | Weighting for $i^{th}$ objective function. |
| $W_{corr}$ | Corrected mass flow rate. |
| $X$ | Design variable vector. |
| $x, y, z$ | Axis coordinates. |
| $\widetilde{Y}$ | Normalized snapshot matrix. |
| $Y$ | Snapshot matrix. |
| $\alpha$ | POD Coefficients. |
| $\Delta s$ | Fuselage design variables. |
| $\Delta s_L$ | Lower bound for fuselage design variables. |
| $\Delta s_U$ | Upper bound for fuselage design variables. |
| $\eta$ | Propulsive efficiency. |
| $\eta_{adiabatic}$ | Adiabatic fan efficiency. |
| $\gamma$ | Ratio of specific heats. |
| $\gamma, \beta$ | Matrices of weights for kriging surrogate model. |
| $\lambda$ | Nonzero values of $\Sigma$. |
| $\mu$ | Mean of ROM error. |
| $\nu$ | User-defined magnitude of node displacement. |
| $\phi$ | POD modes. |
| $\bar{\psi}$ | Mean of ensemble of snapshots for primitive variable $\psi$. |
| $\psi$ | Primitive variable vector. |
| $\rho$ | Density. |
| $\rho_b$ | Density at boundary. |
| $\sigma$ | Standard deviation of ROM error. |

| | |
|---|---|
| $\Sigma$ | Diagonal matrix of singular values of $\widetilde{Y}$. |
| $\theta$ | Design variable combination. |
| $\theta_{\bar{i}\bar{k}}$ | Circumferential extent of single low pressure region. |
| $\theta_{\bar{i}}$ | Circumferential extent of low pressure region for ARP1420 ring. |
| $\xi_n, \eta_n$ | Bivariate coordinates. |

# SUMMARY

The requirements for commercial aviation are constantly becoming more stringent. In response, NASA has quantified goals for the fuel burn, noise, emissions, and takeoff field length of the next generations of aircraft. These goals have led to the investigation of a variety of technologies to meet these goals. One such technology is Boundary Layer Ingestion (BLI) propulsion, which has been identified as a technology to reduce the aircraft fuel burn. Preliminary investigations have shown that BLI propulsion can potentially result in a 5-12% reduction in fuel burn depending on the configuration. A variety of BLI configurations have been proposed. The present work considers a BLI configuration known as the tail-cone thruster (TCT), which consists of an aft-propulsor that is powered by two underwing turbofans.

BLI configurations pose significant challenges to aircraft designers due to strong coupling between the airframe aerodynamics and the propulsion system performance. These configurations require the use of coupled Multidisciplinary Analysis (MDA) consisting of the airframe aerodynamics and propulsion system performance to be analyzed in an iterative fashion. For the present case, the aerodynamic analysis is performed using Computational Fluid Dynamics (CFD). This is necessary to accurately predict the interaction between the airframe aerodynamics and the propulsion system. Additionally, the design of unconventional configurations cannot rely solely on intuition for making design decisions. Multidisciplinary Analysis and Optimization (MDAO) is a method for performing design based on a user-defined objective function. MDAO can be applied to problems with coupled subsystems and allow the objectives to be targeted directly. This would allow for consideration of both intuitive and nonintuitive designs in an effort to obtain the design with the best

overall performance. Further, design space exploration is needed to develop a better understanding of the multidisciplinary trades and to identify important trends. This information could provide better insight and allow for better design decisions. However, the ability to perform MDAO for a BLI concept requiring CFD coupled to a propulsion system analysis is computationally expensive to the point of limited applicability and design space exploration is, generally, not practical.

The research objective for this thesis is to develop a computationally efficient method for the coupled MDA of BLI configurations. This would enable the MDAO and design space exploration of BLI configurations by reducing the computational cost of each design evaluation. Reduced-order modeling is discussed as a potential method to reduce the computational cost associated with coupled MDA. Recent work by the German Aerospace Center (DLR) has illustrated the usefulness of ROMs in an MDAO framework. ROMs can be created from high-fidelity analysis models based on snapshots. This requires a fixed number of function evaluations upfront in what is referred to as the offline portion of the ROM. Once the ROM is built, it can be used in place of the high-fidelity analysis models resulting in a significant reduction in computational cost. This is particularly valuable for the present case, which requires an iterative analysis between high-fidelity CFD and a propulsion model for each design evaluation. The application of ROMs to this problem can result in a practical method for performing MDAO for BLI configurations and allow for greater design space exploration.

The proposed methodology involves creating an aerodynamic ROM based on flow-field snapshots where the snapshots are produced using decoupled MDA consisting of CFD and a propulsion model. The ROM is then coupled to a propulsion model to enable computationally efficient coupled MDA for BLI configurations. The ROM method for the proposed methodology is an interpolation-based ROM based on Proper Orthogonal Decomposition (POD). The proposed methodology is applied to the shape

optimization of a tail-cone thruster concept derived from the Single-aisle Turboelectric AiRCraft with Aft-Boundary Layer ingestion (STARC-ABL) aircraft concept.

The proposed ROM-based, coupled MDA approach is evaluated through comparisons to results obtained from CFD for both decoupled and coupled solution strategies where the decoupled comparisons are performed to evaluate the aerodynamic prediction capabilities of the ROM and the coupled comparisons evaluate the ability of the ROM to accurately predict the interactions between the propulsion system and the airframe. The comparisons were provided as a function of the number of snapshots used to develop the aerodynamic ROM to assess the tradeoff between the computational cost and accuracy of the ROM. The results illustrate that the distortion at the fan face displayed the highest error, in general, along with the highest sensitivity to the number of samples used to develop the ROM. As a result, the computational cost of the ROM is driven by the desired accuracy of the distortion calculations. Finally, the computational cost of the ROM-based, coupled MDA approach for the application of shape optimization was compared to the computational cost of an equivalent CFD-based approach and an adjoint-based approach. The results show that the ROM-based approach offers a significant reduction in computational cost over the equivalent CFD-based approach while the adjoint-based approach was estimated to have a lower computational cost for a single optimization due to the high upfront cost associated with the ROM-based approach. However, for as few as two optimizations, the ROM-based approach offers a reduction in computational cost relative to the adjoint-based approach. This is an important finding since the best objective function and constraints are not always known and the adjoint-based approach is highly-dependent on the starting solution.

# CHAPTER I

# INTRODUCTION

The following sections give a brief overview of the motivation for this thesis. The topics discussed include Boundary Layer Ingestion (BLI) propulsion concepts and the challenges associated with the design of these types of highly-coupled aeropropulsive systems. The associated challenges necessitate alternative approaches for aeropropulsive analysis and design. The modeling requirements for new methods are discussed and reduced-order modeling is presented as a key enabler for the design of BLI configurations.

## *1.1 Boundary Layer Ingestion Propulsion*

The requirements for commercial aviation are constantly becoming more stringent. In an effort to meet the increasing requirements for commercial aviation, NASA has quantified goals for the next generations of aircraft. These goals include improvements in aircraft noise, emissions, and performance and are illustrated in Table 1.

Table 1: NASA Subsonic Transport System Level Metrics [1].

| **TECHNOLOGY BENEFITS** | **TECHNOLOGY GENERATIONS** (Technology Readiness Level = 5-6) | | |
|---|---|---|---|
| | **Near Term** 2015-2025 | **Mid Term** 2025-2035 | **Far Term** beyond 2035 |
| Noise Reduction (cum below Stage 4) | 22 – 32 dB | 32 – 42 dB | 42 – 52 dB |
| LTO $No_x$ Emissions Reduction (below CAEP 6) | 70 – 75% | 80% | >80% |
| Cruise $No_x$ Emissions Reduction (rel. to 2005 best in class) | 65 – 70% | 80% | >80% |
| Fuel/Energy Consumption Reduction (rel. to 2005 best in class) | 40 – 50% | 50 – 60% | 60 – 80% |

The goals listed in Table 1 have guided research efforts toward the exploration of a variety of new technologies and unconventional configurations. One notable technology that is being considered is known as BLI propulsion. BLI propulsion has been a topic of research since the 1940s and has been successfully applied to marine applications such as ships, submarines, and torpedos since the 1960s [15, 16]. The BLI propulsion concept aims to obtain an increase in propulsive efficiency by ingesting the boundary layer from the fuselage into the engine [17]. This idea is based on the fact that it is more efficient to accelerate a flow that has a lower initial velocity. Compared to a standard podded configuration that ingests freestream flow, the BLI concept will experience a much lower inflow velocity due to boundary layer effects. Systems studies have shown that a 5-12% reduction in aircraft fuel burn is possible [18, 19, 20].

To understand how BLI works, an idealistic model will be discussed here. This model has been described in Plas [2, 21] and will be summarized here. The simplified BLI model is shown in Figure 1. The illustration provided in Figure 1 describes two systems; the conventional podded system and the BLI system. For an aircraft in cruise, the purpose of the propulsion system is to overcome the momentum deficit that results from viscous forces acting on the aircraft surface. This balance of momentum can be summarized by the well-known expression for an aircraft in steady-level flight given in Equation 1.

$$F = \dot{m}(u_j - u_\infty) = \dot{m}(u_\infty - u_w) = D \tag{1}$$

Equation 1 illustrates the balance between the thrust, $F$, and drag, $D$, where $\dot{m}$ is the mass flow rate through the propulsor, $u_j$ is the jet velocity for the podded configuration, $u_\infty$ is the freestream velocity, and $u_w$ is the wake velocity. For the podded engine system, the thrust and drag can be easily separated and Equation 1 directly applies. However, this is not the case for the BLI system. For the BLI system, the requirement for momentum balance still holds, but it is difficult to separate the thrust

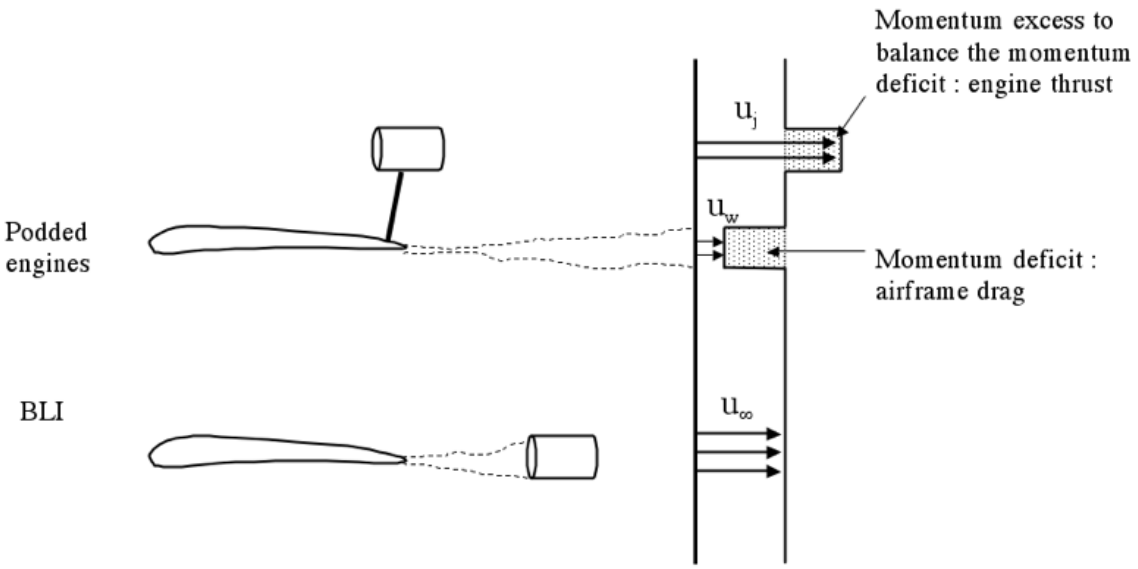


Figure 1: Idealistic BLI Illustration [2].

and drag forces. This will be discussed further in future sections. For the simplified discussion here, the assumption is made that thrust and drag can be separated for both systems such that Equation 1 applies.

To understand the potential benefits of BLI systems, it is important to consider the power required for each system. For the podded configuration, the power required is given in Equation 2.

$$P_{req,podded} = \frac{\dot{m}}{2}(u_j^2 - u_\infty^2) \tag{2}$$

Equation 2 can then be simplified by factoring and substituting the expression for thrust given in Equation 1. The final expression for the power required of the podded system is then given in Equation 3.

$$P_{req,podded} = \frac{\dot{m}}{2}(u_j - u_\infty)(u_j + u_\infty) = \frac{F}{2}(u_j + u_\infty) \tag{3}$$

The same process can be performed for the BLI system. The result is provided as Equation 4.

$$P_{req,BLI} = \frac{\dot{m}}{2}(u_\infty^2 - u_w^2) = \frac{F}{2}(u_\infty + u_w) \tag{4}$$

Note that the power required for both the podded and BLI systems have the common term $\frac{F}{2}u_\infty$. The important observation to be made here is that the power required for the podded system is also a function of the term $\frac{F}{2}u_j$ while the power required for the BLI system is dependent on $\frac{F}{2}u_w$. Since $u_w$ will always be less than $u_j$, the power required for the BLI system will always be less than the power required for the podded system. This statement is formally provided as Equation 5.

$$u_j > u_w \rightarrow P_{req,podded} > P_{req,BLI} \tag{5}$$

The general expression for the propulsive efficiency of an airbreathing engine is provided in Equation 6.

$$\eta_p = \frac{2}{1 + \frac{u_exit}{u_inlet}} \tag{6}$$

Based on the previous discussion and the definition provided in Equation 6, the propulsive efficiencies for two systems are provided in Equations 7 and 8.

$$\eta_{podded} = \frac{2}{1 + \frac{u_j}{u_\infty}} \tag{7}$$

$$\eta_{BLI} = \frac{2}{1 + \frac{u_\infty}{u_w}} \tag{8}$$

Because $u_j$ is always greater than $u_\infty$ and since $u_w$ is always less than $u_\infty$, then $\eta_{podded}$ will always be less than 1 and $\eta_{BLI}$ will always be greater than 1 but less than 2. The result is that for a required level of thrust, the BLI system will require less power and therefore, will burn less fuel. It is important to reiterate that the simple description provided here was just to illustrate the concept of BLI and does so by means of gross simplification.

## *1.2 BLI Design Challenges*

The design of BLI configurations offers many challenges. The traditional method of designing the airframe and propulsion systems for commercial aircraft is no longer

sufficient and a paradigm shift is needed. This section will discuss some of the design challenges associated with BLI configurations.

### 1.2.1 Need for Coupled Multidisciplinary Analysis

For commercial aircraft, traditional approaches for designing the airframe and propulsion systems consider the systems independently. For example, the traditional engine sizing process first requires an aerodynamic analysis to obtain the airframe drag. Then, the engine is sized using a cycle analysis to provide the required thrust. The resulting performance of the system is then based on independent analyses of the airframe and propulsion system. This method is sufficient for a conventional podded configuration; however, this is no longer applicable to BLI configurations. One of the challenges in designing a BLI configuration is that the aerodynamic and propulsion disciplines are highly coupled. Just as with the conventional podded configurations, the propulsion system performance is a direct function of the inflow for BLI configurations. The main difference is that the inflow is strongly impacted by the airframe for the BLI configuration. In order to capture these strong interactions, a coupled Multidisciplinary Analysis (MDA) approach needs to be utilized. An illustration of the differences between coupled and uncoupled MDA is shown in Figure 2.

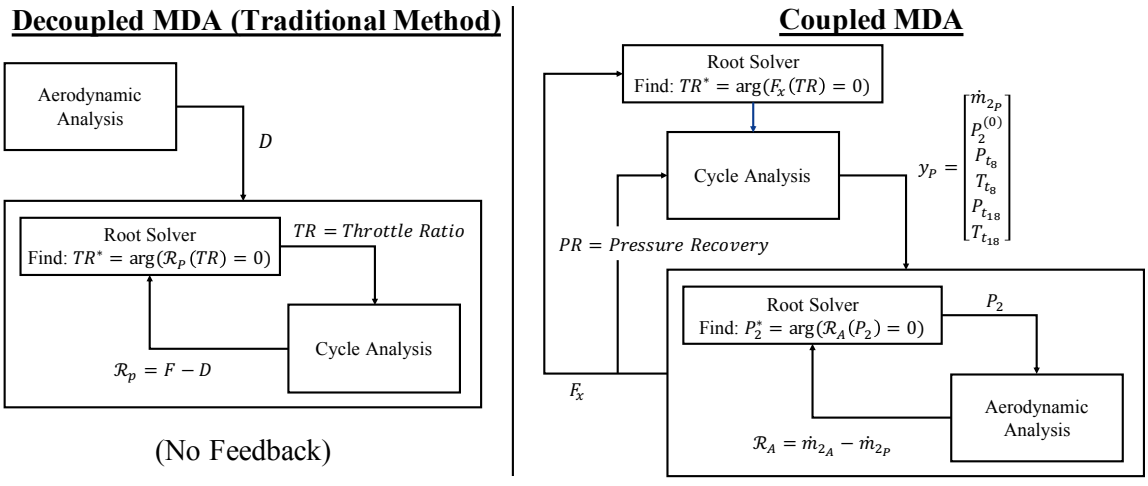


Figure 2: Required Paradigm Shift for the Design of BLI Configurations [3, 4].

The decoupled MDA approach, illustrated on the left of Figure 2, represents the traditional method of designing the airframe and propulsion systems that was previously discussed. The aerodynamic analysis provides the drag of the airframe, which is subsequently used to size the engine via cycle analysis. The coupled MDA approach, illustrated on the right of Figure 2, represents the required method for designing BLI configurations. The main difference is that the aerodynamic analysis is embedded in three iterative loops for the coupled MDA approach, but is only evaluated once in the decoupled MDA approach. For the coupled MDA approach, the coupling variables are the massflow rate and pressure recovery at the inlet boundary. This results in two inner loops. Provided an initial guess of massflow rate, the most inner loop consists of iteratively performing the aerodynamic analysis until the input massflow rate at the inlet boundary is matched. This is generally performed by changing the static pressure at the inlet boundary. The most inner loop provides an updated prediction of the pressure recovery at the inlet boundary that is then provided to the cycle analysis. The other inner loop consists of iterating between the cycle analysis and the most inner loop until the pressure recovery is converged. Finally, the outer loop is the engine sizing loop. This loop performs the sizing of the engine that is used in the cycle analysis in order to balance the axial force of the system. For BLI configurations, the process of separating the force and drag requires careful definition of the control volumes and can be ambiguous since no standard currently exists. To account for this, the goal for the BLI configuration is set to target the force balance, ($F_x = 0$), directly in Figure 2. The resulting solution from the coupled MDA approach provides the performance of an appropriately sized BLI configuration.

An example from the literature is provided here to quantify the differences between a decoupled and coupled MDA approach for analyzing a BLI configuration. The example is provided by Reference [5] where MDA was performed on the Single-Aisle

Turboelectric Aircraft with Aft-Boundary Layer Ingestion (STARC-ABL) configuration. The analysis consisted of using a 1D parametric cycle analysis tool, known as pyCycle, for the propulsion system analysis and a structured RANS solver known as ADFlow for the aerodynamic analysis. The analysis considered both a podded configuration and a BLI configuration. An illustration of these configurations is given in Figure 3. For the podded configuration, the propulsor and airframe were analyzed separately. Also note that the propulsor for the podded configuration ingested freestream flow. This case was used as a reference configuration to illustrate the differences between a podded configuration and a BLI configuration. For the BLI configuration, both coupled and decoupled MDA approaches were considered. Select results of the study are illustrated in Figure 4.

The results shown in Figure 4 illustrate a comparison between the predicted total pressure at the fan face as a function of fan pressure ratio ($FPR$) for the three cases discussed. The study shows that there is roughly a 15% difference in total pressure at the fan face between the podded and BLI configuration as expected since the podded configuration ingests freestream flow. Note that this difference is considering the coupled BLI analysis. Furthermore, the results depict roughly a 5% difference in the total pressure at the fan face for the coupled and decoupled BLI configurations, where the decoupled approach predicts higher pressures. The author states that this results in an overprediction in the thrust for the decoupled approach by roughly 5%, and the results could be even more significant for a turbofan type engine. Based on these results and the previous discussion, it is apparent that a coupled MDA approach is required for BLI configurations in order to obtain accurate predictions of performance.

### 1.2.2 Need for High-Fidelity Analyses

An additional challenge associated with the design of BLI configurations is the need for high-fidelity analyses, which are typically computationally expensive. The goal

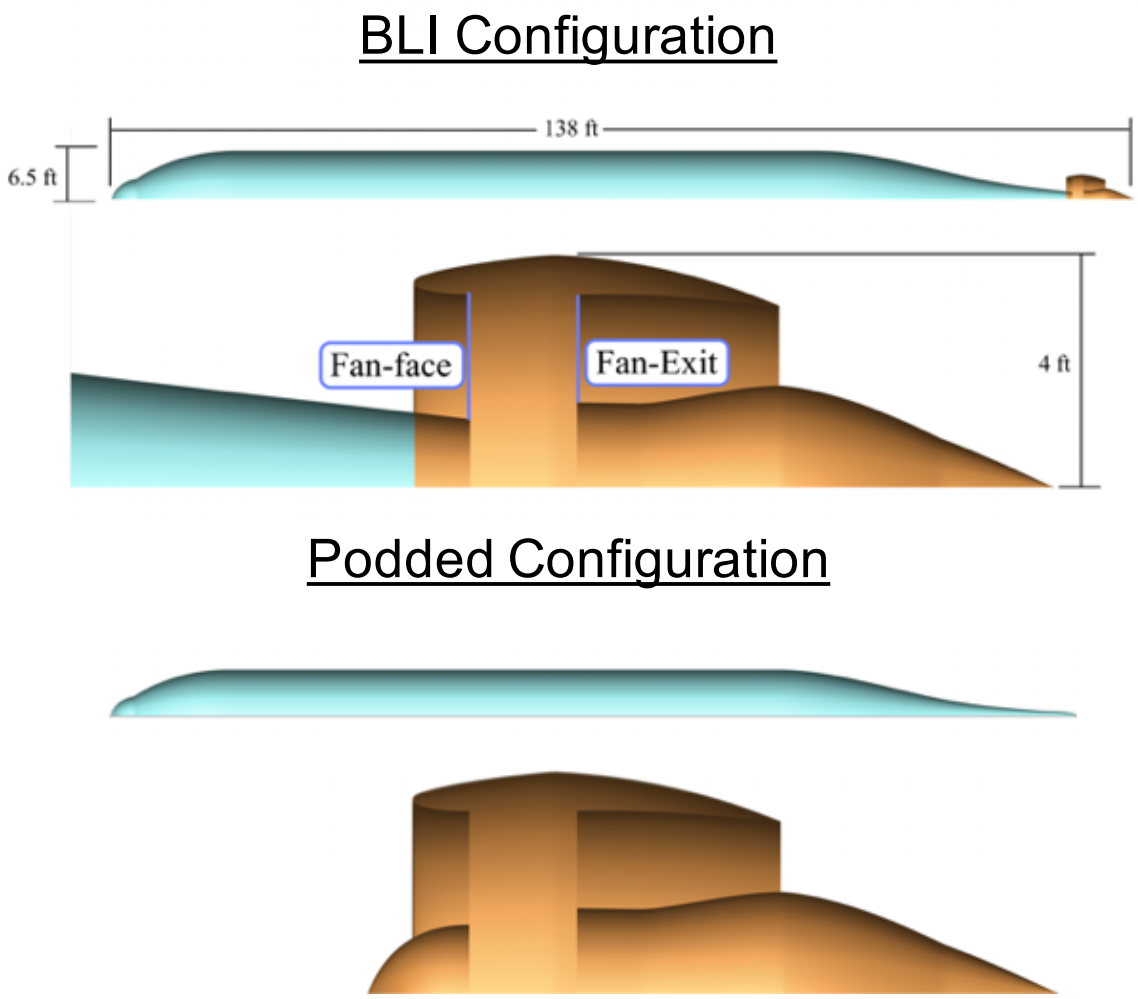


Figure 3: Illustration of BLI and Podded Configurations [5].

of BLI predictions is to assess the degree of system benefit obtained relative to a non-BLI system, where system benefit is simply defined to be a fuel burn reduction here for the sake of discussion. For BLI, the system benefit can be traced back to two effects: change in pressure distribution on the airframe upstream of the propulsor and improved propulsive efficiency associated with the engine having to accelerate a slower moving inflow. From a subsystem view, the aerodynamic analysis has to accurately predict the flow entering the propulsor, as well as the airframe aerodynamics. The propulsion analysis must accurately predict the performance of the propulsor

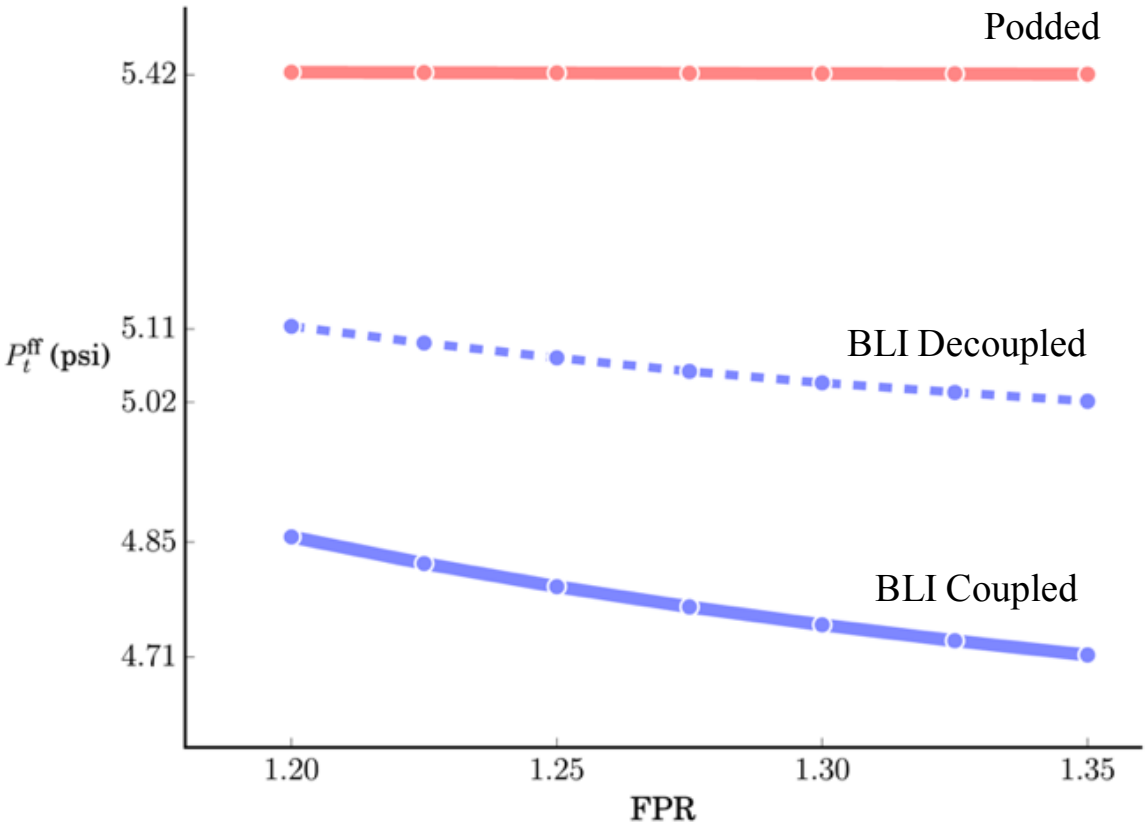


Figure 4: Total Pressure at Fan Face as a Function of Fan Pressure Ratio (FPR) [5].

subjected to inflow that is potentially asymmetric and highly distorted. To understand the need for high-fidelity analyses, each of the subsystem analysis requirements will be discussed separately.

The aerodynamic analysis is responsible for predicting both the flow properties entering the propulsor and the airframe aerodynamics. For the airframe aerodynamics, the goal is to obtain accurate prediction of the forces acting on the aircraft. Traditionally, empirical models have been heavily utilized in the early stages of aircraft design. However, these models do not exist for unconventional configurations, such as the BLI propulsion configuration. The flow properties entering the propulsor require accurate predictions of the boundary layer and its interaction with the propulsor. Additionally, the flow entering the propulsor will be asymmetric and distorted. In the context of design, the geometry upstream of the propulsor can have a measurable

impact on the pressure losses and the distortion entering the propulsor. For this reason, the aerodynamic analysis must also provide a means of predicting the changes in the boundary layer flow entering the propulsor as a function of geometry. To the author's knowledge, there are currently no low-fidelity models that can provide accurate predictions of all the discussed properties. This problem requires the use of high-fidelity computational fluid dynamics (CFD) for the aerodynamic analysis.

Now, if we consider the propulsion analysis, the requirement is to accurately predict the performance of the propulsor subject to inflow that is asymmetric and distorted. Specifically, the degradation in performance associated with the asymmetric and distorted inflow needs to be accurately predicted. Recently, a study was performed to look at the impact of the model fidelity on the predicted benefit for a BLI configuration. The analysis looked at four models of various fidelities. The lowest fidelity model was for a BLI configuration with no loss mechanisms. The other three fidelities were developed by including loss mechanisms in an additive fashion for the inlet, fan, and nozzle. The study looked at the predicted Thrust Specific Fuel Consumption (TSFC) improvement for each model as a function of the normalized thrust of the BLI engine. The results of this study are shown in the Figure 5.

The results show that the predicted TSFC of the propulsor is very sensitive to model fidelity. For the configuration studied here, there is a drastic difference in the predicted performance for the BLI system with no losses relative to the highest fidelity system that included all of the loss mechanisms. The results of this study illustrate the importance of both having accurate flow predictions entering the propulsor, as well as accurate predictions for the propulsion system analysis.

### 1.2.3 Need for Multidisciplinary Optimization and Design Space Exploration

When designing coupled systems such as BLI configurations, traditional decoupled design methods are less effective. For decoupled (or weakly coupled) subsystems,

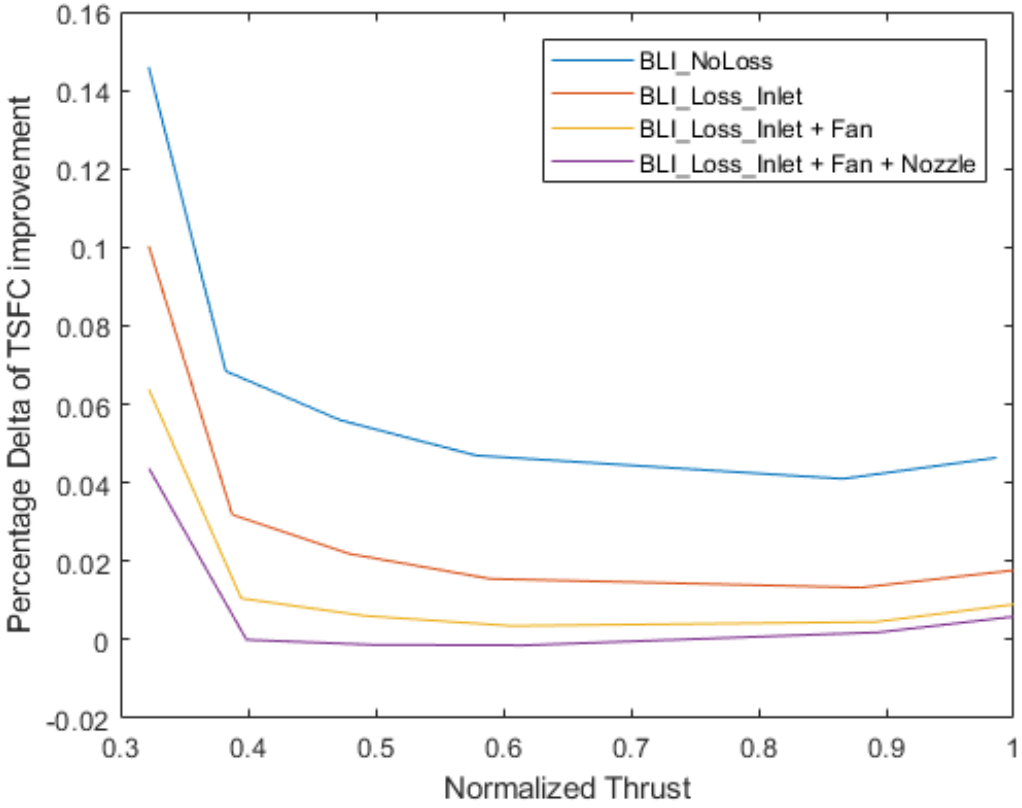


Figure 5: BLI Model Fidelity Study [6].

design decisions can be made for each subsystem separately based on additive metrics that contribute to the overall system performance. For example, one can design the airframe for minimum drag and the propulsor for maximum efficiency. The metrics are additive since they both have a direct impact on the fuel burn of the aircraft. This is no longer true for the BLI configuration where the propulsion system performance is tightly coupled with the airframe aerodynamics. The subsystems must be designed in a coupled fashion that aims to improve the fuel burn directly where each subsystem is not necessarily optimal when analyzed independently. Returning to the previous example of designing an airframe and a propulsion system, let's now consider a BLI system where the propulsion system is tightly integrated with the airframe. Based on intuition, the goal would still be to maximize the performance of each subsystem. So the goal would be to minimize the drag of the airframe and maximize the efficiency of

the propulsor. However, changes in the airframe to minimize the drag could actually have a negative impact on the propulsor performance. Instead, the fuel burn needs to be targeted directly for the coupled problem.

To illustrate this further, an example is provided from the literature in Reference [7]. In this work, the Constrained Direct Iterative Surface Curvature (CDISC) Aerodynamic Design Software was used to perform knowledge-based design of a tail-cone thruster (TCT) concept. CDISC is a knowledge-based design software developed by the NASA Langley Research Center [22]. CDISC allows the user to define target pressure distributions at specified design stations. An iterative analysis is then performed where CFD is used to predict the current pressure distributions at each station and then CDISC modifies the shape at each station to try and match the target pressure distribution. This works well if the user has intuition about what pressure distributions are desirable at each station. However, this may not be the case for the BLI concept. In the noted work, the pressure distributions were set based on the intuition that a reduced airframe drag is the goal. The resulting fuselage design was then analyzed for both a BLI configuration and non-BLI configuration. Note that this comparison was possible to make since the BLI configuration simply consisted of an actuator disk at the aft-end of the fuselage. The results of the design study are shown in Figure 6.

The results shown here compare the engine power coefficient as a function of axial force coefficient for three power settings. The geometry being considered for this study is the Common Research Model (CRM) with two underwing turbofans with an aft boundary layer ingestion propulsor. The purpose of this plot is to identify the power required from the underwing turbofans with and without the aft boundary layer propulsor. The results show that the power required for the BLI geometry was decreased as a result of the CDISC design study. However, if the results are compared for the base geometries, it is clear that the improvement was made to the

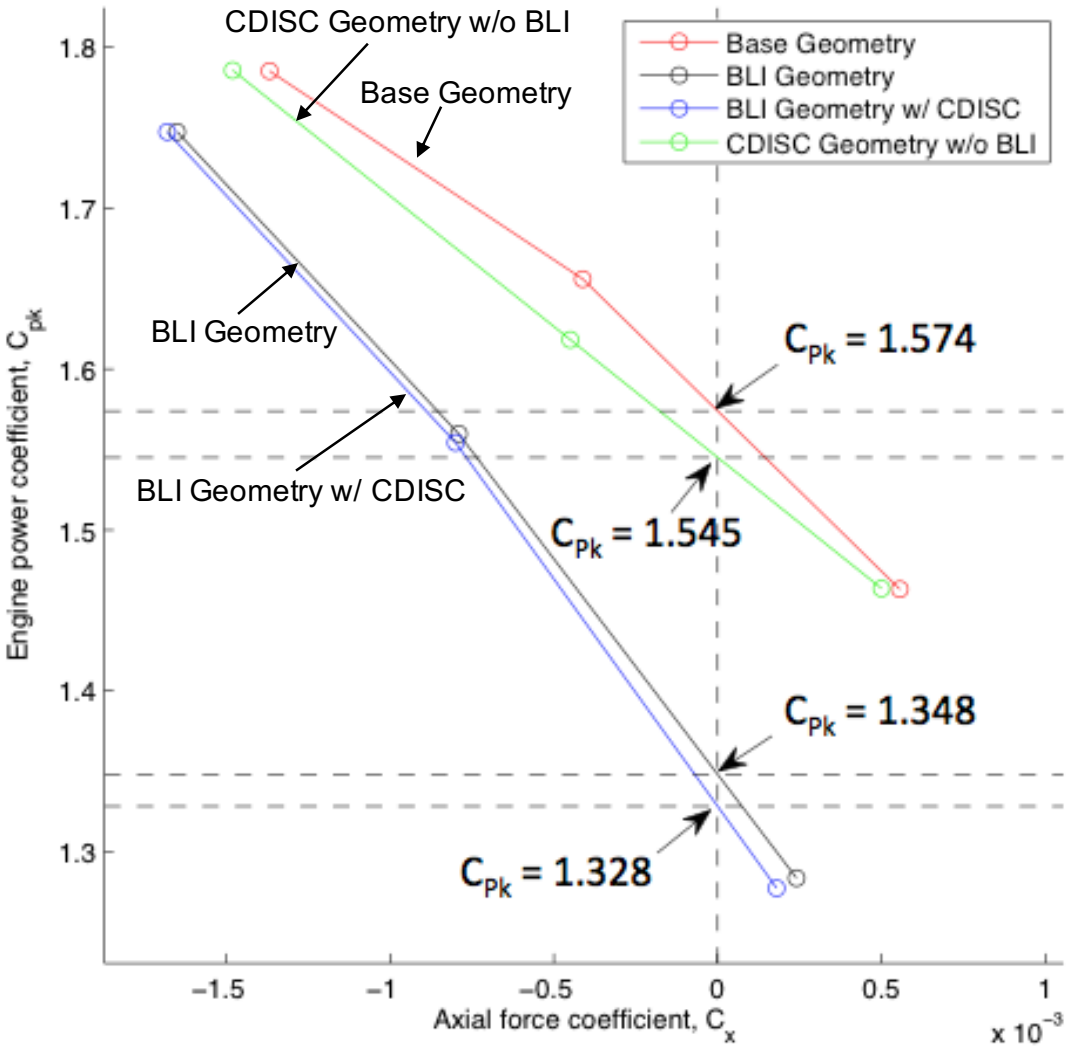


Figure 6: BLI CDISC Study [7].

base geometry and not necessarily to the BLI geometry. The question remains: can we do better? To answer this question, Multidisciplinary Analysis and Optimization (MDAO) is needed. MDAO can be applied to problems with coupled subsystems and allow the objectives to be targeted directly, which would allow for consideration of both intuitive and nonintuitive designs in an effort to obtain the design with the best performance. Further, design space exploration is needed to develop a better understanding of the multidisciplinary trades and to identify important trends [3]. This information could provide better insight and allow for better design decisions.

### 1.2.4 Summary of Design Challenges

The previous sections have illustrated the difficulties associated with the design of BLI configurations. This is a highly-coupled design problem that requires the use of expensive, high-fidelity models. Additionally, intuition alone is not sufficient for the design of BLI configurations. In order to take full advantage of the BLI technology, MDAO and design space exploration are needed. These methods could allow for design decisions to be made based on the desired objective function and provide valuable insight to design trends. While practical methods, such as the adjoint-based methods discussed in Chapter 2, do exist for MDAO using fully-coupled, high-fidelity analysis models, they are still limited in ability to allow for design trades and design space exploration due to extreme computational cost. A method is, therefore, needed to reduce the computational requirements for the coupled MDA of BLI configurations to enable MDAO and design space exploration.

## *1.3 Problem Statement*

Unconventional designs, such as BLI configurations, challenge the way that we perform design and analysis. The design of BLI configurations is a very challenging problem. It is a highly-coupled problem that requires the use of high-fidelity analysis models. Additionally, design optimization and design space exploration is need to take advantage of the BLI technology. This requires a large number of design evaluations using coupled, high-fidelity analyses. In order to enable MDAO and design space exploration for the design of BLI configurations, the computational cost associated with the coupled MDA must be reduced. Based on this discussion, the research objective for this thesis is given:

**Research Objective**:

Develop a computationally efficient method for the coupled MDA of BLI configurations.

The focus of this thesis is on the development of a methodology for the coupled MDA of BLI configurations to enable MDAO and design space exploration. It is important to note that the aerodynamic analysis consisting of CFD is the computationally limiting component for the analyses discussed here. Therefore, the focus of this thesis is to reduce the computational cost specific to the aerodynamic analysis, which directly reduces the cost of the coupled MDA problem. The following chapters discuss the development of the model starting with a description of the previous approaches for the design and analysis of BLI configurations in Chapter 2. Then, the problem formulation including the test geometry and computational methods is discussed in Chapter 3. In Chapters 4 and 5, the proposed approach is developed to allow for a computationally efficient method for coupled MDA for a BLI concept over a range of propulsor operating conditions. Then, the methodology is extended to include the effect of shape variables and applied to coupled MDAO in Chapter 6. Finally, the methodology is summarized in Chapter 7 and a summary of the work and future research opportunities is provided in Chapter 8.

# CHAPTER II

# BACKGROUND AND LITERATURE REVIEW

## *2.1 Design Approaches for BLI Configurations*

Several approaches have been proposed for the design and analysis of BLI configurations. These methods can be separated into two categories: decoupled approaches and coupled approaches. Before discussing the two methods, it is important to define coupled and decoupled in the present context. For the discussion presented here, a coupled approach refers to an analysis of two or more disciplines that includes a feedback loop between the disciplines whereas a decoupled approach refers to an analysis of two or more disciplines with no feedback loop between the disciplines. The need for coupled analysis methods for the design of BLI configurations was already discussed. However, it is important to include both the coupled and decoupled approaches in the provided discussion to obtain a better overall understanding of BLI analysis. The following discussion presents some key approaches for the design and analysis of BLI configurations.

### 2.1.1 Decoupled Approaches

The decoupled approach is the typical method employed for the design and analysis of BLI configurations because of the high computational cost associated with the coupled approach. A variety of decoupled approaches have been considered for BLI configurations. This typically involves focusing on one system and approximating or neglecting the other. The following dicussion provides an overview of some of the decoupled approaches for the design and/or analysis of BLI configurations that are available in the literature. The discussion is divided into two categories: propulsion

focused approaches and aerodynamic focused approaches.

**Propulsion Focused Approaches**

Propulsion focused approaches typically consist of modeling and/or characterizing the performance of a BLI propulsion system. These types of approaches requires an estimate of the aerodynamics of the vehicle to obtain the inflow conditions for the propulsion system. A variety of methods have been employed for this. These approaches are described in the following discussion.

**Felder et al.**

In the work by Felder et al. [19], analyses were performed for a Turboelectric Distributed Propulsion (TeDP) configuration. This is a hybrid wing body (HWB) configuration with distributed asymmetric boundary layer propulsors. The goal of this work was to assess the impact of the BLI system on the system performance over a range of design conditions. The boundary layer ingested by the propulsion system was approximated using CFD of the NASA N2A configuration with an extended trailing edge, which is a podded configuration. This was performed for a single flight condition. The boundary layer profiles were then normalized and scaled for various flight conditions. The propulsion model employed for this work consisted of modeling the various components individually where the components were the inlet, fan, and nozzle. Note that the fan model did not directly predict the impact of distortion on the fan performance. Instead, a constant efficiency decrease of 1% was assumed based on previous studies.

The boundary layer for this work was determined based on a non-BLI configuration. So the interaction between the aerodynamic and propulsion systems was not accounted for. However, the boundary layer was calculated based on the actual geometry.

**Plas**

Plas [2, 21] developed a methodology to assess the impact of BLI propulsion systems based on parallel compressor theory and the Integral Boundary Layer Equations (IBLE). IBLE is a model derived to calculate the viscous-inviscid flow interactions in a 2D duct. In the noted work, IBLE was used to approximate the boundary layer properties upstream of the propulsor. The inflow was then divided into two streams: one for the low-momentum boundary layer and one for the freestream. Plas noted that the propulsion system impacts the flow upstream and applied an exponential decay with an assumed length scale of two inlet heights to the inflow. Parallel compressor (PC) theory was then applied to obtain the performance of the propulsion system. PC theory is a method to analyze each uniform velocity distribution separately and obtain an overall performance through averaging.

This work illustrates an early effort for quantifying BLI. It attempts to account for the boundary layer upstream of the propulsion system as well as the upstream impact of the propulsion system on the inflow. However, the common theme for the approaches discussed here is that they are unable to account for realistic airframe effects on the inflow ingested by the propulsion system. Also, specific to this method, the interaction between the aerodynamics and propulsion system is not resolved. Instead, the interaction is addressed by assuming that the boundary layer varies exponentially as it approaches the inlet.

**Hardin et al.**

Hardin et al. [23] performed analyses of an HWB configuration with asymmetric BLI propulsion. The study looked at the impact of BLI relative to a podded configuration. The boundary layer was obtained from CFD simulations of the NASA N2A configuration with an extended trailing edge, which is a podded configuration. The boundary layer approximation obtained from the non-BLI configuration was then used to define

the inflow to the engines. The propulsion model used for this work was the Numerical Propulsion System Simulation (NPSS) tool [24]. Specifically, a typical Ultra High Bypass (UHB) turbofan NPSS model was modified to allow for the ingestion of the boundary layer. The developed methodology allowed for the prediction of the BLI propulsion system for various operating conditions and a fixed boundary layer based on a non-BLI configuration.

This work was not focused on design. The goal was to simply quantify the impact of a BLI configuration. In order to do that, the interaction between the airframe and the propulsor was neglected. The boundary layer ingested by the engines not only were for a non-BLI configuration but they were also fixed with no influence from the propulsor.

**Gladin**

Gladin [25] developed a sizing methodology for BLI propulsion systems. The boundary layer ingested by the propulsor was obtained using XFOIL, which is a 2D airfoil design tool. Similar to the work of Plas [2, 21], the influence of the propulsor on the boundary layer was modeled. The region of influence upstream of the inlet was referred to as the preentry zone. In the preentry zone, this model allowed the boundary layer thickness to increase parametrically as the flow approaches the inlet. The boundary layer was used along with the freestream flow conditions to define two uniform velocity profiles entering the propulsor. PC theory was then employed to model the propulsor performance. This model was used to create a BLI propulsor module for the NPSS cycle analysis tool.

This work provides a valuable tool for the conceptual sizing of BLI systems. However, the use of XFOIL for defining the boundary layer ingested by the propulsor effectively decouples the engine from the airframe. The author does model the coupling between the inflow and the propulsor but this work still neglects the dependency between the airframe and the inflow.

**Welstead et al.**

Welstead et al. [18] performed studies to quantify the performance of the STARC-ABL configuration and obtain a realistic prediction of the fuel reduction benefit that includes the losses associated with the turboelectric system. The boundary layer ingested by the tail-cone thruster was obtained from CFD simulations of the aft region of a modified Boeing fuselage, which was a non-BLI configuration. The resulting boundary layer profiles were then normalized and scaled to accomodate a range of flight conditions that were not simulated using CFD. Finally, the boundary layer profiles were used to calculate mass-averaged values of total pressure and Mach number to be used as inputs to the propulsion model. The propulsion model used for this work was the GE hFan propulsion model that was developed by Georgia Tech and implemented in the NPSS cycle analysis tool. This model allows for the simulation of both conventional turbofans and electrically driven fans.

The goal of the noted work was to quantify the performance of the STARC-ABL and obtain a realistic prediction of the benefit including the losses associated with the turboelectric system. The boundary layer ingested by the propulsor were obtained based on simulations of a non-BLI configuration and the analysis assumed a fixed boundary layer. This does not model the impact of the propulsor on the boundary layer upstream.

**Budziszewski et al.**

Budziszewski et al. [12] performed analyses to assess the impact of the boundary layer on the performance of a BLI propulsor. The boundary layer was obtained using XFOIL, a 2D design tool for airfoils. Since XFOIL doesn't provide velocity distributions, the boundary layer results from XFOIL were combined with the definitions of momentum and displacement thicknesses to obtain a velocity distribution. This velocity distribution was then separated into two uniform velocities entering the propulsor; one for freestream conditions and one to represent the low momentum flow

in the boundary layer. Finally, the propulsor was modeled using parallel compressor theory.

This work provides a valuable methodology for analyzing the variation in performance of a given propulsor for variations in inflow. However, it is limited for the application of multidisciplinary design since the analysis is decoupled from a concrete design. Not only is the impact of the propulsor on the inflow not accounted for here, but the inflow is also independent of the airframe.

**Aerodynamic Focused Approaches**

Aerodynamic focused approaches generally aim to quantify the aerodynamics of BLI configurations while either defaulting the propulsion system or leaving it out completely. These approaches offer insight into the various ways that the propulsion system influence can be included in the aerodynamic analysis. The following discussions present some key approaches that are available in the literature.

**Kawai et al.**

Kawai et al. [26] performed design analyses for an HWB configuration with BLI propulsion and Active Flow Control (AFC). AFC was used in the study to control the boundary layer upstream of the inlet. The goal of the work was to assess the tradeoffs between various podded and BLI nacelle installations with and without AFC. The analysis performed consisted of performing CFD where the propulsion system was included via boundary conditions. For this case, the boundary conditions consisted of specifying the mass-flow rate through the propulsor based on some typical values. Additionally, some of the cases were performed using CFD with flow-through nacelles to investigate the propulsion airframe integration (PAI) effects.

This work is an example of a case where the impact of a propulsor on the airframe is considered. However, the coupling between the two systems is not considered.

Additionally, the propulsor performance inflow is not necessarily known prior to performing the analysis. So a method such as this would not be sufficient for the design of the aeropropulsive system. This work did not aim to necessarily design both systems but instead investigated the tradeoffs associated with the various installations.

**Carter et al.**

Carter et al. [27] employed CDISC and the USM3D flow solver to perform knowledge-based design of inlets for an HWB configuration with asymmetric BLI propulsors. The design study was performed in preparation of a wind-tunnel test. The goal of the inlet design was to improve some undesirable flow observations such as shocks and flow separation based on some previous analyses. The model considered here had only flow-through nacelles to represent the model that was to be tested in the wind tunnel.

This work is an example of performing decoupled design. Note that the goal for this work was not to consider the interaction between the airframe and the propulsor. Because of that, the propulsion system was not considered.

**Atinault et al.**

In this work, a numerical method for simulating a BLI configuration using an actuator disk [28] was conducted. The actuator disk was developed based on experimental results obtained from a wind tunnel test of a BLI configuration model with an electrically powered fan. The results of the study allowed for the development of an actuator disk model for the given configuration and propulsor. This actuator disk was then used in a CFD simulation to include the impact of the propulsion system.

This work illustrates a valuable method for including the impact of a propulsion system on the airframe and includes the interaction between the two systems. However, actuator disk methods require user-specified definitions to define the pressure jump across the disk. In general, this information is not known prior to performing the analysis. Additionally, methods like this do not directly allow for performing

design of the propulsion system.

**Elmiligui et al.**

In this work, a study was performed to investigate the performance tradeoffs for four different BLI configurations and to look at the sensitivities of the performance to the inlet area and the inlet to exit area ratio [29]. The four BLI configurations considered for this study were full-annular BLI variations with a thruster at the aft end of the fuselage. The analyses consisted of performing RANS simulations using sink/source boundary conditions (BCs) to include the impacts of the propulsor. The sink was applied at the inlet BC and the source applied to the exit BC. The source BC requires user-specified values of total pressure and total temperature. The solver then automatically determines the sink boundary conditions by adjusting the back pressure at the inlet to match the mass flux consistent with the source condition.

This work illustrates a valuable method for including the impact of the propulsor on the airframe. But again, this method requires the output of the propulsor to be known prior to the analysis. It also does not consider the impact of the airframe on the propulsion system performance.

**Sharma**

Sharma [30] developed a methodology for the design of an inlet for an HWB configuration with asymmetric BLI. Specifically, the work aimed to provide a method for designing inlets that maximize pressure recovery while minimizing the distortion going into the fan. The boundary layer profiles upstream of the inlet were obtained using Reynolds-Averaged Navier-Stokes (RANS) simulations of the configuration without engines. These profiles are then used as the inflow boundary conditions for a separate RANS simulations of the inlets to perform the design aspect of the work.

This work attempted to perform design of a BLI inlet to maximize the pressure recovery and minimize the flow distortion at the Aerodynamic Interface Plane (AIP).

Only the aerodynamic discipline was considered and, therefore, the interaction between the propulsor and the airframe was neglected.

**Blumenthal et al.**

In this work, a tail-cone thruster was integrated onto the common research model (CRM) [7]. The analysis consisted of RANS simulation with an actuator disk for the tail-cone thruster and NPSS for the two underwing turbofans. In this case, the actuator disk was included with no nacelle. The developed model was used to investigate the performance benefit of BLI relative to a non-BLI baseline configuration.

This work illustrates another application of actuator disk method for including the impacts of the propulsion system on the airframe. The method assumes a thrust for the tail-cone thruster and determines the necessary thrust from the underwing turbofans. Since the thrust is defined prior to the analysis, the impact of the airframe on the propulsion system performance is not included in this method.

**Kenway et al.**

In this work, adjoint-based shape optimization was performed on the STARC-ABL concept to minimize inlet distortion for the aft propulsor [31]. The aerodynamic analysis was performed using a RANS solver. The propulsion system was included in the RANS solver using the actuator zone method with uniform thrust and no swirl components. The analysis also included a parametric geometry model in the OpenVSP tool that was linked directly to the CFD analysis used in the shape optimization. The RANS solver included mesh movement capability to account for the changes in shape of the geometry during the optimization process.

Similar to the other methods, the propulsion system performance is defined prior to the analysis and, therefore, the impact of the airframe aerodynamics on the propulsion system is not considered.

**Summary of Decoupled Approaches**

The decoupled approaches discussed here illustrate some typical examples of methods

used to design and analyze BLI configurations. These approaches differ in various ways but they all have one thing in common; they do not resolve the strong coupling between the aerodynamics and propulsion system. The propulsion focused approaches do not include the impact of airframe shape on the inflow and do not resolve the coupling between the propulsion system and the aerodynamics. The aerodynamic focused approaches illustrate useful ways to perform aerodynamic predictions including the impact of a BLI propulsion system. However, they do not simulate the impact of the aerodynamics on the propulsion system and also do not resolve the coupling between the aerodynamics and propulsion system. The following discussion will present some coupled approaches that address these limitations.

### 2.1.2 Coupled Approaches

Unlike the decoupled approaches, there are fewer examples available in the literature of the implementation of fully-coupled approaches for performing BLI design. Three key approaches involving the shape optimization of a BLI configuration using coupled MDA are discussed in this section.

**Rodriguez**

Rodriguez [32] developed a methodology to perform shape optimization of an inlet for an HWB configuration with asymmetric BLI. The BLI system analysis was performed by coupled MDA consisting of the CFL3D flow solver coupled to the NEEP cycle analysis tool. CFL3D is a structured RANS solver developed at the NASA Langley Research Center and NEEP is a one-dimensional, steady state cycle model developed at the NASA Glenn Research Center. The coupled MDA was implemented into NPSOL, which is a gradient-based nonlinear optimizer capable of handling both linear and nonlinear constraints. The optimization problem consisted of minimizing the fuel burn by changing the shape of the inlet while holding the engine and aircraft weight constant. The gradients for the optimization problem were computed based

on the complex variables method. This method was chosen due to an improvement in robustness relative to the standard finite differencing method. However, the complex arithmetic required for gradient computations significantly increased the time per solution relative to the finite differencing method. Two optimizations were performed in this work. The first optimization problem considered the standard podded HWB configuration. This analysis considered 18 design variables including angle of attack, inlet back pressure, wing twist, and 15 variables describing the shape and orientation of the inlets. The results of this optimization were a 10% reduction in fuel burn by way of 23 counts reduction in drag. Interestingly, the pressure recovery of the inlets actually decreased relative to the baseline in order to further reduce drag. This is a great example of a nonintuitive solution that can be obtained using MDAO even for a standard podded configuration. The second optimization problem was for the BLI configuration. This problem was separated into two suboptimization problems that considered the centerline nacelle and outer nacelle individually. The centerline nacelle was optimized using 16 design variables while 22 design variables were used for the outboard nacelle due to its asymmetry. The result of this optimization was a 7% reduction in fuel burn relative to the baseline BLI configuration.

This work has illustrated the application of coupled MDAO to BLI design. The developed method was shown to be very computationally expensive. It also was not robust due to issues with convergence and proper computation of the gradients. Because of this, the podded configuration was actually shown to be the optimal configuration for this study. The author notes that this is likely due to the small number of design variables considered because of the extreme computational requirements.

**Gray et al.**

In this work, an adjoint-based method was developed to perform shape optimization of the STARC-ABL configuration [5, 33]. The coupled MDA approach employed for this work consisted of the ADFlow flow solver coupled to the pyCycle propulsion

modeling tool. ADFlow is a structured RANS solver with adjoint capability and pyCycle is a 1-D thermodynamic cycle model developed using OpenMDAO. pyCycle allows the propulsion model to be described component by component. It also has the capability of computing adjoint derivatives. OpenMDAO was used to calculate the coupling derivatives between the two subsystems. The optimization problem for this work aimed to minimize the shaft power required from the BLI propulsor for a given net force requirement by modifying the shapes of both the inlet and the aft-portion of the fuselage. Three cases were considered with three net force requirements of 9,000 N, 11,000 N, and 13,000 N, where these values represent the amount of thrust provided from the under-wing turbofans. Note that this optimization problem did not consider the under-wing turbofans in the analysis. The thrust provided by the under-wing turbofans are simply provided as an input to the analysis to consider the trades between different power splits.

The resulting optimization problem illustrates a promising step in the right direction for the design of BLI propulsion configurations. The coupling between the aerodynamics and the propulsion system is fully resolved and application of the adjoint method for gradient computations results in a drastic decrease in computional cost relative to the previously discussed method.

**Ordaz et al.**

Similar to the previous work, Ordaz et al. implemented an aeropropulsive adjoint approach into the FUN3D flow solver to perform shape optmization [34]. FUN3D is an unstructured RANS solver with adjoint capability developed at the NASA Langley Research Center. The propulsion system analysis used for this work consisted of an actuator disk model. The developed approach was employed to optimize the aft-portion of the fuselage along with three design variables defining the thrust coefficient, tip speed ratio, and diameter for the actuator disks representing the wing-tip and tail-cone rotors of the PEGASUS hybrid electric aircraft concept. The shape optimization

was performed to minimize the total flow power for the wing-tip and tail-cone rotors with the results showing a modest improvement.

This work illustrates another example of an adjoint-based approach for the application of shape optimization for BLI configurations. The coupling between the aerodynamics and the propulsion system was fully resolved and application of the adjoint method for gradient computations resulted in a computationally efficient means for performing shape optimization.

### 2.1.3 Summary of Observations

From the provided discussion, it is clear that the decoupled approach has been heavily utilized for the analysis and design of BLI systems. This approach has been shown to be insufficient for resolving the strong coupling between the aerodynamics and propulsion systems. Additionally, three promising methods for performing coupled MDAO were discussed. The methodology employed by Rodriguez accounts for the coupling between the disciplines [32]. However, it has limited application in design due to its extreme computational cost. Finally, Gray et al. and Ordaz et al. employed adjoint-based approaches to perform coupled MDAO of BLI configurations [5, 33, 35]. The application of the adjoint resulted in a practical method for performing coupled MDAO of BLI configurations due to the reduced cost associated with the derivative calculations. However, adjoint-based approaches exhibit limitations that have yet to be discussed. One limitation is that while adjoint methods result in significantly reduced computational cost for gradient-based optimization, they are still limited for the application of design space exploration. Performing design space exploration using a gradient-based approach, such as the adjoint method, would require optimizations at a large number of starting points in the design space. This process would be prohibitively expensive. Another limitation is that the adjoint method consists of rigid formulations with fixed objective functions. Any changes to objective functions

or the addition of disciplinary models to the analysis require modification to the source code. This is an important limitation that needs to be discussed further. Adjoint methods are intrusive in nature, as they require access to the source code. The issue that arises is that access to the source code is not always available to the user. Additionally, every user will not initially possess the knowledge and experience required to efficiently implement such a method to realize the computational benefit. A desirable method, therefore, should not require access to the source code. Based on this discussion, a method is needed that is not computationally restrictive and does not require access to the source code since it is not always available to the user.

## *2.2 Reduced-Order Modeling*

One potential solution to this problem is reduced-order modeling. Reduced-order models (ROMs) allow for rapid predictions of field variables based on a given high-fidelity analysis. ROMs have been used in a variety of applications such as unsteady aerodynamic predictions, flutter predictions, and design optimization of airfoils [36, 37]. Recently, the German Aerospace Center (DLR) has illustrated the use of ROMs in an MDAO framework [8, 38]. In the work by DLR, an MDAO framework was developed to perform shape optimization and structural sizing of an aircraft. The MDAO framework consisted of an outer loop and an inner loop. In the outer loop, the aircraft shape optimization was performed based on an aerodynamic analysis. In the inner loop, the internal structure was sized based on critical load analysis performed by simulating the aeroelastic system for a range of load conditions. This is a very expensive analysis if only high-fidelity models are used. In order to reduce the computational cost, DLR employed ROMs. The ROMs were created based on a set of snapshots produced by the full-order model (FOM) at select parameter combinations and then interpolation methods were used for predicting untried parameter combinations. An illustration of the ROM-based MDAO framework used by DLR is

provided in Figure 7.

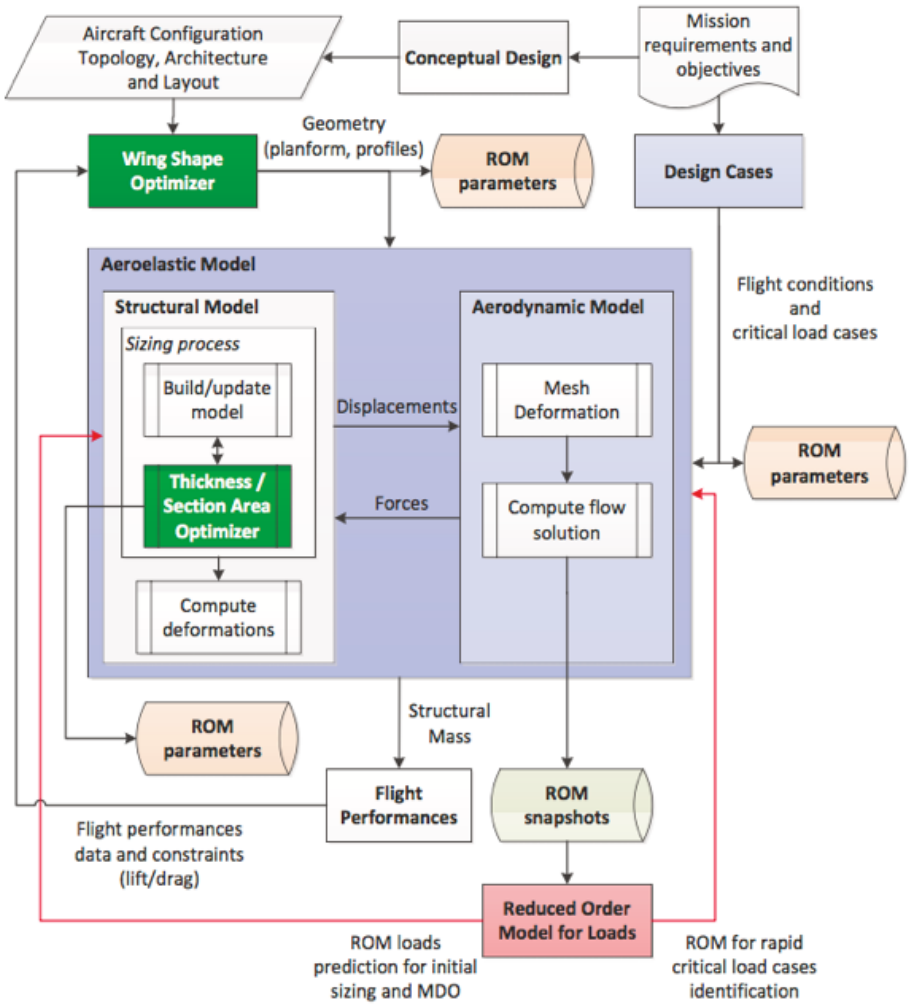


Figure 7: DLR MDAO Framework [8].

As shown in Figure 7, ROMs were employed in both the inner and outer loops. For the outer loop, a ROM was created based on flowfield snapshots of the CFD. The parameter combinations for this ROM consisted of wing shape variables and were obtained by performing a Design of Experiments (DOE). Each wing shape in the DOE was simulated in CFD and the resulting flowfield snapshots were used to create a ROM. The resulting aerodynamic ROM provided a capability of rapid flowfield predictions at untried wing shapes. Note that this ROM only had to be created once prior to the optimization. An illustration of the prediction capability of this

aerodynamic ROM is illustrated in Figure 8.

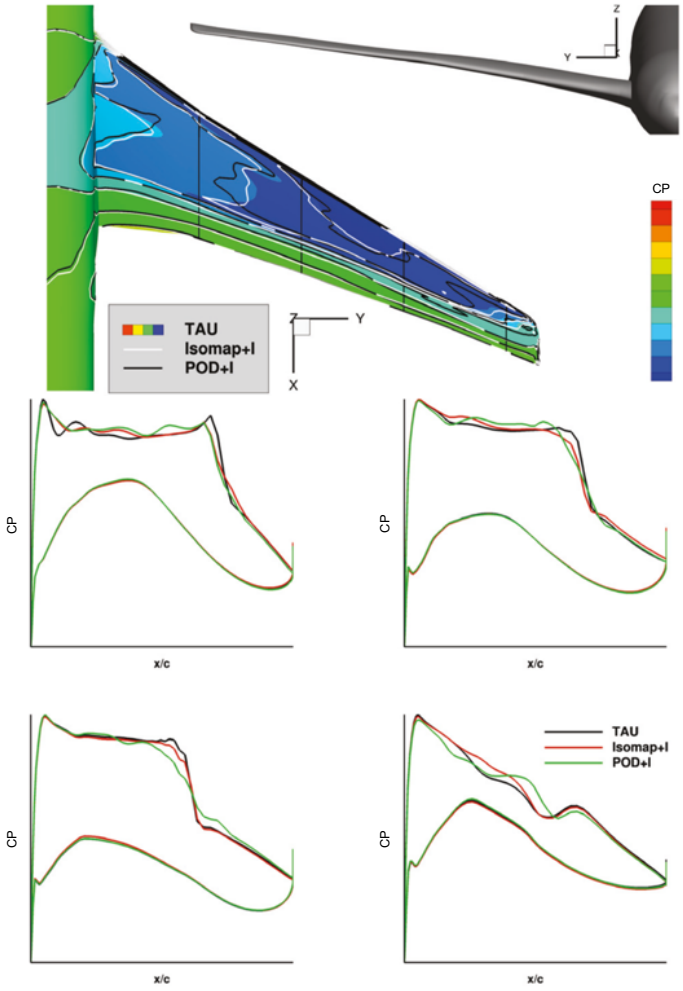


Figure 8: Aerodynamic ROM [8].

In the inner loop, a ROM was created of the aeroelastic model, which consisted of CFD coupled to a Finite Element Analysis (FEA). The DOE for this ROM consisted of sampling the ranges of Mach numbers and altitudes shown in Figure 9. Note that this ROM had to be created once per outer iteration due to the changes in the wing shape. As a result, the high-fidelity aeroelastic model consisting of CFD coupled to FEA still had to be used in the iterative loop. However, a much smaller number of load cases had to be simulated using the high-fidelity aeroelastic model. The ROM could then be used to rapidly predict a large number of load cases. Because of the rapid predictions of load cases provided by the ROM, DLR found that they could actually

consider significantly more load cases than if using only the high-fidelity models. This resulted in the ability to identify critical load cases that otherwise would have been missed. An illustration of the prediction capability of this aeroelastic ROM is illustrated in Figure 10.

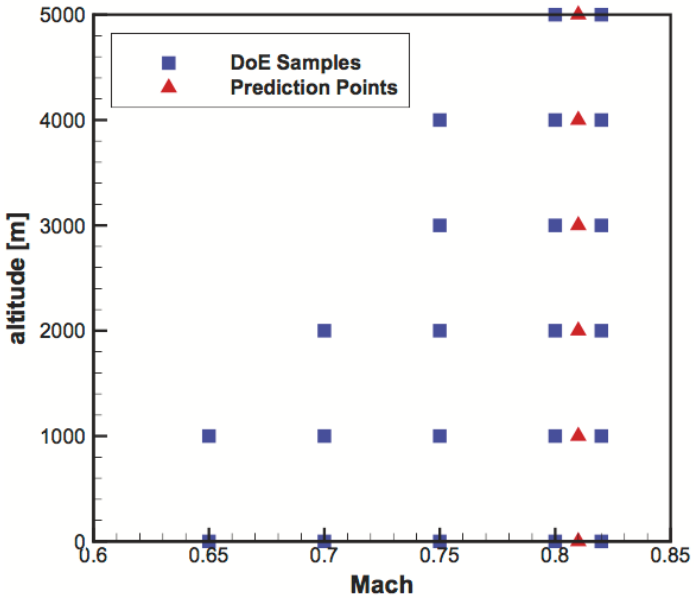


Figure 9: DOE for Aeroelastic ROM [8].

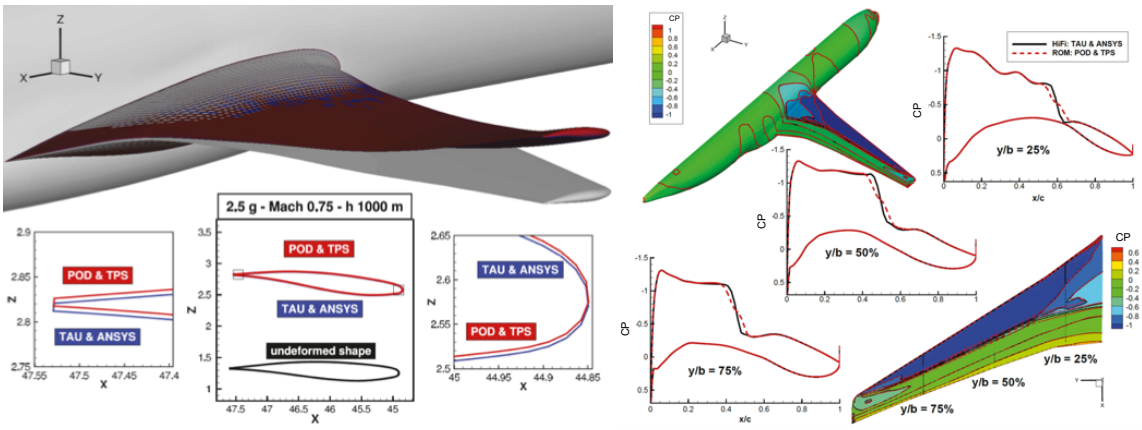


Figure 10: Aeroelastic ROM [8].

The work presented here illustrates a useful application of reduced-order modeling that can be applied to other problems such as the analysis of BLI configurations discussed in this thesis. ROMs could be used in place of the expensive full-order models

to drastically reduce the computational requirements. For this work, a CFD-based ROM can be created to perform aerodynamic predictions, which can be subsequently coupled to a propulsion model to provide a practical method for performing MDAO and design space exploration for BLI configurations. The following subsections provide an overview of reduced-order modeling for the prediction of steady aerodynamics and a detailed discussion of the ROM method used for this work.

### 2.2.1 ROM Overview

Reduced-order modeling is one of three classifications of surrogate modeling with the other two classifications being data-fit and model hierarchy [39]. Data-fit surrogate models, which involve the regression of a set of data, are the most common surrogate model classification. A well-known example of this is the Response Surface Methodology (RSM). The model hierarchy classification involves a reduction in model fidelity. This typically involves making simplifying assumptions. A well-known example would be the Euler equations. The Euler equations represent a surrogate model of the Navier-Stokes equations based on the simplifying assumption of negligible viscous effects. Finally, the reduced order modeling classification involves the reduction in dimensionality of either a set of data or the governing equations. This is the classification being considered for the present work. Reduced-order modeling was selected over data-fit surrogates and model hierarchy for the following reasons. Data-fit surrogate modeling does not allow for the prediction of field variables. This is an issue for the present problem since one of the goals is to be able to provide pressure distributions and velocity profiles in the boundary layer. Additionally, model hierarchy methods consist of simplifying assumptions to the governing equations, and, therefore, reduce the fidelity of the analysis. This is not to say that ROMs are definitively higher fidelity but since ROMs consist of reductions in the dimensionality and not simplifying assumptions related to the physics of the problem, they offer the potential to provide

higher fidelity predictions.

Reduced-order modeling can be broken down to three steps. The first step is to perform a DOE of the design space. The second step is to simulate the DOE using the FOM to provide snapshots. Note that each snapshot represents a unique parameter combination from the DOE. The third and final step is to fit the reduced-order model. This step varies depending on the method used but the basic concept is to represent the high-dimensional space described by the snapshots as a reduced-dimensional space that can then be used for predictions at untried parameter combinations.

ROMs can be either projection-based or interpolation-based. Projection-based ROMs are a class of intrusive methods, which operate on the governing equations directly. These methods work by substituting the reduced-dimensional representation of the solution space into the governing equations. The governing equations are then projected onto the reduced-dimensional space. Finally, the governing equations are solved on the reduced-dimensional space to perform predictions at untried parameter combinations. This class of ROMs offers the benefit of being physics-based but requires access to the governing equations. Interpolation-based methods, on the other hand, are nonintrusive. These methods provide predictions at untried parameter combinations by performing interpolation on the reduced space directly. As discussed previously, nonintrusive methods offer the benefit of greater applicability due to the fact that the governing equations are not always accessible to the user. Based on this discussion, interpolation-based ROMs were used for this thesis.

Based on the provided discussion, an interpolation-based ROM method is needed that is capable of performing predictions of field variables at untried parameter combinations. Interpolation-based ROMs depend on a method for determining a reduced-space based on the snapshots obtained from the full-order model. A variety of methods exist for obtaining the reduced-space such as Proper Orthogonal Decomposition (POD), isomap, Fourier Model Reduction (FMR), Reduced-Basis (RB) method, along

with various other techniques [40, 41, 42, 43, 44, 45, 46, 47, 48, 49, 50, 51, 52, 53, 54]. For this work, the POD method was employed for obtaining the reduced-space due to the following reasons:

1. POD has extensive engineering applications and has proved to be reliable for aerodynamic predictions.

2. It is readily available in a variety of platforms such as Matlab, Python, etc.

It is important to note that the methodology discussed in this work does not depend on the POD method. Any ROM method meeting the given criteria of providing a reduced-space based on a given set of snapshots could be substituted for this component.

POD is a reduced-order modeling method that determines the optimal *linear* basis of a high-dimensional space [55]. It is a highly popularized method and has been applied to a variety of applications such as random variables, image processing, signal analysis, and a variety of aerospace applications. Aerospace applications of POD include steady and unsteady aerodynamic predictions, turbulence modeling, flutter predictions, and spacecraft thermal analysis [37, 56, 57]. POD has also been successfully applied for the application of multidisciplinary analysis and optimization [38, 8, 39, 58]. Prior to providing the details of the POD ROM method, the preliminary step of generating the snapshot matrix is discussed.

### 2.2.2 Generating the Snapshot Matrix

In order to illustrate the process of generating the snapshot matrix, consider the three-dimensional Navier-Stokes equations [59]. The system of equations consist of six unknowns, which are the density, $\rho$, pressure, $p$, temperature, $T$, and velocity

components in all three coordinate directions, $u, v, w$. Any solution to the Navier-Stokes can be expressed using the definition of the residual in Equation 9.

$$\partial_t W + R(W) = 0 \tag{9}$$

Note that $W$ in Equation 9 is the vector of primitive variables and $R$ is the flux residual. This equation represents any solution to the time-dependent Navier-Stokes in three dimensions. For steady-state, the time derivative approaches zero resulting in Equation 10.

$$R(W) = 0 \in \mathbb{R}^{N=nxm} \tag{10}$$

Note that $N$ represents the total dimension of a single solution to Equation 10 where $n$ and $m$ are the number of grid points and primitive variables, respectively. Now consider $S$ combinations of parameters, i.e., DoE entries, that include design variables and/or flow quantities. These combinations result in $S$ solutions to Equation 10 referred to as snapshots. The snapshots can be expressed in matrix form, denoted as $Y$, by Equation 11.

$$Y = (W^1, ..., W^S) \in \mathbb{R}^{NxS} \tag{11}$$

The following discussions will describe how the snapshot matrix in Equation 11 is used to create a ROM using POD.

### 2.2.3 Proper Orthogonal Decomposition

It is important to note that POD can be used for both projection- and interpolation-based reduced-order modeling. The discussion here is limited to the interpolation-based approach. For interpolation-based POD, the process can be described as two steps: 1) obtaining a modal basis and 2) interpolation in the reduced-space.

**Obtaining the Modal Basis**

POD consists of approximating the primitive variables based on a linear superposition of fundamental modes. In order to obtain these fundamental modes, Singular Value Decomposition (SVD) is used. This process will be summarized here. The full derivation can be found in Reference [59]. The process begins by normalizing the snapshot matrix with columns defined in Equation 12 [60].

$$\widetilde{Y}_k = Y_k - \frac{1}{S}\sum_{k=1}^{S} Y_k \tag{12}$$

SVD is applied to the normalized snapshot matrix given in Equation 12. This is shown in Equation 13 [60].

$$\widetilde{Y} = U \sum V^T \tag{13}$$

Note that the matrices $U \in \mathbb{R}^{N\times N}$ and $V \in \mathbb{R}^{S\times S}$ consist of the orthogonal vectors for $\widetilde{Y}\widetilde{Y}^T$ and $\widetilde{Y}^T\widetilde{Y}$ [60]. Also, $\sum \in \mathbb{R}^{N\times S}$ is a diagonal matrix whose entries are obtained by taking the singular values of $\widetilde{Y}$. The nonzero values of $\sum$ are arranged in decreasing order and denoted as $\lambda_k, k = 1, 2, ..., S$ [60]. Then, the next step is to renormalize the projections of $\widetilde{Y}$ onto the column vectors of $V$ to obtain the POD modes as shown in Equation 14 [60].

$$\phi_k = \frac{\widetilde{Y}V_k}{\sqrt{\lambda_k}} \tag{14}$$

Finally, any primitive variable, $\psi$, can be predicted using the expression given in Equation 15 [60].

$$\psi(\theta) = \overline{\psi} + \sum_{j=1}^{S} \alpha_j(\theta)\phi_j \tag{15}$$

The term $\bar{\psi}$ in Equation 15 represents the mean of the ensemble of snapshots for the primitive variable $\psi$ and the $\alpha_j$ terms are the unknown POD coefficients. Note that the $\alpha_j$ terms are a function of the design variables [60].

#### Interpolation in the Reduced-Space

The final step is to use interpolation to perform predictions at untried parameter combinations. This consists of interpolating the POD coefficients, $\alpha_j$, in Equation 15. The coefficients are known for the snapshots. The goal is to interpolate the known values from the snapshots to obtain a prediction for the untried combination. Note that the interpolated solution is given in the original high-dimensional space with no requirement for back-mapping. This is not the case for the next method that will be discussed.

#### POD+I Algorithm

Finally, the algorithm for the interpolation-based POD method can be formally defined. The method is referred to as POD+I following the convention of Reference [54]. The method can be summarized in three steps:

1. Given a DoE of design variables, $\theta$, with $S$ combinations, employ the FOM to obtain snapshots $W = (W^1, ..., W^S)$;
2. Perform POD to obtain reduced basis $\psi(\theta) = \overline{\psi} + \sum_{j=1}^{S} \alpha_j(\theta)\phi_j$;
3. Given new variable combination, $\theta^*$, interpolate POD coefficients to obtain prediction at untried combination $\psi(\theta^*)$.

Note that steps 1 and 2 are by far the most computationally expensive steps of the entire process. However, they are performed offline and only once.

### 2.2.4 ROM Summary

Reduced-order modeling has been presented as a potential method to reduce the computational cost associated with MDAO for highly-coupled design problems and enable design space exploration. ROM methods can be divided into intrusive and nonintrusive methods where intrusive methods require access to the source code of

the analysis model and nonintrusive methods do not. Since access to the source code is not always available, a nonintrusive method known as interpolation-based POD was selected for this work. POD was described to be a method to provide an optimal *linear* basis provided a set of snapshots $W = (W^1, ..., W^S)$ obtained from the FOM. The predictions at untried parameter combinations are then performed by interpolation in the reduced-space. The previous subsections outlined an algorithm to perform interpolation-based POD referred to as the POD+I method. The POD+I method is used for this work to provide coupled predictions for BLI configurations. This is discussed further in Chapter 4. The following chapter provides a detailed description of the objective for this research along with descriptions of the computational methods used.

# CHAPTER III

# PROBLEM FORMULATION

## *3.1 Research Objective*

The previous sections have highlighted the difficulty of performing the design and analysis of BLI configurations due to the strong coupling between the airframe aerodynamics and the propulsion system performance. The design of BLI configurations requires coupled MDA consisting of high-fidelity models for the analyses of both the airframe and propulsion system. Further, MDAO and design space exploration are needed to take full advantage of the BLI technology by allowing for nonintuitive design decisions, which is computationally expensive due to the large number of coupled MDA solutions required. Reduced-order modeling was presented as an enabler for MDAO and design space exploration of BLI configurations. ROMs can be used to reduce the computational cost associated with performing coupled MDA with high-fidelity models. Based on this discussion, ROMs could be employed to accomplish the research objective given below:

| **Research Objective**: |
| --- |
| Develop a computationally efficient methodology for the coupled MDA of BLI configurations. |

The focus of the present research will be to reduce the computational cost associated with coupled MDA to make the MDAO problem more practical. The proposed approach consists of developing a ROM of the aerodynamics as a function of the propulsor operating conditions. The aerodynamic ROM can then be coupled to a propulsion model to provide an efficient means of performing coupled MDA of BLI

configurations. Finally, the ROM-based, coupled MDA approach can be employed for the application of MDAO to evaluate the time-savings offered by the proposed approach. This final step requires the aerodynamic ROM to be extended to include the effect of shape changes on the airframe aerodynamics. This research can be separated into two distinct phases:

1. Development and validation of the ROM-based coupled MDA approach for a fixed configuration

2. Extension and validation of the ROM-based coupled MDA approach for including shape changes and its application to shape optimization

The first phase is discussed in the Chapters 4 and 5 while the second phase is discussed in the Chapter 6. This chapter provides brief explanations of the computational methods employed for this research.

## *3.2 Computational Methods*

This research requires a variety of analysis capabilities including disciplinary models for both the aerodynamic and propulsion system analyses, as well methods for the reduced-order modeling, surrogate modeling, and shape parameterization components of the work. The following subsections present the requirements for each analysis component as well as descriptions of the selected computational methods.

### 3.2.1 Propulsion System Analysis

The propulsion system analysis requirements are as follows:

1. Provide predictions for the increase in total pressure and temperature across the fan as a function of $PR$ and $FPR$

2. Provide predictions for the required shaft power supplied to the fan for the given operating conditions

3. Allow for predictions without the need for a detailed fan performance model

A typical approach to performing propulsion system analysis consists of the application of a fan performance map, which defines the relationships between $FPR$, $\eta_{adiabatic}$, corrected mass flow rate $W_{corr}$, and the corrected fan speed $N_{corr}$ [61, 62]. An example fan performance map is provided in Figure 11. For a given $FPR$ and

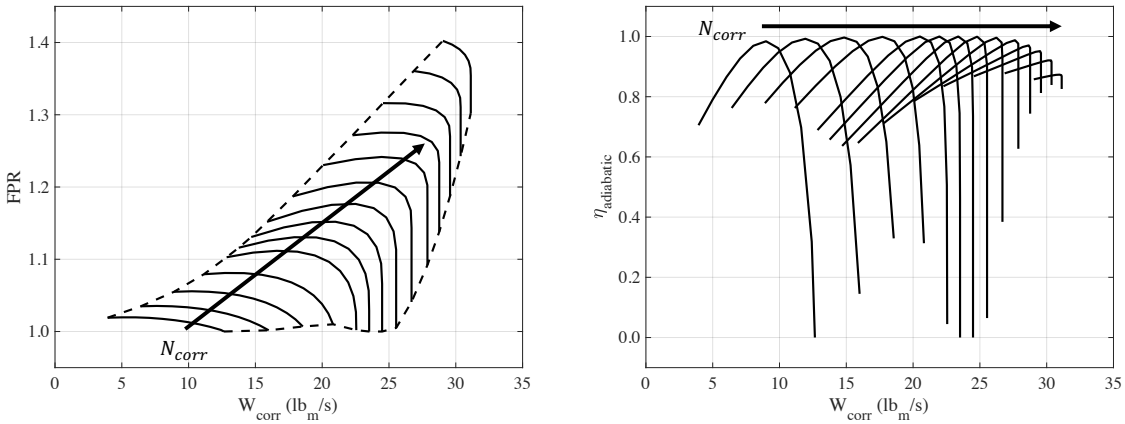


Figure 11: Notional fan performance map.

$N_{corr}$, the fan performance map provides the corresponding $W_{corr}$ and $\eta_{adiabatic}$. There are two main issues with this approach for application to this work:

1. The anlaysis requires a fan performance map, which is not readily available for the considered geometry

2. The outputs of the fan analysis are used as inputs to the aerodynamic analysis and the simultaneous specification of total pressure, total temperature, and mass flow rate is generally not allowed in the aerodynamic analysis

One solution strategy to address the second issue is to have an inner loop consisting of scaling the fan diameter to obtain the mass flow rate provided by the propulsion system analysis [5]. This allows for the total pressure, total temperature, and mass flow rate to be applied simultaneously. For the present work, the fan diameter will be held constant. To accomodate the constant fan diameter, a rubberized fan is

considered for this work. Note that the rubberized component of the fan refers to the actual performance. With this goal in mind, a simple thermodynamic model was selected. This model is outlined in Equations 16 through 19.

$$\eta_{adiabatic} = 1.066 - 0.0866 * FPR \tag{16}$$

$$PR = P_{t,2}/P_{t,\infty} \tag{17}$$

$$P_{t,3} = PR * FPR * P_{t,\infty} \tag{18}$$

$$T_{t,3} = T_{t,2} * [1 + \frac{FPR^{\frac{\gamma-1}{\gamma}} - 1}{\eta_{adiabatic}}] \tag{19}$$

In Equation 16, the adiabatic efficiency is expressed as a linearly dependent function of $FPR$. This model has been employed for similar studies involving BLI configurations [18, 63, 5]. The pressure rise, given in Equation 18, is derived from the definition of $FPR$. Finally, the temperature rise, provided in Equation 19, describes an isentropic compression with a correction for losses. This model is simple and meets all of the given requirements for the propulsion system analysis.

### 3.2.2 Aerodynamic Analysis - FUN3D

The aerodynamic analysis requirements are as follows:

1. Provide viscous flow predictions as a function of the propulsor operating conditions and geometry

2. Allow for direct coupling to a propulsion system analysis via boundary condition specification

For the present work, the FUN3D flow solver was identified to meet the given requirements while also being readily available. FUN3D is an unstructured, node-based, three-dimensional Euler and RANS solver developed at the NASA Langley

Research Center [64]. It is capable of performing steady and time-accurate simulations for both compressible and incompressible flows. A variety of numerical schemes are provided for calculating the inviscid flux quantities, along with various flux limiters and turbulence models. For this work, the Roe flux difference splitting method [65] with the minmod flux limiter was employed for the inviscid flux calculations and the Spalart-Allmaras one-equation turbulence model [66] was employed for the turbulent quantities.

#### *3.2.2.1 Inflow/Outflow Boundary Conditions*

FUN3D includes a variety of boundary condition options for a wide range of applications. The aerodynamic and propulsion system analyses interface at the boundary conditions corresponding to the fan face and exit. In the CFD analysis, the general solution strategy consists of applying an outflow boundary condition at the fan face with a specified back pressure and an inflow boundary condition at the fan exit with a specified total pressure and temperature.

At each point on the outflow boundary, the specified back pressure is applied. For subsonic flow, the velocity and temperature at each point are extrapolated from the interior solution and the density is updated using the equation of state provided by Equation 20. For supersonic flow, the velocity, temperature, and density are all extrapolated from the interior solution.

$$\rho = \frac{\gamma p}{T} \tag{20}$$

The inflow boundary condition consists of applying a specified total pressure and temperature. Additionally, the specification of the velocity direction at the boundary is required. Note that this boundary condition is only applicable to subsonic flow. For this boundary, none of the primitive variables are specified explicitly. Assuming the flow through the boundary is adiabatic and isentropic, the solution process begins with a statement of conservation of total enthalpy, $H_t$, across the boundary, Equation

21, in addition to the outward propagating invariant, $R^+$, illustrated in Figure 12 [9, 67].

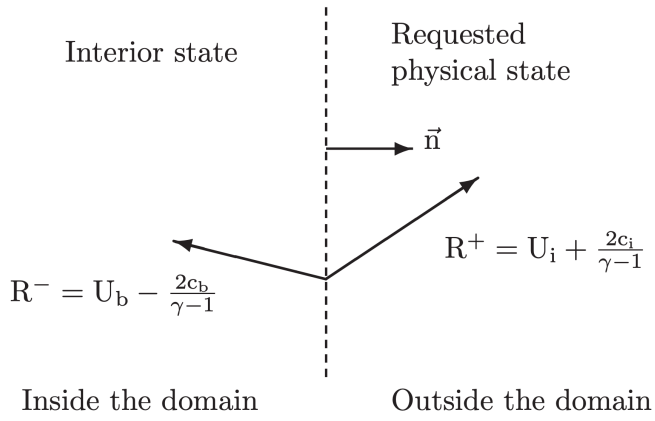


Figure 12: Riemann invariants at a boundary [9].

$$H_t = H_{t_b} = \frac{c_b^2}{\gamma - 1} + \frac{1}{2}(u_b^2 + v_b^2 + w_b^2) \tag{21}$$

The interior propagating Riemann invariant, $R^-$, can be extrapolated to the boundary, resulting in the expression provided by Equation 22.

$$R^+ = -U_b - \frac{2c_b}{\gamma - 1} \tag{22}$$

Equations 21 and 22 can then be combined to obtain the expression provided by Equation 23.

$$H_t = \frac{c_b^2}{\gamma - 1} + \frac{1}{2}(R^+ + \frac{2c_b}{\gamma - 1})^2 \tag{23}$$

Equation 23 can be solved for the speed of sound at the boundary, $c_b$, resulting in the expression provided by Equation 24.

$$[1 + \frac{2}{\gamma - 1}]c_b^2 + 2R^+ c_b + \frac{\gamma - 1}{2}(R^{+2} - 2H_t) = 0 \tag{24}$$

The solution to Equation 24 has the form shown in Equation 25.

$$c_b = -\frac{b}{2a} \pm \frac{\sqrt{b^2 - 4ac}}{2a} \tag{25}$$

Solving for the coefficients provides the expressions provided by Equation 26.

$$a = 1 + \frac{2}{\gamma - 1}, \qquad b = 2R^{+}, \qquad c = \frac{\gamma - 1}{2}(R^{+2} - 2H_t) \tag{26}$$

Finally, the physically consistent result is the maximum of the two roots to the system in Equation 25. The resulting expression for the speed of sound at the boundary is provided in Equation 27.

$$c_b = \frac{\gamma - 1}{\gamma + 1}\left(-R^{+} + \sqrt{\left(1 - \frac{\gamma}{2}\right)R^{+2} + \gamma H_t}\right) \tag{27}$$

Note that this expression is valid for the case of air where $\gamma = 1.4$. For other values of $\gamma$, $a$ in Equation 26 has the potential to become negative. In this case, both outcomes of Equation 25 must be considered with the largest value being the physically consistent solution. The speed of sound at the boundary, $c_b$, can then be used to determine the velocity, $U_b$, Mach number, $M_b$, static pressure, $p_b$, and static temperature, $T_b$, for each point on the boundary using the expressions provided in Equations 28-31. Finally, the density, $\rho_b$, is obtained using Equation 20.

$$U_b = \frac{2c_b}{\gamma - 1} - R^{+} \tag{28}$$

$$M_b = \frac{U_b}{c_b} \tag{29}$$

$$p_b = p_{t,b}\left(1 + \frac{\gamma - 1}{2}M_b^2\right)^{\frac{\gamma}{\gamma - 1}} \tag{30}$$

$$T_b = T_{t,b}\left(\frac{p_b}{p_{t,b}}\right)^{\frac{\gamma - 1}{\gamma}} \tag{31}$$

Based on the inflow/outflow boundary conditions described, the fan boundary conditions are illustrated in Figure 13.

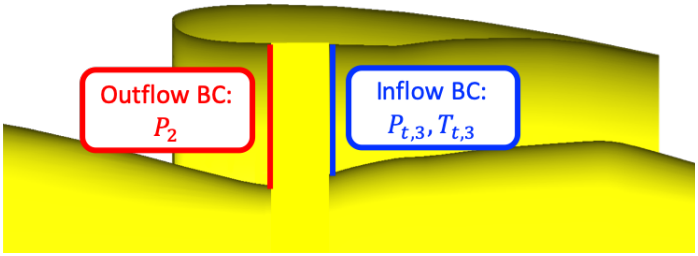


Figure 13: Boundary conditions at the fan face and fan exit.

#### *3.2.2.2 Propulsion BC Coupling*

Additionally, FUN3D offers a capability for propulsion boundary condition coupling. A consistent CFD solution requires mass conservation between the inflow and outflow boundaries. The outputs of the propulsion system analysis are the total conditions at the inflow boundary, i.e., fan exit. The velocity at the inflow boundary is then determined using the method described in Section 3.2.2.1. For a fixed fan diameter, the total pressure, total temperature, and Mach number uniquely define the mass flow rate at the inflow boundary. Similarly, the mass flow rate at the outflow boundary is uniquely defined by the specified back pressure. However, the back pressure and corresponding mass flow rate are not known prior to the CFD simulation. Generally, this requires an iterative CFD analysis consisting of updating the back pressure at the outflow boundary until the target mass flow rate is acheived. This can add unnecessary computational cost due to the required manual restarts of the simulation and slow convergence. The FUN3D propulsion boundary condition capability provides a means to perform this analysis internally without requiring manual restarts of the simulation. At each iteration, the mass flow rate at the inflow boundary is calculated. This is referred to as the driving boundary. Then, FUN3D adjusts the back pressure at the outflow/matching boundary to obtain the target mass flow rate for the following iteration. The process is illustrated in Figure 14. This method allows

each boundary to converge together resulting in a more efficient overall solution.

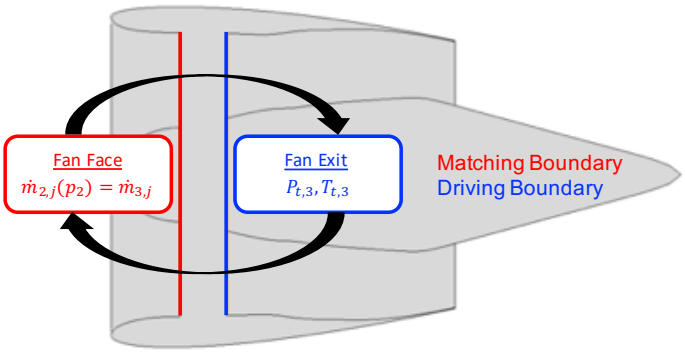


Figure 14: Boundary condition matching process in FUN3D.

#### *3.2.2.3 Grid Deformation Capability*

FUN3D also offers a grid deformation capability. This allows movement of the surface to propagate into the volume of the computational grid by means of solving a linear elasticity system of equations [68]. This prevents the need for recomputing the volume grid when performing shape changes to the surface or body motion.

### 3.2.3 Shape Parameterization - BandAids

The optimization portion of this work requires a shape parameterization method. The requirements for the shape parameterization are the following:

1. Allow for discrete changes of the underlying geometry

2. Perform mapping of the surface grid to the perturbed geometry

There are a variety of methods that are available to perform the shape parameterization [69, 70, 71, 72]. For the present work, the shape parameterization was performed using BandAids, a free-form deformation tool for aerodynamic shape parameterization that is precompiled with the FUN3D software [73, 11].

Given a computational surface grid, BandAids allows the user to isolate the design region of interest and parameterize the surface grid in three steps:

1. Create bivariate surfaces, referred to as marking surfaces
2. Project the surface grid onto the marking surfaces
3. Create a nonuniform rational basis spline (NURBS) representation of the defined design surfaces

An illustration of a marking surface is provided in Figure 15. Additionally, a simple illustration of changes in surface shape due to the movement of the marking surface nodes is provided in Figure 16.

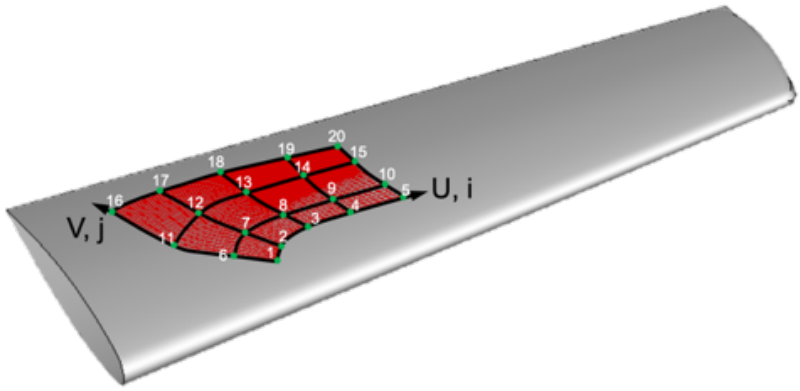


Figure 15: Example marking surface parameterized by 5x4 design variables [10].

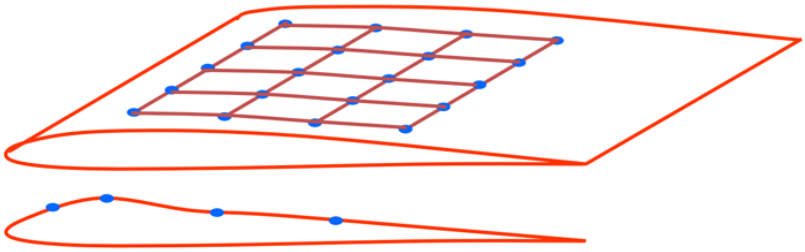

Figure 16: Surface perturbation based on marking surface nodes [11].

Following Step 3, the final result is a NURBS representation of the design surface defined by Equations 32-34.

$$r_n(\nu) = r_n^b + \Delta r_n(\nu) \tag{32}$$

$$\Delta r_n(\nu) = \Delta r(\nu, \xi_n, \eta_n) = \sum_m^M C_m(\xi_n, \eta_n)\nu_m \tag{33}$$

$$C_m(\xi_n, \eta_n) = \frac{\partial r_n(\nu)}{\partial \nu_m} \tag{34}$$

The expression provided by Equation 32 describes the movement of each node of the baseline grid. For each node, the term $r_n^b$ represents the position of the baseline surface, $\Delta r_n$ represents the change in position of the node, and $r_n$ represents the updated position of the node. Note that $\nu$ is the user input for the magnitude of the design variable change at that node location. The change in position of the node is governed by the sensitivity derivatives, given by Equation 34, that are calculated during Step 3. The result is a parameterized model that creates discrete, user-defined surface changes that are propagated to the underlying surface grid. The deformed grid is read into FUN3D, and grid deformation is performed in the volume to accomodate the new surface shape. For more information about the BandAids software, the reader is referred to the original publication [11] and the FUN3D user manual [64].

### 3.2.4 Reduced-Order Modeling - POD+I

The reduced-order modeling method used in this work is referred to as POD+I and was described in Section 2.2.2. The method can be separated into two components:

1. Dimensionality reduction via POD

2. Interpolation

POD has been widely used and implemented into a variety of software platforms. The POD method available in MATLAB's Statistics and Machine Learning Toolbox was used for this work [74].

For the interpolation, the objective is to solve for the POD coefficients given an untried design variable combination not included in the snapshots. For this work, the

interpolation was performed using the surrogate modeling method known as kriging. Kriging is a surrogate modeling method based on solving an optimization problem to minimize the mean squared error of the predictions and has been successfully applied to a variety of applications, including the prediction of POD coefficients [75, 76, 59]. The Design and Analysis of Computer Experiments (DACE) toolbox was utilized for the kriging model in this work [77].

The inputs to the kriging model are the $X \in \mathbb{R}^{S \times d}$ design sites, the $Y = \alpha \in \mathbb{R}^{S \times M}$ responses corresponding to the POD coefficients, and the new design site $\theta^* \in \mathbb{R}^d$. Note that $S$, $M$, and $d$ correspond to the number of snapshots, the number of POD modes, and the number of design variables. The kriging model prediction for the new design site is given by Equation 35.

$$\alpha_i(\theta^*) = \sum_{n=1}^{j} \beta_{n,i} f_n(\theta^*) + \sum_{n=1}^{S} \gamma_{n,i} r(\theta^*) \tag{35}$$

Note that the prediction provided in Equation 35 corresponds to the POD coefficient at the untried design site for the $i^{th}$ POD mode. This prediction is then repeated for all $M$ modes. The first summation in Equation 35 represents the regression function for the prediction where $f$ and $\beta$ are the function terms and weights, respectively, and $j$ depends on the user-defined order of the polynomial regression function. The second summation represents the error estimate resulting from the least squares regression, where $r$ and $\gamma$ are the correlation function and weights, respectively. Note that the $\beta$ and $\gamma$ matrices are the most computationally expensive part of the kriging model prediction due to the requirement of solving an optimization problem to minimize the mean squared error. However, these terms are only computed once during the offline phase of the POD+I method, and only the $f$ and $r$ vectors have to be recomputed during the online phase. For full details of the kriging model used in this work, the reader is referred to the DACE toolbox documentation [77].

## *3.3 Research Scope*

The primary goal of this research is to develop an efficient method for coupled MDA, using reduced-order modeling, to enable the coupled MDAO of BLI configurations. With that goal in mind, certain aspects of the work have been simplified such as the propulsion system analysis model that was discussed in the previous section. Additional simplifications include the geometry and flight condition, which are discussed in the following subsections.

### 3.3.1 Tail-cone Thruster Concept

BLI concepts have been separated into two categories: full annular BLI (BLI-FA) and asymmetric BLI (BLI-Asym) [12]. This terminology is in reference to both how the propulsion system is mounted on the airframe and the nature of the flow entering the engine. Asymmetric BLI consists of engines that are integrated into the airframe, whereas full-annular BLI typically consists of mounting the propulsion system on the aft-portion of the fuselage. The full-annular configuration has also been referred to as the Tail-cone Thruster (TCT) concept. An illustration of full-annular and asymmetric BLI configurations is given in Figure 17.

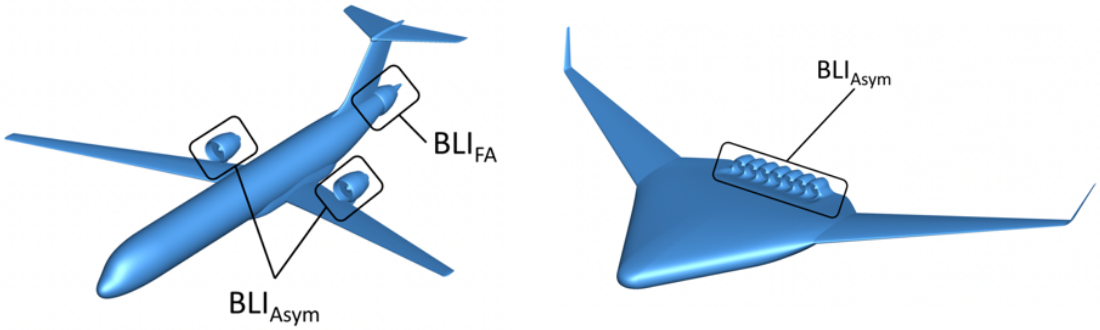


Figure 17: BLI Categories [12].

Both categories of BLI potentially offer fuel burn reduction benefits. However, the design of the asymmetric BLI is much more challenging due to the highly nonuniform flow ingested by the engine. This highly nonuniform flow can have detrimental

effects on the propulsion system performance and potentially even result in damage to the fan and/or compressor blades. Full-annular BLI configurations also experience nonuniform flow with both radial and circumferential distortion. However, the circumferential distortion for full-annular BLI configurations will generally be less significant relative to asymmetric BLI configurations. And since radial distortion is presumed easier to mitigate by tailoring the twist of the fan and/or compressor blades, the full-annular BLI category is generally regarded as a lower risk option. This has led organizations such as NASA and GE to pursue the TCT configuration [13]. The primary concept being considered is known as the STARC-ABL concept, which is illustrated in Figure 18. This concept employs an electrically driven, ducted fan on the aft portion of the fuselage, which is powered by two under-wing turbofans as illustrated in Figure 18. Preliminary analysis of the STARC-ABL concept projects the benefits to include an increase of 2.6% in TSFC and a 3 to 4% reduction in fuel burn with only a 1% empty weight penalty [13]. Current efforts by NASA and GE aim to test this configuration in the wind tunnel to better quantify the aeropropulsive benefits. Because of the current interest in the TCT configuration, it will be the focus of this thesis.

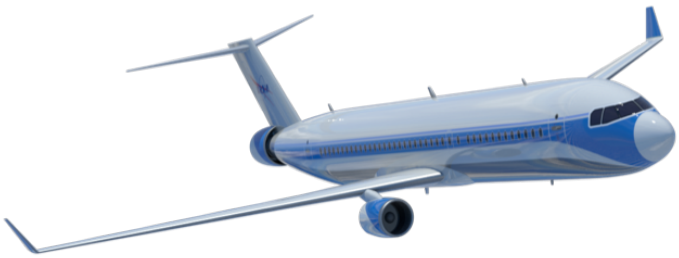

Figure 18: Single-aisle Turboelectric AiRCraft with Aft Boundary Layer (STARC-ABL) Propulsion [13].

### 3.3.2 Test Configuration

The test configuration for the present work is representative of a wind tunnel configuration derived from the STARC-ABL concept. The wings were removed from the

configuration due to sizing constraints in the wind tunnel. Additionally, the tail was removed for the present analyses. These simplifications reduce the complexity of the shape parameterization. In reality, the tail, and potentially the wings, will increase the distortion experienced at the fan face and reduce the fan efficiency. Because of this, the shape optimization results would likely be different with the tail and wings included on the geometry. However, since the purpose of the shape optimization is simply to demonstrate the ROM-based, coupled MDA approach, the simplification was considered acceptable. The simplified geometry is referred to as the TCT concept for the remainder of this work. An illustration of the TCT concept is provided in Figure 19.

Figure 19: TCT concept.

The geometry in Figure 19 measures 18.2 ft in length with a maximum diameter of 1.96 ft and a 1 ft fan diameter. This geometry is representative of a proposed model designed for a test in the 11-ft Wind Tunnel at the NASA Ames Research Center.

### 3.3.3 Flight Condition

Since this is a concept that was developed for wind tunnel testing purposes, the design flight condition is not available. For this work, a representative cruise condition is used for the STARC-ABL concept consistent with the work of Gray [5, 33]. The flight conditions are provided in Table 2. Note that these conditions are used for all analyses conducted for this research.

Table 2: Representative cruise condition for TCT concept analysis.

| | |
|---|---|
| Cruise Altitude | 37,000 ft. |
| Mach number | 0.72 |
| AoA | 0° |

### 3.3.4 Shape Optimization

The shape optimization for BLI configurations is a complex problem that consists of simultaneously optimizing the fuselage design, propulsor size, and nacelle design with the performance of each being highly coupled. For the present work, the optimization is limited to the aft-portion of the fuselage with the goal of improving the flow quality ingested by the fan. An extension of this to a more complex shape optimization, including sizing of the propulsor and shaping the nacelle, may be considered in future studies. The exact details of the optimization are provided in Chapter 6.

## *3.4 Computational Grid*

The grid generation was performed using Pointwise® v18.2 [78]. Pointwise® is a structured and unstructured grid generation software with an intuitive interface and CAD clean-up capabilities. The geometry surface is divided into user-defined computational domains. For each domain, the user can specify the point density and spacings on the connectors defining the outer edges of the computational domains. Additionally, Pointwise® offers the user a variety of metrics for controlling the density of the interior of the domains. For unstructured grids, Pointwise® is capable of generating both mixed-element and all-tetrahedral grids. The boundary layer is resolved using anisotropic tetrahedra known as T-Rex cells, which can be combined into prisms to generate mixed-element grids. Grid generation is a two-step process consisting of generating the surface grids and volume grids separately. This allows for more control compared to single-step grid generation software. Pointwise® is heavily documented, including a variety of tutorials, theory description, and a wide array of

scripts available that enable automation of common grid generation problems.

For the present work, Pointwise® was used to generate an unstructured, mixed-element grid for the TCT concept. The surface grids consist of isotropic triangle elements with the exception of the leading edge of the nacelle, where quadrilateral elements were used to better resolve the surface curvature. The quadrilateral elements provide enhanced curvature resolution with fewer cells due to the option for aspect ratios greater than one. The boundary layer was resolved using T-Rex cells that were then converted to prisms. The boundary layer growth rate was specified to be 1.2 corresponding to a 20% growth rate with a $y^+$ of 1 based on the length of the fuselage. Additionally, the fan face and exit boundaries were constrained by the match boundary condition to allow proper boundary layer growth from the adjacent surfaces. Note that both half- and full-span versions of the computational grid were used for this research, where the full-span was created by mirroring the half-span grid. The half-span grid was employed for the development and validation of the coupled MDA approach, while the full-span grid was employed for the shape optimization to eliminate grid deformation issues at the symmetry plane. An illustration of the computational grid for the TCT concept is provided in Figures 20 and 21. Additionally, the grid metrics for both the half- and full-span versions of the grid are provided in Table 3.

It is important to note that a grid resolution study was not performed for this work. This research focused on the development and demonstration of a ROM-based, coupled MDA approach where the CFD analysis was assumed to be the truth model. For real-world applications, a grid resolution study would be needed to increase the confidence in the CFD analyses, since the ROM predictions are only as accurate as the underlying CFD solutions.

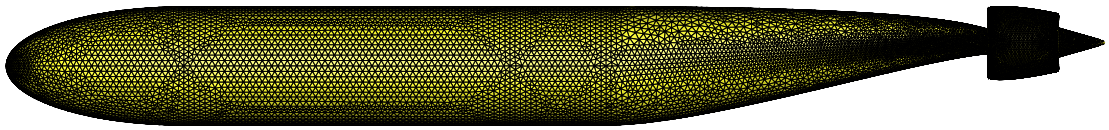

(a) Side view

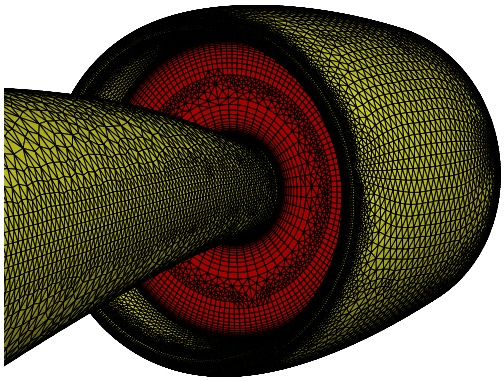

(b) Fan face

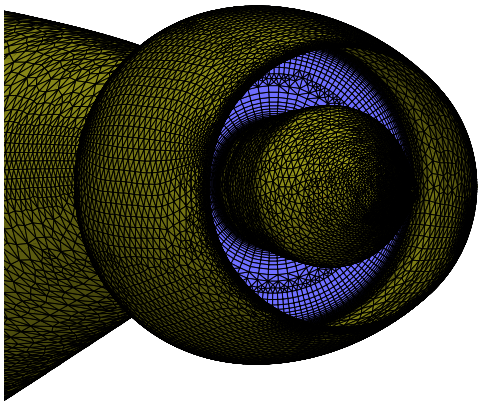

(c) Fan exit

Figure 20: Computational grid for the TCT configuration.

Table 3: Grid metrics for TCT concept.

| | Half-Span | Full-Span |
|---|---|---|
| Nodes (millions) | 0.96 | 1.93 |
| Cells (millions) | 2.01 | 4.02 |

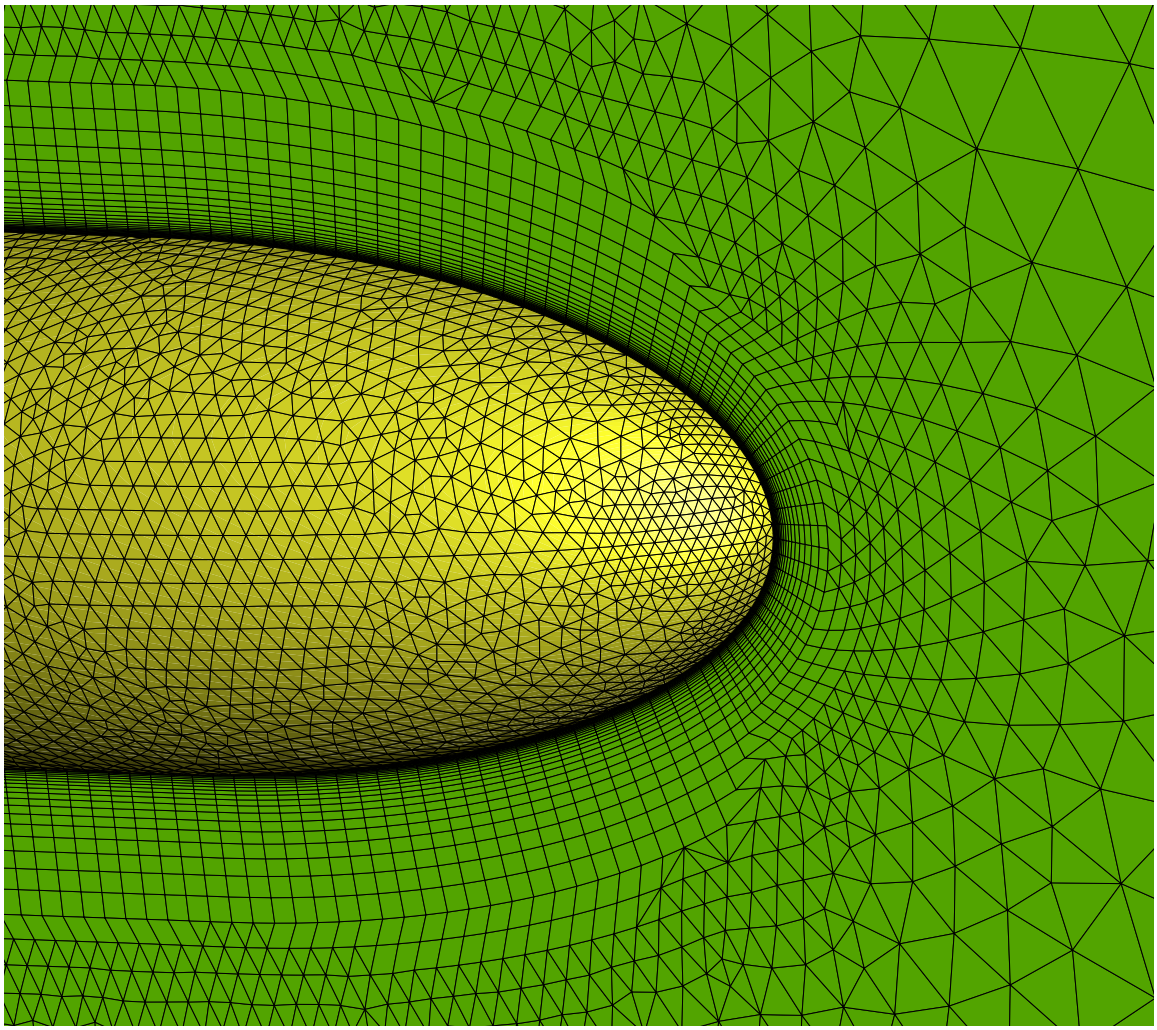

Figure 21: Boundary layer growth on fuselage surface.

# CHAPTER IV

# AERODYNAMIC ROM (RESEARCH QUESTION 1)

As a first step toward the proposed ROM-based coupled MDA approach, this chapter focuses on the development and validatation of the aerodynamic ROM. The goal is to create a ROM capable of performing predictions over a range of propulsor operating conditions. The challenge is to create the ROM in such a way that it is amenable to the multidisciplinary design and analysis of BLI configurations. This leads to the first research question of this thesis:

| **Research Question 1**: |
| --- |
| How can reduced-order modeling be used to develop a coupled MDA approach that enables multidisciplinary design and analysis of BLI configurations? |

Coupled MDA for BLI configurations requires models for both the aerodynamic and propulsion system analyses. For this work, the propulsion system analysis is performed using the simple fan model discussed in Chapter 3. This is an inexpensive analysis model compared to the aerodynamic analysis performed using the FUN3D flow solver. Therefore, the reduced-order modeling is focused only on the more expensive aerodynamic analysis. The aerodynamic ROM will be created from snapshots of the CFD analysis, and, subsequently, coupled to the simple fan model to provide rapid coupled MDA predictions. To accomplish this, the aerodynamic ROM must capture the impact of the propulsion system on the aerodynamics over a range of operating conditions, as defined by the $FPR$ and power required. For BLI configurations, each operating condition requires an iterative analysis between the propulsion system and aerodynamic models due to the strong coupling at the fan face. This

would be prohibitively expensive if the CFD snapshots used to create the aerodynamic ROM were produced in this manner. The goal is then to intelligently create the snapshots, such that the coupled nature of the analysis is captured without the requirement of performing coupled MDA.

## *4.1 Snapshot Strategy for the Aerodynamic ROM*

Based on the previous discussion, the following research question is posed:

| **Research Question 1.1**: |
| --- |
| What is an appropriate strategy for generating the aerodynamic analysis snapshots? |

To understand the process better, the coupled MDA strategy employed in the work of Gray [5] is provided in Figure 22.

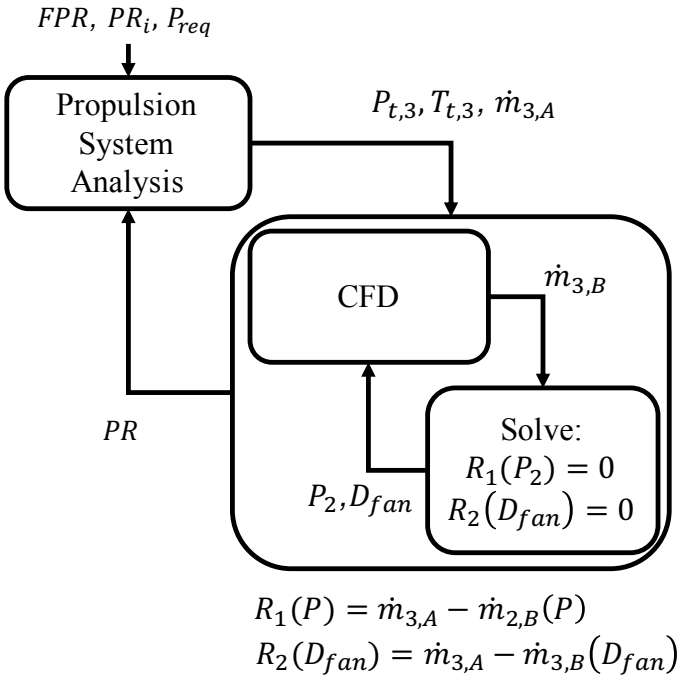


Figure 22: Coupled MDA strategy employed by Gray [5].

The process illustrated in Figure 22 consists of three iterative loops. The most outer loop is between the propulsion system analysis and the CFD solver. The analysis

begins by specifying a desired fan pressure ratio, power required for the propulsor, and an initial guess for the pressure recovery at the fan face. Based on the given inputs, the propulsion system analysis provides the necessary total pressure and tempature at the fan exit along with the required mass flow rate through the propulsor. This information is then used to set the boundary conditions for the propulsor in the CFD analysis. The CFD analysis consists of two iterative loops. The most inner loop consists of an iterative analysis to determine the required fan diameter of the propulsor. This loop is required due to the inability to simultaneously specify all the total pressure, total temperature, and mass flow rate provided from the propulsion system analysis on a single boundary. To accomodate for this, the total pressure and total temperature are specified at the fan exit boundary and the inner loop solves for the necessary fan diameter to provide the required mass flow rate. The second iterative loop for the CFD analysis is required to enforce conservation of mass across the fan boundaries. This process consists of iteratively solving for the required back pressure at the fan face to obtain an equal mass flow rate to that specified at the fan exit boundary.

For this research, the fan diameter is fixed. As a consequence, the total pressure, total temperature, and mass flow rate cannot simultaneously be enforced. The options are to either specify both the total pressure and temperature at the fan exit or specify the total temperature and mass flow rate. For the first option, the Mach number at the fan exit is calculated using the method discussed in Chapter 3. This results in a unique mass flow rate for the fixed fan diameter. Based on the simple fan model described in Chapter 3, the resulting mass flow rate and total temperature rise across the fan can be used to calculate the power required for the propulsor using Equation 36.

$$P_{req} = \dot{m} c_p (T_{t,3} - T_{t,2}) \tag{36}$$

Using similar assumptions to those made for the subsonic inflow boundary conditions discussed in Chapter 3, the second option consists of using the specified total temperature and mass flow rate to solve for the static pressure, static temperature, and velocity at the fan exit. This strategy retains the ability to specify the power required as an input to the analysis. However, the total pressure and, therefore, the fan pressure ratio is an output. The issue that arises is that for a specified power required (Equation 36), the total temperature and mass flow rate are not uniquely defined so that the system is underdetermined. As a result, this option is not consistent with the propulsion model employed for this research. This leads to the following observation:

Observation 1: To allow for coupling to the propulsion system analysis, the total pressure and temperature are required at the fan exit. The total conditions are then used to determine the mass flow rate. The resulting system is uniquely defined by the specified $FPR$ value with the power required being an output.

For this work, the first option is used and the total conditions are specified at the fan exit boundary with the mass flow rate being an output. The updated simulation strategy is provided in Figure 23. Note that the discussion so far has focused only on the coupled analysis. However, the goal is to perform the snapshots using a decoupled anlaysis. The decoupled analysis consists of a single evaluation of both the propulsion system and aerodynamic analyses with no feedback loop. The fan pressure ratio and pressure recovery at the fan face are provided to the propulsion system analysis to obtain the total pressure and total temperature. The total conditions are then specified at the fan exit boundary in the CFD analysis. Finally, the required back pressure at the fan face is iteratively solved in the CFD analysis to provide consistent mass flow rate across the fan. Note that the propulsion BC in FUN3D is employed for

this step, as discussed in Chapter 3. The resulting decoupled analysis is illustrated in Figure 24.

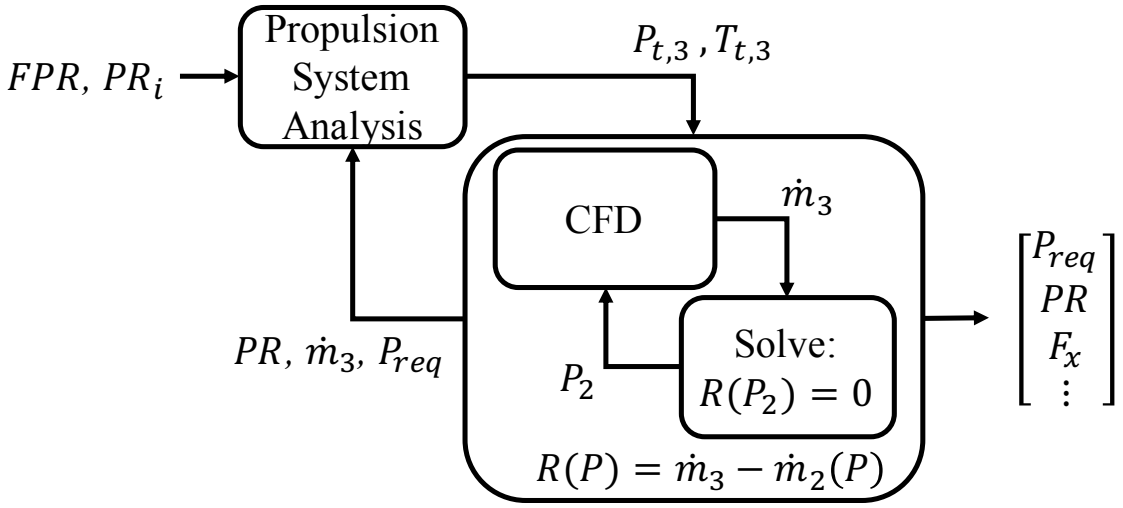


Figure 23: Updated coupled simulation strategy for fixed fan diameter.

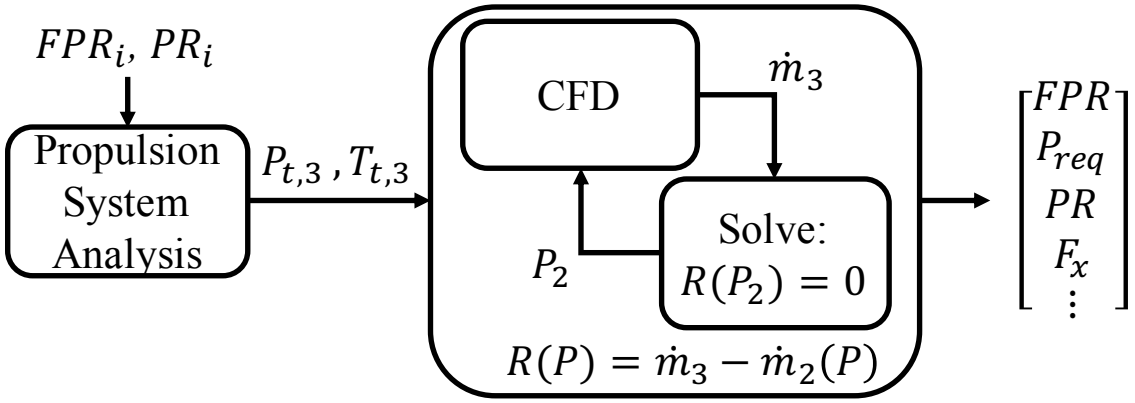


Figure 24: Decoupled simulation strategy for generating snapshots.

It is important to note that the primary differences between the analyses shown in Figures 23 and 24 are the inputs and outputs. For the coupled analysis, the inputs are the desired fan pressure ratio and the initial guess for the pressure recovery at the fan face. The outputs are then the power required along with other important metrics such as the actual pressure recovery and axial force. For the decoupled analysis, the inputs are still the fan pressure ratio and pressure recovery. However, both values are initial guesses for this case. The initial guesses provide the total conditions to

be enforced at the fan exit. The CFD analysis iteratively updates the fan face to match the resulting mass flow rate at the fan exit corresponding to the specified total conditions and finally, the outputs of the analysis are the actual fan pressure ratio, pressure recovery, and power required, along with the other metrics mentioned. This leads to the following observation:

Observation 2: For the decoupled simulation, both the power required and the fan pressure ratio are outputs of the analysis based on initial guesses of the fan pressure ratio and pressure recovery.

This observation has important implications for generating the snapshots of the CFD analysis. For the decoupled approach, the propulsor operating conditions are now the outputs of the analysis, which are uniquely defined by the total conditions at the fan exit. Additionally, the total conditions at the fan exit are uniquely defined by the initial guesses for the fan pressure ratio and pressure recovery. This leads to the final observation of this section:

Observation 3: For the decoupled analysis, the inputs are the initial guesses for fan pressure ratio and pressure recovery. Therefore, the design of experiments must be performed on these values. The actual range of propulsor operating conditions, defined by the fan pressure ratio, can then be obtained indirectly through the decoupled analysis.

Based on the observations discussed in this section, the snapshots can be generated using the decoupled analysis strategy with the caveat that the desired propulsor operating conditions are the output of the analysis. The unknown pressure recovery at the fan face results in differences between the fan pressure ratio used as input to

the propulsion system analysis and the actual fan pressure ratio output from the CFD analysis. The task for this work is to define adequate ranges for the total pressure and temperature at the fan exit to ensure that the desired range of fan pressure ratio is obtained using the decoupled analysis strategy outlined in this section. For this work, the fan pressure ratio input used for the design of experiments is defined by the desired range of operating conditions. Therefore, in order to obtain the desired range of operating conditions using the decoupled approach, an appropriate range of pressure recovery values must be defined in the design of experiments. This leads to the following hypothesis:

**Hypothesis 1.1**: *With adequately defined ranges for the initial guesses of both pressure recovery and fan pressure ratio and a consistent mass flow rate across the fan, a decoupled simulation strategy will provide snapshots over the desired range of fan pressure ratio.*

### 4.1.1 Experiment 1.1

To test Hypothesis 1.1, the requirements are to evaluate the ability to obtain a set of snapshots over the desired range of fan pressure ratios using the decoupled simulation strategy discussed above. Note that the inputs to decoupled analysis were defined to be the initial guesses for the pressure recovery and fan pressure ratio. Therefore, an appropriate experiment was to perform simulations over a defined range of initial guesses for the pressure recovery and fan pressure ratio using the decoupled strategy, where the success was measured by evaluating the resulting range of fan pressure ratios obtained from the simulations. Based on this discussion, Experiment 1.1 consisted of defining an appropriate range for the initial guesses of pressure recovery and fan pressure ratio, performing a design of experiments using the defined range of initial guesses, simulating the DOE using the decoupled solution strategy, and evaluating the

resulting fan pressure ratios obtained from the simulations. These steps are discussed in more detail in the following subsections.

### 4.1.2 Design of Experiments

In order to perform the design of experiments, the ranges for the fan pressure ratio and pressure recovery have to be defined. The range for the fan pressure ratio is selected based on the desired range of propulsor operating conditions. For this work, the design range for fan pressure ratio is not available. Therefore, a representative range of 1.1 to 1.35 is used based on values used for similar studies [5, 18]. Ideally, an approximate range for the pressure recovery over the design range of fan pressure ratio is known for a given design. For this work, an approximate range is determined through preliminary analyses.

To determine the appropriate range of pressure recovery, coupled MDA was used to simulate FPR values of 1.1 and 1.35. The resulting values of pressure recovery were given to be 0.874 and 0.897 for fan pressure ratios of 1.1 and 1.35, respectively. It is important to note that the pressure recovery, provided in Equation 17, is defined by the ratio of the total pressure at the fan face to the freestream total pressure. The result is that the pressure recovery value at the fan face includes effects from both the deceleration that occurs in the inlet of the propulsor and the boundary layer resulting from the upstream geometry. Therefore, the pressure recovery is not defined strictly as an inlet performance variable. As a result, the pressure recovery values shown here are much lower than values typically observed for commercial propulsion systems. From a systems-level perspective, this definition of pressure recovery is adequate. However, if the goal is to specifically target the efficiency of the inlet, the definition of pressure recovery requires modification to isolate losses occuring only during the flow deceleration occuring in the inlet.

Based on the results of this preliminary analysis, a range was defined for the

pressure recovery to ensure adequate converage of the edges of the design space. The ranges were then evaluated using the simple fan analysis discussed in Chapter 3 to obtain the necessary ranges for the total pressure and temperature at the fan exit. The defined ranges for the design of experiments along with the resulting total pressure and temperature ranges are provided in Table 10.

Table 4: DOE Ranges for Aerodynamic Snapshots.

| | Minimum | Maximum |
|---|---|---|
| FPR | 1.1 | 1.35 |
| PR | 0.86 | 0.92 |
| $P_t/P_\infty$ | 1.34 | 1.75 |
| $T_t/T_\infty$ | 1.14 | 1.21 |

The ranges in Table 10 were used to generate 100 combinations of total pressure and temperature at the fan exit using a Latin Hypercube sampling strategy. The resulting DOE is illustrated in Figure 25.

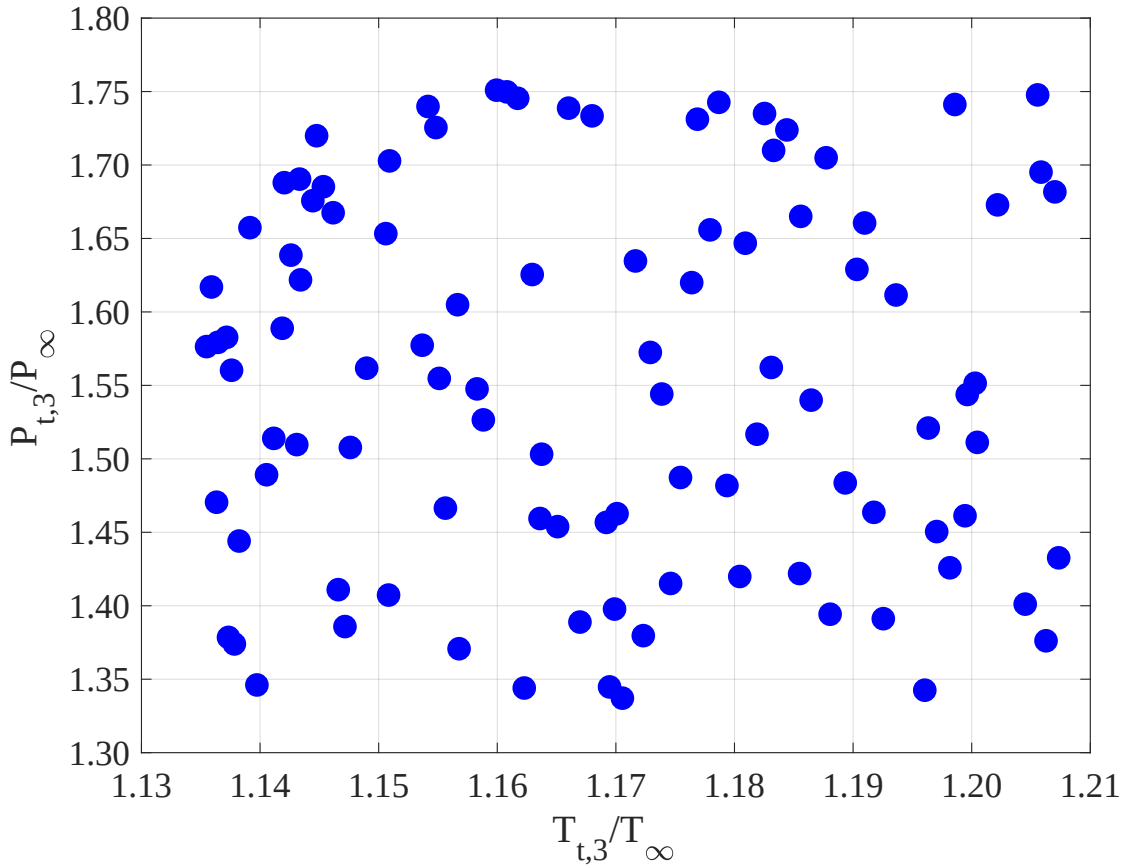


Figure 25: 100 case DOE for decoupled snapshots.

### 4.1.3 Convergence Requirements

Prior to simulating the DOE discussed in the previous section, an additional study was performed to establish the requirements for convergence. The goal of this analysis was to establish the convergence criteria and to identify the number of iterations required for convergence, which has direct implications on the computational cost to produce the snapshots. The preliminary analysis consisted of performing a single decoupled simulation with $P_t/P_\infty$ and $T_t/T_\infty$ values of 1.55 and 1.175, which correspond to the mean values of DOE ranges. The simulations were performed for 5,000 iterations with CFL ramping over the first 250 iterations from 1 to 100 for the mean flow equations and 1 to 20 for the turbulence equation to accelerate convergence. To evaluate the

convergence of the simulation, the solution residuals and boundary condition values were plotted as a function of iteration in Figures 26 and 27, respectively.

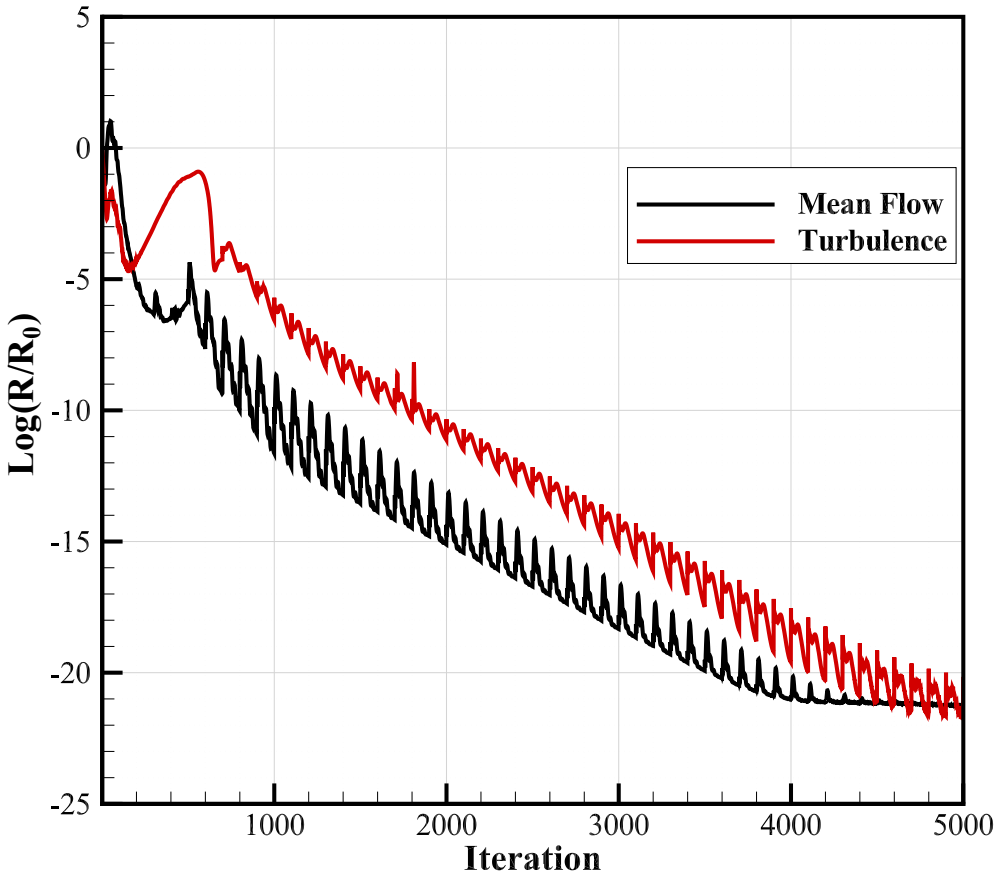


Figure 26: Convergence history of FUN3D for decoupled solution strategy.

The results shown in Figure 26 illustrate the solution histories for both the mean flow and turbulence residuals, where the mean flow residuals correspond to the mass, momentum, and energy equations. For this work, one of the convergence criterions was a three orders of magnitude drop in the flow residuals. From the results shown in Figure 26, that criterion is met within the first 1,000 iterations. The propulsion BC was employed to iteratively update the back pressure at the fan face to match the mass flow rate obtained at the fan exit boundary. Therefore, another important

consideration for convergence is the achievement of mass conservation across the fan. The solution histories at the fan boundaries are shown in Figure 27.

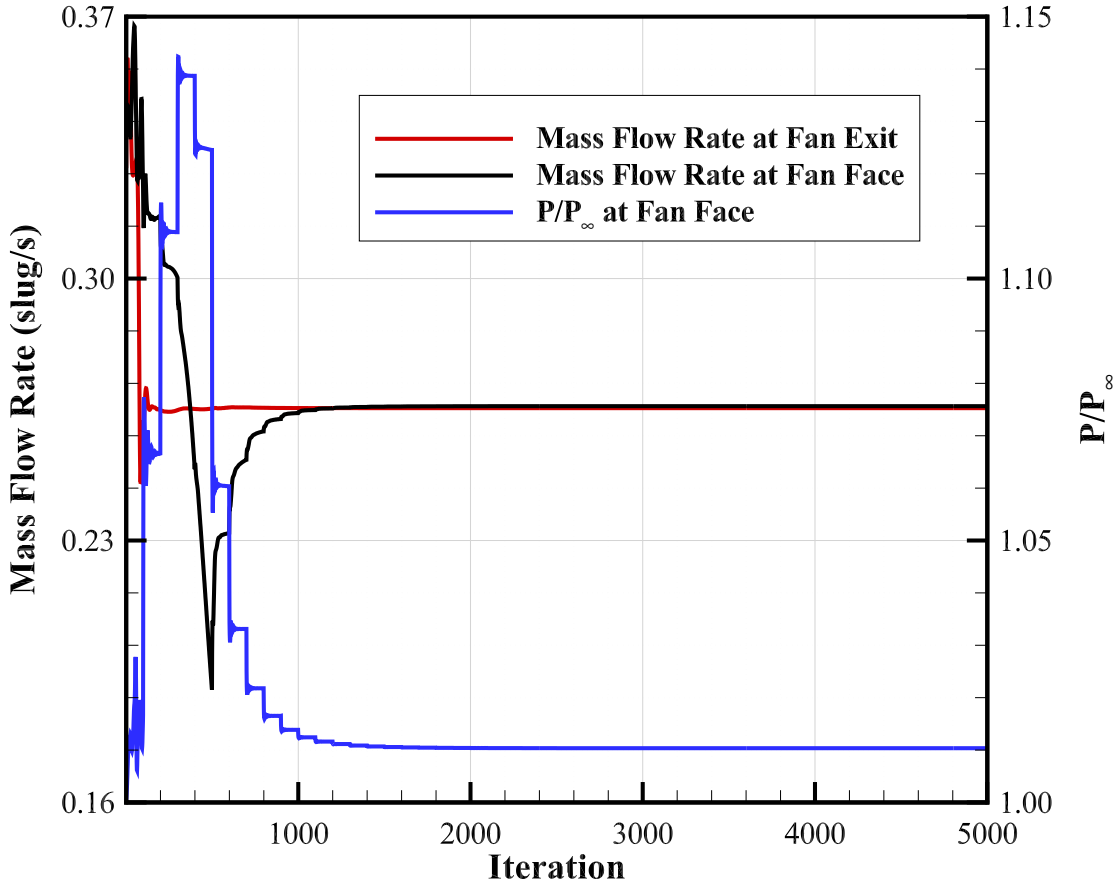


Figure 27: Boundary condition convergence history for decoupled solution strategy.

The results shown in Figure 27 show the histories of the mass flow rates at both the fan face and fan exit along with the back pressure at the fan face. The convergence criterion enforced for the boundary conditions consisted of a qualitative assessment of the mass flow rate and back pressure histories at the fan face and fan exit boundaries. The histories show that changes in the mass flow rate at the fan exit appear to be damp out in less than 500 iterations. The back pressure is updated every 100 iterations to match the mass flow rate at the fan exit. From the results, the boundary conditions

appear to be static by roughly 1,500 iterations. To ensure adequate convergence, all of the simulations in this experiment were performed for 2,000 iterations. Note that a more quantitative measure of convergence could be employed for the boundary conditions to force the analysis to stop after the changes at the fan face and fan exit boundaries have reduced below some defined value. This could potentially reduce the overall computational cost of the snapshots. However, this approach would require a more detailed book keeping for the computational cost of the flow solutions since each solution could potentially require a different number of iterations to meet the criteria for convergence. As such, the qualitative method discussed here was employed for this work.

### 4.1.4 Results

The results of the DOE simulations using the decoupled strategy are provided in Figures 28-30.

The results in Figure 28 illustrate the resulting mass flow rates at the fan face and fan exit. The results illustrate very good agreement between the fan face and fan exit for all samples generated, which confirms that mass conservation was achieved.

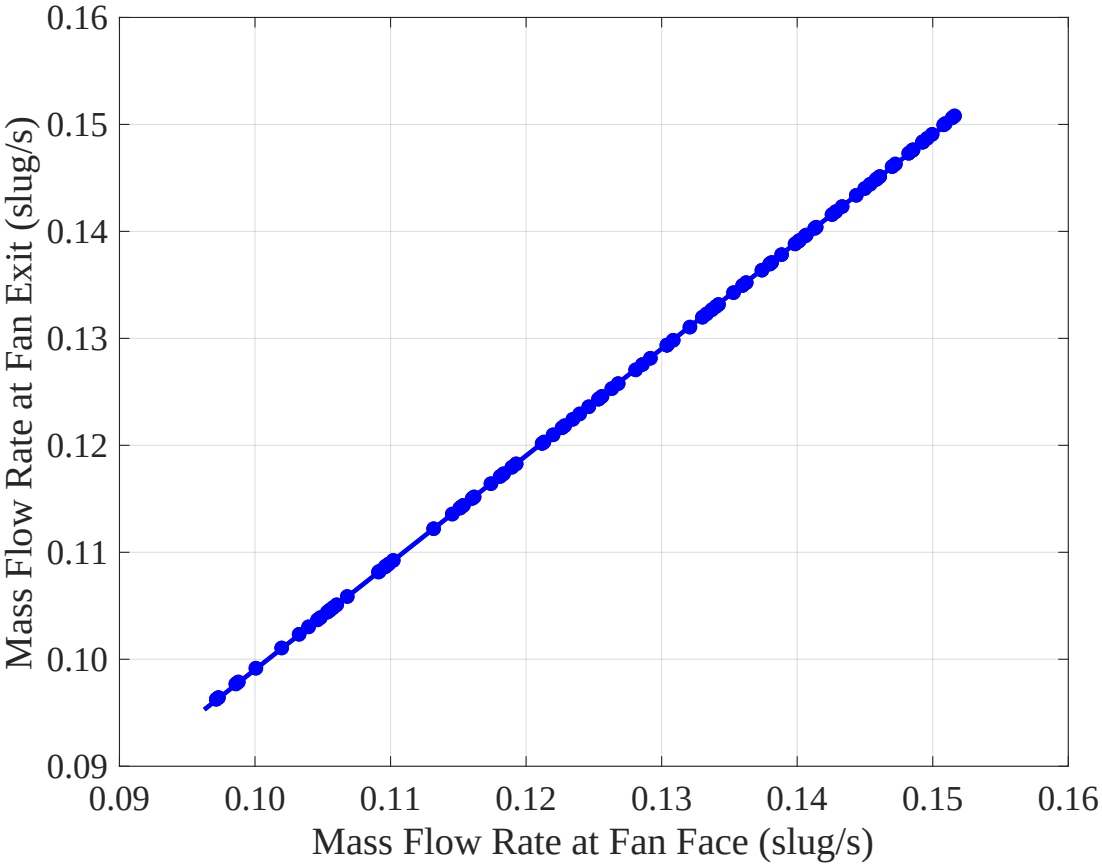


Figure 28: Mass conservation across the fan.

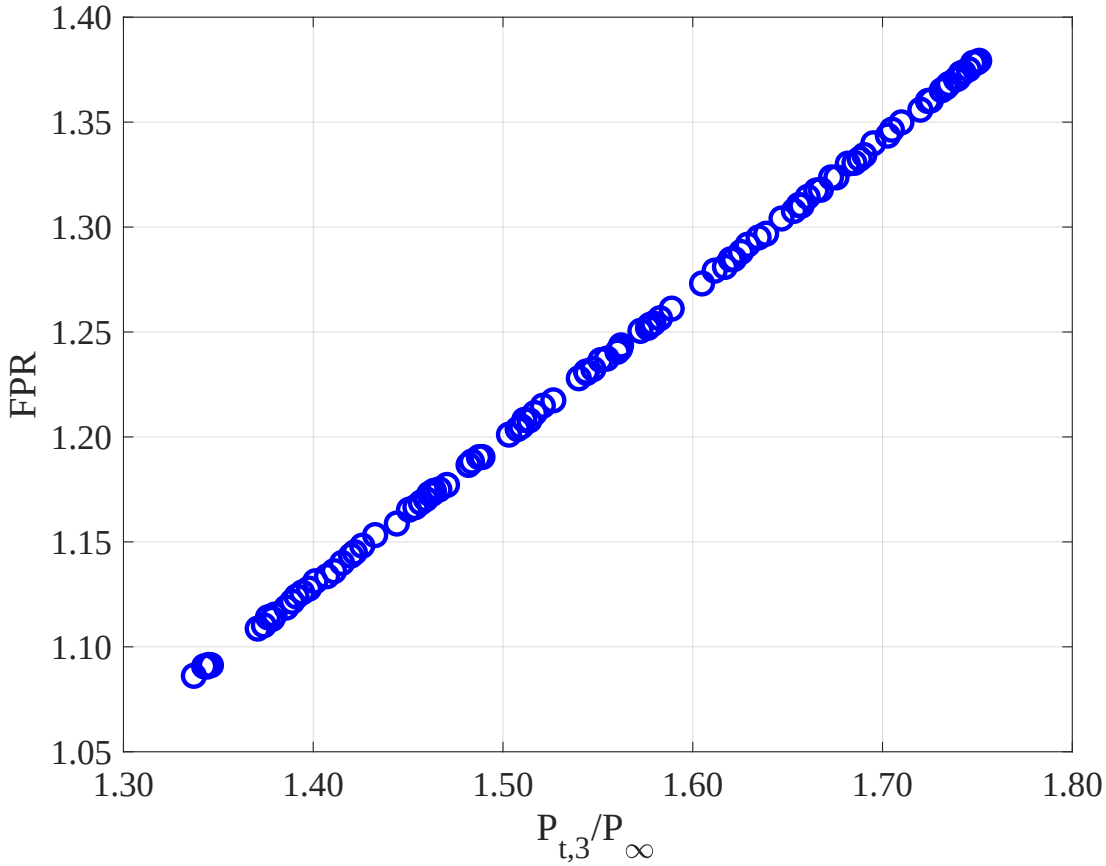


Figure 29: Illustration of $FPR$ range captured by decoupled simulations.

The results shown in Figure 29 illustrate the resulting fan pressure ratios obtained from the simulations plotted against the total pressure, normalized by the freestream static pressure, at the fan exit. The results show that fan pressure ratios ranging from 1.08 to 1.38 were obtained using the described approach. Note that this includes the desired range of 1.1 to 1.35 with some of the values being above and below the desired range, which is a result of the conservative range of pressure recovery values used for the DOE.

Finally, the results in Figure 30 illustrate the actual range of pressure recovery values plotted against the mass flow rate through the fan for the fan pressure range shown in Figure 29. The results depict a nearly linear trend between pressure recovery and mass flow rate for the lower values and an increasingly nonlinear relationship as

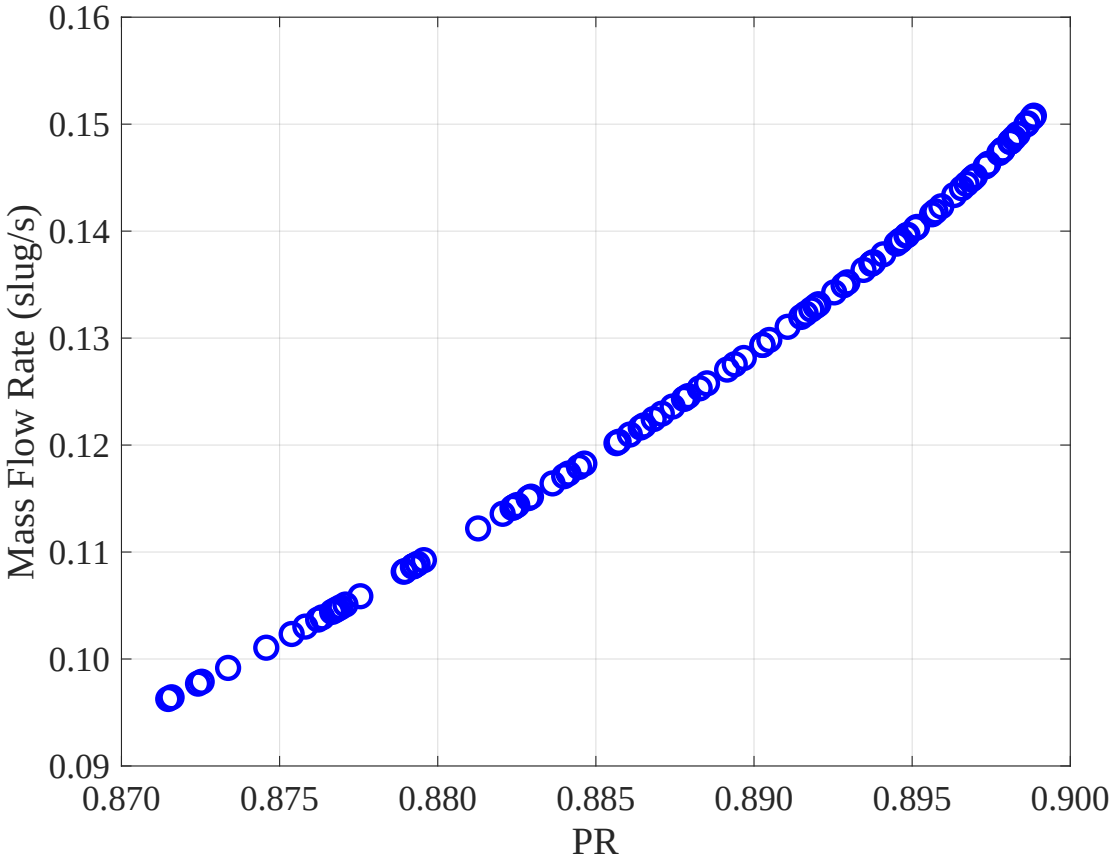


Figure 30: Illustration of $PR$ range captured by decoupled simulations.

mass flow rate is increased. Additionally, it is observed that the pressure recovery range assumed for the DOE was conservative with the actual range being roughly half of the assumed range. As a consequence, some of the resulting snapshots are outside of the desired range of fan pressure ratio, as previously discussed. With a more refined pressure recovery range, the interior coverage of the design space could be improved for the same number of snapshots. However, this information is not always available. Additionally, the Latin Hypercube sampling method has been shown to have issues with sampling densities at the edges of the design space [79]. For this work, the conservative range of pressure recovery helps to overcome this issue by essentially extending the edges of the design space to beyond the desired operating conditions.

### 4.1.5 Summary

Due to the increased computational requirements associated with coupled MDA, a decoupled strategy was used to obtain snapshots over a range of operating conditions. For this work, the fan diameter was held constant and the desired range of operating conditions was defined by $1.1 \leq FPR \leq 1.35$. The inputs to the decoupled analysis are the initial guesses for the fan pressure ratio and pressure recovery. These initial guesses are then provided to the simple fan analysis to calculate the total pressure and temperature at the fan exit. These total conditions are then applied to the fan exit in the CFD analysis. The CFD analysis is performed with an inner loop to match the mass flow rate between the fan face and fan exit. The outputs to the analysis are then the actual fan pressure ratio and pressure recovery for the given total conditions at the fan exit. A DOE was performed over a range of total pressure and temperature based on the desired range of fan pressure ratio and a conservative range of pressure recovery. The results show that the proposed strategy was successful, and the snapshots were obtained over the desired range of operating conditions using the decoupled strategy. The results, therefore, confirm Hypothesis 1.1.

## *4.2 Aerodynamic ROM Evaluation*

Having generated the snapshots over the desired range of propulsor operating conditions, the next step is to create and evaluate the accuracy of the aerodynamic ROM, where the accuracy will depend on the number of snapshots used to create the ROM. This leads to the following research question:

| **Research Question 1.2**: |
| --- |
| What are the prediction capabilities and sampling requirements of the aerodynamic ROM? |

The development of the aerodynamic ROM is performed using the POD method

discussed in Chapter 3. Then, interpolation is used to provide predictions over the range of desired operating conditions. The application of POD for aerodynamic predictions have shown to be generally accurate with issues being encountered for highly nonlinear flow phenomena such as shocks and flow separation [8, 38]. For this work, the flow field is to be predicted for the TCT concept at a transonic flight condition. Thus, shocks and other nonlinearities are potentially present in the flow. Nevertheless, the flight conditions are constant, and the only changes are occuring in a limited domain that includes the propulsor. Additionally, performance constraints generally result in well-behaved flow in the vicinity of the propulsor. The implication of this is that even if the POD ROM proved inaccurate for strong nonlinearities near the fan, these conditions would not be of interest anyway. Note that these constraints are reflected in the feasible operating range. Finally, the aerodynamic ROM is a function of only two variables for the present case. Based on this discussion, the following is hypothesized:

**Hypothesis 1.2**: *If the POD ROM is created using snapshots that were parameterized by only two variables defining the feasible range of operating conditions for the propulsor, then the POD ROM will accurately predict the aerodynamics with minimal sampling requirements.*

### 4.2.1 Experiment 1.2

To test Hypothesis 1.2, the requirement for the numerical experiment is to provide the ability to assess the accuracy of the ROM predictions relative to the full-order model over the desired range of operating conditions, and as a function of the sampling density. The information gained from this experiment allows for an assessment of the tradeoff between computational cost and accuracy of the ROM, which can be

used to establish the sampling requirements of the ROM. In order to assess the accuracy of the ROM, the ROM predictions need to be compared to the CFD results over the desired range of operating conditions, which requires solutions corresponding to combinations of the initial guesses for the pressure recovery and fan pressure ratio that were not used to create the ROM. Additionally, the ROM will need to be created using varying numbers of snapshots to allow for the assessment of the sensitivity of the prediction accuracy to sampling density. Based on this discussion, Experiment 1.2 was designed to include three components consisting of ROM development, ROM validation, and an assessment of sensitivity to sampling density. The ROM development component consists of building the ROM using a given set of snapshots. This part of the experiment focuses on the details of the how the aerodynamic ROM is constructed including the required inputs and outputs. Next, the ROM validation consists of performing simulations for untried combinations of the initial guesses for the pressure recovery and fan pressure ratio using the decoupled simulation strategy and comparing the results to predictions obtained using the POD ROM. Finally, the sensitivity of the ROM accuracy to the sampling density is performed by creating the POD ROMs using subsets of the snapshots produced in Experiment 1.1 and comparing to the validation cases produced using the decoupled simulation strategy. These steps are discussed in detail in the following subsections.

### 4.2.2 ROM Development

The first step for Experiment 1.2 is to develop the aerodynamic ROM. In order to develop the ROM, the computational domain must be defined along with the appropriate variables. In the CFD analysis, the computational domain is divided and grouped by boundary conditions. The resulting domains are the fan face, fan exit, and configuration surface, which includes both the fuselage and nacelle. Note that this division is not required for the aerodynamic ROM. However, a gain in efficiency

can be obtained by including the domain division in the aerodynamic ROM by allowing the number of variables predicted on each domain to vary based on the desired information. Ultimately, one of the powerful attributes of reduced-order modeling includes the prediction of field variables. Compared to creating surrogate models of integrated quantities of interest, reduced-order modeling allows for the prediction of the quantities of interest distributed over the entire computational domain. This capability provides enhanced insight and improves overall confidence in the predictions. At the fan face and exit boundaries, a variety of quantities are of interest, including the mass flow rate, pressure recovery, distortion, etc. These metrics require all five primitive variables provided by the CFD solution, density ($\rho$), x-component of velocity ($u$), y-component of velocity ($v$), z-component of velocity ($w$), and static pressure ($p$). For the surface, the only quantity of interest in this work is the axial force contribution, which only requires the distribution of pressure, $p$, and the axial skin friction coefficient, $c_{f,x}$. Note that all of the velocity components on the surface are zero by definition and splitting the computational domain prevents the requirement of carrying these unneeded quantities. Based on this discussion and snapshots produced in Experiment 1.1, the components of the aerodynamic ROM were developed as illustrated in Figure 87.

Figure 31: Aerodynamic ROM development.

The process illustrated in Figure 87 shows the ROM development for each of the three domains corresponding to the fan face, fan exit, and surface. For the given set of snapshots, POD is applied to each of the desired variables for the three domains to provide the corresponding POD coefficients and modes. Note that this is performed only once, during the offline phase of the ROM development. For the online phase, the POD coefficients are interpolated using the kriging model discussed in Chapter 3 for an untried combination of total pressure and temperature at the fan exit. The interpolated POD coefficients are then used in the equations, shown in Figure 87, to provide the final predictions for each of the variables and domains. The final process for the online aerodynamic ROM prediction is illustrated in Figure 32. The resulting aerodynamic ROM predicts each of the quantities of interest for the three computational domains as a function of the propulsor operating conditions.

Figure 32: Aerodynamic ROM prediction model.

### 4.2.3 ROM Validation

The next step in Experiment 1.2 consists of assessing the accuracy of the aerodynamic ROM, which is referred to as the ROM validation step. This step consists of comparing the ROM predictions to the results obtained by CFD at untried combinations of total pressure and total temperature. Note that this validation exercise employs the aerodynamic ROM that was developed using the 100 snapshots produced in Experiment 1.1. To allow for comparisons between the ROM and CFD, 100 additional snapshots were produced using the process described for Experiment 1.1. The snapshots used to develop the ROM and for the validation are illustrated in Figure 33.

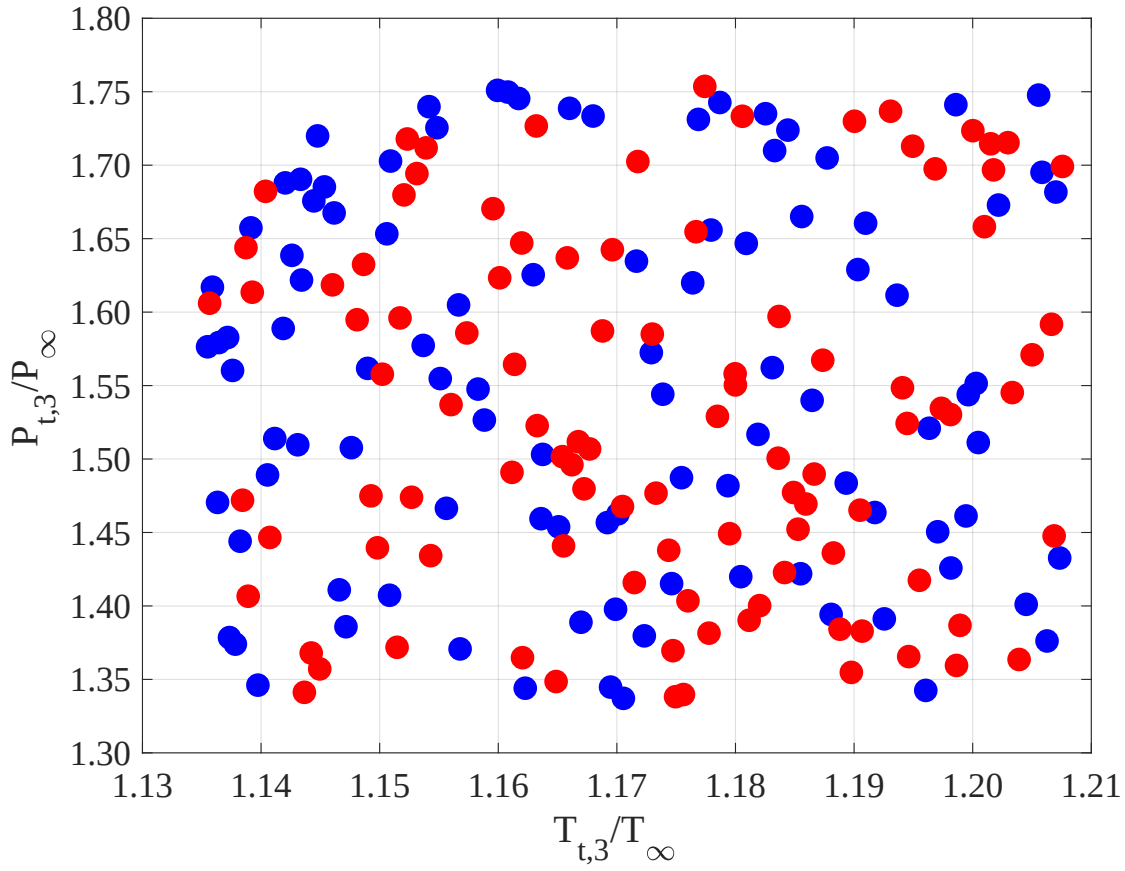


Figure 33: Illustration of total pressure and total temperature combinations for ROM development (blue) and validation (red).

First, the evaluation metrics are defined here. These are the metrics that will be employed for the comparisons between the ROM predictions and CFD results. The metrics used for this work are the total axial force, power required for the propulsor, fan pressure ratio, pressure recovery at the fan face, and distortion at the fan face. These metrics were chosen based on their importance for the overall performance of the BLI concept and for the coupled MDA analysis that will be discussed in Chapter 5. The total axial force and power required for the propulsor provide a means of assessing the BLI design performance, where the axial force represents either thrust produced or a thrust requirement, and the power required represents the amount of power that must be provided to the fan. These variables are crucial for the sizing of the underwing turbofans, which both provide the required thrust and power the fan. Note that this component of the analysis is beyond the scope of this work. However, the implications of these metrics are considered. The fan pressure ratio and pressure recovery at the fan face are required for performing coupled MDA predictions, as discussed in Section 4.1. Finally, the distortion at the fan face is an important metric for the design of the fan. Distortion is a measure of variations in flow velocity and/or pressure at the fan face caused by upstream disturbances. Distortion is a significant concern because it can lead to stall in the fan/compressor blades and potentially even result in damage to the blades [80, 81]. For BLI configurations, this is a very important metric since the flow entering the propulsor is not uniform. Relative to a conventional configuration with podded engines, a BLI configuration will experience additional distortion from the upstream components of the aircraft including the wings, tail, and fuselage. This can lead to the BLI propulsor ingesting highly distorted flow, which could potentially negate any benefit gained from the BLI technology. There are various methods for quantifying the distortion entering the propulsor. The industry standard known as ARP1420 is used for this work [14].

**ARP1420 Distortion Calculation**

The ARP1420 measure of distortion depends on the nomenclature provided by Figure 34. For the distortion calculation, the Aerodynamic Interface Plane (AIP) is decomposed into five equal area rings with eight circumferential stations per ring. Note that the fan face is designated as the AIP for this work. The distortion is calculated for each ring using Equation 37, where $P_{avg_{low}}$ is defined via Equation 38. An illustration of the total pressure distortion for a single ring is provided in Figure 35. The final distortion value is obtained by taking the average over the five equal area rings as shown in Equation 39.

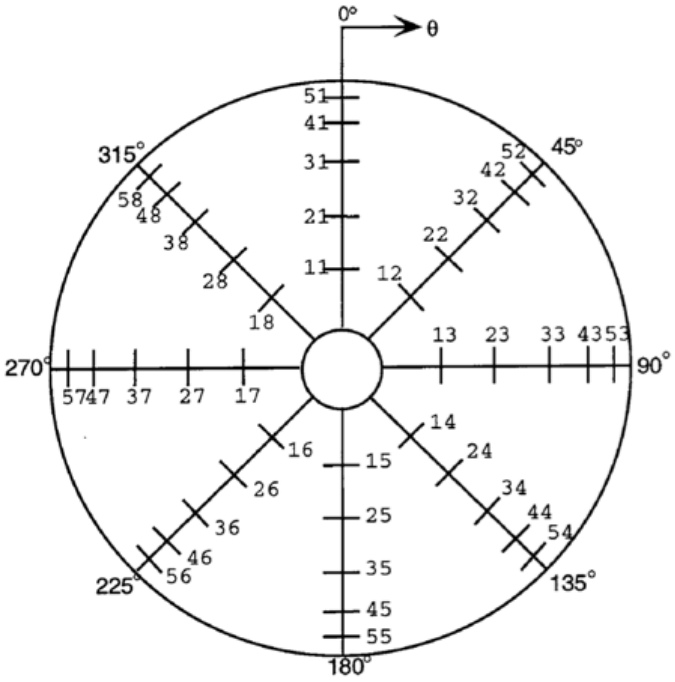


Figure 34: Nomenclature for ARP1420 [14].

$$DPCP = \frac{P_{t,avg} - P_{t,avg_{low}}}{P_{t,avg}} \tag{37}$$

$$P_{t,avg_{low}} = \frac{1}{\theta_{\bar{i}}} \sum_{k=1}^{Q} \int_{\theta_{\bar{i}\bar{k}}} P_t(\theta)_i \, d\theta \tag{38}$$

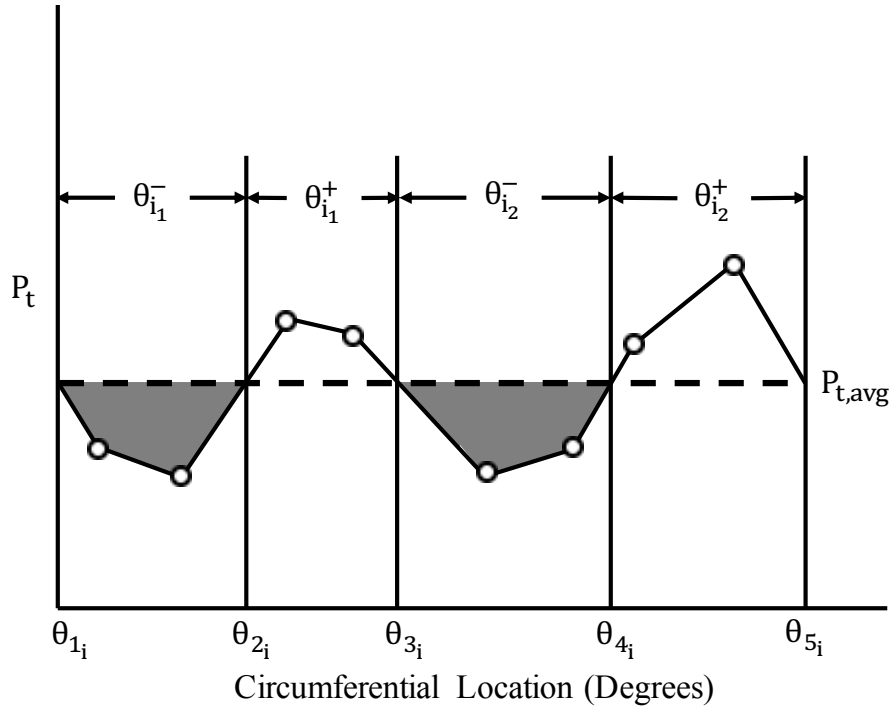


Figure 35: Illustration of Circumferential Distortion [14].

$$DPCP_{avg} = \frac{1}{5}\sum_{i=1}^{5} DPCP_i \tag{39}$$

**Evaluating Accuracy**

This section reviews the goodness-of-fit metrics used in assessing the accuracy of the aerodynamic ROM predictions. These metrics allow for comparisons over a large range of predictions in an efficient manner. For this work, the goodness-of-fit metrics consisted of a combination of qualitative and quantitative measures. The quantitive measures included the coefficient of determination ($R^2$), mean error ($\mu$), and standard deviation ($\sigma$). The $R^2$ value is a measure of the variance of the predictions, where a perfect fit corresponds to a value of 1.0. The mean error and standard deviation give insight to the distribution and spread of the error, where a good model will exhibit a normally distributed error. The qualitative measures included the actual-by-predicted plots, histograms, and error-by-predicted plots. The actual-by-predicted plots are used to evaluate the $R^2$ value, and the histograms are used to evaluate the

distribution of the error along with the mean and standard deviations. Finally, the error-by-predicted plots qualitatively give insight to the distribution of the error. A good model will have error that is randomly distributed with no discernible trends. Each of these quanitities are provided for the evaluation metrics discussed in this section.

**ROM Validation Results**

The results shown in Figures 36-40 illustrate very good agreement between the CFD and ROM solutions. For all five metrics shown, the actual-by-predicted results illustrate a coefficient of variance of 1, which is the maximum achievable value. Additionally, the histogram results show that the error tends to resemble a normal distribution with mean errors near zero and standard deviations much less than 1%. Note that the $F_x$ results shown in Figure 40a illustrate a range spanning roughly
-50 lb to 20 lb. This range resulted in issues with the percent error calculation near the zero crossing. To account for this observation, the histogram of the $F_x$ error in Figure 40 is given in absolute units. Also, the results shown for both $P_{req}$ and $F_x$ correspond to the half-span grids and the values for the full-span are, therefore, double the magnitude of these values. The axial force for the half-span, unpowered aircraft is 35 lb for reference. Finally, the error-by-predicted plots show that the error from the ROM tends to be randomly distributed with the exception of points near the edges of the design space, where the error is generally larger. One of the potential causes of the increase in error is the observed decrease in sampling density with distance from the center of the design space that is observed using the Latin Hypercube sampling method [79]. Note that for this work, the sampling was performed over a larger range of operating conditions than desired, which helps to provide better sampling near the actual edges of the design space. Therefore, the error tends to be higher in regions that are outside the desired range of operating conditions.

It is important to note that the error between the ROM and CFD, shown in Figures 36-40, is very small. This is to be expected given that the DOE consisted of only two variables with a limited domain of influence in the actual aerodynamic predictions. The experiment conducted here provides preliminary validation of the capability of the aerodynamic ROM to capture the impact of the propulsion system on the aerodynamics.

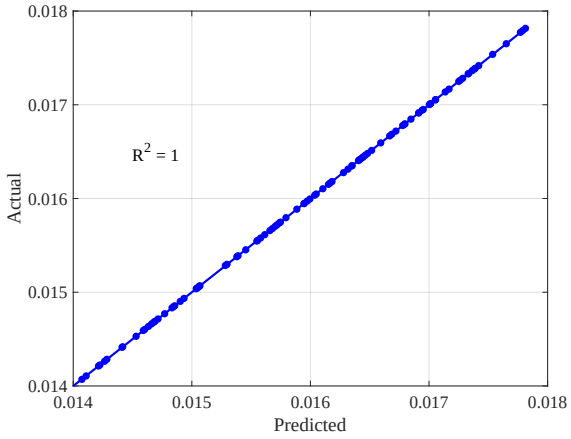


(a) Actual-by-predicted

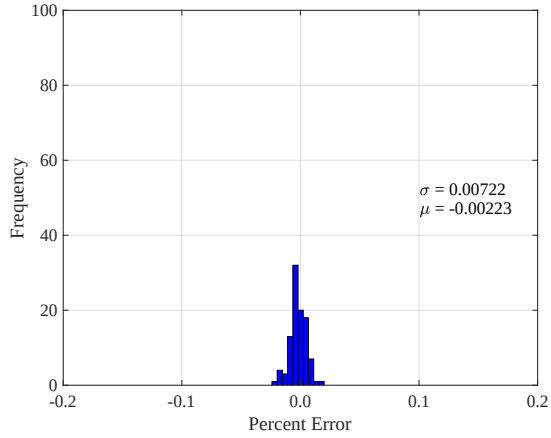


(b) Histogram

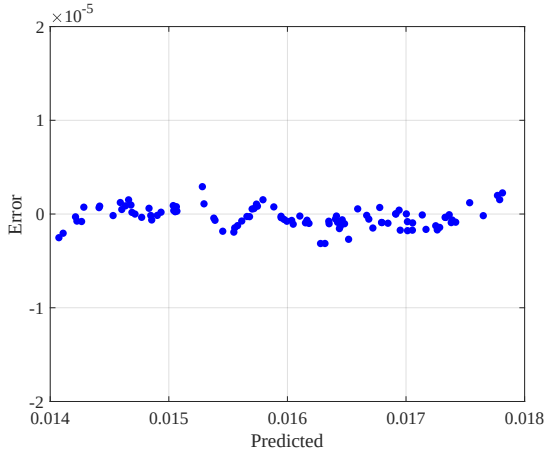


(c) Error-by-predicted

Figure 36: $DPCP_{avg}$ error metrics.

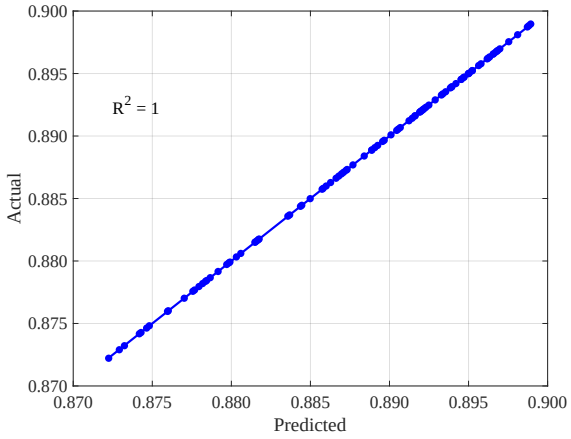


(a) Actual-by-predicted

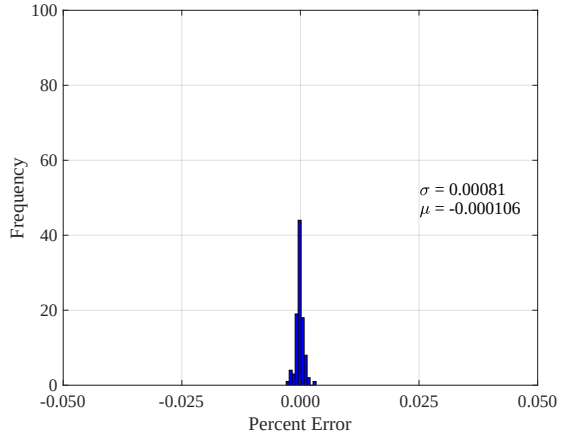


(b) Histogram

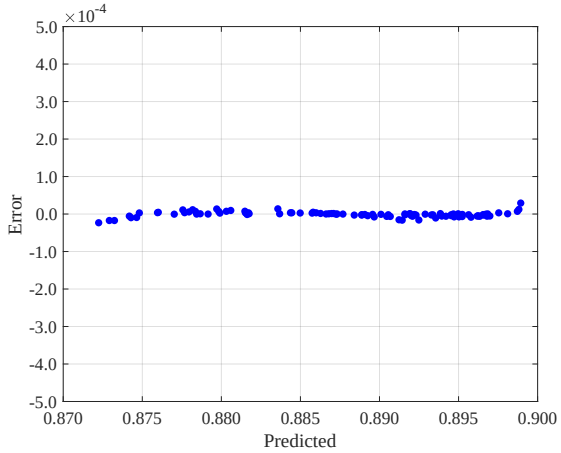


(c) Error-by-predicted

Figure 37: $PR$ error metrics.

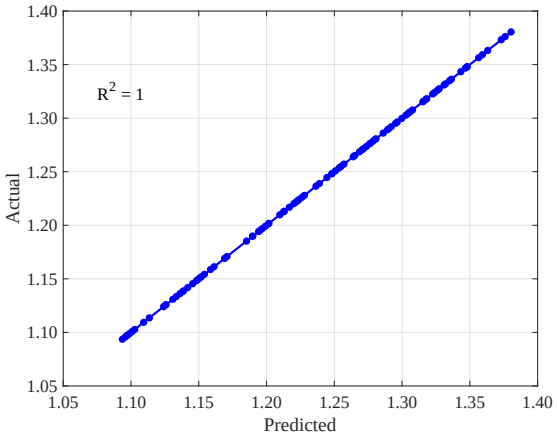


(a) Actual-by-predicted

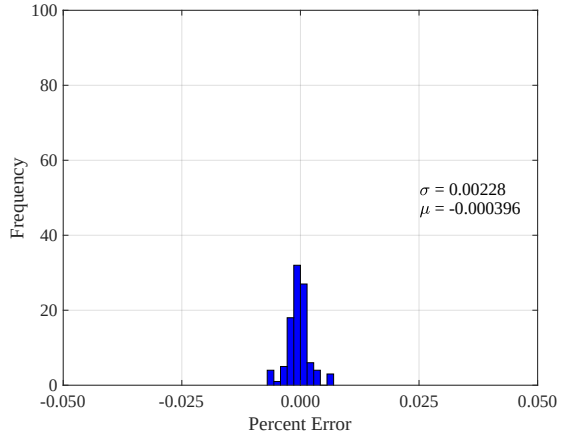


(b) Histogram

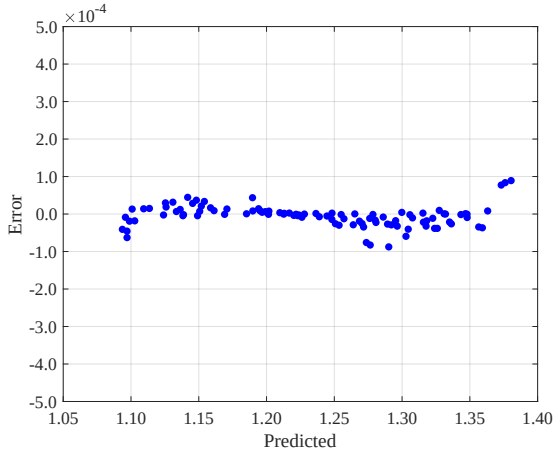


(c) Error-by-predicted

Figure 38: $FPR$ error metrics.

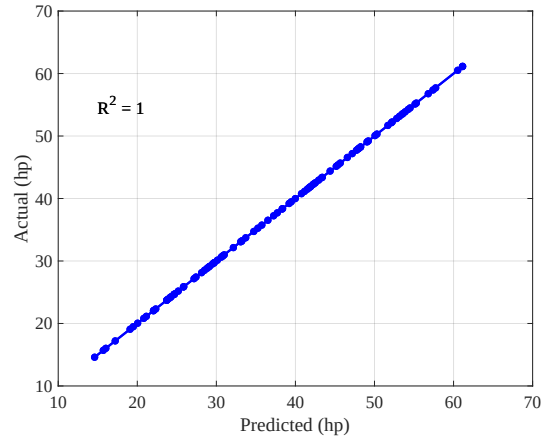


(a) Actual-by-predicted

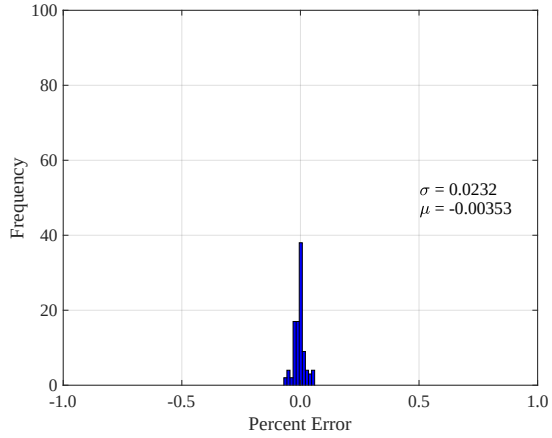


(b) Histogram

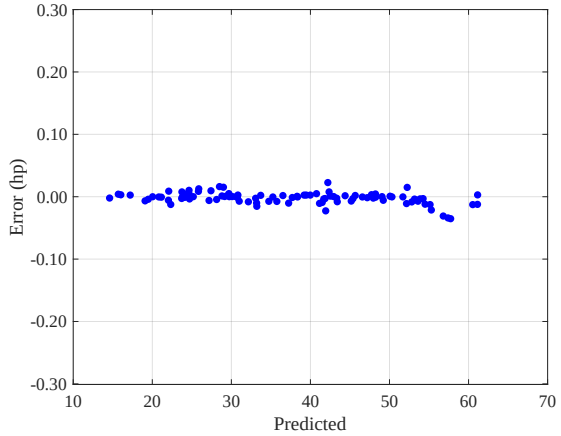


(c) Error-by-predicted

Figure 39: $P_{req}$ error metrics.

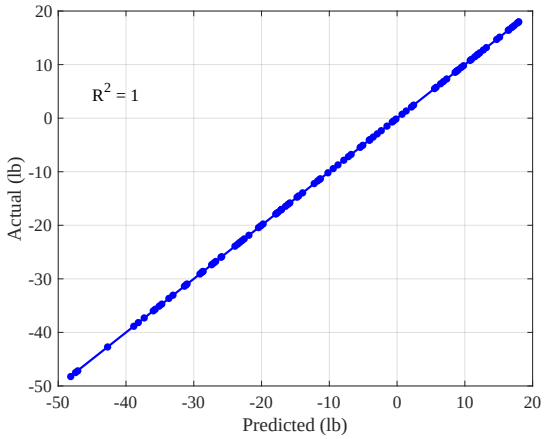


(a) Actual-by-predicted

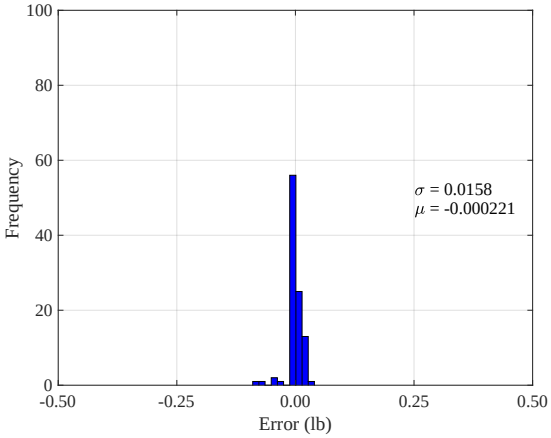


(b) Histogram

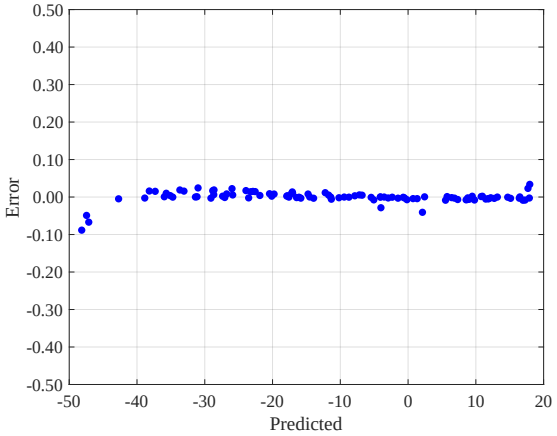


(c) Error-by-predicted

Figure 40: $F_x$ error metrics.

### 4.2.4 Sensitivity to Sampling Density

The final component of Experiment 1.2 is to evaluate the sensitivity of the previous predictions relative to the sampling density used in developing the aerodynamic ROM. To perform this experimental step, the process discussed in Section 4.2.2 was used to develop the aerodynamic ROM using subsets of the snapshots produced in Experiment 1.1. The subsets included 100, 50, 25, and 15 snapshots. An illustration of the subsets of snapshots is provided in Figure 41.

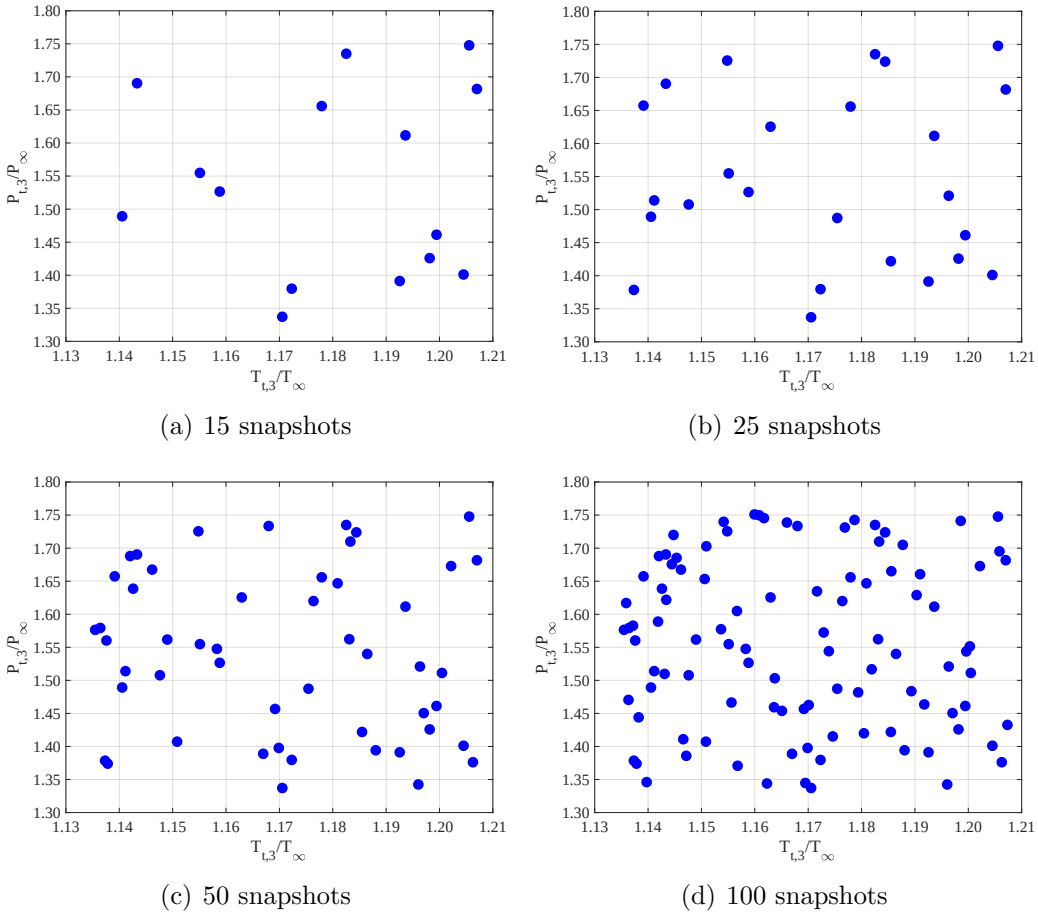


(a) 15 snapshots

(b) 25 snapshots

(c) 50 snapshots

(d) 100 snapshots

Figure 41: Subsets of snapshots used for sampling density study.

To assess the sensitivity of the aerodynamic ROM predictions to the sampling density, the means and standard deviations of the ROM prediction error are considered for each of the subsets shown in Figure 41. The results are provided in Figures

42-46.

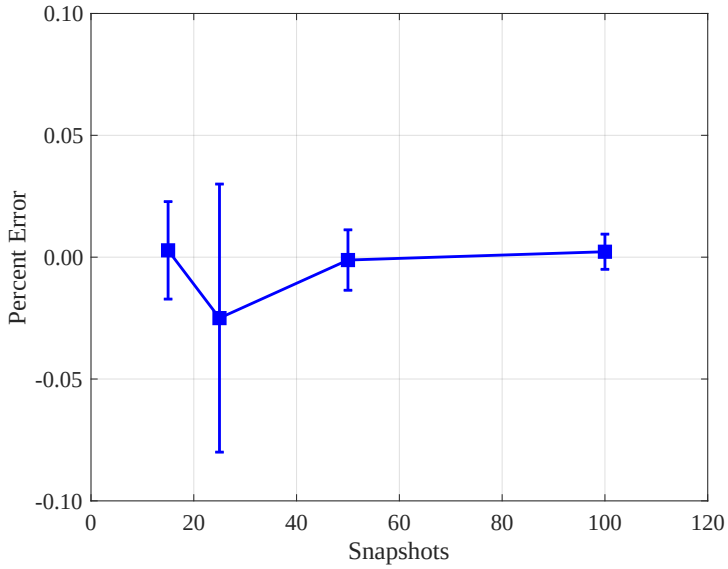


Figure 42: $DPCP_{avg}$ prediction error as a function of sampling density.

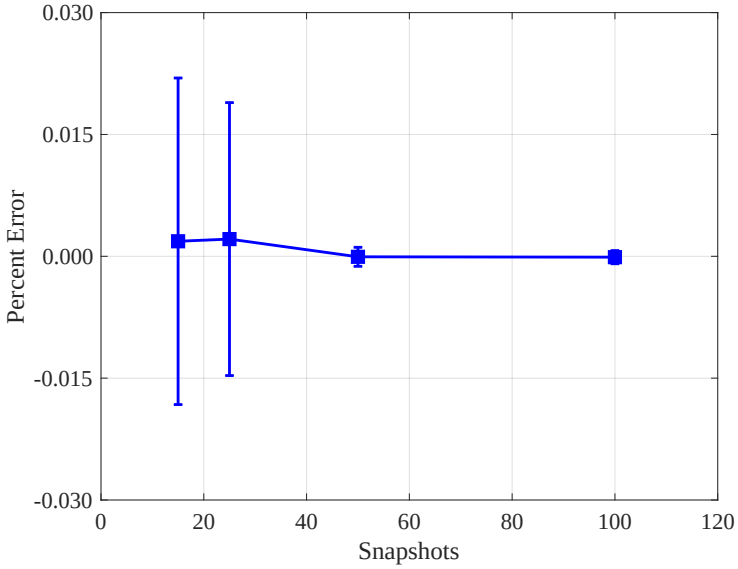


Figure 43: $PR$ prediction error as a function of sampling density.

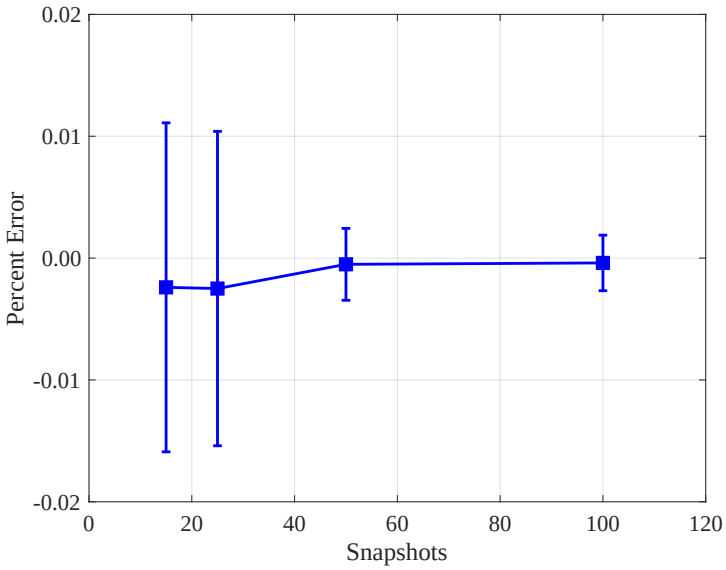


Figure 44: $FPR$ prediction error as a function of sampling density.

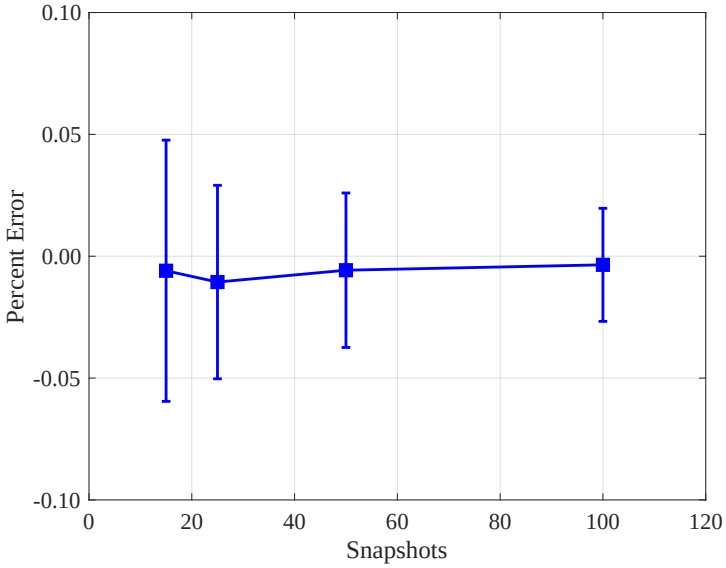


Figure 45: $P_{req}$ prediction error as a function of sampling density.

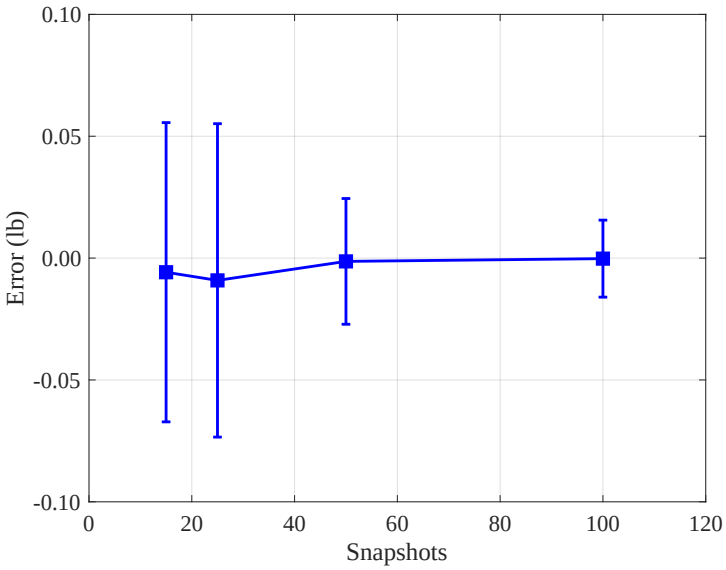


Figure 46: $F_x$ prediction error as a function of sampling density.

The sampling density results shown in Figures 42-46 illustrate the trend for the mean and standard deviations of the modeling error as a function of the number of snapshots used to generate the ROM. Note that the standard deviations are represented as error bars around the mean values. The results show that the ROM prediction error has a tendency to increase with a decrease in the number of samples used to create the model. However, the trend is not linear, and there are some cases, e.g., Figure 42, where the mean error and standard deviation is smaller for the 15 sample case than for the 25 sample case. Some of this behavior can be attributed to the method used to create the subsets of the snapshots. As previously discussed, the 100 snapshots were generated using Latin Hypercube sampling. The subsets were then obtained by only retaining the first 50, 25, or 15 snapshots of the full set. As a result, the coverage of the design space is not as well distributed for the smaller subsets. This could have been improved by creating additional DOEs using Latin Hypercube sampling for the 50, 25, and 15 snapshot ROMs. However, this would have significantly increased the computational requirements for the experiment. Additionally, the error is still very small and did not warrant further effort. In fact, the

results show that very good predictions are obtained for as little as 15 snapshots.

### 4.2.5 Summary

Experiment 1.2 was performed to assess the prediction capabilities of the aerodynamic ROM over ranges of propulsor operating conditions, as defined by the fan pressure ratio. The experiment also included an assessment of the impact of sampling density on the quality of the ROM predictions. The results show that the aerodynamic ROM provides very accurate predictions when using only 15 snapshots to develop the ROM. Note that it is likely that even fewer snapshots could be employed for the ROM; however, the design space coverage would be insufficient due to the method used to obtain the subsets of data. The results of the experiment discussed here confirm Hypothesis 1.2.

Also, the goodness of fit metrics discussed in the chapter only considered the ROM developed using 100 snapshots while the snapshot sensitivity study considered the ROMs developed using 15, 25, 50, and 100 snapshots. The goodness of fit metrics for all four ROMs are provided in Appendix A.

# CHAPTER V

# ROM-BASED, COUPLED MULTIDISCIPLINARY ANALYSIS (RESEARCH QUESTION 2)

In the previous chapter, the aerodynamic ROM was shown to provide excellent predictions over a range of propulsor operating conditions. This chapter focuses on the application of the aerodynamic ROM to coupled MDA with the ultimate goal of validating the proposed approach against a CFD-based, coupled MDA approach. Based on this, the following research question is posed:

| **Research Question 2**: |
| --- |
| What are the prediction capabilities of the aerodynamic ROM for coupled MDA over a range of propulsor operating conditions? |

The capability of the ROM for providing accurate predictions for the decoupled analysis was previously demonstrated in Section 3.2. The question that remains is whether the ROM can accurately capture the coupling between the aerodynamics and the propulsion system. From the discussion in Chapter 4, the primary differences between the coupled and decoupled analyses are the inputs and outputs. Note that this is assuming that consistent mass flow rate has been enforced at the fan face and fan exit boundaries. For the decoupled analysis, the inputs are the total pressure and temperature at the fan exit, and the outputs are $FPR$ and $PR$ along with the other quantities that have been discussed. For the coupled analysis discussed in Chapter 4, $FPR$ is the input to the analysis with the total pressure and temperature being outputs. The coupled analysis consists of iterating on the total conditions at the fan exit to obtain the desired $FPR$ with $PR$ being the coupling variable between

the aerodynamic and propulsion system analyses. It is important to note that at each iteration during the coupled analysis, a decoupled analysis is performed. The prediction capability of the aerodynamic ROM for coupled MDA is narrowed down to the ability of the aerodynamic ROM to provide predictions over the appropriate range of total conditions such that the target range of $FPR$ is obtained. This ability has already been demonstrated from the results of Experiment 1.1. Based on this discussion, the following hypothesis is formulated:

**Hypothesis 2**: *If the POD ROM accurately predicts the aerodynamics over a feasible range of propulsor operating conditions, then the POD ROM accurately captures the coupling between the propulsion system and airframe and, therefore, will provide accurate predictions when employed for coupled MDA.*

## *5.1 Experiment 2*

To test Hypothesis 2, the requirements for the experiment are to provide a means of evaluating the ability of the aerodynamic ROM for capturing the interactions between the propulsion system and the airframe. As previously discussed, the aerodynamic ROM was shown to provide accurate predictions for the aerodynamics over the entire range of propulsor operating conditions. To evaluate the ability of the aerodynamic ROM to capture the interactions between the airframe and propulsion system analysis, the aerodynamic ROM will need to be coupled to the propulsion system analysis to perform coupled MDA. The ROM-based, coupled MDA approach will then need to be compared to the full-order model, which consists of the CFD analysis coupled to the propulsion system analysis. This will allow the accuracy of the ROM-based, coupled MDA approach to be evaluated relative to the CFD-based, coupled MDA approach for a given fan pressure ratio. Then, to evaluate the ability to capture the

interactions over the feasible range of operating conditions, the ROM-based and CFD-based approaches need to be used to perform predictions over the desired range of fan pressure ratios. Finally, the resulting coupled MDA predictions for the ROM-based and CFD-based approaches can be compared over the desired range of operating conditions to test Hypothesis 2. The range of fan pressure ratios for this experiment is provided in Table 5, which corresponds to increments of 0.05 with the upper and lower limits that were defined in Chapter 3. The details of this experiment are discussed in the following sections.

Table 5: FPR range for Experiment 2.

| Case | FPR |
|---|---|
| 1 | 1.10 |
| 2 | 1.15 |
| 3 | 1.20 |
| 4 | 1.25 |
| 5 | 1.30 |
| 6 | 1.35 |

## *5.2 CFD-Based, Coupled MDA*

The CFD-based, coupled MDA approach was discussed in detail in Chapter 4 and is briefly described again in this section. The inputs to the coupled analysis is the $FPR$ and an initial guess for the pressure recovery $PR_0$. These values are provided to the simple fan model to obtain the required total pressure and temperature at the fan exit. The total conditions are then enforced in the CFD analysis, which is performed in an iterative loop to ensure consistent mass flow rate across the fan. Note that the mass flow rate matching is performed using the propulsion BC in FUN3D. The resulting $PR$ at the fan face is then fed back to the simple fan model to provide the total pressure and temperature for the next iteration. This process is repeated until the $PR$ at the fan face is converged within a user-specified tolerance. The CFD-based, coupled MDA approach used for this work is summarized in Figure 47.

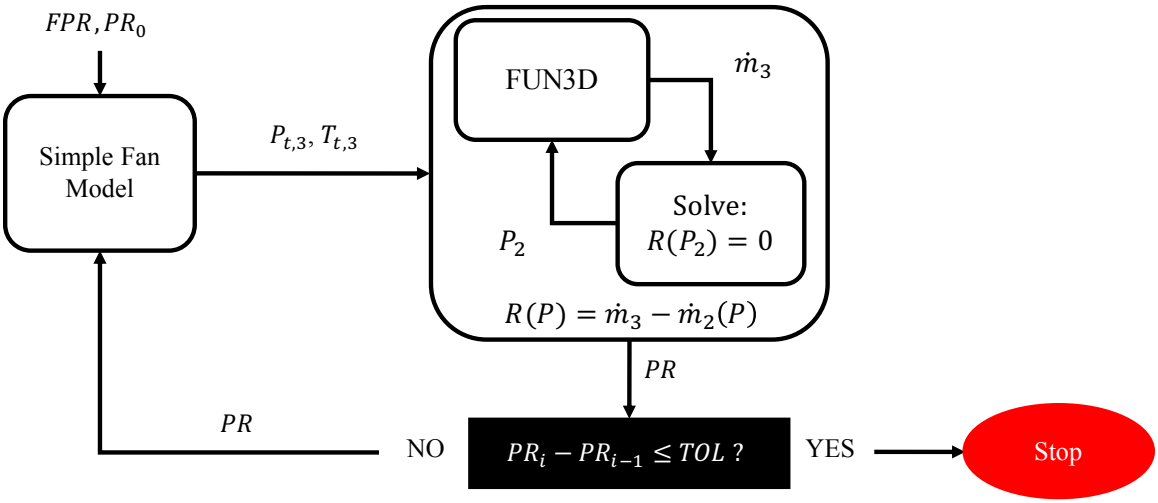


Figure 47: CFD-based, coupled MDA approach.

Additionally, the convergence behavior of the CFD-based, coupled MDA approach is illustrated in Figures 48 and 49 for the case of an $FPR$ of 1.1.

Figure 48 illustrates the behavior of the flow residuals over 5,000 iterations. Overall, both the mean flow and turbulence residuals are reduced by greater than 20 orders of magnitude. Some oscillitary behavior is observed in both residuals in part due to the iterative loops that are inducing periodic changes to the flow. Note that for this work, the first outer loop iteration consisted of 1,000 inner iterations to provide a well-converged mass flow rate at the fan exit and fan face using the propulsion BC. The inner loop consists of updating the back pressure at the fan face every 100 iterations to match the mass flow rate to that obtained at the fan exit boundary. After this initial startup, 500 iterations were performed in the inner loop for every outer loop iteration.

The results shown in Figure 49 illustrates the convergence behavior at the fan face and fan exit boundaries. Once again, the boundary conditions appear to converge much faster than the flow residuals shown in Figure 48 and are practically constant after 2,000 iterations. This behavior was also observed for the decoupled snapshots in Experiment 1.1. The primary difference here is the required start/stop of the

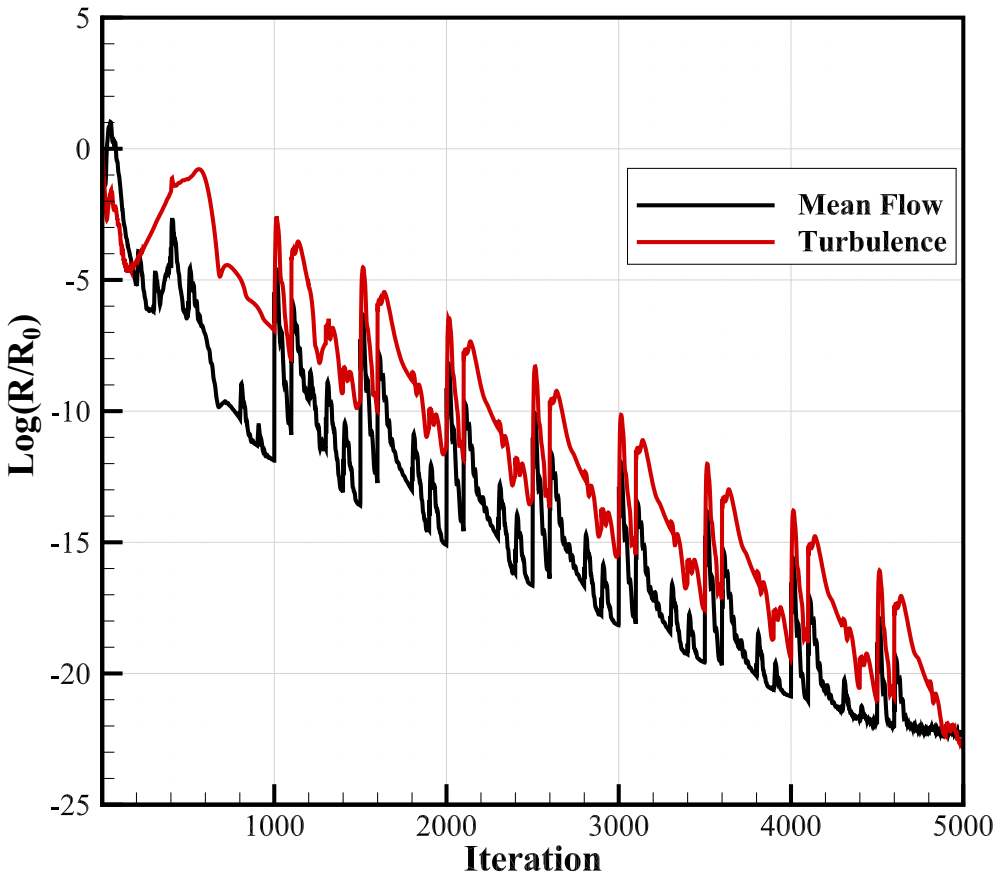


Figure 48: Convergence history for CFD-based, coupled MDA approach.

CFD solver due to the additional outer loop including the propulsion system analysis. Based on the observed convergence behavior, the CFD-based, coupled MDA simulations were performed for 2,000 iterations for each of the $FPR$ values given in Table 5.

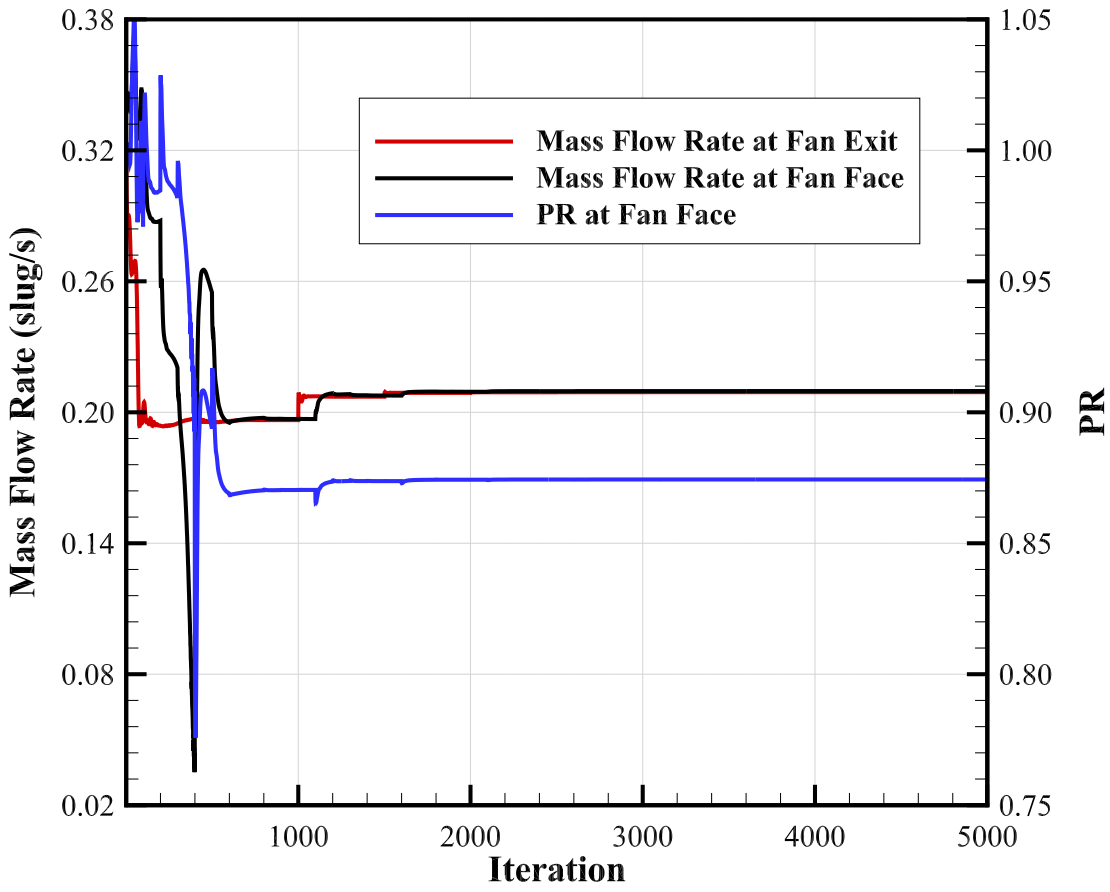


Figure 49: Convergence history at fan face and exit boundaries for CFD-based, coupled MDA approach.

## 5.3 ROM-Based, Coupled MDA

The ROM-based, coupled MDA approach is structured similarly to the CFD-based, coupled MDA approach with the primary difference being the substitution of the aerodynamic ROM for the CFD analysis. The inputs to the analysis are still $FPR$ and $PR_0$. These inputs are provided to the simple fan model to obtain the initial values for the total pressure and total temperature at the fan exit. These values are supplied to the fan face ROM to obtain the updated $PR$ value at the fan face. This value is fed back to the simple fan model to update the total conditions at the fan exit boundary. The process is repeated until the pressure recovery is converged within a user-defined tolerance. Once $PR$ at the fan face is converged, the final values of total pressure and temperature are provided to the surface and fan exit ROMs to obtain predictions for $p$ and $c_{f,x}$ on the surface of the aircraft. The ROM-based, coupled MDA approach is illustrated in Figure 89.

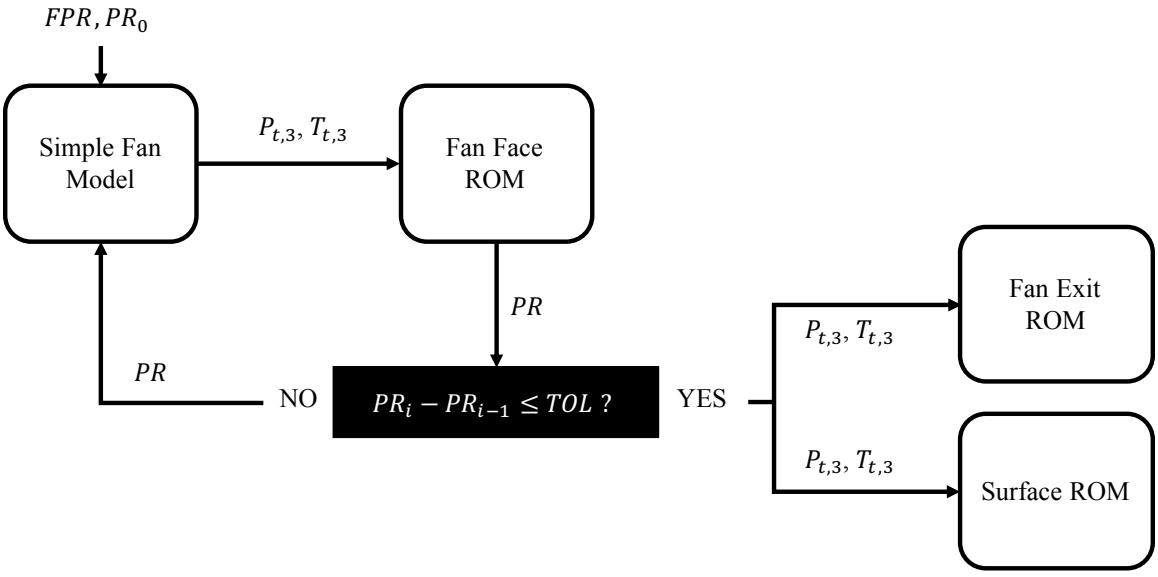


Figure 50: ROM-based, coupled MDA approach.

Additionally, an illustration of the convergence behavior for the ROM-based, coupled MDA approach is provided in Figure 51.

Figure 51 illustrates the $PR$ at the fan face as a function of iteration for an $FPR$

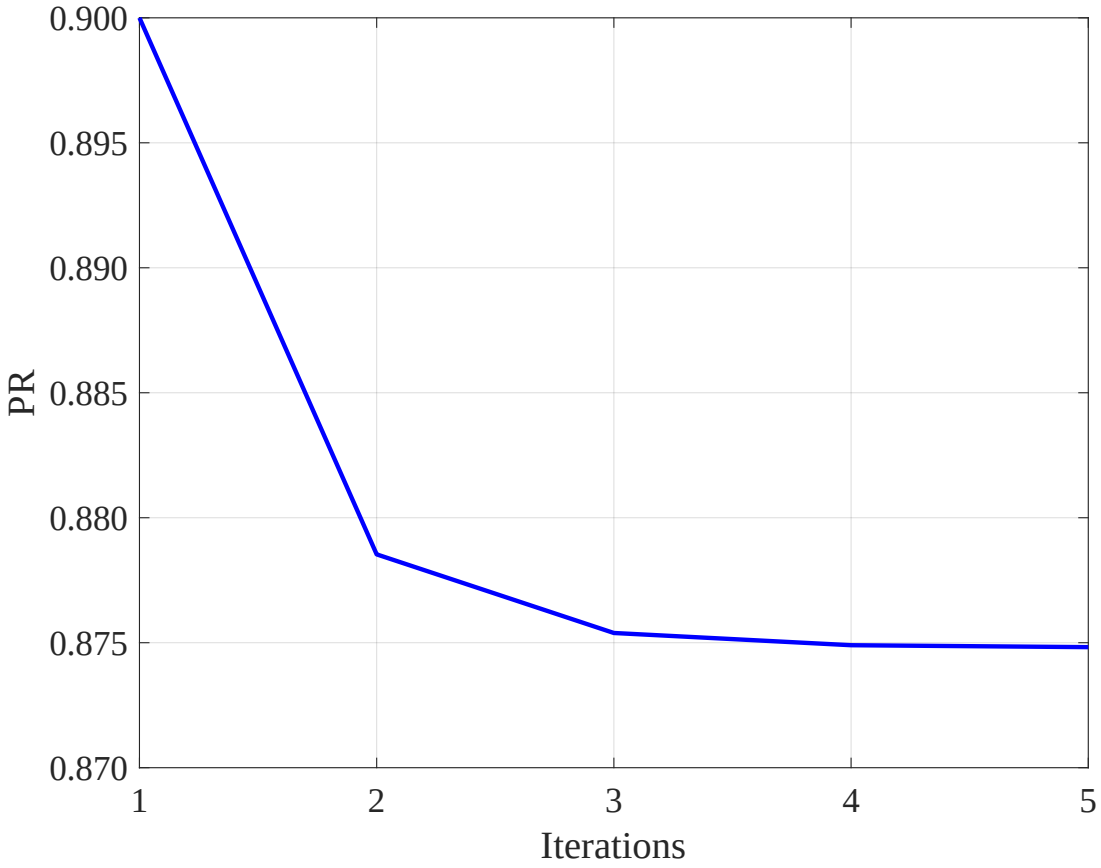


Figure 51: Convergence history for ROM-based, coupled MDA approach.

of 1.1. The results show that the solution converges in only five iterations.

## *5.4 Results*

Both the CFD-based and ROM-based coupled MDA approaches were used to simulate the $FPR$ values given in Table 5. The results are illustrated in Figures 52-55.

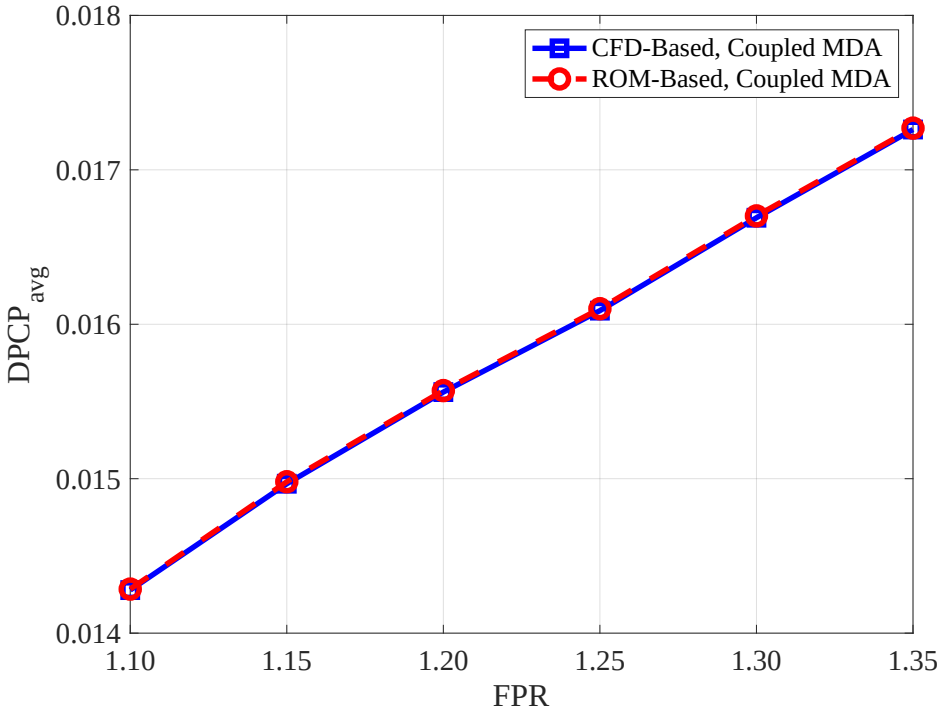


Figure 52: Distortion vs. fan pressure ratio.

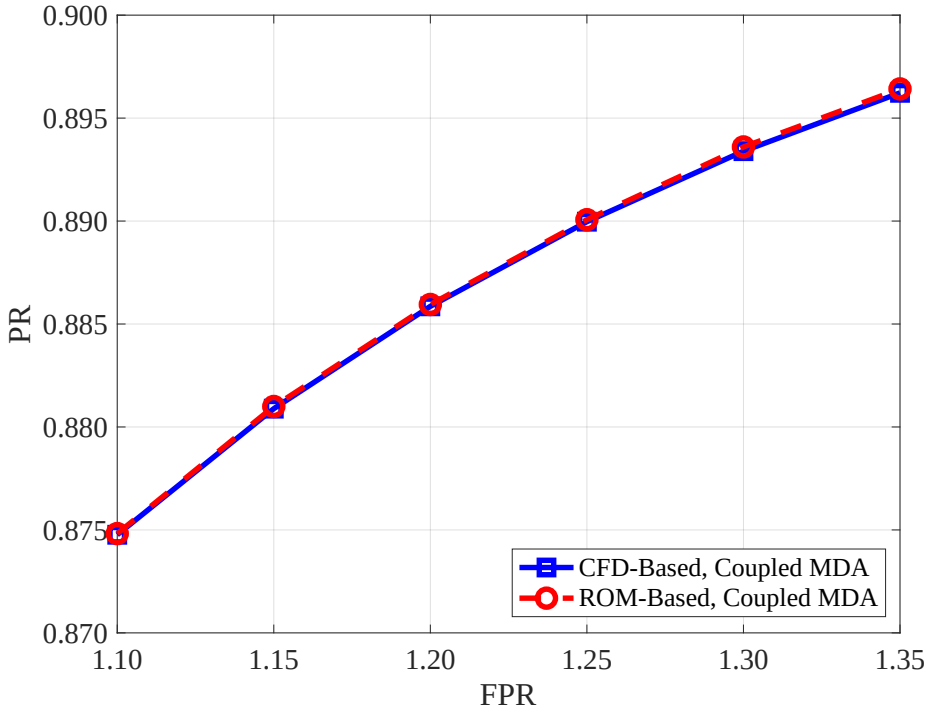


Figure 53: Pressure recovery at fan face vs. fan pressure ratio.

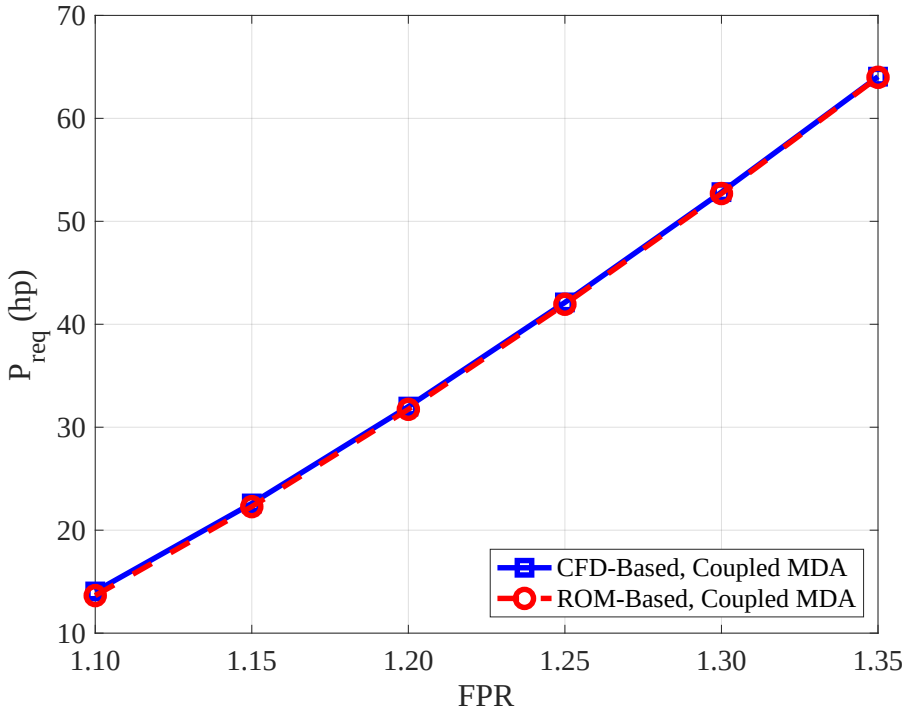


Figure 54: Power required vs. fan pressure ratio.

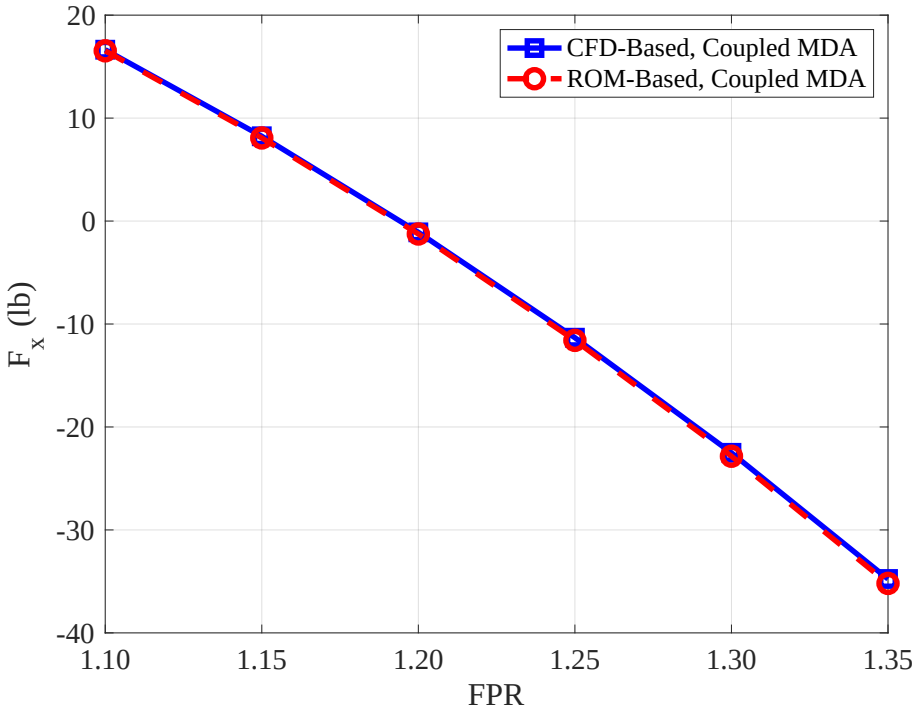


Figure 55: Axial force vs. fan pressure ratio.

The results in Figures 52-55 illustrate excellent agreement between the CFD-based, coupled MDA approach and ROM-based, coupled MDA approach over the entire range of $FPR$ values considered. Similar to the results provided in Chapter 4 for Experiments 1.1 and 1.2, the results shown for both $P_{req}$ and $F_x$ correspond to the half-span grids and the values for the full-span are, therefore, double the magnitude of these values. It is important to note that the aerodynamic ROM used in this experiment was developed using only 15 snapshots. The results shown here confirm Hypothesis 2.

## *5.5 Summary*

In this chapter, the aerodynamic ROM was applied to coupled MDA to perform predictions over a range of operating conditions. The goal was to validate the aerodynamic ROM for the application of coupled MDA. The resulting ROM-based, coupled MDA approach consisted of the aerodynamic ROM coupled to a propulsion system model. It was noted that the primary difference between the coupled and decoupled analyses is the inputs and outputs and that at each iteration in the coupled MDA, a decoupled analysis is performed. The coupled anlaysis consists of iteratively solving for the total conditions at the fan exit to provide the desired $FPR$. Since the aerodynamic ROM was parameterized over a range of $FPR$, via the total pressure and temperature at the fan face, Hypothesis 2 states that aerodynamic ROM can provide accurate predictions when coupled to a propulsion system analysis for coupled MDA. The results confirmed Hypothesis 2 by showing that the ROM-based, coupled MDA approach agreed favorably with the CFD-based, coupled MDA approach.

Also, the goodness of fit metrics discussed in the chapter only considered the ROM developed using 400 snapshots while the snapshot sensitivity study considered the ROMs developed using 50, 100, 200, and 400 snapshots. The goodness of fit metrics for all four ROMs are provided in Appendix B.

# CHAPTER VI

# ROM-BASED, COUPLED MDAO (RESEARCH QUESTION 3)

The previous two chapters have focused on the development and validation of the ROM-based, coupled MDA approach. The results show that accurate coupled MDA predictions were obtained with as few as 15 decoupled CFD simulations using only $FPR$ and $PR$ as the design variables. This chapter focuses on the extension of the ROM-based, coupled MDA approach to include the effect of shape changes. The resulting coupled MDA approach is applied to perform shape optimization of the aft-portion of the TCT concept with the ultimate goal of quantifying the approach's computational benefits relative to alternative methods.

## *6.1 Extended Aerodynamic ROM*

The first step is to extend the aerodynamic ROM that was developed in Chapter 4 to include the impact of shape changes. Then, in order to quantify the computational benefits, the sampling requirements for the aerodynamic ROM must be established. This leads to the following research question:

| **Research Question 3.1**: |
| --- |
| With the aerodynamic ROM extended to include shape variables, what is the tradeoff between computational cost and accuracy? What are the driving parameters? |

It is important to consider that the accuracy requirements are ultimately problem dependent. The purpose of this study is not to define a required number of samples.

Instead, the goal is to evaluate the tradeoff between computational cost and accuracy. The results of Experiment 1.2 showed that while there was a tradeoff between computational cost and accuracy for the case of two design variables, the error was negligible, and accurate predictions were obtained when only using 15 snapshots to create the ROM. For shape optimization, the required number of design variables in the DOE is increased due to the addition of shape parameterization variables, which inevitably requires an increase in the number of snapshots to ensure adequate coverage of the design space. The results of Experiment 1.2 also showed that while the overall error was small, the distortion at the fan face displayed the largest error, along with the highest sensitivity to sampling density. For the extended aerodynamic ROM, the flow at the fan face will include variations resulting from both changes in operating conditions and upstream shape changes. Therefore, the distortion at the fan face is expected to exhibit greater variation for the larger design space, which should increase the sensitivity of the distortion prediction to sampling density. Based on these observations, the following hypothesis is stated:

**Hypothesis 3.1**: *If the aerodynamic ROM is extended to include the impact of shape variables, then the sampling requirements for the POD ROM will increase with the accuracy of the distortion metric driving the sampling requirements.*

### 6.1.1 Experiment 3.1

In order to test Hypothesis 3.1, the requirements for the experiment were consistent with those given for Experiment 1.2. The primary difference is the addition of the shape variables, which the hypothesis states will increase the sampling requirements. Note that Experiment 2 demonstrated that the ability to accurately perform coupled MDA with the aerodynamic ROM depends only on the ability to accurately perform decoupled predictions. Therefore, the ROM validation step is only peformed for the

decoupled predictions in this chapter. Similar to Experiment 1.2, the results of Experiment 3.1 will be used to assess the tradeoffs between computational cost and accuracy of the ROM to determine the number of samples required for accurate predictions, and, therefore, establish the computational cost of the ROM to be employed for the design study performed in Section 6.2.

### 6.1.2 Shape Parameterization

The first step to the ROM development is the definition of shape variables. As discussed in Chapter 3, the BandAids software was used to perform the desired shape changes. Additionally, the shape changes were limited to the aft-portion of the fuselage. The marking surface used to designate the design region for the TCT concept is illustrated in Figure 84. Based on the designated design region, BandAids was employed to create a 10x10 parameterization as illustrated in Figure 85. The resulting parameterization consists of 100 total design nodes.

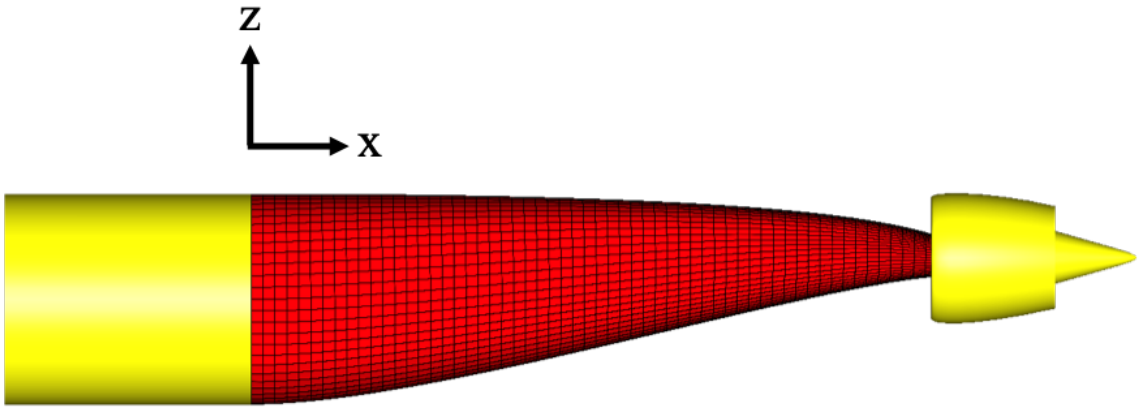


Figure 56: Design marking surface for shape parameterization.

The shape parameterization given in Figure 85a illustrates the 10 axial stations resulting from the BandAids parameterization. Note that only six are designated as design stations while four are held fixed. BandAids does not automatically enforce continuity of slope at the edges of the design region. To accomodate this and ensure good quality shape changes, the two stations closest to both edges were held fixed.

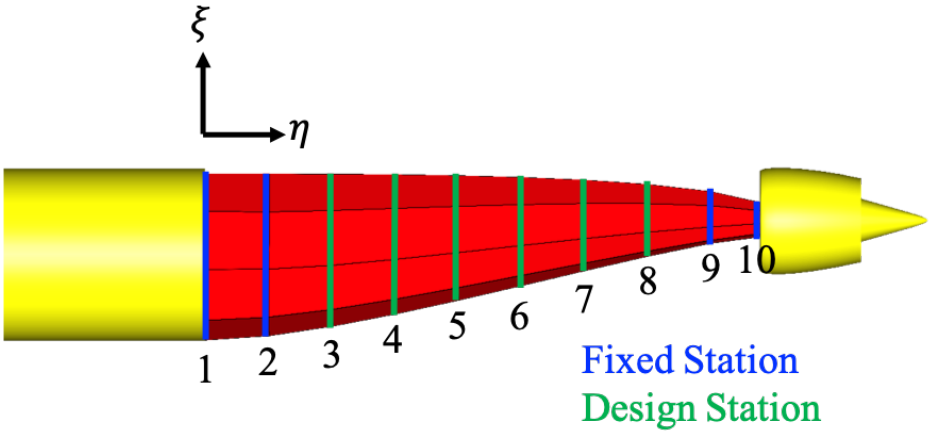


(a) Axial stations

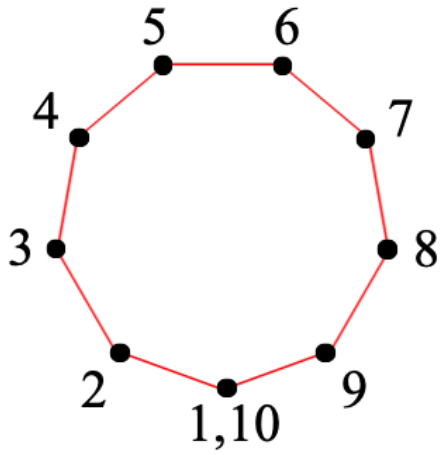


(b) Design nodes at each axial station

Figure 57: 10x10 parameterized design surface.

At each of the six design stations, the cross-section is parameterized by 10 nodes, as shown in Figure 85b, for a total of 60 design variables. The design variables in BandAids correspond to the normal displacement of each node in the parameterized space. Compared to methods that employ variables with engineering definitions to parameterize the shape, such as the Vehicle Sketch Pad (OpenVSP) and Engineering Sketch Pad (ESP), the design variables used by BandAids are less intuitive [70, 71].

There are two main challenges associated with this type of parameterization. The first challenge is the relatively large number of design variables that are required to describe the shape changes, and the second challenge is that unrealistic shapes may be produced due to the ability to move each node independently. One potential solution involves grouping the movement of the surface nodes. This can drastically reduce the number of design variables and provide the ability to reduce the occurence of unrealistic shapes through proper constraint. However, grouping the node movement can limit design changes, and, ultimately, prevent the ability to obtain nonintuitive designs.

For this work, one of the objective functions considered for optimization is the distortion at the fan face. To better understand how to group the surface nodes, a contour plot of the pressure recovery at the fan face for the baseline configuration is shown in Figure 58.

In observing the contour plot, there is a region of high total pressure at the top of the fan face. This region results in a one-per-revolution distortion component in an otherwise fairly uniform distribution of total pressure. To reduce the distortion at the fan face, the options are to either remove the high pressure region all together or to increase the total pressure around the bottom and side portions of the fan. Note that all of the simulations performed for this work were for cruise at 0° angle of attack. One potential means of reducing the distortion at the fan face would be to simply vary the angle of attack. However, the angle of attack for cruise depends on other factors such as the lift-to-drag ratio and cruise speed. For this work, it is assumed that the design cruise angle of attack is 0°, such that the goal is to maximize the performance of the aircraft at this condition. Additionally, the distortion at the fan face for this case could be reduced by decreasing the fan diameter. As discussed in Chapter 4, the fan diameter was held fixed for this exercise. Based on this discussion, the options are then to either increase the boundary layer thickness over the top half of the fuselage

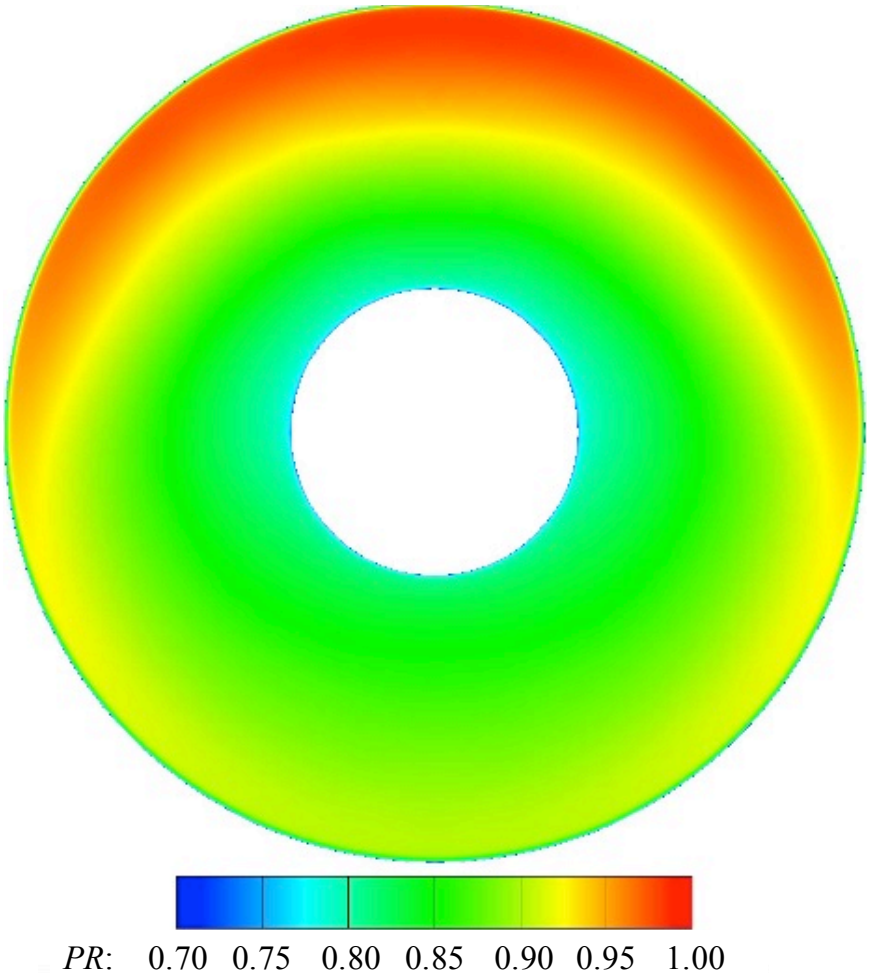


Figure 58: Pressure recovery contour map at fan face for the baseline configuration.

to reduce the total pressure at the top of the fan face or to reduce the boundary layer thickness along the bottom of the fuselage to increase the total pressure at the bottom half of the fan face. In general, modifying the fuselage shape to increase the boundary layer thickness could potentially reduce or eliminate any benefit gained from the BLI technology due to an increase in momentum deficit. Based on this discussion, the target of the design study was to optimize the shape of the bottom portion of the fuselage to allow for a reduction in distortion while also maintaining, and potentially even improving, the performance of the aircraft. As previously discussed, the overall goal for the BLI technology is to reduce the aircraft fuel burn. The purpose of the aft-propulsor is to reduce the thrust required from the underwing turbofans. Note that

the underwing turbofans must also provide power to the aft-propulsor. Therefore, the balance between the reduction in the thrust requirements of the underwing turbofans and the power required for the aft-propulsor must be such that the fuel burn reduction goal is achieved. For this work, the underwing turbofans were not modeled so the actual fuel burn was not considered. As a result, the performance of the TCT concept was characterized by the axial force and the power required for the propulsor. This is discussed in more detail in the optimization problem in Section 6.2.

To isolate the design study to the bottom portion of the fuselage, the points at each cross-section, corresponding to the design stations in Figure 85a, were grouped to a single design variable, $\Delta s$, as shown in Figure 59.

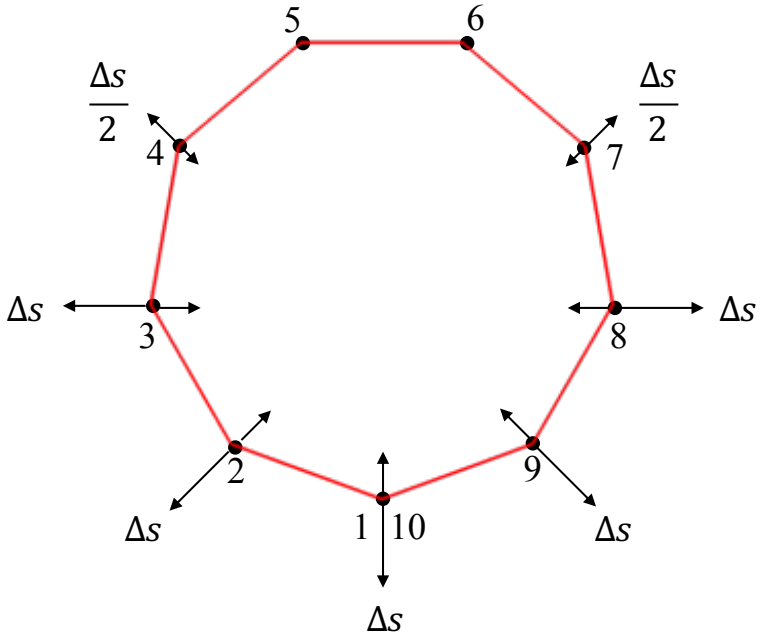


Figure 59: Final shape variables for each cross-section.

At each of the six design stations shown in Figure 85a, nodes 1, 2, 3, 8, 9, and 10 move in unison with a range of $-1" \leq \Delta s \leq 2"$. Nodes 5 and 6 define the movement of the top portion of the fuselage and are held fixed. Finally, nodes 4 and 7 are linearly interpolated to provide smooth shape changes. Note that the asymmetric range for the node movement is due to limitations imposed by BandAids. These

ranges represent the upper and lower limits of surface movement that were achievable with BandAids for the TCT concept without obtaining kinks in the geometry.

The shape parameterization employed for this work was simplistic and, as such, chosen to initially demonstrate ROM-based, coupled MDAO. The quality of the optimization results are going to heavily depend on the shape parameterization. Future work should focus on providing the capability for more complex shape changes with a larger range to allow for nonintuitive shapes with potentially better performance.

### 6.1.3 ROM Development

With the shape parameterization defined, the next steps are to create the DOE, simulate the DOE using the full-order model to obtain the snapshots, and generate the aerodynamic ROM. The DOE consisted of a total of eight variables: two for the propulsor ($PR_i, FPR_i$) and six for the shape changes ($\Delta s_3, \Delta s_4, \Delta s_5, \Delta s_6, \Delta s_7, \Delta s_8$). The ranges are provided in Table 11.

Table 6: DOE ranges for the extended aerodynamic ROM.

| | Minimum | Maximum |
|---|---|---|
| $FPR_i$ | 1.10 | 1.35 |
| $PR_i$ | 0.86 | 0.92 |
| $\Delta s$ | -1.00 | 2.00 |

A total of 400 DOE cases were generated using a Latin Hypercube design. The snapshot generation process discussed in Chapter 4 is followed for the current model with an additional step of deforming the surface grid to reflect the shape variable DOE values. The updated process, shown in Figure 86, consists of two branches to provide the necessary inputs for FUN3D. The $FPR_i$ and $PR_i$ values from the DOE are supplied to the simple fan model to obtain $P_{t,3}$ and $T_{t,3}$, and the shape variables are supplied to BandAids to obtain the deformed surface grid. The deformed surface grid and the fan exit boundary conditions, $P_{t,3}$ and $T_{t,3}$, are finally supplied to FUN3D to obtain the snapshots.

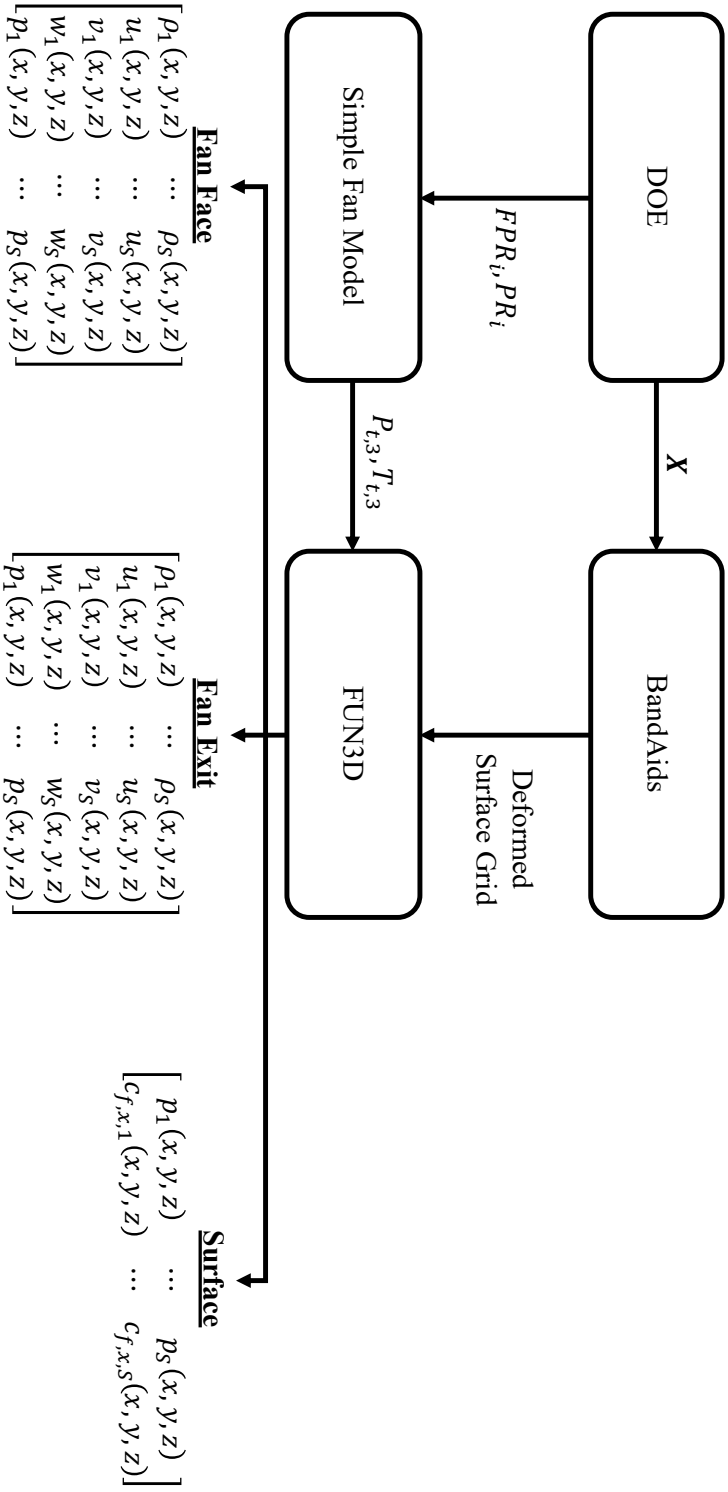


Figure 60: Snapshot generation process for the extended aerodynamic ROM.

Once the snapshots were generated, the next step was to develop the aerodynamic ROM, as discussed in Chapter 4. This aerodynamic ROM generation process is

summarized in Figure 88.

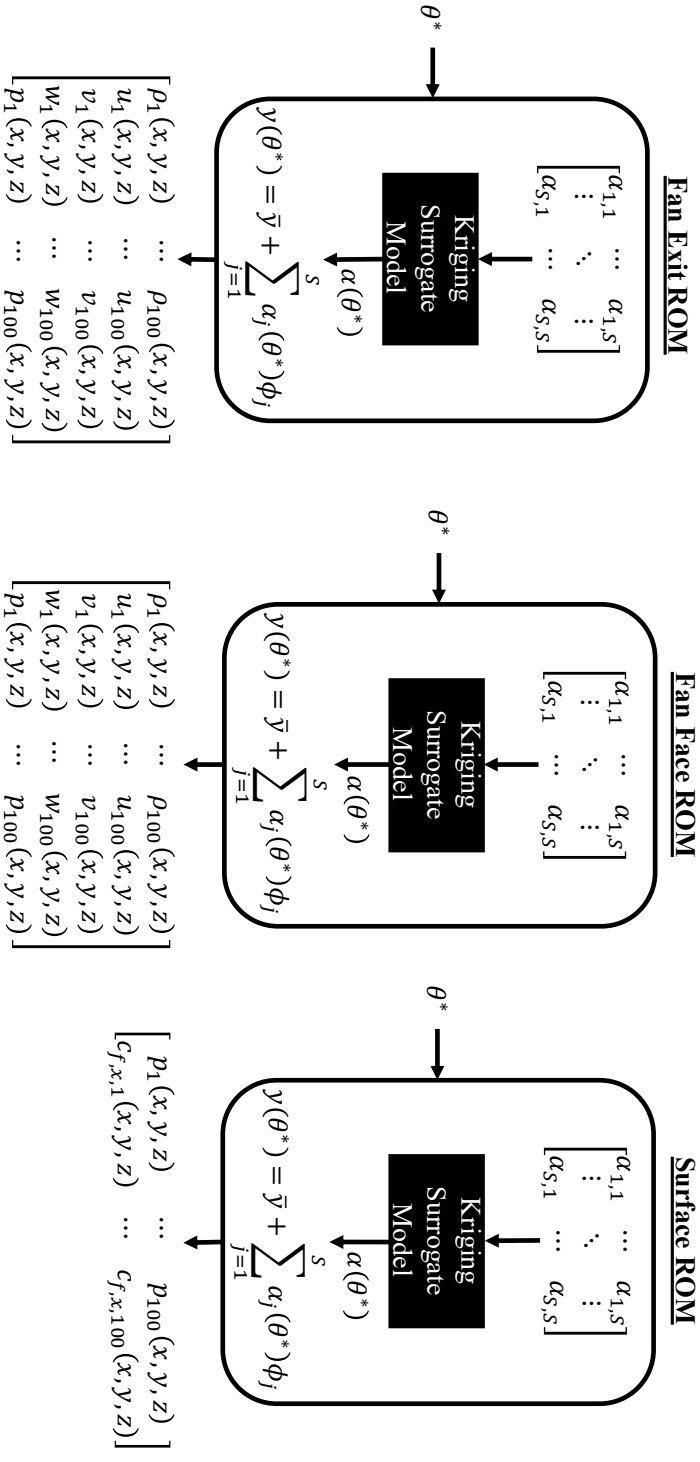


Figure 61: Online prediction process for the extended aerodynamic ROM.

### 6.1.4 Results

To assess the accuracy of the extended aerodynamic ROM, 100 additional snapshots were produced over the range of variables defined in Table 11. Similar to Experiment 1.2, these snapshots were not used to build the ROM, but instead were used to compare the ROM predictions to the CFD analysis through the goodness of fit metrics. First, the goodness of fit metrics are compared in Figures 62-66 for the five evaluation metrics $DPCP_{avg}$, $PR$, $FPR$, $P_{req}$, and $F_x$, respectively. This step employs the ROM that was developed using all 400 snapshots. So far, the ROM vs. CFD comparisons have only considered integrated quantities. However, one of the benefits offered by reduced-order modeling is the prediction of field variables. Comparing the accuracy of the field variable distributions relative to the CFD analyses is a much more difficult task and becomes even more difficult when attempting to compare a large number of solutions. One method is to simply analyze the results independently. A qualitative assessment of the solution quality can be obtained for an individual case by plotting the distribution of the difference between the ROM prediction and the CFD solution. This distribution can be used to review cases exhibiting larger error and get an idea of the cause and develop a higher level of confidence in the model predictions. For example, if the error distribution shows relatively large errors in areas of the computational domain where no shape or boundary condition changes are occuring, this could indicate a problem with the model. To demonstrate this, two cases are considered that correspond to the largest errors in the $DPCP_{avg}$ predictions. The comparisons, provided in Figures 67-70, show contour plots of the error in the predicted total pressure distribution on both the fan face and fan exit boundaries, along with the error in the predicted axial force per area for each cell on the surface domain. This qualitative assessment was not considered for the results of Experiment 1.2 since the errors were negligible. Finally, the sensitivity of the predictions to sampling density is assessed by comparing the mean and standard deviations of the modeling error for the five

evaluation metrics. These comparisons were performed using ROMs developed using 50, 100, 200, and 400 snapshots. The results of this study are provided in Figures 72-76.

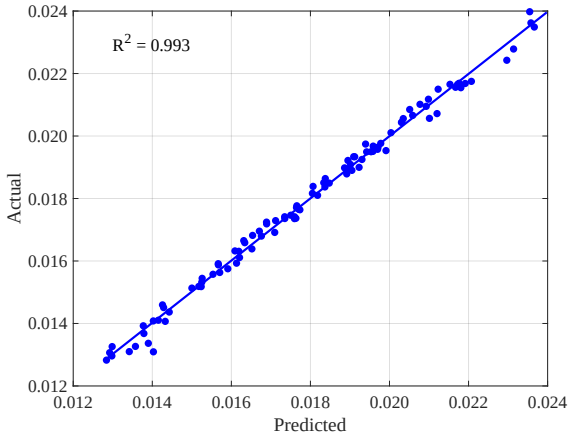


(a) Actual-by-predicted

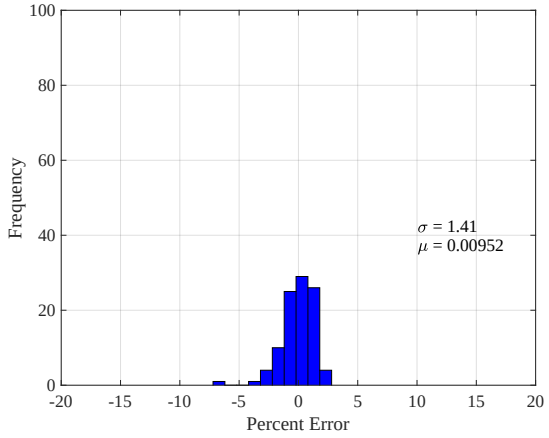


(b) Histogram

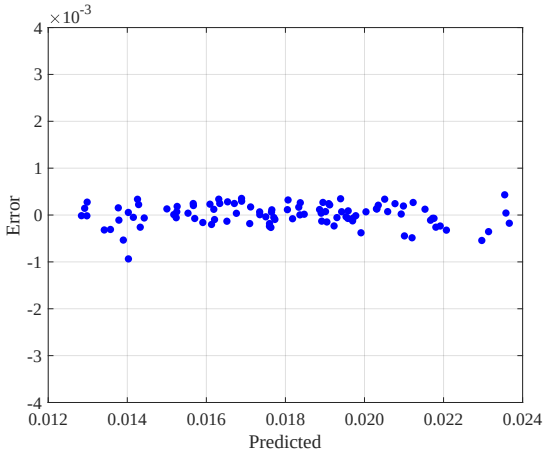


(c) Error-by-predicted

Figure 62: $DPCP_{avg}$ error metrics.

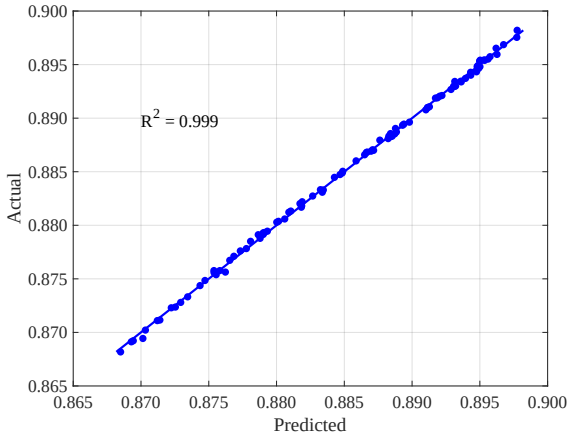


(a) Actual-by-predicted

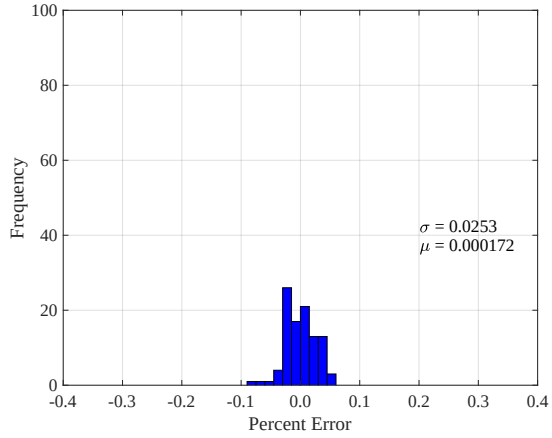


(b) Histogram

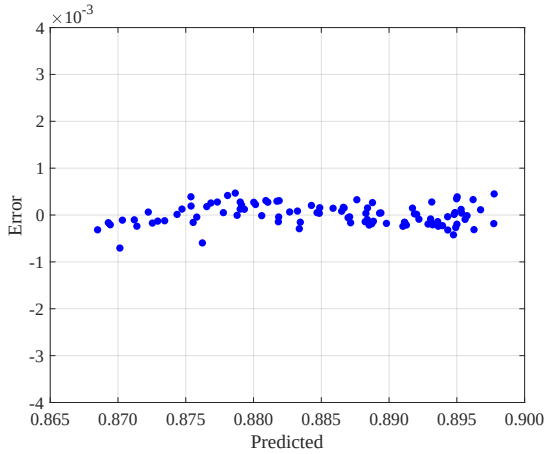


(c) Error-by-predicted

Figure 63: $PR$ error metrics.

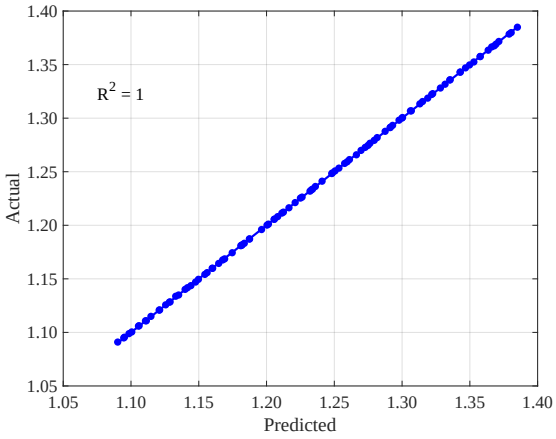


(a) Actual-by-predicted

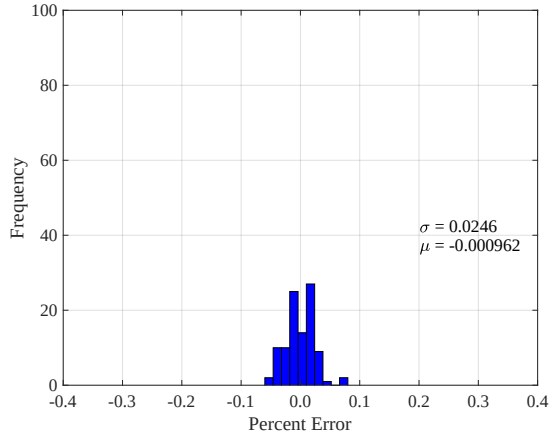


(b) Histogram

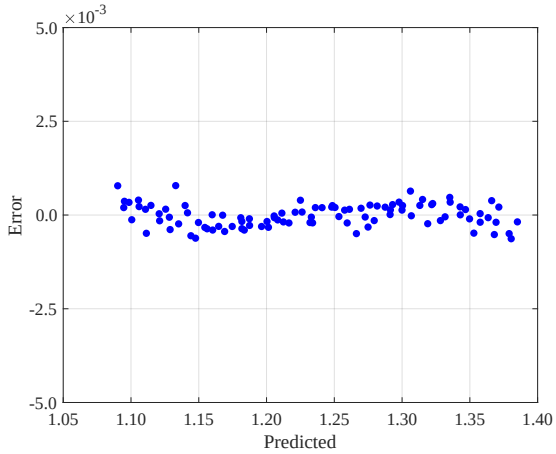


(c) Error-by-predicted

Figure 64: $FPR$ error metrics.

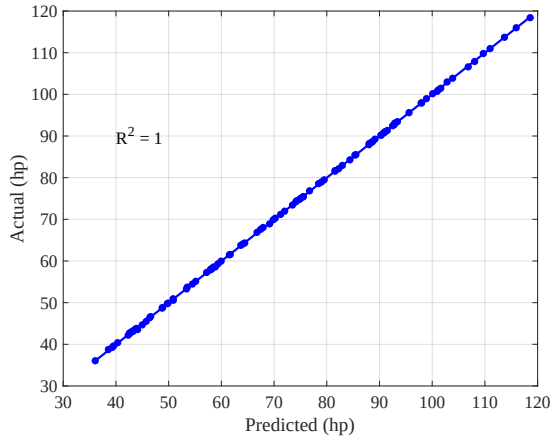


(a) Actual-by-predicted

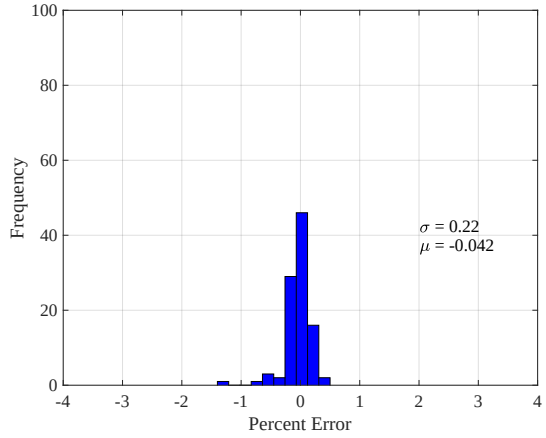


(b) Histogram

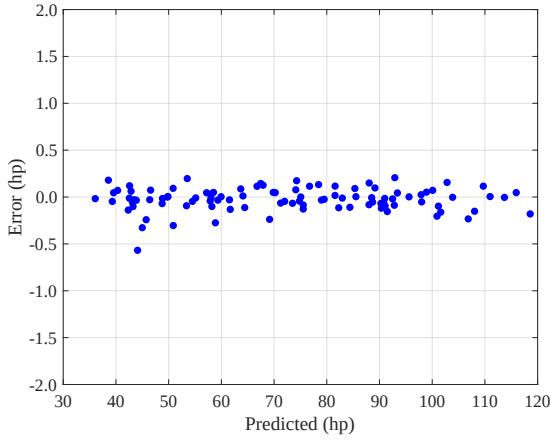


(c) Error-by-predicted

Figure 65: $P_{req}$ error metrics.

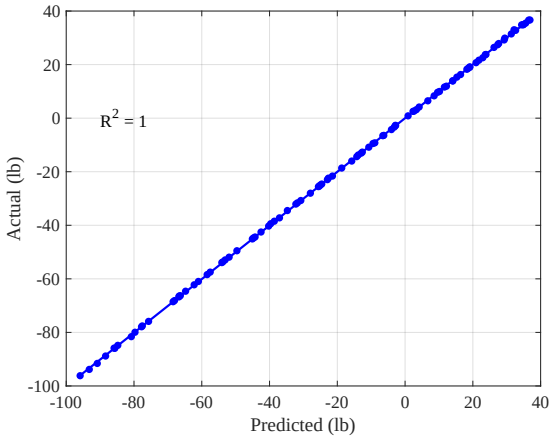


(a) Actual-by-predicted

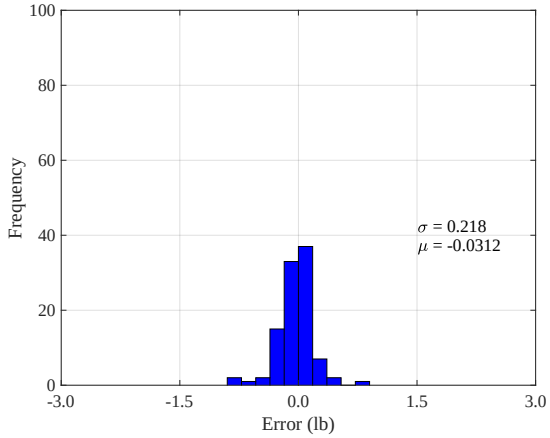


(b) Histogram

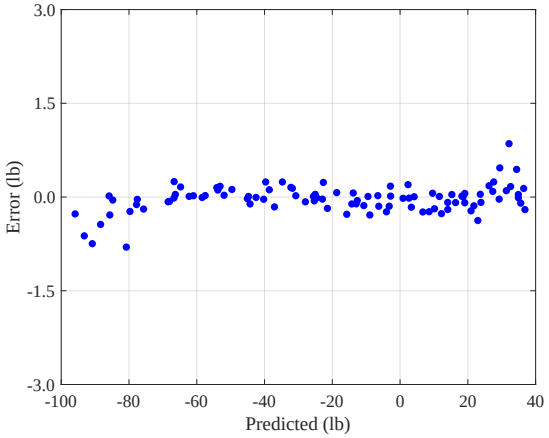


(c) Error-by-predicted

Figure 66: $F_x$ error metrics.

The results show that while the error is larger relative to the ROM developed in Chapter 4, favorable agreement between the aerodynamic ROM predictions and the CFD is still achieved. All of the results provided have an $R^2$ value of ≈1 with mean errors near zero and standard deviations less than 1% with the exception of the $DPCP_{avg}$ predictions. Here, the error for the axial force is again provided in units of lb due to issues near the zero crossing. The axial force for the unpowered aircraft is 70 lb for reference. For the $DPCP_{avg}$ predictions, the histogram illustrates a mean error near zero, but the standard deviation is 1.41%. However, the error-by-predicted results shown in Figure 62c illustrate the predicted error is bounded by ±0.001. This is excellent agreement, and the larger percent errors are considered acceptable.

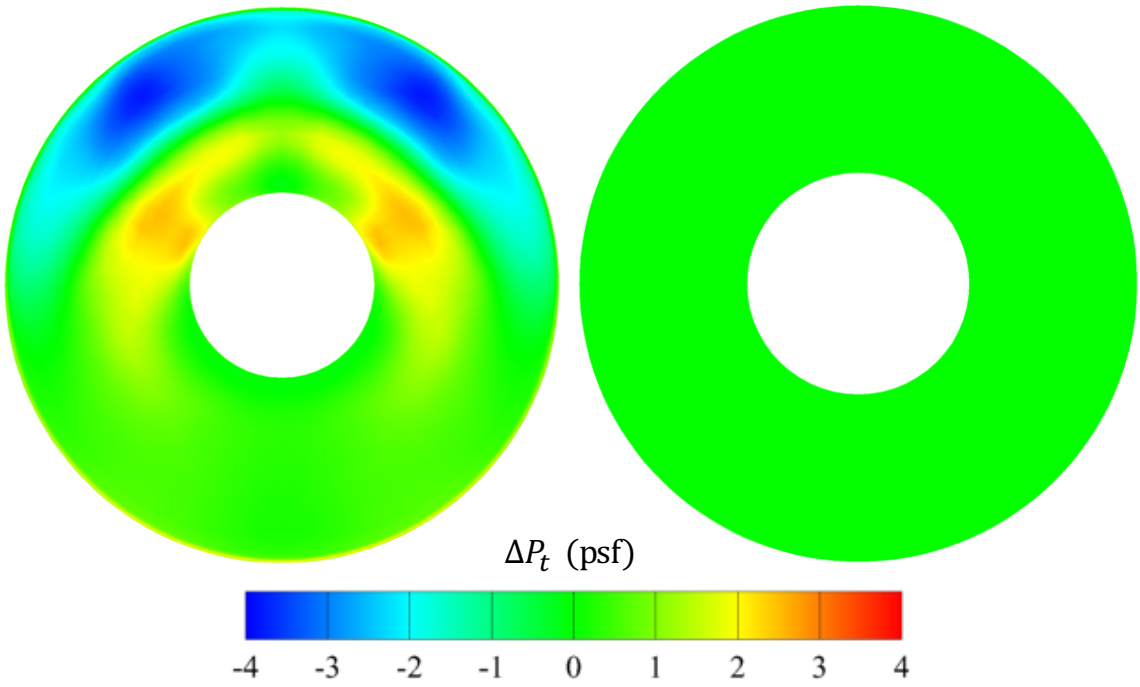


Figure 67: $P_t$ error distribution on fan face (left) and fan exit (right) for case 61.

The results shown in Figures 67 and 68 correspond to case 61 of the 100 validation cases, which exhibits the largest error in $DPCP_{avg}$ with -7.15% error and is an outlier in the histogram shown in Figure 62. For the results, positive and negative values correspond to the ROM underpredicting and overpredicting results relative to the

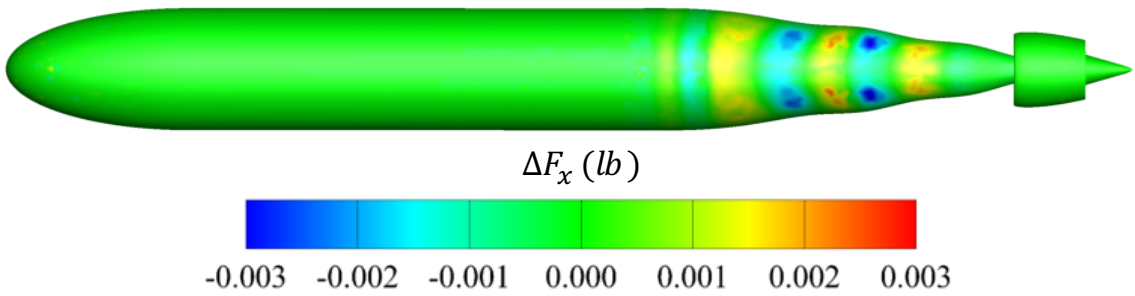


Figure 68: $F_x$ error distribution on surface for case 61.

CFD, respectively. The error in total pressure at the fan face shows that the largest difference occurs near the top of the domain with the ROM predicting higher total pressures. The ROM also predicts lower total pressures near the hub on the top half of the fan face. The relatively large errors in total pressure on the fan face is not typical of the ROM predictions. The contour plots of the fan exit illustrate excellent agreement, which is expected since the fan exit boundary experiences only changes in total pressure and temperature. In Figure 68, the distribution of $\Delta F_x$ on the surface illustrates very good agreement overall, where the largest errors occur in the fuselage design region. This is an important result since the rest of the surface is not changing, and any errors shown there would demonstrate issues with the aerodynamic ROM.

The results shown in Figures 69 and 70 correspond to case 36, which exhibits the maximum error in the predicted $DPCP_{avg}$ on the other end of the spectrum with an error of roughly 2.3%. The results show that the error is smaller relative to the previous case. The error in total pressure at the fan face is bounded by $\pm 1$ psf with the exception of a thin region in the boundary layer that exhibits a maximum total pressure error of roughly 3 psf. To examine this difference further, a closeup view of the boundary layer profile in this region is provided in Figure 71. The results show that the aerodynamic ROM compares favorably to the CFD predicted boundary layer profile with differences of up to 3 psf observed in a very small region near the peak. Again, the fan face results show very good agreement, and the surface results show

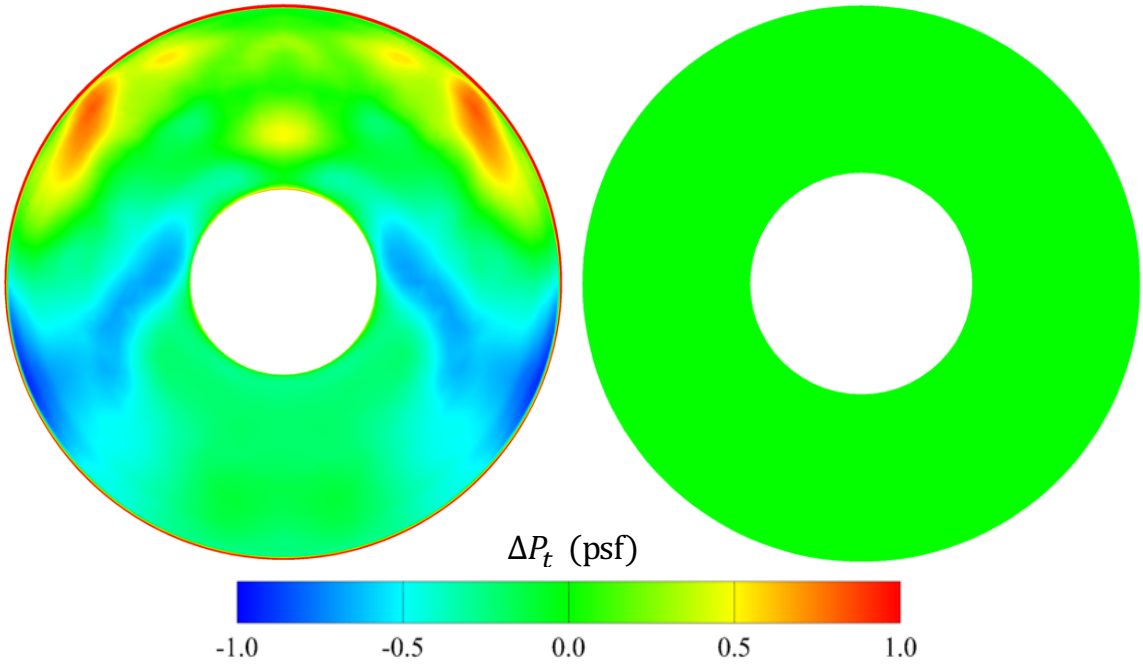


Figure 69: $P_t$ error distribution on fan face (left) and fan exit (right) for case 36.

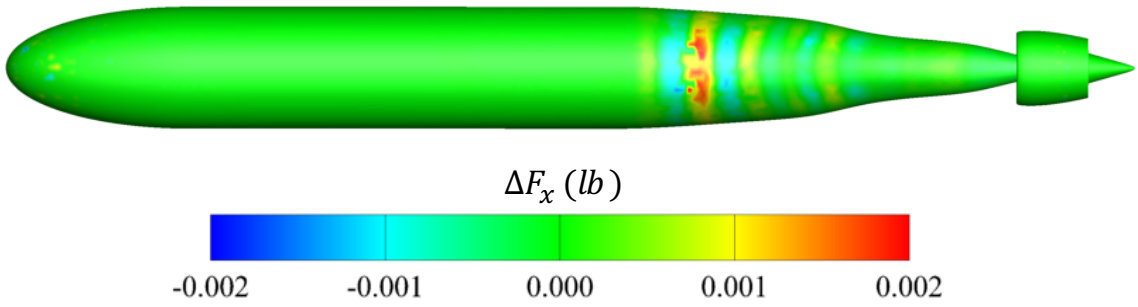


Figure 70: $F_x$ error distribution on surface corresponding for case 36.

slight differences in the force contribution in the design region. Based on the error distributions and goodness of fit metrics, the aerodynamic ROM provides accurate predictions with errors concentrated in regions of the computational domain that experience large changes.

The sampling density results shown in Figures 72-76 illustrate the mean and standard deviations of the modeling error as a function of the number of snapshots used to generate the ROM. Note that the standard deviations are represented as error bars around the mean values. The results show a general trend of an increase in error

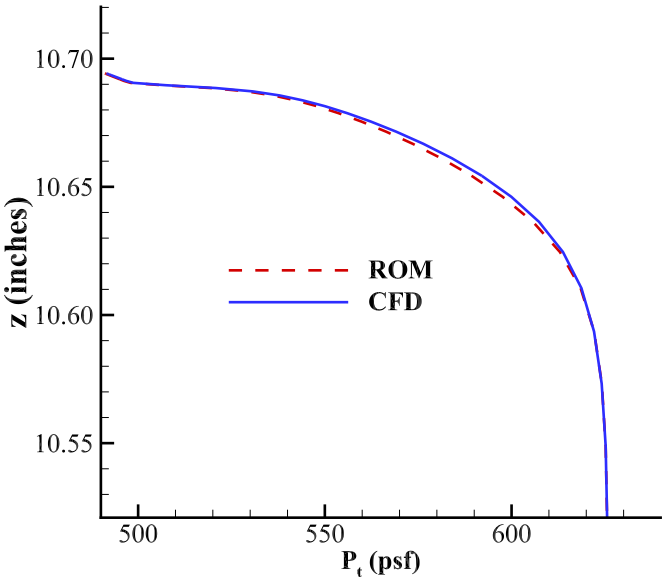


Figure 71: Boundary layer comparison at location of largest difference.

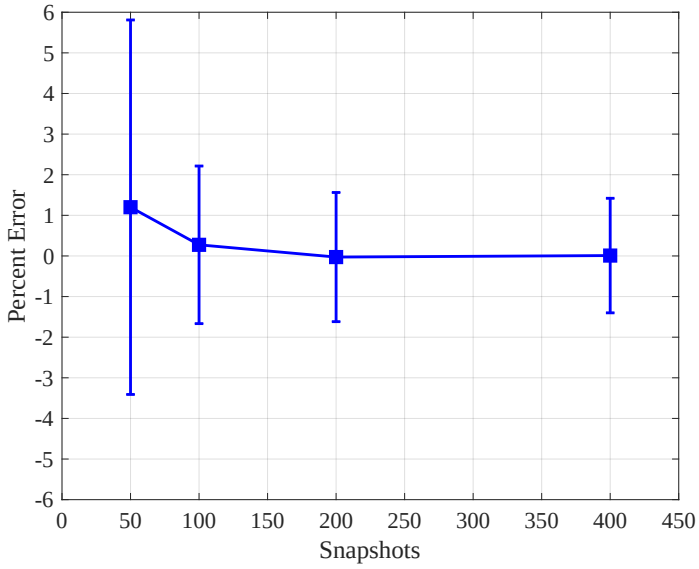


Figure 72: $DPCP_{avg}$ prediction error as a function of sampling density.

with a decrease in the number of snapshots used to generate the aerodynamic ROM. One interesting observation is that in some cases, the standard deviation decreases as the number of snapshots decreases from 400 to 200. However, the differences are insignificant and are likely due to the differences in the sampling distribution between

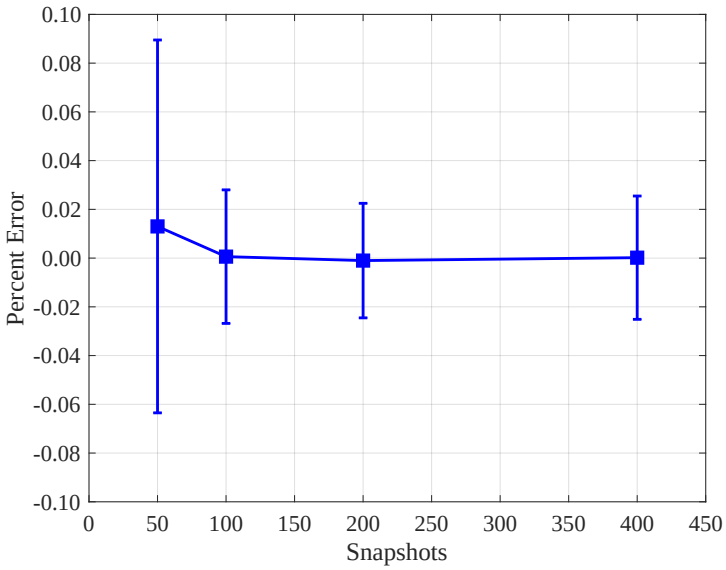


Figure 73: $PR$ prediction error as a function of sampling density.

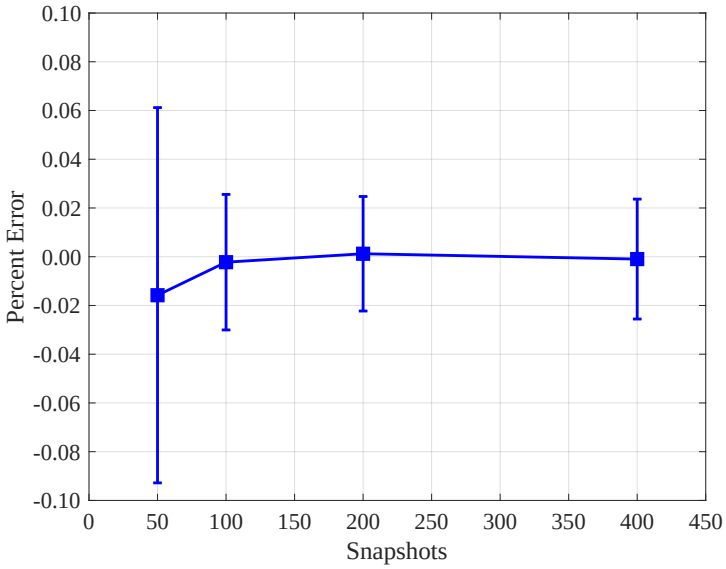


Figure 74: $FPR$ prediction error as a function of sampling density.

the subsets of snapshots, as mentioned in Chapter 4. Also, note that the full-span geometry was employed for the analyses performed in this Chapter. All of the metrics exhibit mean errors near zero with standard deviations less than 1% for the ROMs developed using 400, 200, 100, and 50 snapshots with the exception of the $DPCP_{avg}$ predictions. For $DPCP_{avg}$, the mean errors are near zero for all subsets, but the

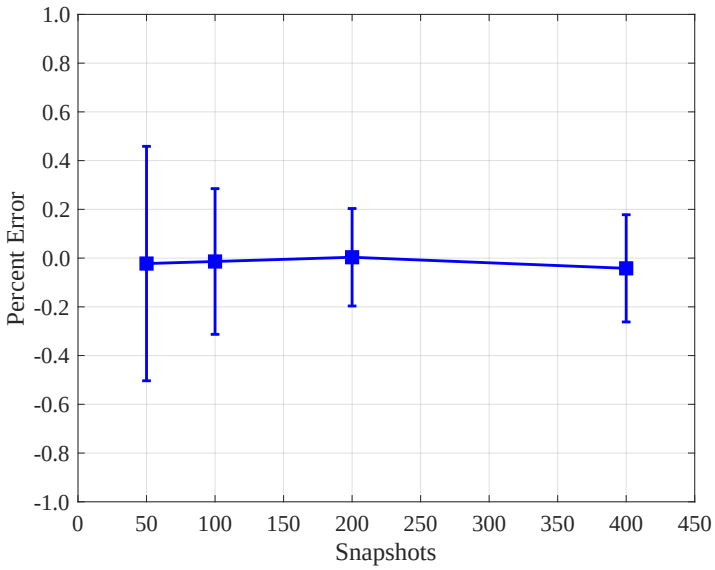


Figure 75: $P_{req}$ prediction error as a function of sampling density.

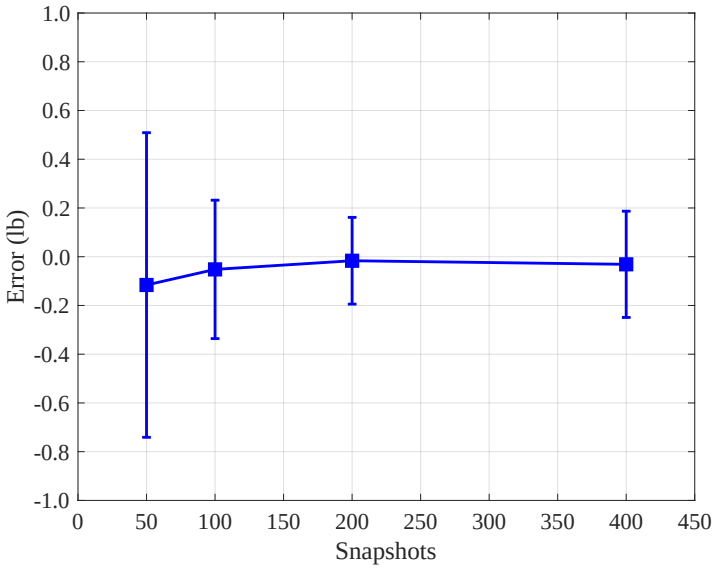


Figure 76: $F_x$ prediction error as a function of sampling density.

standard deviations range from 1.4% for the 400 snapshot ROM to 4.6% for the 50 snapshot ROM. However, as previously discussed, the values of $DPCP_{avg}$ are generally small, leading to a larger percent error. It is important to note that reducing the number of samples from 400 to 100 results in a change of 1.4% to 1.9% in the standard deviation. Then, the standard deviation increases from 1.9% to 4.6% when

decreasing the number of snapshots from 100 to 50. Therefore, the computational cost can be decreased by a factor of four relative to the full 400 snapshots for only a 0.5% increase in the standard deviation, which corresponds to an error increase on the order of 0.0001. Further reductions in computational cost lead to significantly increased error with values as large as 17.5%. Considering the error-by-predicted results provided in Figure 77, the errors obtained using the 50 snapshot ROM are generally bounded by $\pm 0.002$ with values as large as 0.004. This is an important consideration for determining the number of samples to be used for generating the aerodynamic ROM. For this research, the baseline distortion values are relatively small. Additionally, the geometry considered for this research has already been optimized to minimize distortion in preparation for the proposed wind tunnel experiment. Note that this optimization was performed for tunnel conditions while this work considers a theoretical cruise condition. Based on this, the improvement in distortion from the baseline are expected to be small and on the order of 0.001, which is the same order of magnitude as the error range shown in Figure 77. However, if the expected improvement was on the order of 0.01 and computational cost was a major concern, the larger errors associated with the 50 snapshot ROM could potentially be acceptable. Based on this observation, the ROM developed using 100 snapshots was chosen for application to the shape optimization problem outlined in Section 6.2.

### 6.1.5 Summary

A ROM was generated to predict the aerodynamics as a function of both fuselage shape and propulsor operating conditions. The shape parameterization was performed using BandAids and was limited to the lower-aft portion of the fuselage to improve the distortion caused by a region of high total pressure at the top of the fan face. The resulting shape parameterization consisted of a single variable defining the change in cross-sectional shape at six axial locations. A 400 case DOE was generated for the

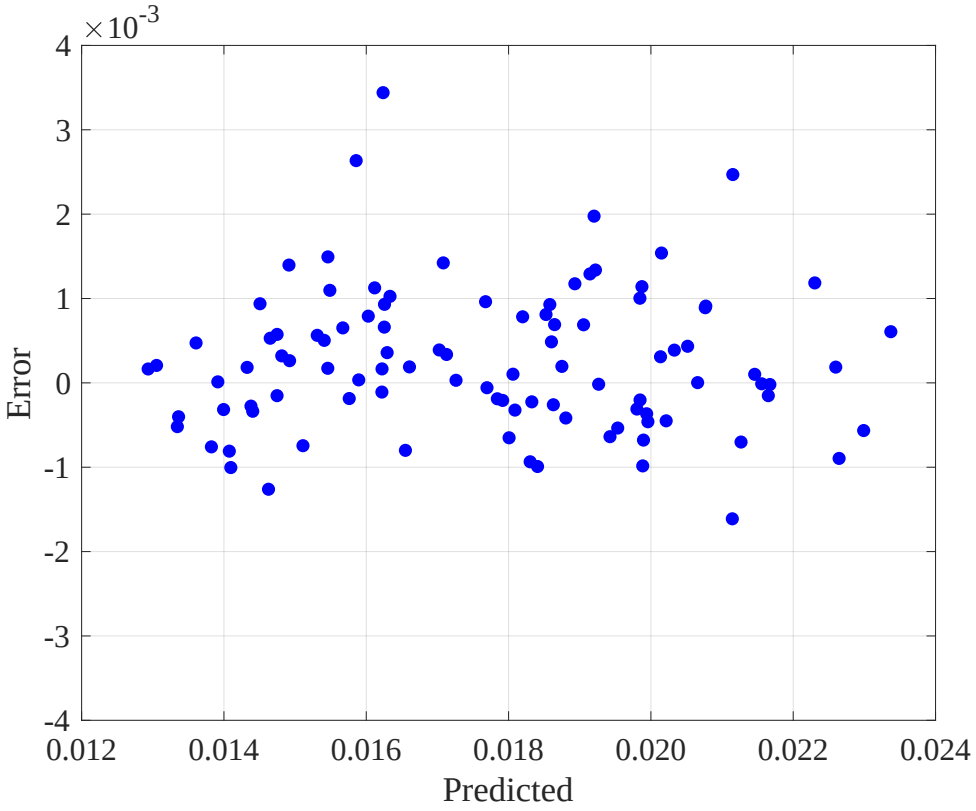


Figure 77: $DPCP_{avg}$ error-by-predicted results for the ROM developed using 50 snapshots.

eight design variables (six shape variables and two variables defining the propulsor operating conditions) using a Latin Hypercube design. The ROM was then developed using 400, 200, 100, and 50 snapshots to allow for an assessment of the tradeoff between the computational cost and accuracy. The results show that the predicted distortion exhibits the largest error and appears to be the most sensitive to sampling density. For the $F_x$, $PR$, $FPR$, and $P_{req}$ metrics, the error generally increases with decreasing snapshots used to develop the ROM. However, the results show that the required accuracy of the distortion predictions drive the sampling requirement and, therefore, the cost of the aerodynamic ROM. The results confirm Hypothesis 3.1. Additionally, the ROM developed using 100 snapshots was selected for application to the shape optimization problem.

## *6.2 Shape Optimization Problem*

The final component of this research is the application of the ROM-based, coupled MDA approach to shape optimization with the goal of quantifying the computational benefits offered by the proposed approach. The motivating applications for the ROM-based, coupled MDA approach included both coupled MDAO and design space exploration. For design space exploration, the comparison of computational cost is challenging due to the ambiguity in the number of design evaluations performed, in addition to the fact that there are no examples of design space exploration for this problem available in the literature for comparison. However, two methods that have been employed for the coupled MDAO of BLI configurations were discussed in Chapter 2. Comparisons to these existing methods for coupled MDAO could provide valuable insight to the potential performance benefits of the proposed approach. This leads to the final research question of this thesis:

**Research Question 3.2**:

What are the performance benefits for the proposed ROM-based, coupled MDA approach applied to coupled MDAO?

The ROM-based, coupled MDA approach was proposed to reduce the computational cost associated with coupled MDA using high-fidelity CFD. Additionally, an argument was made for a nonintrusive method such that access to the source code is not required. To evaluate the actual cost savings achieved with the proposed approach for coupled MDAO, a comparison to a nonintrusive, CFD-based, approach is the only requirement. However, a comparison to the adjoint-based method, previously utilized for this problem, could also provide insight to the overall potential of the proposed approach. The nonintrusive, CFD-based approach considered for the

comparisons consists of a gradient-based optimization that utilizes the finite differencing method for gradient computations. As a result, the performance benefits for the ROM-based approach relative to this nonintrusive, CFD-based approach should be readily apparent due to the large number of coupled MDA solutions required for the finite difference calculations. On the other hand, due to the large upfront cost to develop the ROM, the adjoint-based approach is likely to be less computationally expensive for a single coupled MDAO problem. However, any changes to the objective function, constraints, or the baseline configuration would result in the requirement for the optimization to be repeated, which incur the full computational cost for the adjoint-based method. Using the ROM-based approach, the optimization could be performed again with no additional CFD analyses. This leads to the final hypothesis of this thesis:

**Hypothesis 3.2**: *If the ROM-based approach is applied to perform the shape optimization of a BLI configuration, then it will offer a computational benefit over the CFD-based approach after a single optimization. However, the ROM-based approach will require multiple optimizations to offer a computational benefit over the adjoint-based approach.*

### 6.2.1 Experiment 3.2

The goal of Experiment 3.2 is to quantify the potential benefits of the proposed ROM-based, coupled MDA approach relative to existing methods. The comparisons for this research are limited to the application of coupled MDAO with the note that the benefits for the ROM-based approach would be more apparent for design space exploration, which would require a much larger number of coupled MDA solutions. The two coupled MDAO methods considered for comparison employed CFD directly to

perform gradient-based optimizations of BLI configurations. The optimization problems focused on the design of the aft-portion of the fuselage for tail-cone thruster concepts similar to the geometry considered for this research. Based on this, Experiment 3.2 was designed to perform similar optimization problems to allow for comparisons between the computational costs. Experiment 3.2 consisted of incorporating the extended aerodynamic ROM from Experiment 3.1 into the ROM-based, coupled MDA approach discussed in Chapter 5, employing the ROM-based, coupled MDA approach for the shape optimization of the TCT concept, and comparing the computational cost between the different methods. Note that while both methods that have been employed for this problem consisted of gradient-based optimizations, the ROM-based approach performed for Experiment 3.2 utilized a gradient-free optimization method known as a genetic algorithm. Gradient-free methods offer the benefit of not requiring gradient computations, which can be challenging for complex design problems. It is important to note that gradient-free methods generally require significantly larger numbers of function evaluations and can be less efficient than gradient-based optimization methods as a result. This could result in an unfair comparison between the methods. However, as discussed in Section 6.2.5, the computational cost of the ROM-based approach is dominated by the offline cost, which includes the contributions of the computational cost required to produce the snapshots and the computational cost required to fit the model. The online portion, which includes the optimization problem, incurs a relatively insignificant cost such that the difference between the efficiency for gradient-based and gradient-free methods does not have a significant impact on the comparisons that are performed in this chapter. Also, note that the computational cost for the current methods are estimated in Section 6.2.5 based on published work to prevent the requirement of actually performing the computationally expensive optimization problems.

The following subsections discuss the details of optimization problems performed

including descriptions of the shape parameterization, the objective functions employed, the resulting solutions, and finally, comparisons of the computational cost of the described methods. The optimization problems performed for this experiment are simple examples that are meant to be representative of the real problem. Note that the goal is to perform the optimizations to allow for an assessment of the required computational cost of the ROM-based approach for the coupled MDAO of BLI configurations. And as previously discussed, the computational cost required for the optimization is insignificant relative to the offline development of the ROM. Therefore, any simplifications that are made to the optimization problem that could potentially impact the efficiency or quality of the optimal solutions are considered acceptable for this research since the impact of the simplifications would not affect the desired outcome of this experiment.

### 6.2.2 Problem Statement

Optimization efforts for BLI configurations have considered a variety of objective functions, such as the distortion at the fan face, axial force, and the power required for the propulsor [31, 33]. While each of these objectives have significant differences, fundamentally, the BLI propulsor is a fuel burn reduction technology. Thus, the ultimate objective is to minimize the fuel burn with the requirement that the propulsor can sustainably support the additional loading resulting from the distortion in the ingested flow. Any objective function employed for the optimization of BLI configurations must, directly or indirectly, target a reduction in fuel burn, an improvement in the flow quality ingested by the propulsor, or both. For this work, no attempt is made to identify the best objective function for the optimization of BLI configurations. One of the primary benefits of the proposed approach for a ROM-based, coupled MDAO method is that the objective function does not have to be known prior to performing

the CFD simulations. Assuming that the design variables appropriately define the design space, the proposed approach not only allows for exploration of the design space but also the ability to consider various objective functions and constraints without having to perform additional CFD analyses.

Recall that the goal of this experiment is to assess the time-savings offered by the proposed approach. In order to accomplish this goal, two optimization problems were considered. The first optimization problem consists of minimizing the axial force of the aircraft, which would impact the fuel burn by reducing the required thrust from the underwing turbofans. Note that a negative value for the axial force represents force in the thrust direction. As previously discussed, other considerations, such as the power required from the underwing turbofans to supply the propulsor, could negate some of the improvements obtained from the optimization. However, the task is to simply assess the time-savings of the method such that this simple objective function was considered acceptable. The second optimization problem considers the propulsor performance by minimizing the distortion of the flow at the fan face. For each of the two optimization problems, an additional objective was included to allow for control over the smoothness of the obtained shape. The result was two multiobjective optimization problems with the objective consisting of a weighted sum of the performance objective and the smoothness objective. The three objective functions are provided in Equations 40-42. The formal problem statement is then given in Equation 43 with the objective function weightings provided in Table 7 for the two optimization problems.

$$OBJ_1(\mathbf{X}) = \frac{F_x}{F_{x,0}} \tag{40}$$

$$OBJ_2(\mathbf{X}) = \frac{DPCP_{avg}}{DPCP_{avg,0}} \tag{41}$$

$$OBJ_3(\mathbf{X}) = \sum_{i=2}^{n} \frac{|\Delta s_i - \Delta s_{i-1}|}{\Delta s_U - \Delta s_L} \tag{42}$$

$$\min \quad W_1 OBJ_1(\mathbf{X}) + W_2 OBJ_2(\mathbf{X}) + W_3 OBJ_3(\mathbf{X}) \qquad \text{s.t.} \quad \Delta s_L \leq \Delta s \leq \Delta s_U \tag{43}$$

Note that the smoothing objective function was not applied for the minimization

Table 7: Weightings for the two optimization problems performed for Experiment 3.2.

| Minimization Target | $W_1$ | $W_2$ | $W_3$ |
|---|---|---|---|
| $F_x(lb)$ | 1.00 | 0.00 | 0.00 |
| $DPCP_{avg}$ | 0.00 | 0.95 | 0.05 |

of the axial force. The results of the optmization showed that the minimum axial force favors a smooth shape. However, the smoothing function was needed for the distortion minimization problem, and a value of 0.05 for the weighting was shown to provide a smooth shape while not significantly altering the optimal distortion value.

### 6.2.3 Optimization Method

The optimization was performed using a genetic algorithm, which is in a category of optimization referred to as gradient-free methods. Gradient-free methods offer the benefit of not requiring a gradient evaluation of the objective function, which has proven difficult for highly nonlinear engineering problems [82]. Genetic algorithms mimic the evolution process based around the Darwin theories of reproduction and survival of the fittest [83, 84, 85]. Starting with an initial population of design candidates with corresponding fitness values, genetic algorithms use combinations of reproduction, crossover, and mutation to create new generations of design candidates. The fitness values represent the objective function values for each of the population members. For this work, a population of 200 individuals were evolved over 50 generations. For each generation, a deterministic tournament method was employed to select the parents for reproduction. Each pair of parent candidates produce two offspring, where the offspring are given a 25% chance to be identical to their parents and a 75% chance of crossover, which consists of randomly combining the chromosomes of the

parents. The chromosomes represent a binary representation of the design variable combination for each individual in the population. Finally, the mutation step consists of performing random perturbations to the chromosomes of the offspring with a mutation rate of 5%. The next generation is obtained by selecting the fittest individuals from the 400 combined parents and offspring to supply the starting 200 individual population for the next generation. This last step is referred to as elitism [86].

### 6.2.4 ROM-Based, MDAO Approach

The previous section discussed the extension of the aerodynamic ROM to include the impact of shape changes. For the shape optimization, the extended aerodynamic ROM is applied to the ROM-based, coupled MDA approach discussed in Chapter 5. The resulting ROM-based approach provides the capability to perform coupled MDA for a user-specified $FPR$ and fuselage shape. For the shape optimization, the $FPR$ is held fixed at the selected design value for the propulsor, and only the fuselage shape is allowed to vary. Note that the design $FPR$ value generally corresponds to a given fan design. However, a fan design does not currently exist for the TCT concept. Based on similar studies, a design $FPR$ value of 1.25 was used for the present optimization cases [18]. The ROM-based MDAO approach is developed by wrapping an optimizer around the ROM-based, coupled MDA method. An illustration of the ROM-based, coupled MDAO approach is provided in Figure 78.

### 6.2.5 Optimization Results

The optimization problems described in Equations 43 were performed using the ROM-based, coupled MDAO approach. The convergence histories for the optimization problems are provided in Figures 79 and 80.

Several observations can be made from the optimization histories. The first observation is that the axial force minimization problem converges to an optimal solution with roughly half the generations required for the distortion minimization problem.

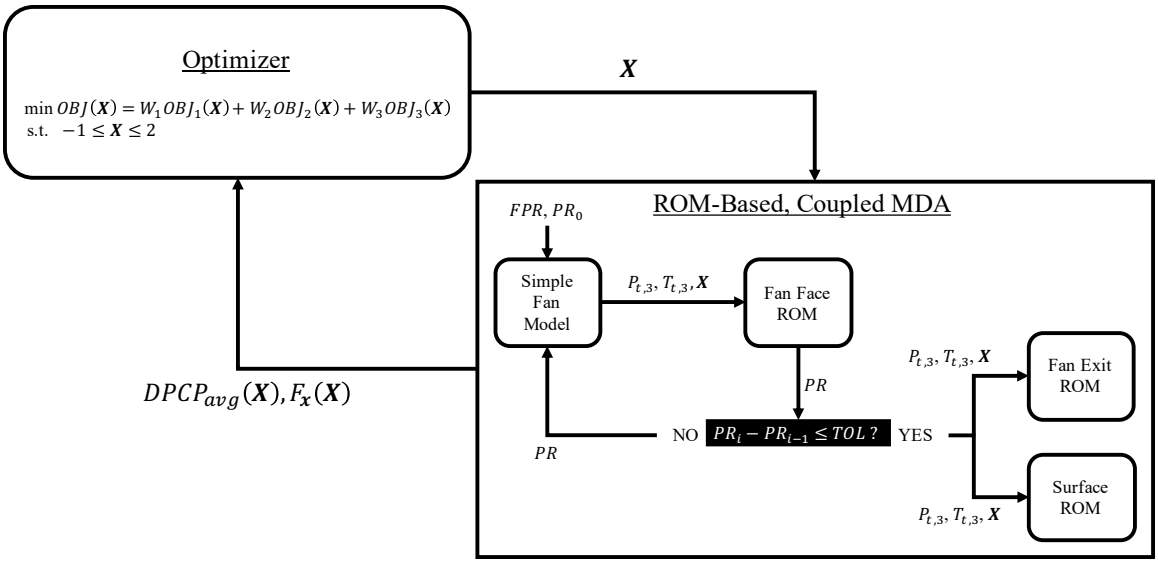


Figure 78: ROM-based, coupled MDAO approach.

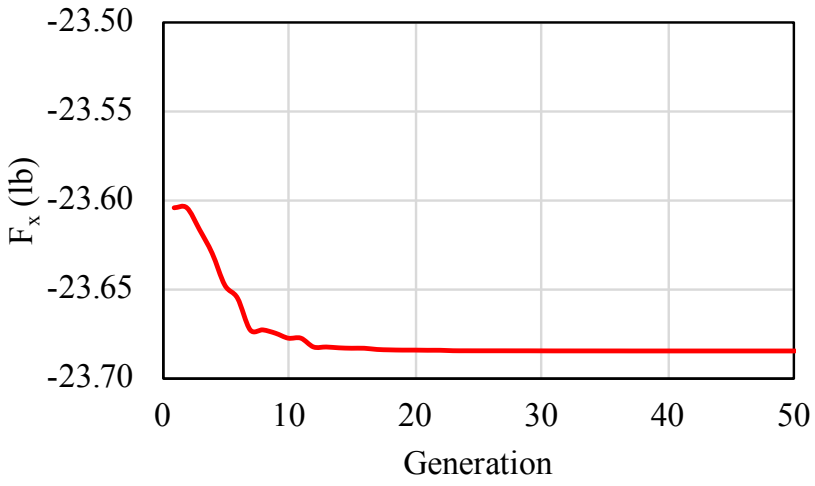


Figure 79: $F_x$ vs. generation for optimization problem 1.

This result is due to the multiobjective nature of the distortion minimization, which included a smoothing function as part of the overall objective. Recall from Table 7 that the smoothing objective was not included for the axial force minimization problem. The second observation is that the first generation of both optimization problems provides a significant improvement over the baseline values, which were given to be $F_x$ = -22.66 lb and $DPCP_{avg}$ = 0.0161. The final observation is that both optimization problems are practically converged after 30 generations, with the axial force

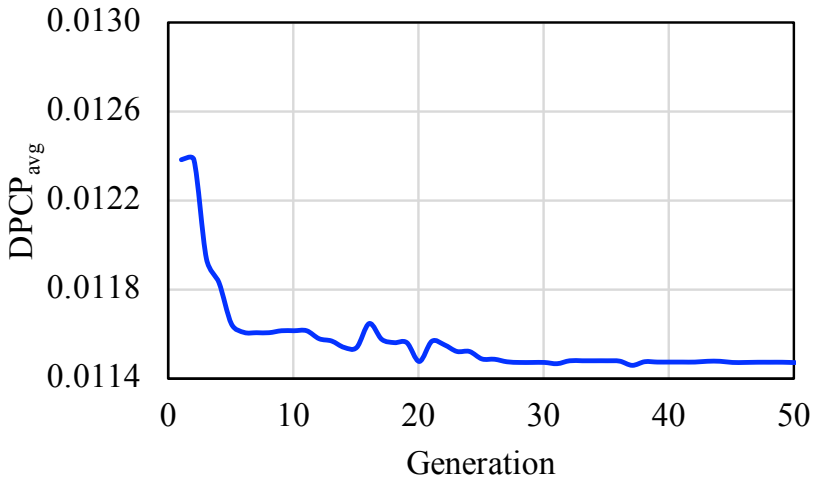


Figure 80: $DPCP_{avg}$ vs. generation for optimization problem 2.

minimization problem converging much faster. This result will be employed for the time-savings assessment portion of this experiment.

The results of the two optimization problems are provided in Table 8. Additionally, the resulting shapes are compared in Figure 81, and a comparison of the resulting pressure recovery contours at the fan face for the two optimization problems is provided in Figure 82. Note that the optimizations performed for this experiment employed the ROM-based approach. The CFD results provided in Table 8 were obtained by simulating the optimum shape obtained from the ROM-based optimization in the CFD analysis.

Table 8: Optimization results.

| | Baseline | Optimized $F_x$ | | Optimized $DPCP_{avg}$ | |
|---|---|---|---|---|---|
| | CFD | ROM | CFD | ROM | CFD |
| $F_x(lb)$ | -22.66 | -23.69 | -23.47 | -22.44 | -22.77 |
| $\Delta F_x$ (%) | - | -4.53 | -3.56 | 0.98 | -0.49 |
| $DPCP_{avg}$ | 0.0161 | 0.0204 | 0.0199 | 0.0115 | 0.0115 |
| $\Delta DPCP_{avg}$ (%) | - | 27.05 | 23.40 | -28.72 | -28.67 |

The results in Table 8 provide the final values of $F_x$ and $DPCP_{avg}$ for the two

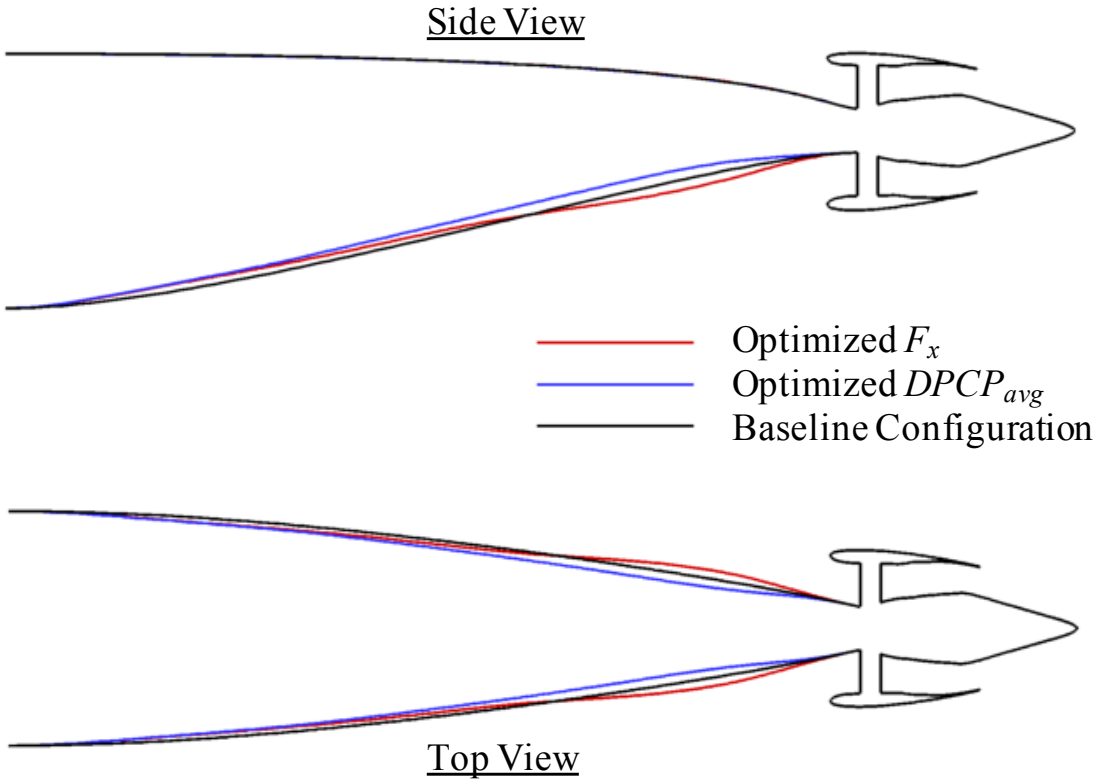


Figure 81: Optimized shapes obtained from the ROM-based approach compared to the baseline.

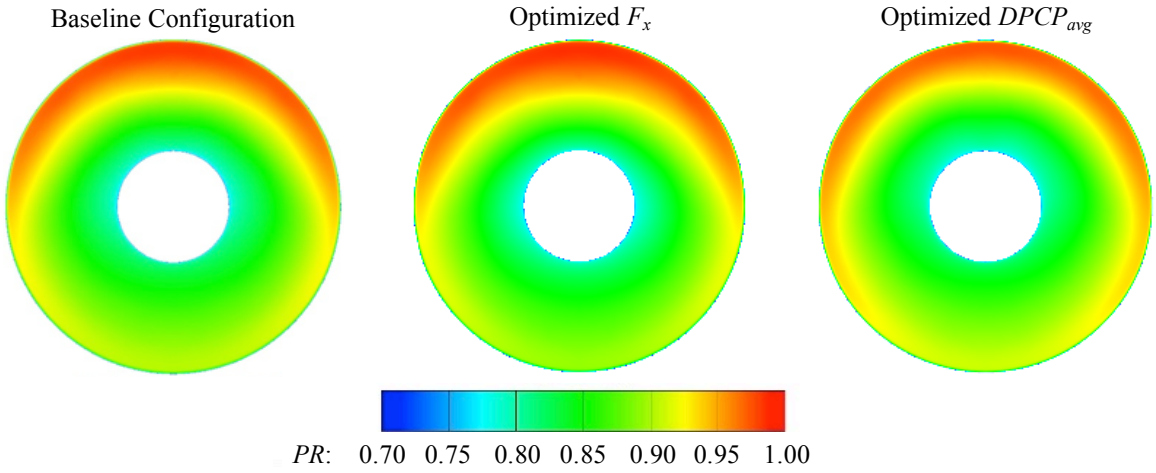


Figure 82: Fan face contour results.

opimization problems obtained using the ROM-based, coupled MDAO approach. Additionally, the optimal shape was simulated using the CFD-based, coupled MDA approach to compare the resulting values. It is important to consider that the baseline

configuration was actually designed well, and the parameterization used for the shape changes did not allow for large variations in shape. This was evident from the distortion minimization problem given that the geometrical constraints were active at the three stations closest to the fan face. Based on this, the optimization results were not expected to be drastic improvements over the baseline configuration. The results of the minimum $F_x$ case show that the ROM-based approach predicted an improvement of 4.53%. Compared to the CFD prediction, the optimal solution results in a reduction of 3.56% with a difference of 0.22 lb between the ROM and CFD predicted values. The resulting values of $DPCP_{avg}$ for the minimum $F_x$ case increased with the ROM-based approach predicting an increase of 27.05%, and the CFD-based approach predicting an increase of 23.40%. While these differences seem rather large, this equates to a difference of 0.0005 in the predicted distortion at the fan face. This result demonstrates one of the important challenges associated with the design of BLI configurations, which is that improvements in one aspect of the design could potentially result in degraded performance for other aspects. For the $DPCP_{avg}$ minimization, the ROM-based approach predicts a reduction of 28.72% compared to the CFD predicted reduction of 28.67%. One interesting result is that while the ROM-based approach predicts an increase of 0.98% in the axial force, the CFD predicted value demonstrates an improvement of 0.49% in the axial force.

Comparing the resulting shapes, as shown in Figure 81, the differences are not drastic. Both optimization problems result in very similar shapes farther upstream with differences becoming more apparent closer to the aft-propulsor. For the minimum distortion case, the optimal shape consists of an increase in the upsweep of the aft-portion of the fuselage, while the minimum axial force case appears to favor a reduced upsweep. Additionally, the top views show that the minimum axial force case favors a more drastic taper near the fan face with less taper farther upstream, while the minimum distortion case exhibits a more gradual taper. Due to the given

shape parameterization, it is unclear if these shape changes are both favorable, or if they are just simply a result of the grouping of the design nodes at each axial station. A more complex shape parameterization may provide more insight by allowing the top, sides, and bottom to change independently.

Finally, the pressure recovery contours shown in Figure 82 illustrate the resulting changes at the fan face for the two optimization cases. The minimum axial force case exhibits a similar overall flow pattern at the fan face with an apparent increase in the size of the high pressure recovery region at the top of the fan. This case resulted in an increase in distortion at the fan face, as shown in Table 8. For the minimum distortion case, the pressure recovery contours show that the high pressure recovery region at the top of the fan has been reduced in extent. Additionally, the high pressure recovery region is extended along the sides and toward the bottom of the fan face. These results show the potential for further improvement due to the lower pressure recovery still present at the bottom of the fan face. Again, this is potentially a result of the shape parameterization not allowing for enough overall change. For the minimum distortion case, the resulting shape variables at the four most axial locations were at the lower limit of -1 inches. Therefore, increasing the shape change magnitude at these stations could potentially provide further improvements.

### 6.2.6 Performance Benefit Assessment

The performance benefit assessment performed in this section consists of comparing the computational cost to build the ROM and perform optimization to the estimated computational cost required for equivalent CFD-based and adjoint-based optimizations.

The computational cost for the ROM-based approach is divided into offline and online portions, where the offline portion consists of the cost of producing the snapshots and building the ROM, and the online portion consists of the optimization.

Based on the results of Experiment 3.1, 100 snapshots were required for the aerodynamic ROM. The computational cost for each of the 100 snapshots was 60 CPU hours resulting in a total of 6,000 CPU hours. The computational cost to build the ROM was 1.32 CPU hours. And, finally, the cost of a single optimization using the ROM-based approach was 0.25 CPU hours.

For the CFD-based approach, the computational cost is calculated based on estimate of the number of coupled MDA solutions that would be required for a gradient-based optimization using finite differencing for the gradient calculations. For the optimization problem, the finite differences are required for the six design variables describing the shape changes of the fuselage where each finite difference calculation would require two coupled MDA solutions. Based on this, each iteration in the optimization would require 12 coupled MDA solutions. Finally, the optimization is assumed to converge after 13 iterations, which is consistent with the results obtained by Ordaz et al [35]. The resulting optimization would require 156 coupled MDA solutions. The computational cost for a single CFD-based CFD simulation performed for this work was 120 CPU hours resulting in a total cost of 18,720 CPU hours.

Finally, the computational cost of a comparable adjoint-based approach is estimated referencing the work of Ordaz et al [35]. In their work, an adjoint capability was implemented into the FUN3D flow solver to minimize the distortion at the fan face of the aft-propulsor for the MTA450 BLI concept. A general rule of thumb is that an adjoint evaluation costs roughly as much as a single CFD evaluation. So a good estimate is that a CFD and adjoint evaluation together costs roughly two flow solutions. For this work, the additional consideration is that each flow solution requires an iterative analysis between the CFD solver and the propulsion system analysis. In this work, the addition of the propulsion system analysis to converge on the $PR$ at the fan face roughly doubles the computational cost for each design evaluation. Based on this discussion, a single iteration in the optimization is estimated to be four times the

computational cost of a single decoupled snapshot, which results in roughly 240 CPU hours per iteration. Additionally, the aeropropulsive adjoint method employed by Ordaz et al. was able to converge on an optimal solution in 13 iterations. The resulting approximation of the computational cost for the equivalent adjoint-based approach is then 3,120 CPU hours. A final breakdown and comparison of the computational cost for each of the approaches is provided in Table 9.

Table 9: Computational cost comparisons.

| | CPU Hours | | |
|---|---|---|---|
| | ROM-based | CFD-based | Adjoint-based |
| Offline | 6,001 | - | - |
| Online | 0.25 | 18,720 | 3,120 |
| Total Cost - Optimization 1 | 6,002 | 18,720 | 3,120 |
| Total Cost - Optimization 2 | 6,002 | 37,440 | 6,240 |

The results show that the ROM-based approach results in a significant improvement in the computational cost relative to the CFD-based approach. However, for a single optimization, the adjoint-based approach is estimated to require roughly half of the computational cost of the ROM-based approach. For the ROM-based approach, the results show that the overwhelming majority of the computational cost is incurred in the offline portion, which is conducted once prior to the analysis. The online portion, consisting of a single optimization, has a computational cost of roughly 0.25 CPU hours. This is important because it means that subsequent optimization would only incur 0.25 CPU hours. For any change to the starting geometry, objective function, constraints, and/or flight condition, the adjoint-based approach will incur the total computational cost of 3,120 CPU hours while the ROM-based approach would only incur 0.25 CPU hours. Based on the estimates provided in Table 9, the ROM-based approach provides a computational performance benefit with as few as two optimizations. The result is a method that enables the enhanced ability to explore the solution space and assess tradeoffs in the design parameters. Note that this is in

addition to the previously discussed benefits over the adjoint-based approach. The results discussed here confirm Hypothesis 3.2.

One important consideration that has not been discussed is scalability. For increases in the number of design variables, the comparisons provided in this section could change drastically. The adjoint-based approach is known to scale very well and can efficiently handle large numbers of design variables [87, 88, 89]. For the ROM-based approach, an increase in the number of design variables would increase the sampling requirements. However, the extent of the increase in sampling density is not known. The scalability of the proposed ROM-based method is left for future research.

### 6.2.7 Summary

To assess the time-savings offered from the proposed ROM-based, coupled MDA approach when applied to shape optimization, a numerical experiment was performed. The experiment consisted of wrapping an optimizer around the extended aerodynamic ROM that was developed in Experiment 3.1 and performing two optimizations to minimize the axial force and distortion at the fan face. The results of the two optimization problems provided an example of the tradeoffs that exist for BLI configurations. For the cases considered, the results showed that the minimum axial force was obtained at the cost of an increase in the distortion at the fan face. The minimum distortion results, on the other hand, actually included a slight improvement in the axial force. The computational cost assessment considered the ROM-based approach, an nonintrusive CFD-based approach, and an adjoint-based approach, where the cost of the latter two was approximated. The results of the experiment show that the ROM-based approach incurred significantly lower costs relative to the CFD-based approach but requires at least two optimizations to become favorable over the adjoint-based approach, confirming Hypothesis 3.2.

# CHAPTER VII

# METHODOLOGY SUMMARY - A STEP-BY-STEP PROCESS FOR THE ROM-BASED, COUPLED MDAO OF A TAIL-CONE THRUSTER CONFIGURATION

Chapters 4, 5, and 6 discussed the development of the aerodynamic ROM both with and without the inclusion of shape variables. The ROMs were developed, validated, and coupled to a propulsion system analysis for ROM-based, coupled MDA. Finally, the ROM-based, coupled MDA approach was employed to demonstrate a cost-effective method for performing coupled MDAO. This chapter demonstrates the step-by-step process using a simple example. An illustration of the ROM-based, coupled MDAO approach is provided in Figure 83.

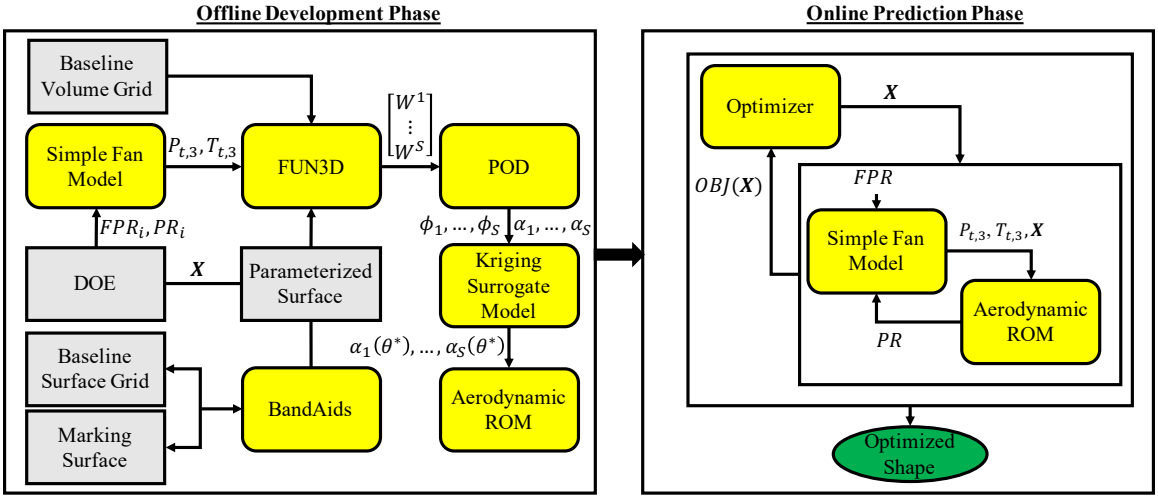


Figure 83: ROM-based, coupled MDAO approach for BLI configurations.

The process consists of two phases, which are the offline development and the online prediction phases. For the offline development, the process consists of producing the flow solutions over a range of design variable combinations defined by a DOE

and generating the aerodynamic ROM. This process is described in Steps 1 through 5 in the following sections. Steps 6 and 7 are then to validate the ROM and develop the ROM-based, coupled MDA approach. Finally, the online prediction phase is contained in Step 8, which consists of employing the ROM-based, coupled MDA approach for shape optimization. The following sections describe each of the steps in more detail.

## *7.1 Step 1 - Define Propulsor Operating Conditions*

The first step is to establish the variables that define the propulsor operating conditions and set their ranges. This step will vary based on the problem of interest. For this work, the goal was to develop an aerodynamic ROM capable of performing coupled MDA over a range of operating conditions, as defined by $FPR$. Based on the discussion in Chapter 4, this requires the user to define a range of initial guesses for the pressure recovery, $PR_i$, and fan pressure ratio, $FPR_i$. The range for the initial guesses of fan pressure ratio, $FPR_i$, was given by the desired range of operating conditions, which was defined to be $1.10 \leq FPR_i \leq 1.35$ based on similar studies for this type of configuration. The task of defining the appropriate range of initial guesses for pressure recovery, $PR_i$, depends on the knowledge base of the given configuration. For this work, there was limited knowledge of the configuration such that preliminary analyses were used to determine the upper and lower limits of the pressure recovery corresponding to the desired range of fan pressure ratios. The preliminary analyses consisted of coupled MDA simulations at fan pressure ratios of 1.10 and 1.35, which resulted in pressure recovery values of 0.874 and 0.897, respectively. Finally, the range of initial guesses for pressure recovery was defined to be $0.86 \leq PR_i \leq 0.92$. Note that range was padded to account for unknowns in the process and to ensure more adequate coverage at the edges of the design space. This was discussed in more detail in Section 4.1. The final ranges of the initial guesses for the pressure recovery and

fan pressure ratio employed for this work are provided in Table 10.

Table 10: DOE Ranges for Aerodynamic Snapshots.

| | Minimum | Maximum |
|---|---|---|
| FPR | 1.1 | 1.35 |
| PR | 0.86 | 0.92 |
| $P_t/P_\infty$ | 1.34 | 1.75 |
| $T_t/T_\infty$ | 1.14 | 1.21 |

Note that the ranges considered here assume that the goal is to allow for predictions over a range of fan pressure ratios. However, if the goal is to simply resolve the coupling between the propulsion system analysis and the airframe for a fixed fan pressure ratio, the process would be slightly different. The aerodynamic ROM would still need to capture a range of conditions due to variations in the flow resulting from changes in the fuselage shape upstream of the fan face. However, the range of conditions for this case could be reduced to only include changes in $PR$.

## *7.2 Step 2 - Define Shape Variables*

The next step is to define the shape variables, which will also vary based on the goal of the design optimization. However, the process remains unchanged. The shape variables are defined based on the shape parameterization method employed for the design. For this work, BandAids was used, which is a free-form deformation tool included with FUN3D. The shape parameterization using BandAids begins with a definition of the marking surface, which is a structured grid representation of the design region for the given geometry. For this example, the design region corresponds to the aft-portion of the fuselage upstream of the tail-cone thruster. The marking surface corresponding to this region was generated in Pointwise, shown in Figure 84, and then exported in Plot3D format to be used by BandAids. Next, the marking surface and baseline surface grid is provided to BandAids along with the user-defined parameterization dimensions to create the parameterized geometry. For this work, a 10x10

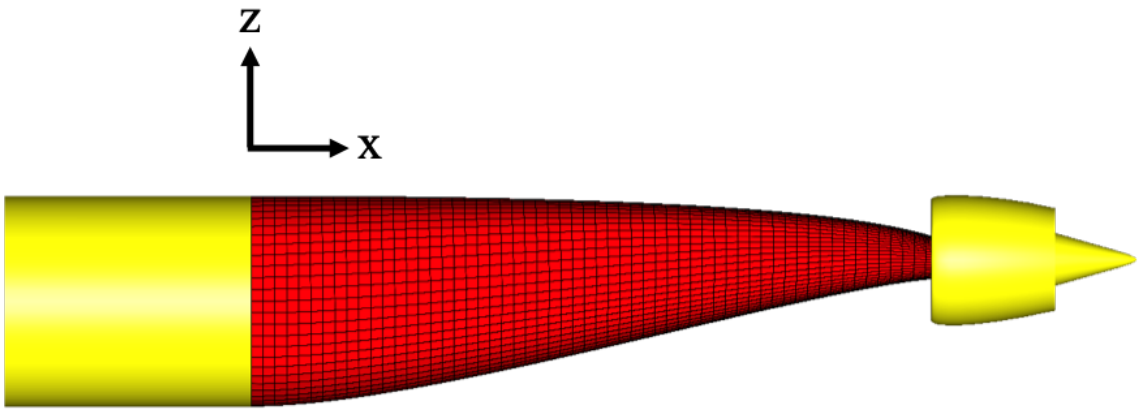


Figure 84: Design marking surface for shape parameterization.

parameterization was defined resulting in 100 design nodes uniformly distributed in the axial and circumferential directions along the aft-portion of the fuselage. Note that the first and last two axial locations were held fixed to ensure smooth shape changes from the design region to the fixed region of the geometry. Also, the design nodes defining each of the remaining six cross-sections were grouped to a single shape variable. This step was performed to both reduce the overall number of shape variables and to prevent unrealistic shape changes. The final number of shape variables was reduced to six, which define the changes in the cross-sections at the six axial locations. The resulting parameterization, illustrated in Figure 85, allows the bottom and side portions of the cross-sections to contract and/or expand while holding the top fixed. The range for the shape variables was defined to be -1" $\leq \Delta s_i \leq$ 2", which was limited to prevent issues with kinks in the fuselage geometry that occured for large changes. The reader is referred to Section 6.1 for more details related to the shape parameterization.

## *7.3 Step 3 - Create the DOE*

Once the design variables and their respective ranges are defined, the next step is to create the DOE. This example consists of eight total design variables including

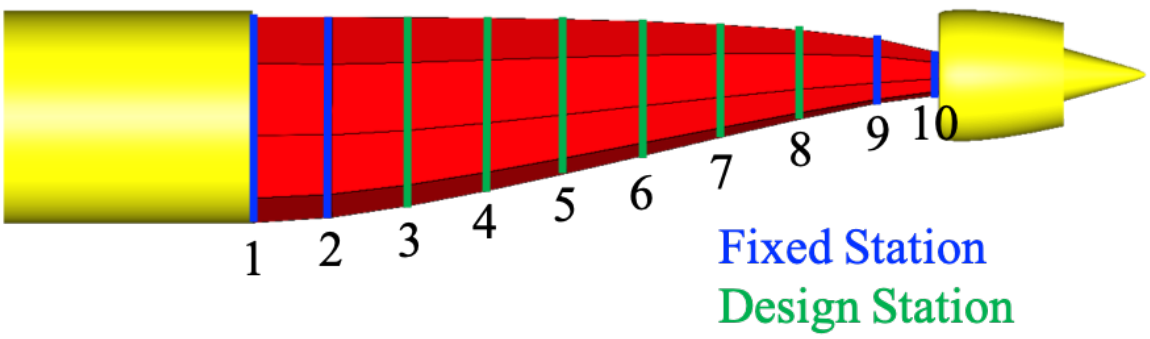


(a) Axial stations

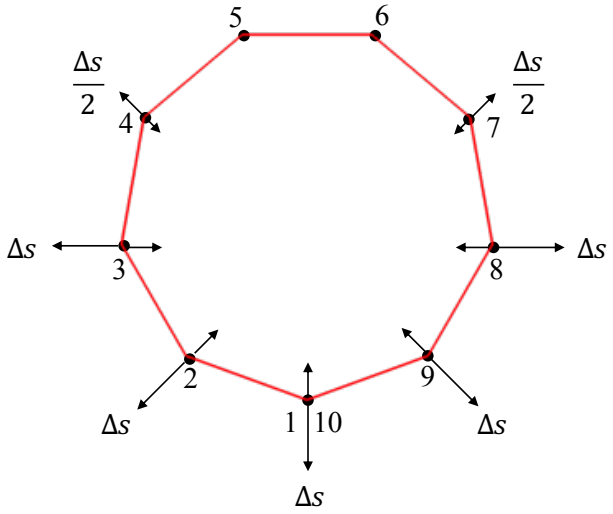


(b) Design nodes at each axial station

Figure 85: 10x10 parameterized design surface.

two for the propulsor $(PR_i, FPR_i)$ and six for the shape changes to the fuselage $(\Delta s_3, \Delta s_4, \Delta s_5, \Delta s_6, \Delta s_7, \Delta s_8)$. The ranges for the design variables are summarized in Table 11.

Using the ranges in Table 11, the Latin Hypercube sampling method was used to create the DOE. Note that the results of Experiment 3.1 showed that 100 samples were sufficient for this case.

Table 11: DOE ranges for the extended aerodynamic ROM.

| | Minimum | Maximum |
|---|---|---|
| $FPR_i$ | 1.10 | 1.35 |
| $PR_i$ | 0.86 | 0.92 |
| $\Delta s$ | -1.00 | 2.00 |

## *7.4 Step 4 - Simulate the DOE using the FOM*

The next step is to simulate the DOE using the full-order model to obtain the required snapshots. The full-order model for this problem consisted of a decoupled simulation, illustrated in Figure 86, between the FUN3D flow solver and the simple fan model discussed in Section 3.2.1.

The analysis process, shown in Figure 86, consists of two branches to provide the necessary inputs to FUN3D. The $FPR_i$ and $PR_i$ values from the DOE are supplied to the simple fan model to obtain $P_{t,3}$ and $T_{t,3}$, and the shape variables are supplied to BandAids to obtain the deformed surface grid. This BandAids step consists of a single iteration analysis of FUN3D to deform the baseline grid and write out the resulting deformed grid, which is then used for the subsequent analysis. Note that this requires a specific directory layout. The top level directory requires the subdirectories **Flow** and **Rubberize** along with the rubber.data file that defines the shape variable values. The **Rubberize** directory contains the bandaid.data.1 file, which is an output of the BandAids parameterization that was performed in Step 2. Finally, the **Flow** directory requires the fun3d.nml along with the baseline grid. Once the directory structure is defined, the process consists of two steps to get the deformed surface grid:

1. Starting in the top-level directory, define the shape variable values in the rubber.data file.

2. From the **Flow** directory, run FUN3D for a single iteration using the *snap_grid* and *write_mesh* options.

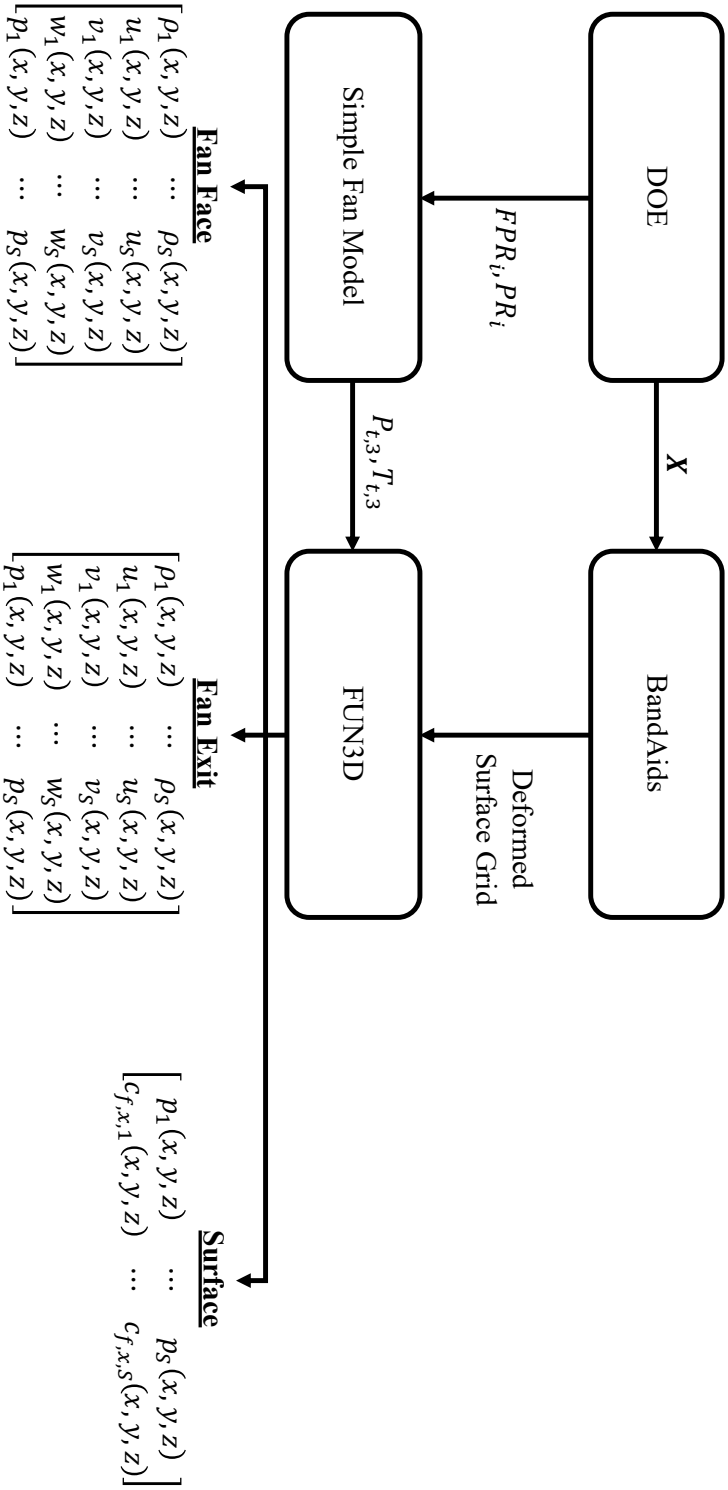


Figure 86: Snapshot generation process for the extended aerodynamic ROM.

The resulting deformed grid is then supplied to FUN3D along with the $P_{t,3}$ and $T_{t,3}$ values obtained from the propulsion system analysis to generate the snapshots.

The resulting snapshots are divided into three computational domains for the fan face, fan exit, and surface domains. Note that snapshots defining the fan face and fan exit domains include all five primitive variables, $\rho$, $u$, $v$, $w$, and $p$, to allow for computation of a variety of metrics including $\dot{m}$ and the contributions to the axial force, $F_x$, while the surface domain only includes two variables, $p$ and $c_{f,x}$, that are needed to calculate the contribution to the axial force $F_x$. This step is discussed in more detail in Sections 4.2.2 and 6.1.3. Also, the reader is referred to the FUN3D website for more information about grid deformation and the BandAids tool [10].

## *7.5 Step 5 - Build the ROM*

Once the snapshots are produced using the FOM, Step 5 is to build the ROM. The requirements for the ROM method were discussed in Section 2.2 and any ROM meeting those requirements could potentially be employed for this methodology. The ROM is divided into two phases; the offline development and the online prediction. The offline development phase consists of generating the snapshots and performing dimensionality reduction to obtain a reduced-order representation of the full-order model. The online development phase consists of performing interpolation in the reduced-space to provide predictions at untried parameter combinations. For this work, Matlab's Statistics and Machine Learning Toolbox was used to perform POD for the dimensionality reduction component, and a kriging surrogate model available in Matlab's DACE toolbox was used to perform the interpolation of the POD coefficients. The snapshot generation portion of the offline development phase was performed in Step 4. Step 5 begins with the dimensionality reduction step, which is illustrated in Figure 87.

Figure 87: Aerodynamic ROM development.

As illustrated in Figure 87, the snapshots are used as inputs to POD to obtain the POD coefficients and modes, $\alpha$ and $\phi$. Using the POD coefficients and modes, the reduced-space is provided by the expression at the bottom of Figure 87, where $y$ represents the field distribution of the primitive variables defined by the snapshots, $\theta$ is any design variable combination, and $\bar{y}$ is the average of $y$ over the snapshots.

Once the reduced-space is obtained, the online prediction process is illustrated in Figure 88. The process consists of performing interpolation using the kriging surrogate model for an untried parameter combination, $\theta^*$, to obtain the corresponding POD coefficients, $\alpha$. The resulting POD coefficients are then used in the expression provided in Figure 88 to provide the predictions of the primitive variables for each of the three computational domains. The resulting ROM allows for aerodynamic predictions as a function of the initial guesses of pressure recovery, $PR_i$, fan pressure ratio, $FPR_i$, and the six shape variables ($\Delta s_3, \Delta s_4, \Delta s_5, \Delta s_6, \Delta s_7, \Delta s_8$).

Figure 88: Online prediction process for the aerodynamic ROM.

## 7.6 Step 6 - ROM Validation

Step 6 is an optional step to validate the aerodynamic ROM. For this work, 100 additional snapshots were produced to allow for the evaluation of the goodness of fit metrics. The process consisted of performing Latin Hypercube sampling to create 100 combinations of the eight design variables described in Step 3 that were were not used to create the ROM. Once the validation DOE was created, the process described in Figure 86 was used to obtain 100 validation snapshots. Finally, the validation DOE was used to perform predictions with the ROM developed in Step 5 and the results were compared to the 100 validation snapshots. The results of the ROM validation are illustrated in Figures 62 through 76, which are provided in Section 6.1.4.

Note that the 100 additional snapshots used for validation in this work doubled the computational cost required to develop the aerodynamic ROM. In reality, the ROM validation step would consider much fewer additional cases to prevent excessive computational cost. The goodness of fit metrics would provide less information about the prediction quality as a result. However, the metrics could still provide useful information, and the qualitative assessment of the error distributions, illustrated in Figures 67 through 70, over the computational domains would provide the same valuable insight for individual cases.

## 7.7 Step 7 - ROM-Based, Coupled MDA

The aerodynamic ROM, developed in Step 5 and validated in Step 6, was then coupled to a propulsion system analysis to enable coupled MDA predictions as a function of both propulsor operating conditions and fuselage shape. The ROM-based, coupled MDA approach is illustrated in Figure 89.

Based on a desired fan pressure ratio, $FPR$, the ROM-based, coupled MDA approach, illustrated in Figure 89, consists of iterating between the simple fan model and the fan face ROM to resolve the pressure recovery, $PR$, at the fan face. Once the

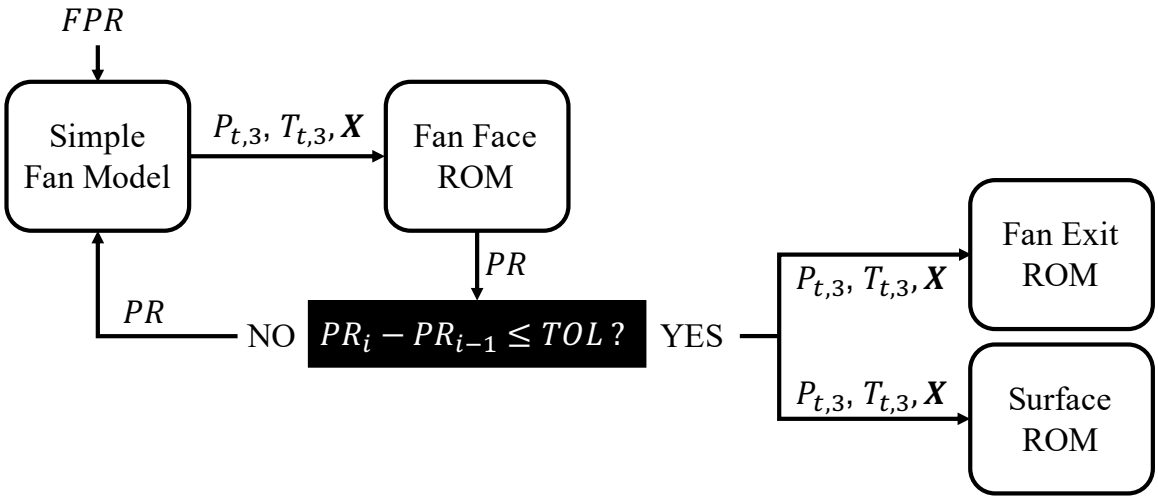


Figure 89: ROM-based, coupled MDA approach.

pressure recovery is converged, the resulting total pressure, $P_{t,3}$, and temperature, $T_{t,3}$, values are used to obtain the predictions for the fan exit and surface domains.

## *7.8 Step 8 - Shape Optimization*

The final step is to employ the ROM-based, coupled MDA approach developed in Step 7 to perform shape optimization for the TCT concept. For this example, the axial force minimization problem discussed in Section 6.2 is considered. The optimization problem statement for this case is provided in Equation 44.

$$\min \quad -\frac{F_x}{F_{x,0}} \qquad \text{s.t.} \quad \Delta s_L \leq \Delta s \leq \Delta s_U \tag{44}$$

It is important to note that the purpose of this section is to provide an example of the application of the ROM-based, coupled MDA approach to shape optimization. As such, the objective function and optimization methods are chosen simply to illustrate the process. Any objective function and/or optimization method could be used for this problem. The optimization method considered for this example is the genetic algorithm that was discussed in Section 6.3. Also, as discussed in Section 6.2, the fan pressure ratio is held at a constant value of 1.25 for the shape optimization. This decision was made to represent an optimization at a point corresponding to a cruise

condition with a fan having a design fan pressure ratio of 1.25. The optimization could also be performed with a variable fan pressure ratio. For example, the goal could be to simultaneously find the fan pressure ratio and fuselage shape to minimize the axial force. However, the fan design is held fixed for the simple example provided in this chapter. The resulting ROM-based, coupled MDAO approach is illustrated in Figure 90.

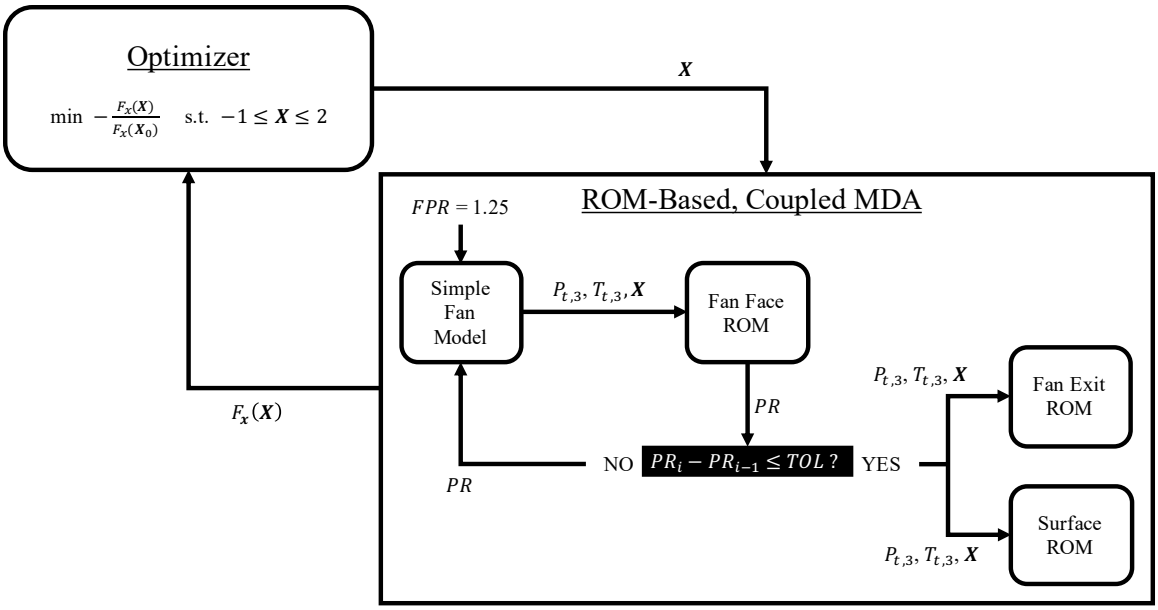


Figure 90: ROM-based, coupled MDAO approach.

The convergence of the optimization problem is illustrated in Figure 91. Also, the resulting shape is compared to the baseline shape in Figure 92. Finally, the quantified results of the optimization are provided in Table 12.

Table 12: Optimization results.

| | Baseline | Optimized $F_x$ | |
|---|---|---|---|
| | CFD | ROM | CFD |
| $F_x(lb)$ | -22.66 | -23.69 | -23.47 |
| $\Delta F_x$ (%) | - | -4.53 | -3.56 |
| $DPCP_{avg}$ | 0.0161 | 0.0204 | 0.0199 |
| $\Delta DPCP_{avg}$ (%) | - | 27.05 | 23.40 |

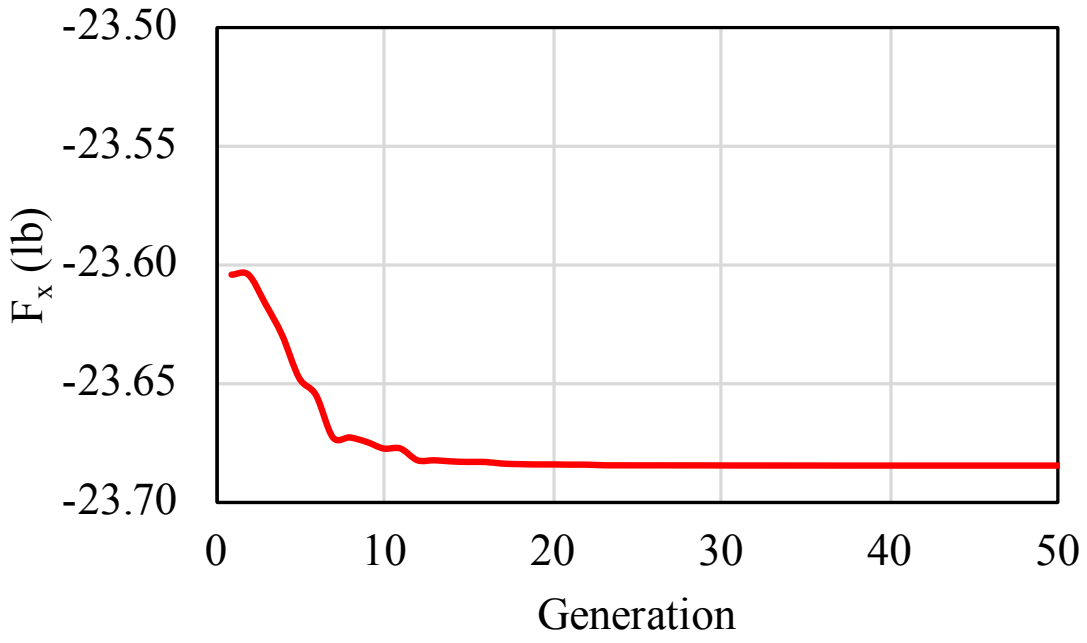


Figure 91: $F_x$ vs. generation.

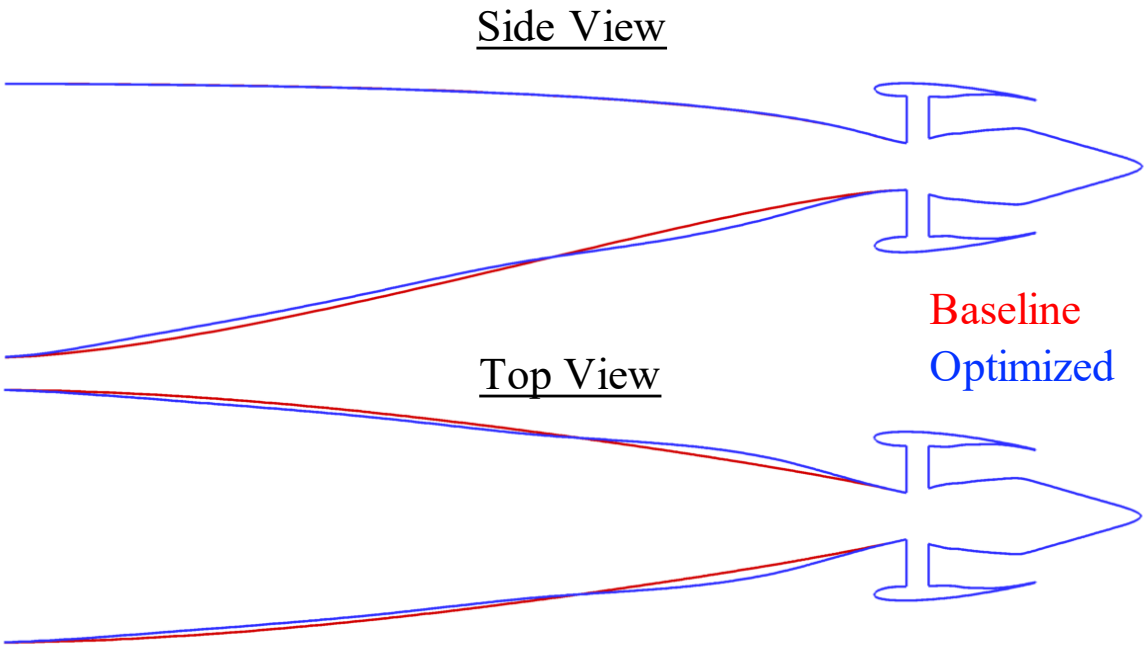


Figure 92: Cross-section comparison between optimizated (blue) and baseline (red).

These results were presented and discussed in the previous chapter. However, they are discussed again here for the sake of completeness. The convergence of the optimization shows that while a total of 50 generations were included in the process, the axial force appears to remain constant after roughly 20 generations. Recall from the discussion in Section 6.3 that each generation considered 200 population members with an additional 200 offspring. The result is 400 evaluations of the ROM-based, coupled MDA method per generation. The optimized shape, shown in Figure 92, displays a more gradual upsweep (side view) and less aggressive taper (top view) relative to the baseline configuration. Finally, the quantified results provided in Table 12 show that the ROM-based, coupled MDAO approach was able to obtain a 4.53% improvement in the axial force and a 27.05% increase in the distortion at the fan face. The optimized shape obtained from the ROM-based approach was then simulated using the CFD-based, coupled MDA approach discussed in Section 5.2. The results show that the actual optimized shape provides a 3.56% improvement in the axial force and a 23.40% increase in the distortion. Note that while the percent differences between the actual optimized results and those obtained using the ROM-based approach appear large, this is a result of the relatively small numbers given in Table 12. For this example, the 0.97% difference between the ROM-based and CFD-based predictions for the axial force equates to an absolute difference of 0.22 lb, and the 3.65% difference in the distortion predictions equates to an absolute difference of 0.0005.

## *7.9 Summary*

This chapter provided a step-by-step process to develop the ROM-based, coupled MDA approach and to apply the approach to perform shape optimization of the TCT concept. The resulting process can be modified in a variety of ways to change the optimization problem, the geometry, the ROM method, and the analysis tools. But the overall process will remain similar with only subtle differences.

# CHAPTER VIII

# CONCLUSION AND FUTURE WORK

The requirements for commercial aviation are constantly becoming more stringent. In response, NASA has quantified goals for the fuel burn, noise, emissions, and takeoff field length of next generation aircraft. These goals have led to the investigation of a variety of technologies designed to address these goals. One such technology is BLI propulsion, which has been identified as a technology to reduce the aircraft fuel burn. Preliminary investigations have shown that BLI propulsion can potentially result in a 5-12% reduction in fuel burn depending on the configuration.

BLI configurations pose significant challenges to aircraft designers due to a strong coupling between the airframe aerodynamics and the propulsion system performance. Traditional design methods consider the airframe design independent of the propulsion system design. However, this method is not sufficient for BLI configurations. BLI configurations require the use of coupled MDA, consisting of the airframe aerodynamics and propulsion system performance to be analyzed in an iterative fashion. For the present case, the aerodynamic analysis was performed using CFD, which is necessary to accurately predict the interaction between the airframe aerodynamics and the propulsion system. Additionally, the design of unconventional configurations can not rely solely on intuition for making design decisions. MDAO was described as a method for performing design based on a user-defined objective function. MDAO can be applied to problems with coupled subsystems and allow the objectives to be targeted directly, which would allow for consideration of both intuitive and nonintuitive designs in an effort to obtain the design with the best performance. Additionally, design space exploration could allow for a better understanding of the multidisciplinary

trades and to identify important trends. This information could provide better insight and allow for better design decisions. However, the ability to perform MDAO for a BLI concept requiring CFD coupled to a propulsion system analysis is extremely computationally expensive to the point of limited applicability and design space exploration is, generally, not practical.

In this work, reduced-order modeling was proposed as an enabler for the MDAO of BLI configurations. The ROMs can be created using snapshots produced by the high-fidelity analysis models. This requires a fixed number of function evaluations upfront in what is referred to as the offline portion of the ROM. Once the ROM is built, it can then be used in place of the high-fidelity analysis models, resulting in a significant reduction in computational cost. This is particularly valuable for the present case, which requires an iterative analysis between high-fidelity CFD and a propulsion system analysis model for each design evaluation. The application of ROMs to this problem can significantly reduce the computational cost for each design evaluation to provide a practical method for performing MDAO for BLI configurations.

The research objective for this thesis was to develop a computationally cost efficient methodology for the coupled MDA of BLI configurations. A ROM-based, coupled MDA approach was developed and applied to perform the shape optimization of a TCT concept. The experiments and results are summarized here.

The aerodynamic ROM was developed in Chapter 4 to enable predictions over a range of propulsor operating conditions. The aerodynamic ROM was then coupled to a propulsion system analysis model to enable coupled MDA predictions over a range of $FPR$ in Chapter 5. Finally, the aerodynamic ROM is extended to include shape variables and the resulting ROM-based, coupled MDA approach was employed to perform the shape optimization of the aft-portion of a TCT concept in Chapter 6.

In order to develop the aerodynamic ROM, snapshots produced by the CFD solver

were required over a range of propulsor operating conditions. Experiment 1.1 was performed to determine an appropriate simulation strategy for producing the snapshots that captured a desired range of $FPR$ without requiring coupled MDA. The proposed method consisted of creating a DOE of the desired $FPR$ range and a range of $PR$ at the fan face, where the appropriate range of $PR$ was estimated based on preliminary analyses. These values were used as inputs to the propulsion system analysis to provide the boundary conditions required for the CFD analysis. The resulting decoupled simulations were shown to provide predictions over the desired range of $FPR$. Next, Experiment 1.2 was performed to assess the prediction capabilities of the aerodynamic ROM and to determine the sensitivity of the prediction accuracy to sampling density. A total of 100 snapshots were generated to develop the ROM along with an additional 100 snaphots for validation. First, the ROM was created using the full 100 snapshots to evaluate the overall prediction capability. Next, ROMs were created using subsets of 15, 25, and 50 snapshots to evaluate the sensitivity of the prediction accuracy to the sampling density. The ROMs were used to perform predictions over the range of input conditions corresponding to the 100 validation cases. Finally, the comparisons to CFD were made for the predicted values of $FPR$, $PR$, $DPCP_{avg}$, $P_{req}$, and $F_x$. The results showed that the aerodynamic ROM provides accurate predictions with as few as 15 snapshots. Using this result, Experiment 2 was performed to assess the prediction capabilities for the application of coupled MDA. The ROM-based, coupled MDA approach was developed by coupling the aerodynamic ROM to the propulsion system analysis. The ROM-based, coupled MDA approach was then used to perform predictions over the desired range of $FPR$ and compare to the results obtained from the CFD-based, coupled MDA approach. The results illustrated exceptional agreement between the ROM-based and CFD-based approaches for the desired range of $FPR$.

In Chapter 6, the ROM-based, coupled MDA approach was extended to include

the effect of shape variables on the predicted aerodynamics. The ROM-based, coupled MDA approach was then employed to perform shape optimization on the aft-portion of the fuselage of a TCT concept. Experiment 3.1 was conducted to the evaluate the accuracy of the extended ROM and to identify the sensitivity of the accuracy to sampling density. A total of 400 snapshots were generated for the eight design variables, including the two propulsion system variables ($PR$ and $FPR$) and six shape variables. Aerodynamic ROMs were created using the full 400 snapshots along with subsets of 50, 100, and 200 snapshots. An additional 100 snapshots were generated for validation of the ROMs. The results show that while there is a general trend of higher accuracy with increased sampling density, the tradeoff between accuracy and computational cost showed that decreasing the number of samples from 400 to 100 reduces the computational cost by a factor of four with an acceptable increase in error. However, reducing the number of samples further from 100 to 50 leads to a relatively large increase in the prediction error for the distortion at the fan face. An important finding from the results of Experiment 3.1 was that the distortion displayed the highest sensitivity to the sampling density. Therefore, the sampling density required for a given problem depends on the desired accuracy of the distortion predictions. For this work, the prediction error for the distortion obtained from the ROM created using 50 snapshots was on the order of the expected improvement in distortion from the shape optimization. As a result, the ROM created using 100 snapshots was retained for the shape optimization problem. Finally, Experiment 3.2 consisted of employing the extended aerodynamic ROM in the ROM-based, coupled MDA approach and performing shape optimization on the aft-portion of the fuselage of a TCT concept. The primary goal was to assess the potential computational benefits offered by the ROM-based approach relative to both an equivalent CFD-based and adjoint-based approach. Note that the adjoint-based was defined to be an intrusive method, while

the ROM-based approach was developed to provide a nonintrusive method. Therefore, the benefit of the proposed approach over an adjoint-based approach was already established. The computational cost comparison includes the adjoint-based approach to provide greater insight into the benefits of the proposed approach. The shape optimization was performed using a genetic algorithm, a gradient-free optimization method. The genetic algorithm starts with an initial population and proceeds to evolve the population toward an optimal solution based on a fitness value. For this work, two optimization problems were performed. The first consisted of minimizing the axial force of the aircraft, and the second optimization aimed to minimize the distortion at the fan face with an added objective to provide a smooth shape. As expected, the results of the optimization showed that the axial force minimization converged in less generations than the multiobjective case of minimizing the distortion at the fan face. However, both optimization problems were converged after 30 generations. The computational cost assessment results showed that the ROM-based approach offers an obvious benefit over a nonintrusive CFD-based approach consisting of gradient based optimization with finite differencing, but only becomes favorable over the adjoint-based approach for two or more optimizations. This is an important result because it means that the proposed approach offers the capability to further explore the design space and to study the impact of different objective functions to assess design trades. The results confirm that the overall research objective for this work was achieved.

## *8.1 Contributions*

A ROM capable of performing predictions as a function of propulsor operating conditions and fuselage shape was developed and coupled to a propulsion system analysis model to perform coupled MDA. The value of the approach was demonstrated

through application to coupled MDAO and computational cost comparisons to equivalent CFD-based and adjoint-based approaches. The contributions of this research are summarized below:

- Demonstration of a computationally efficient method for generating snapshots of a coupled system using a decoupled analysis
- Development of a reduced-order modeling capability for the coupled MDA of BLI configurations
- Improved understanding of the analysis and design of BLI configurations
- Improved understanding of the coupling mechanisms between the airframe and propulsion system for BLI configurations
- Demonstration of a computationally efficient method for performing MDAO and design space exploration for BLI configurations

## *8.2 Opportunities for Future Research*

The ROM-based, coupled MDA approach was shown to provide a practical means of performing coupled MDAO for BLI configurations and to enable greater exploration of the design space. To develop and demonstrate the approach, a simplified propulsion system analysis was employed. This model provided the necessary information for the fan exit boundary conditions based on a user-defined fan pressure ratio and the pressure recovery at the fan face. However, as discussed in Chapter 3, the model is not directly applicable for the sizing of the propulsion system. Given a fan design with an associated performance map and desired operating condition, the ROM-based, coupled MDA approach requires the ability to scale the fan diameter to obtain the required mass flow rate. The fan diameter would, therefore, be an additional design variable in the DOE for the aerodynamic ROM.

Another area of potential research is the shape parameterization. One of the most significant bottlenecks associated with the MDAO problem performed in this work is the shape parameterization and the propagation of shape changes to the CFD grid. There are three primary issues that were identified for the shape parameterization component:

1. Obtaining a shape parameterization with the appropriate balance between the number of design variables, the quality of the shape changes, and design freedom
2. Generating high quality surface grids mappings for shape perturbations
3. Propagating the shape changes to the interior of the CFD grid in a way that is both robust and automated

The shape parameterization needs to include enough design freedom such that it allows for nonintuitive design changes. However, too much design freedom can be detrimental to the practicality of the ROM-based, coupled MDA approach since an increase in design variables will require an increase in the number of snapshots to obtain accurate predictions from the ROM. Parameterization tools, such as OpenVSP and ESP, are potential options that offer the ability to parameterize the shape through a reduced set of shape variables, which provide meaningful shape changes. However, neither tool provides a direct path for addressing the second issue, which is the mapping of the changes in the surface shape to a high quality grid. The third issue that was identified with the shape parameterization is the difficulty associated with propagating the changes in surface shape to the grid volume. For this work, FUN3D's internal grid deformation was employed to eliminate the need to generate a new grid volume for every change in shape. However, grid deformation can have issues with cell folding and negative volumes, resulting in the need to limit surface movement. Future research should aim to address these issues, which would not only

improve the ROM-based, coupled MDAO approach developed in this work but also any problem that requires changes in shape to be propagated to a computational grid.

A potential extension of this work that could be valuable would be to incorporate the adjoint-method into the ROM-based approach. Gradient information obtained from the adjoint method could be used to improve the prediction capabilities of the aerodynamic ROM. This could be performed by including an adjoint evaluation with each of the snapshots used to create the aerodynamic ROM. The ROM would then provide predictions of both the flow quantities and the gradients to allow for efficient gradient-based optimization. The addition of the adjoint evaluation would increase the computational cost for each snapshot. However, by obtaining the gradient information at each design variable combinations, the number of snapshots required for accurate predictions could potentially decrease such that the increase in computational cost per snapshot is acceptable. It is important to note that this would no longer be a nonintrusive method but it could be useful in the case that the adjoint method is available for use.

# APPENDIX A

# EXPERIMENT 1.2 - ROM VALIDATION RESULTS

## *A.1* $DPCP_{avg}$

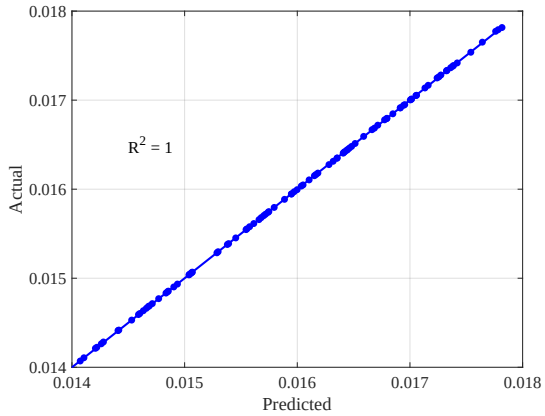


(a) Actual-by-predicted

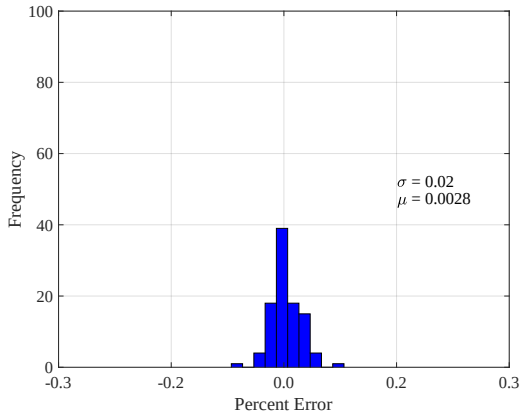


(b) Histogram

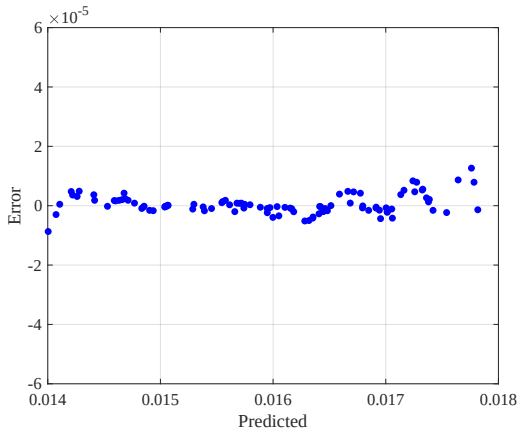


(c) Error-by-predicted

Figure 93: $DPCP_{avg}$ error metrics - 15 snapshots.

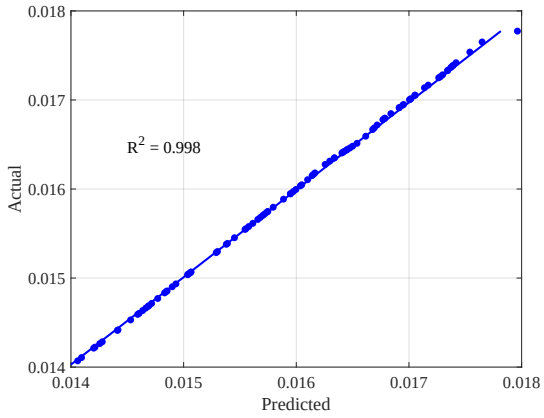


(a) Actual-by-predicted

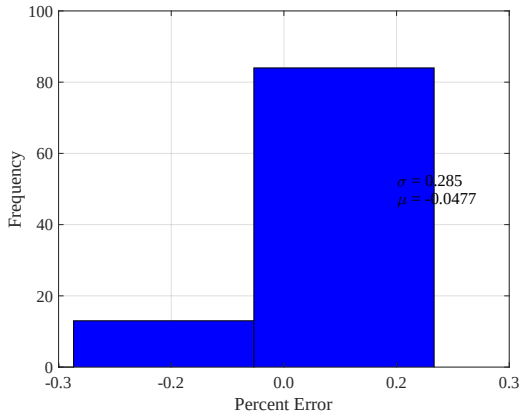


(b) Histogram

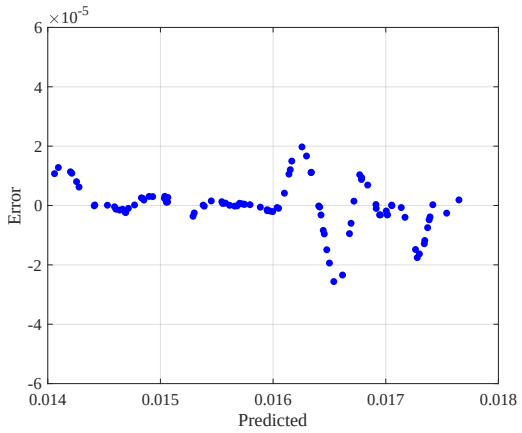


(c) Error-by-predicted

Figure 94: $DPCP_{avg}$ error metrics - 25 snapshots.

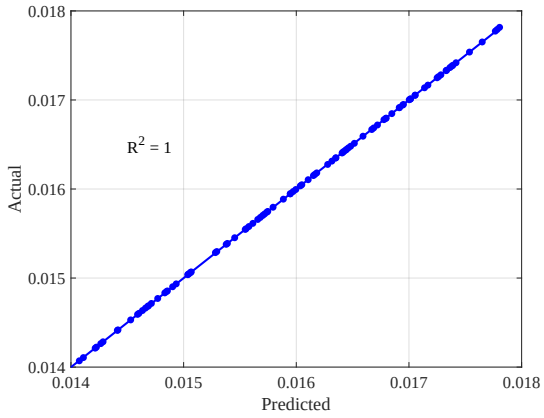


(a) Actual-by-predicted

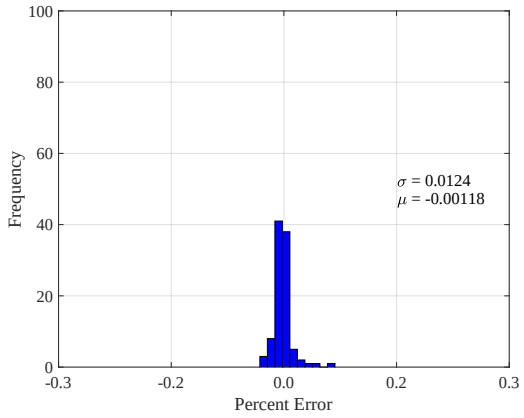


(b) Histogram

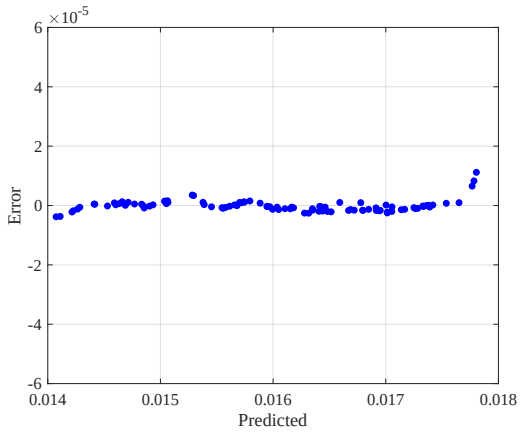


(c) Error-by-predicted

Figure 95: $DPCP_{avg}$ error metrics - 50 snapshots.

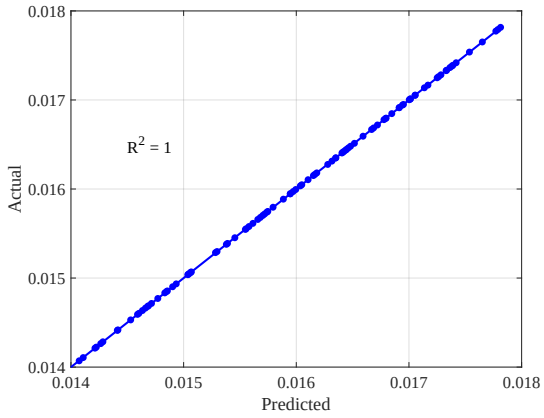


(a) Actual-by-predicted

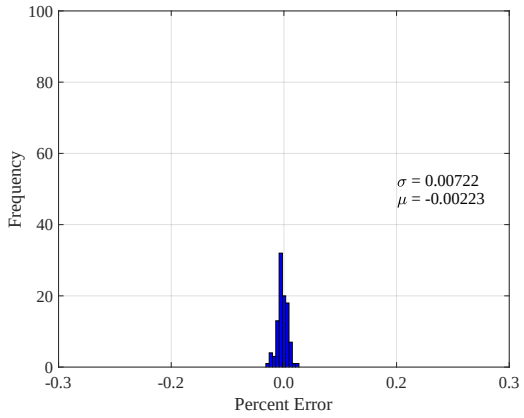


(b) Histogram

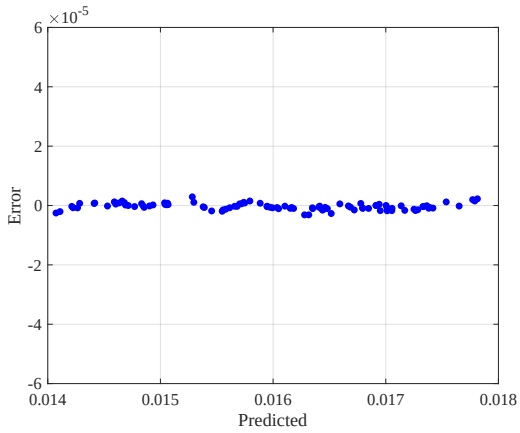


(c) Error-by-predicted

Figure 96: $DPCP_{avg}$ error metrics - 100 snapshots.

## *A.2* $PR$

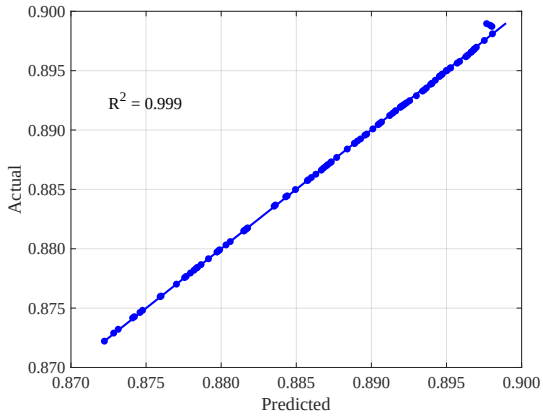


(a) Actual-by-predicted

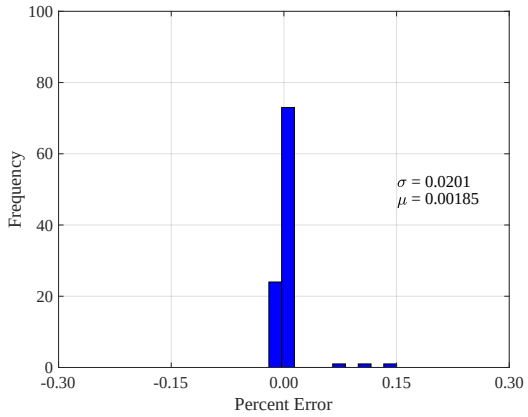


(b) Histogram

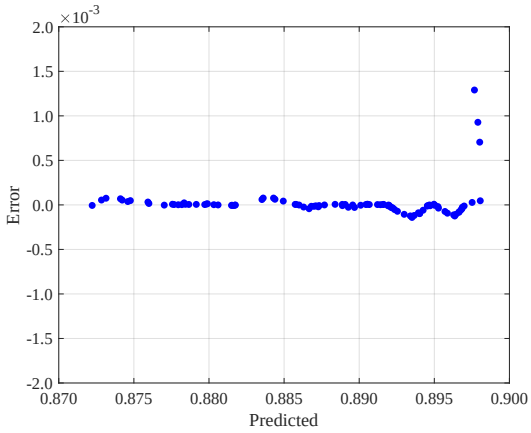


(c) Error-by-predicted

Figure 97: $PR$ error metrics - 15 snapshots.

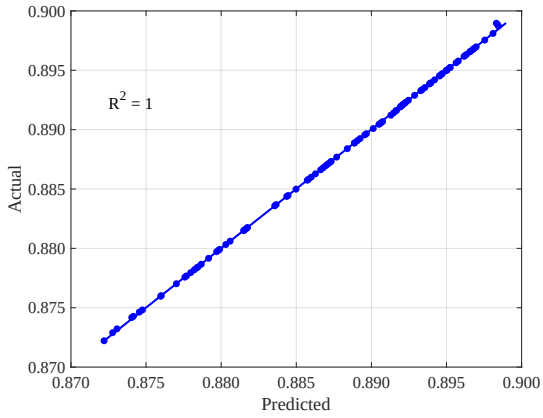


(a) Actual-by-predicted

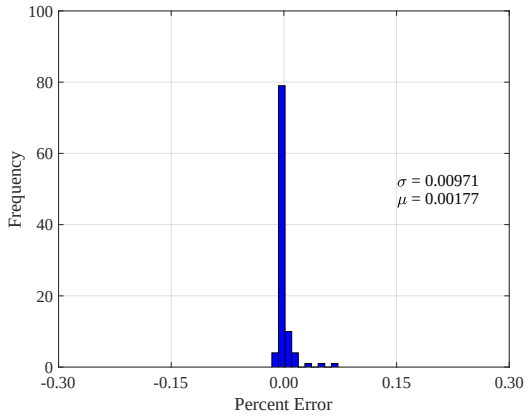


(b) Histogram

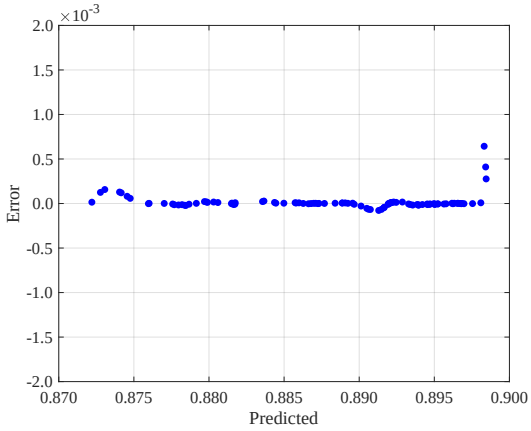


(c) Error-by-predicted

Figure 98: $PR$ error metrics - 25 snapshots.

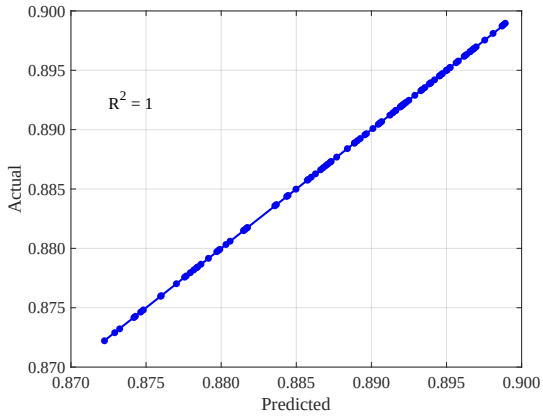


(a) Actual-by-predicted

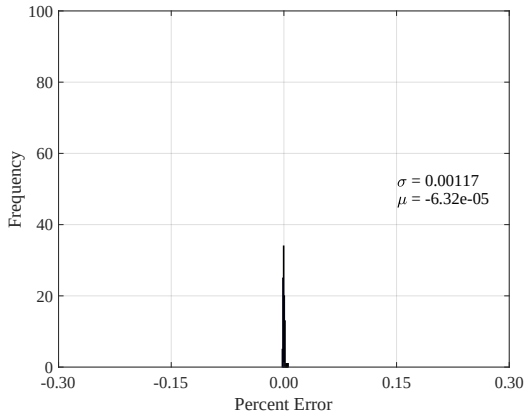


(b) Histogram

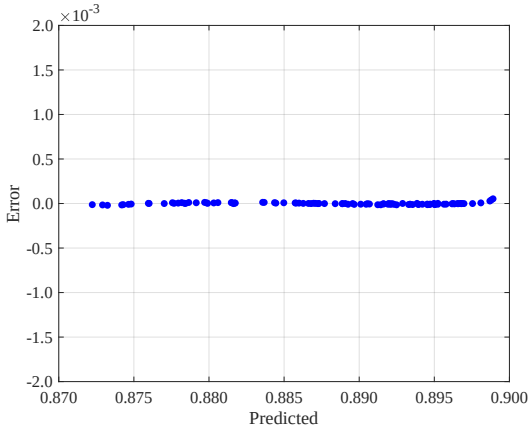


(c) Error-by-predicted

Figure 99: $PR$ error metrics - 50 snapshots.

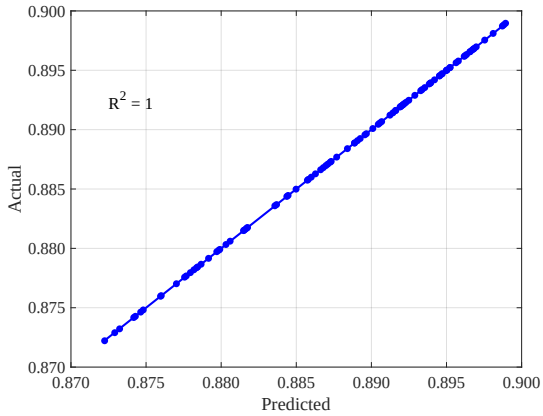


(a) Actual-by-predicted

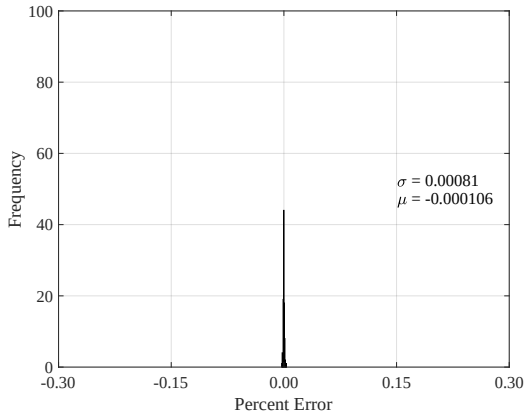


(b) Histogram

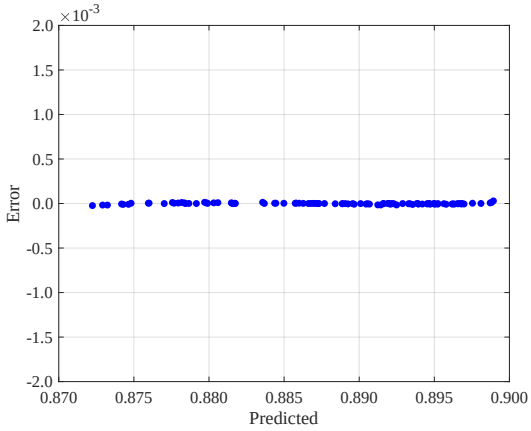


(c) Error-by-predicted

Figure 100: $PR$ error metrics - 100 snapshots.

## *A.3* $FPR$

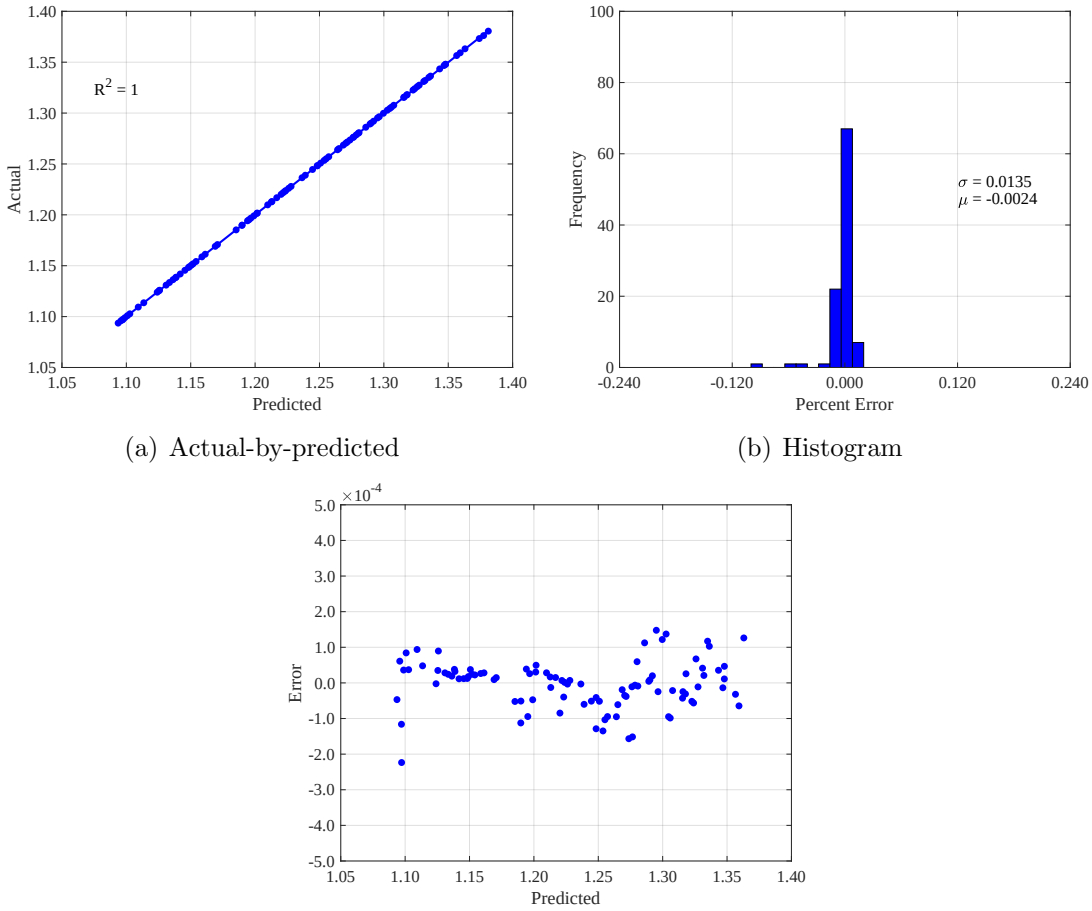


(a) Actual-by-predicted

(b) Histogram

(c) Error-by-predicted

Figure 101: $FPR$ error metrics - 15 snapshots.

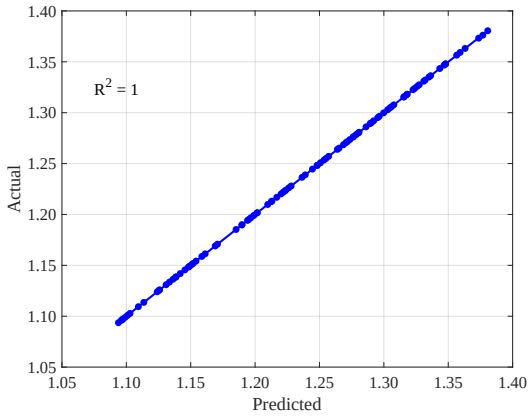


(a) Actual-by-predicted

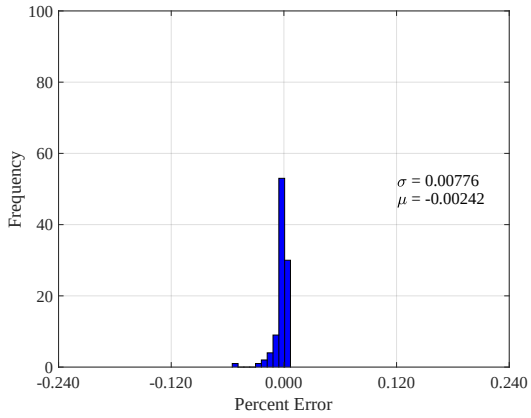


(b) Histogram

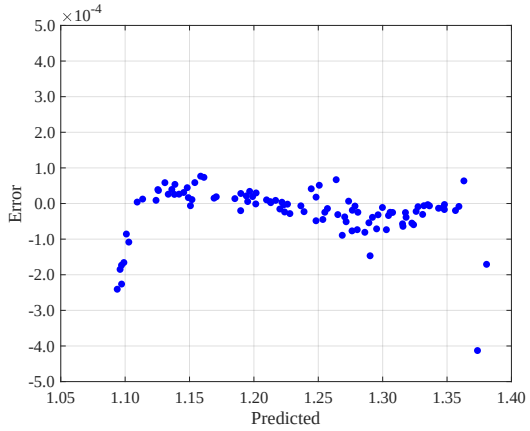


(c) Error-by-predicted

Figure 102: $FPR$ error metrics - 25 snapshots.

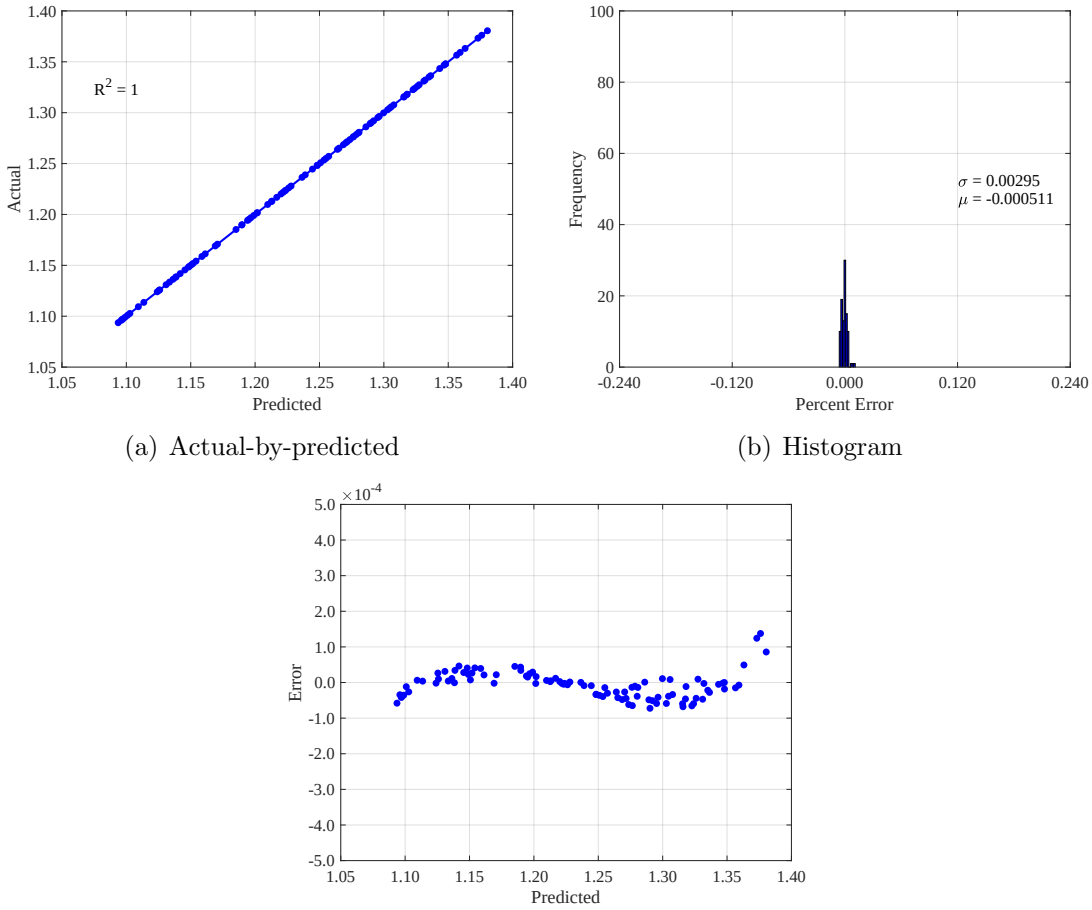


(a) Actual-by-predicted

(b) Histogram

(c) Error-by-predicted

Figure 103: $FPR$ error metrics - 50 snapshots.

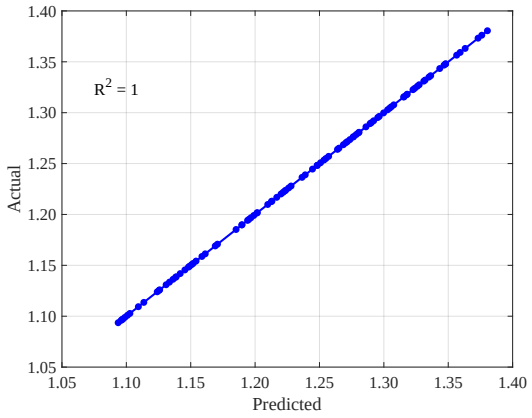


(a) Actual-by-predicted

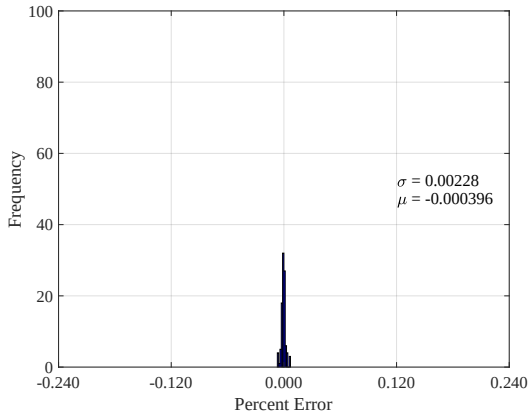


(b) Histogram

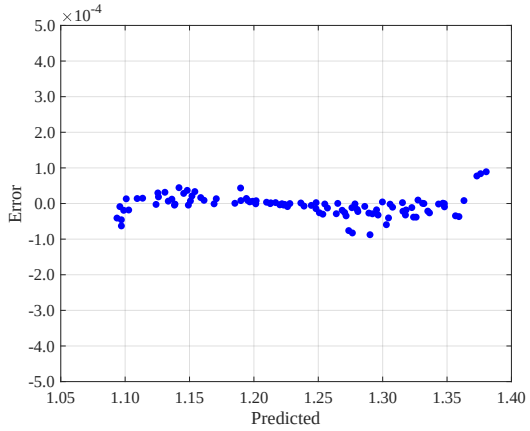


(c) Error-by-predicted

Figure 104: $FPR$ error metrics - 100 snapshots.

## *A.4* $P_{req}$

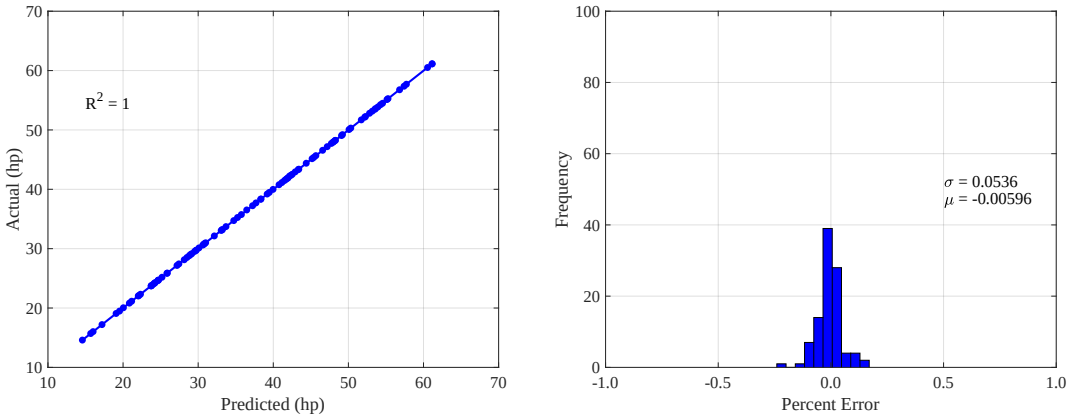


(a) Actual-by-predicted

(b) Histogram

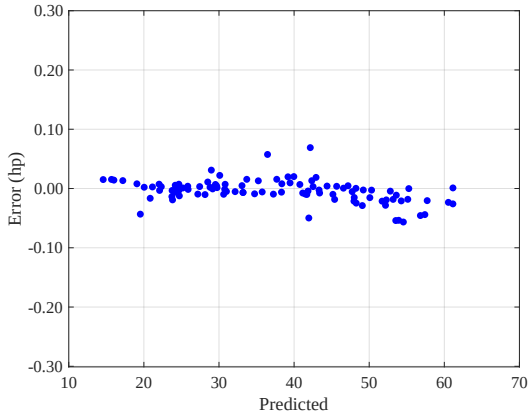


(c) Error-by-predicted

Figure 105: $P_{req}$ error metrics - 15 snapshots.

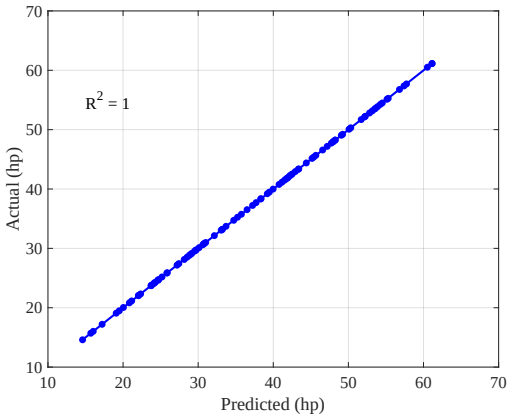


(a) Actual-by-predicted

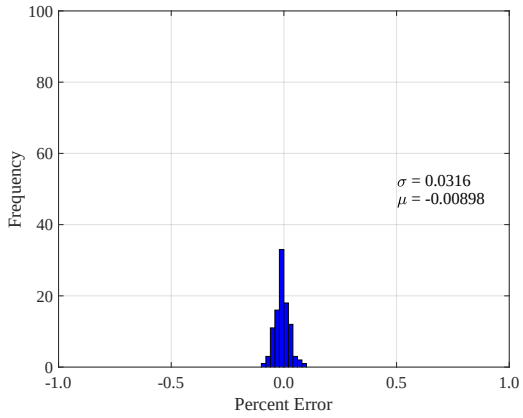


(b) Histogram

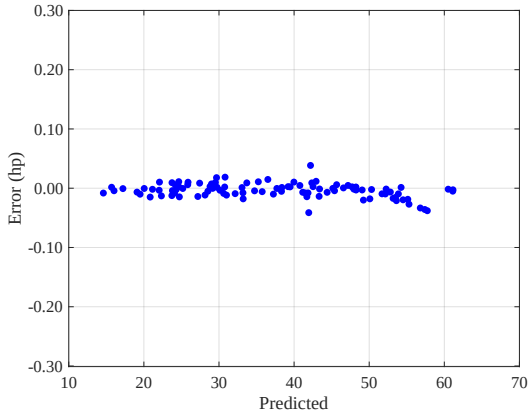


(c) Error-by-predicted

Figure 106: $P_{req}$ error metrics - 25 snapshots.

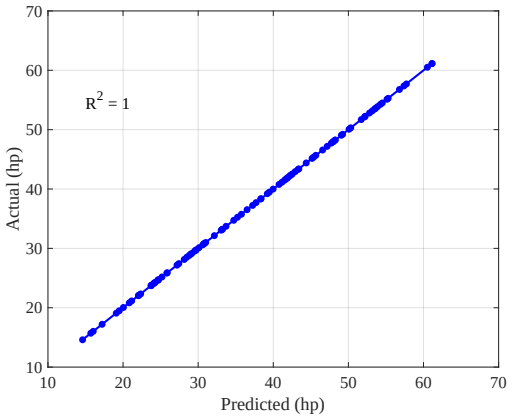


(a) Actual-by-predicted

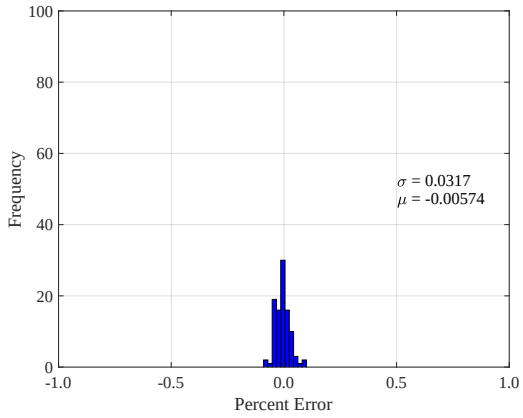


(b) Histogram

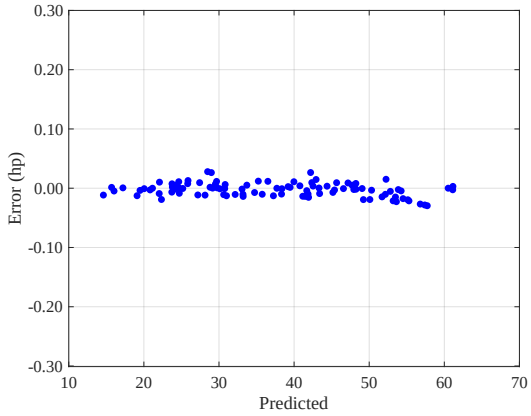


(c) Error-by-predicted

Figure 107: $P_{req}$ error metrics - 50 snapshots.

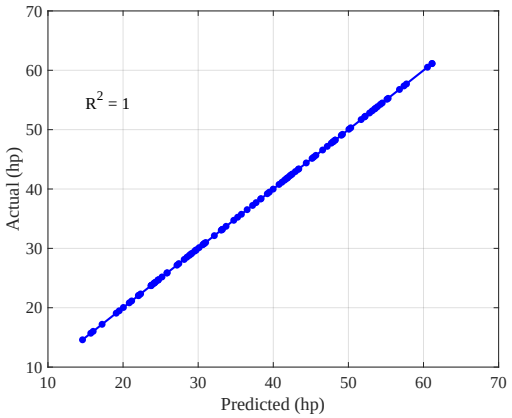


(a) Actual-by-predicted

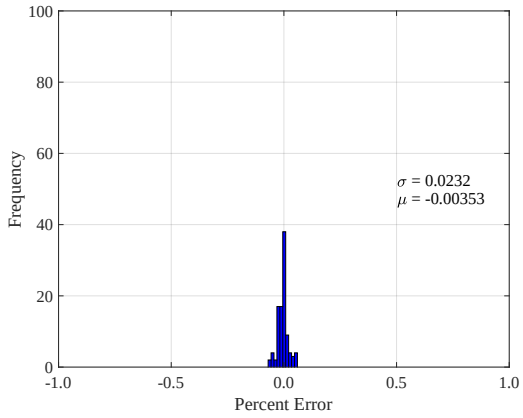


(b) Histogram

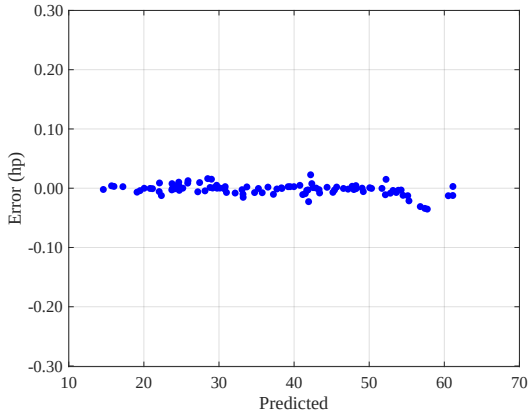


(c) Error-by-predicted

Figure 108: $P_{req}$ error metrics - 100 snapshots.

## *A.5* $F_x$

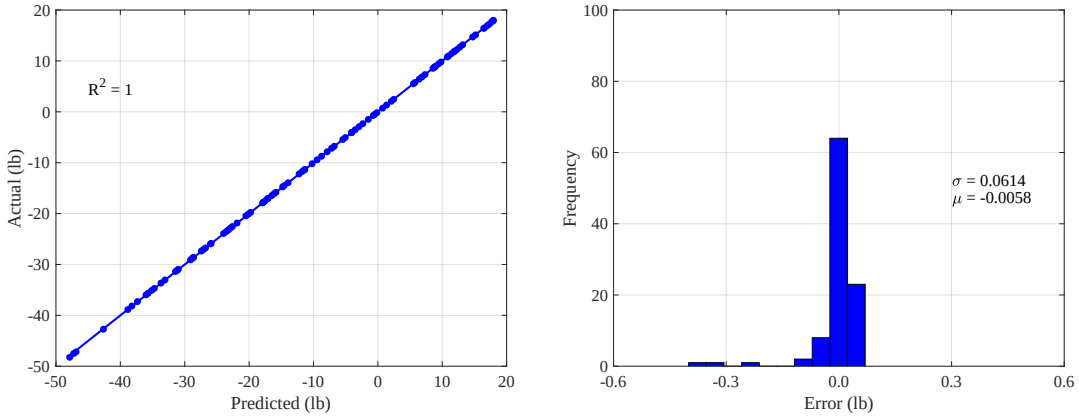


(a) Actual-by-predicted

(b) Histogram

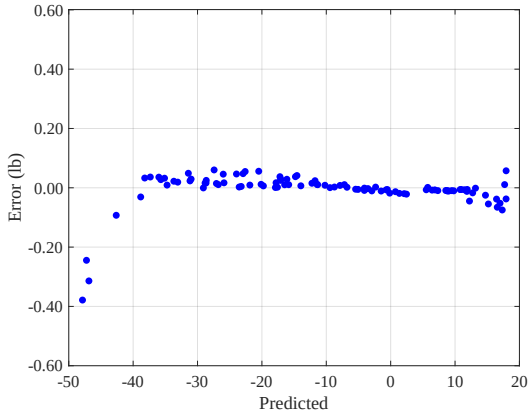


(c) Error-by-predicted

Figure 109: $F_x$ error metrics - 15 snapshots.

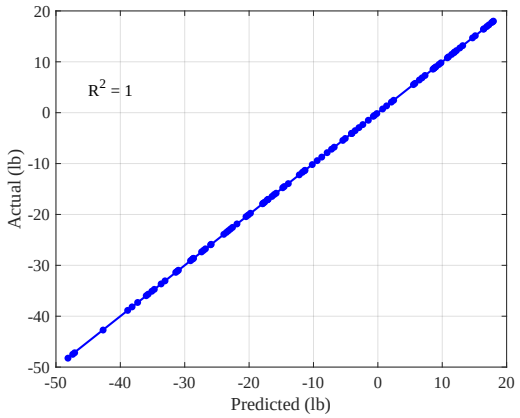


(a) Actual-by-predicted

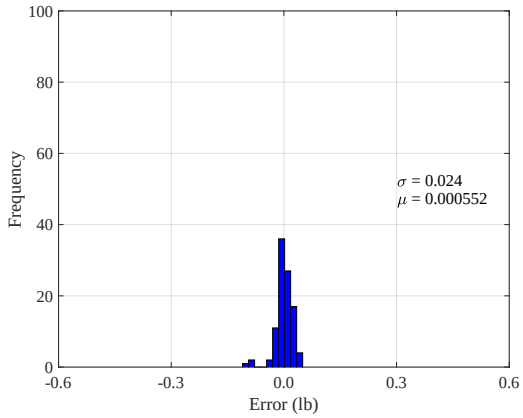


(b) Histogram

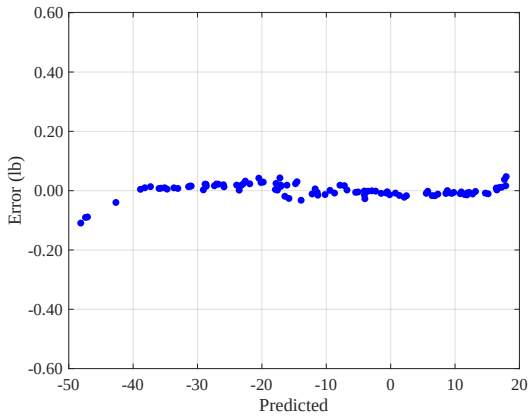


(c) Error-by-predicted

Figure 110: $F_x$ error metrics - 25 snapshots.

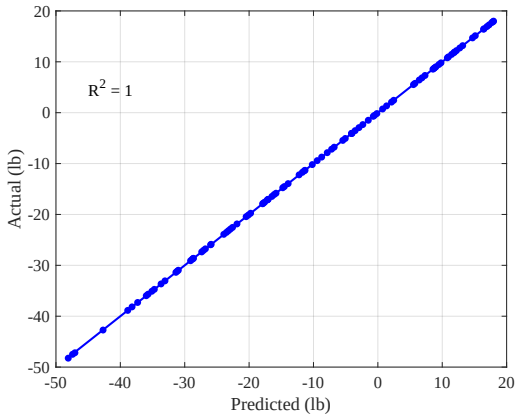


(a) Actual-by-predicted

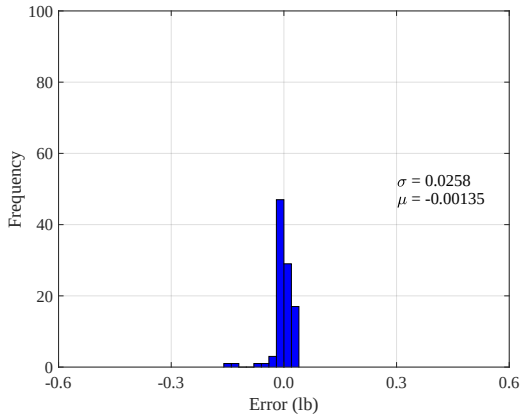


(b) Histogram

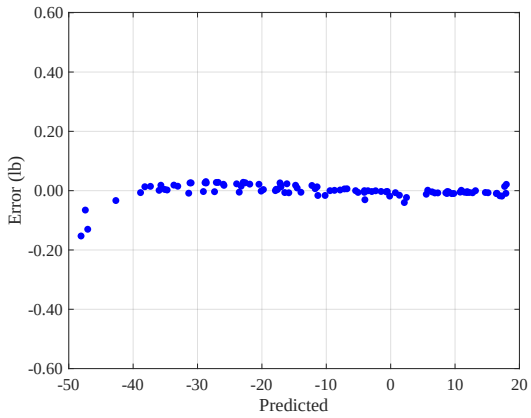


(c) Error-by-predicted

Figure 111: $F_x$ error metrics - 50 snapshots.

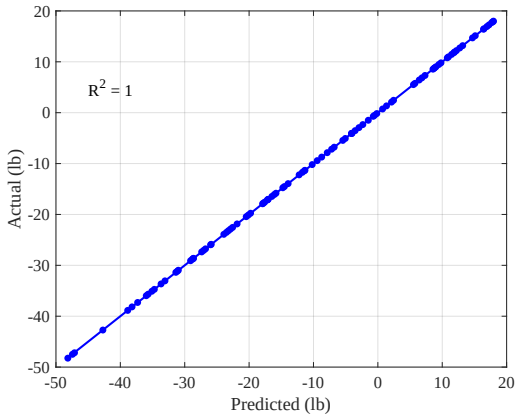


(a) Actual-by-predicted

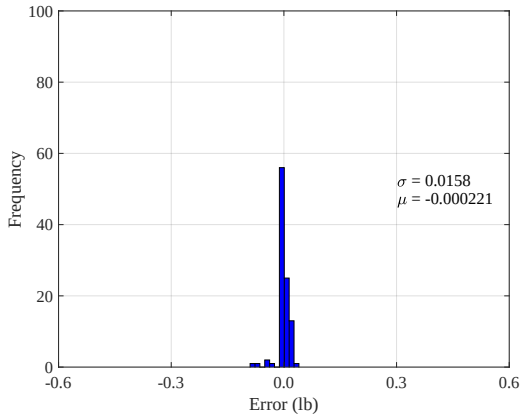


(b) Histogram

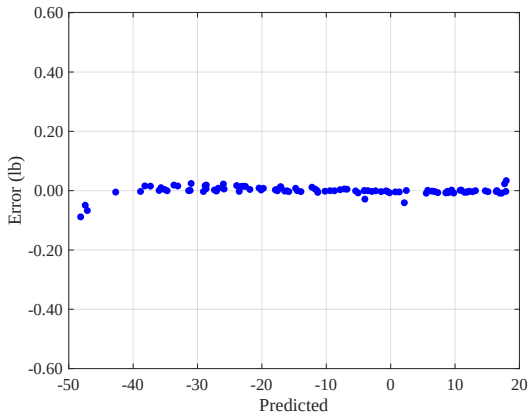


(c) Error-by-predicted

Figure 112: $F_x$ error metrics - 100 snapshots.

# APPENDIX B

# EXPERIMENT 3.1 - ROM VALIDATION RESULTS

## *B.1* $DPCP_{avg}$

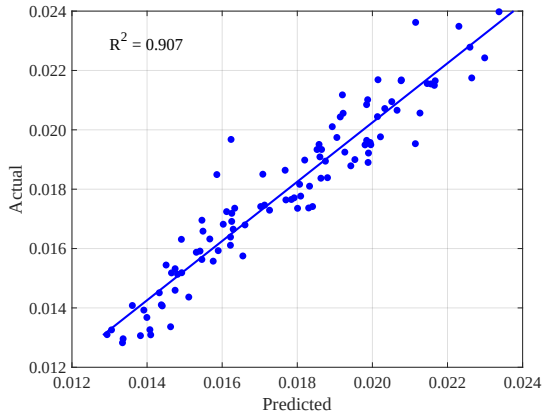


(a) Actual-by-predicted

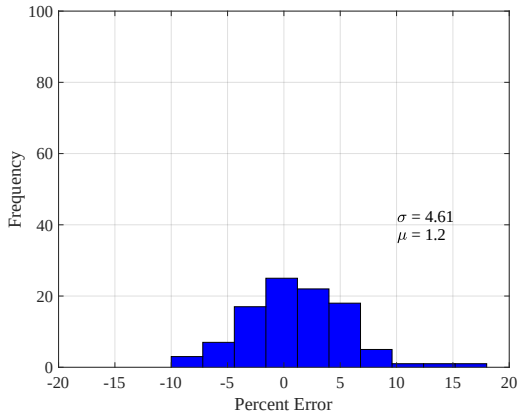


(b) Histogram

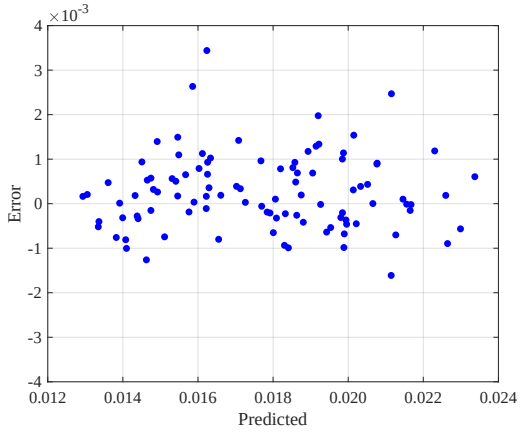


(c) Error-by-predicted

Figure 113: $DPCP_{avg}$ error metrics - 50 snapshots.

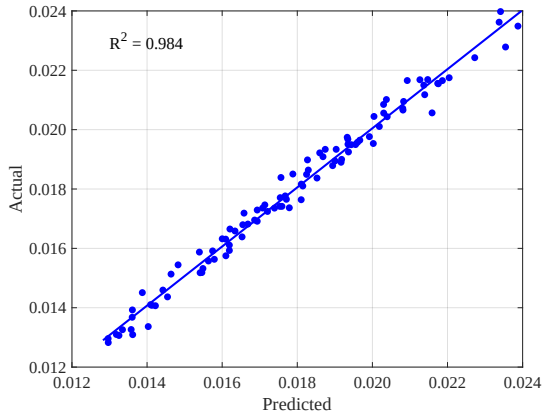


(a) Actual-by-predicted

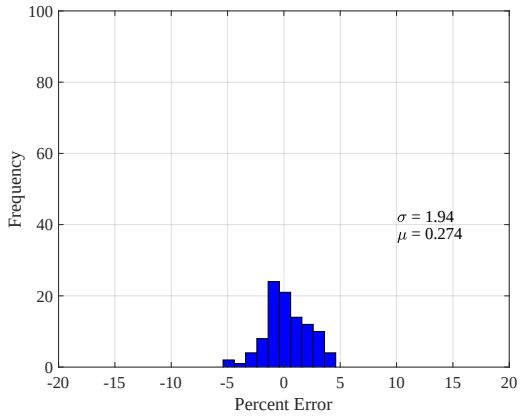


(b) Histogram

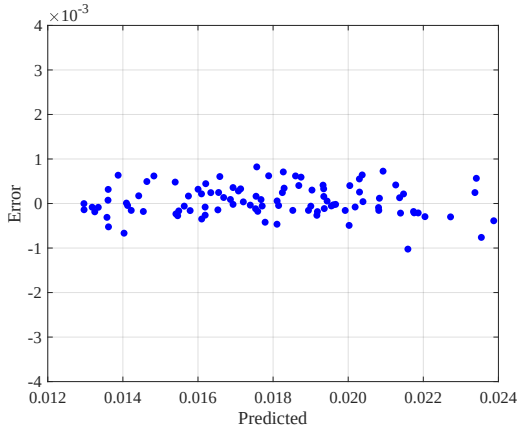


(c) Error-by-predicted

Figure 114: $DPCP_{avg}$ error metrics - 100 snapshots.

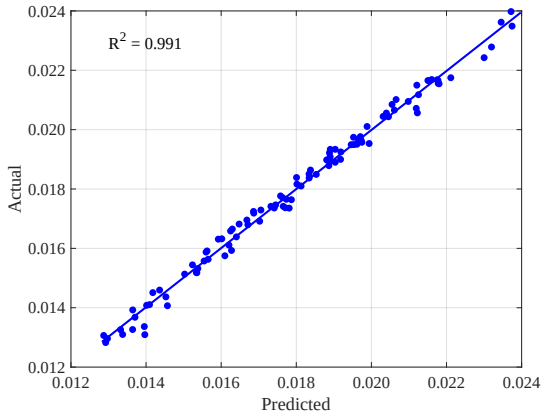


(a) Actual-by-predicted

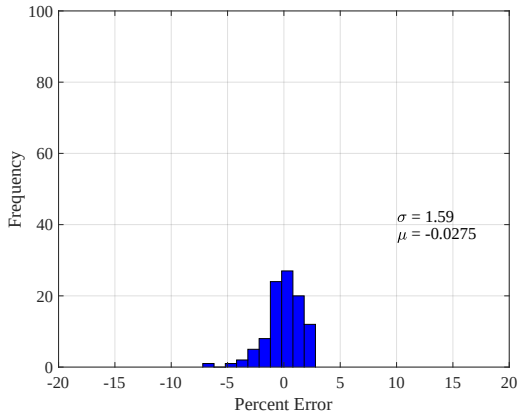


(b) Histogram

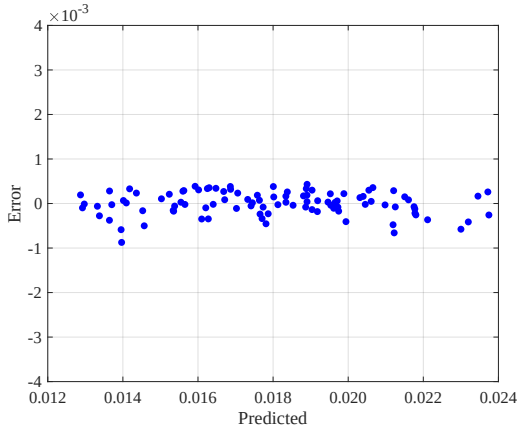


(c) Error-by-predicted

Figure 115: $DPCP_{avg}$ error metrics - 200 snapshots.

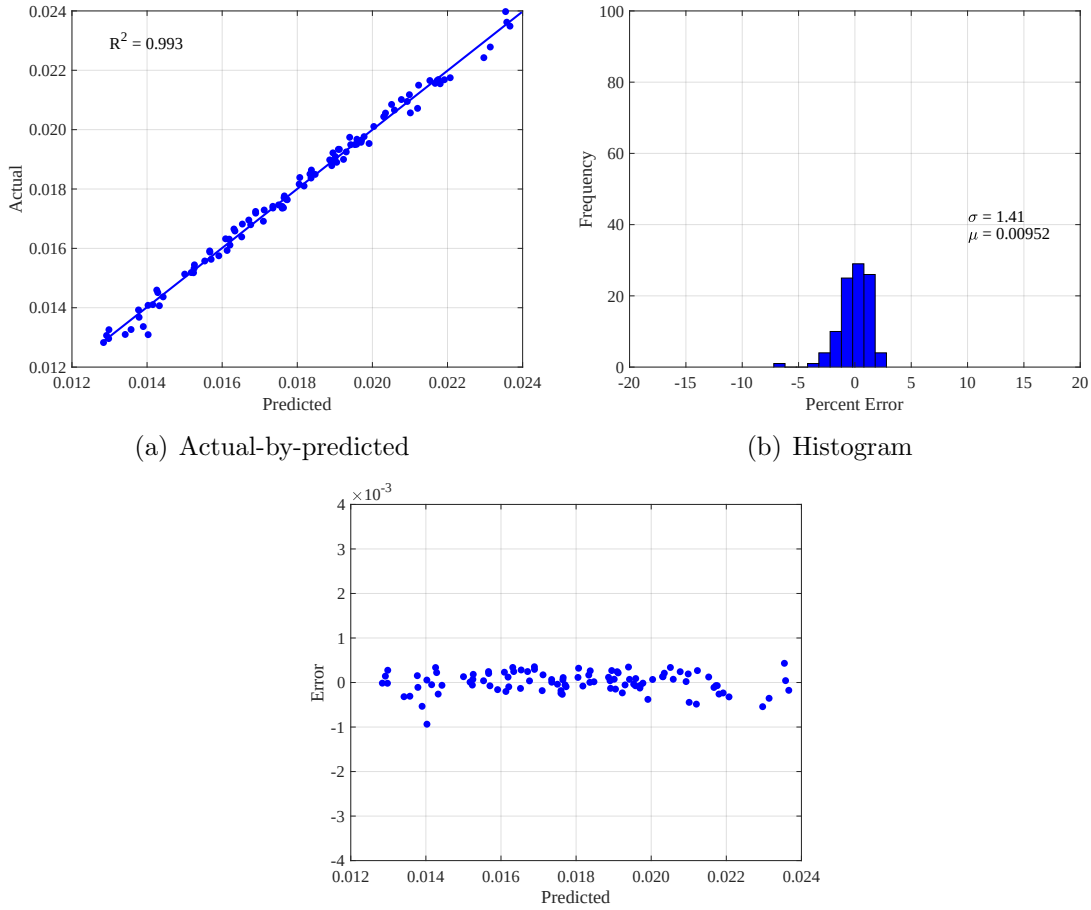


(a) Actual-by-predicted

(b) Histogram

(c) Error-by-predicted

Figure 116: $DPCP_{avg}$ error metrics - 400 snapshots.

## *B.2* $PR$

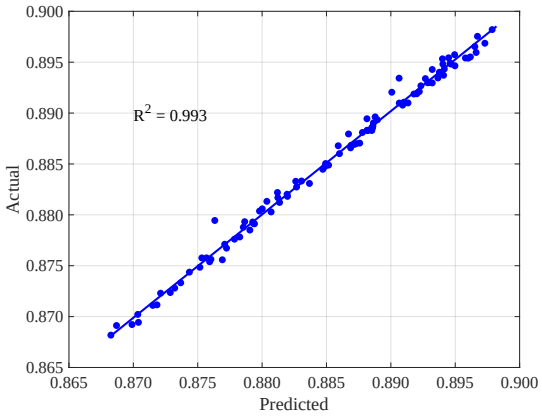


(a) Actual-by-predicted

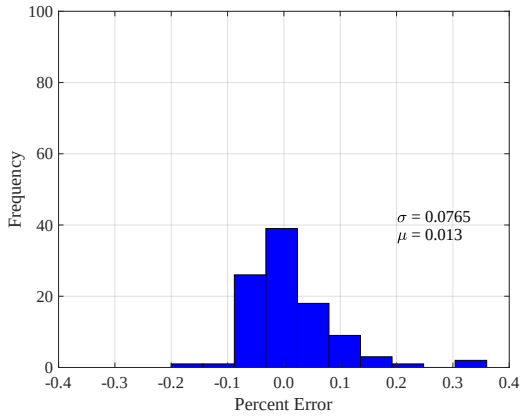


(b) Histogram

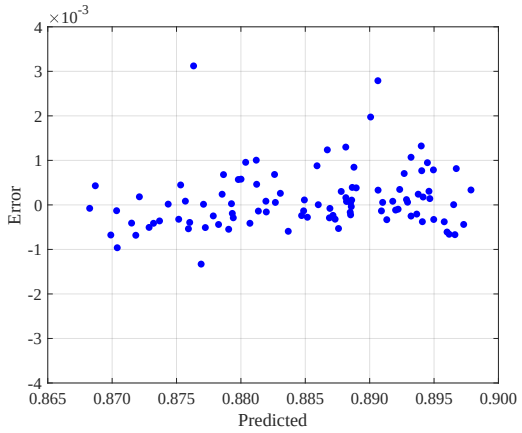


(c) Error-by-predicted

Figure 117: $PR$ error metrics - 50 snapshots.

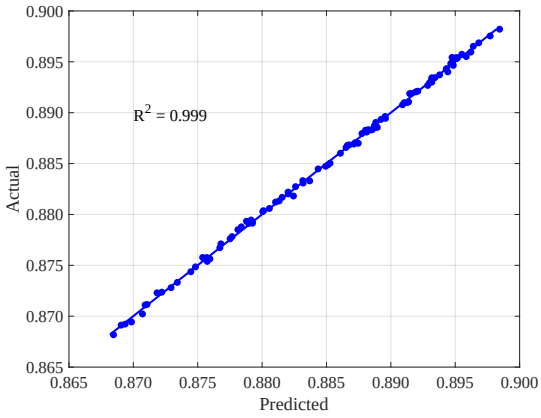


(a) Actual-by-predicted

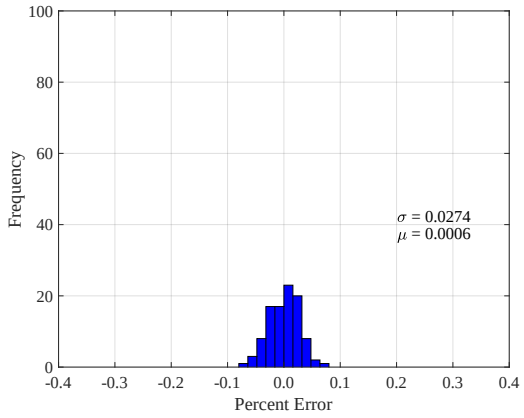


(b) Histogram

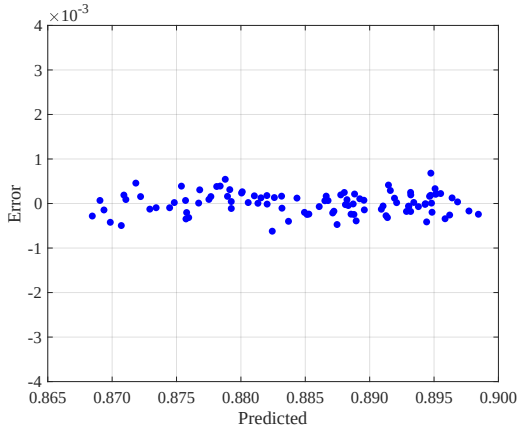


(c) Error-by-predicted

Figure 118: $PR$ error metrics - 100 snapshots.

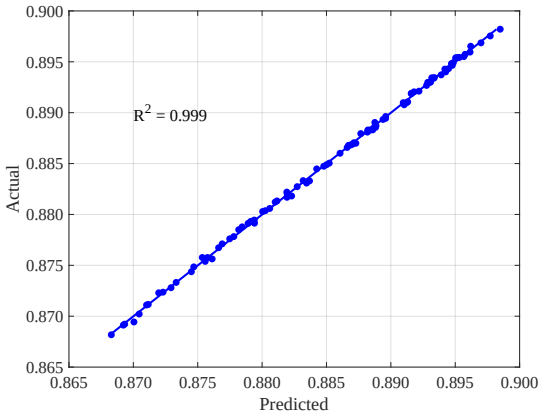


(a) Actual-by-predicted

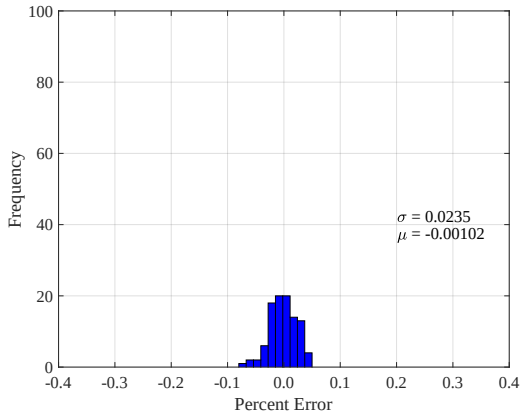


(b) Histogram

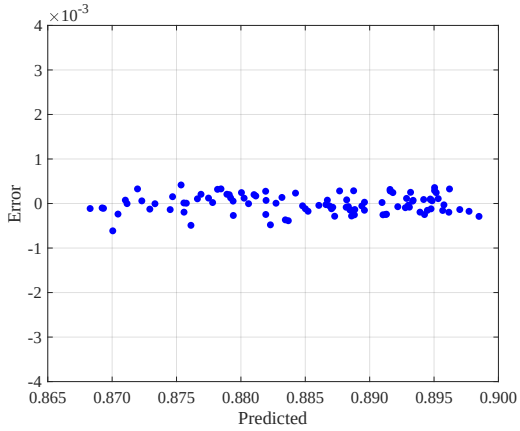


(c) Error-by-predicted

Figure 119: $PR$ error metrics - 200 snapshots.

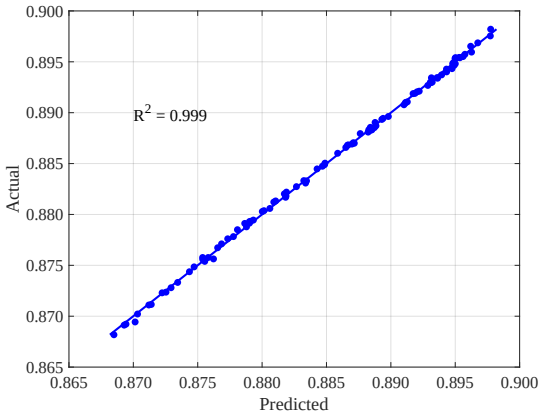


(a) Actual-by-predicted

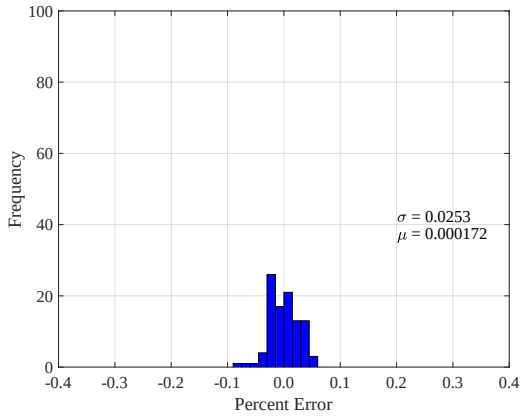


(b) Histogram

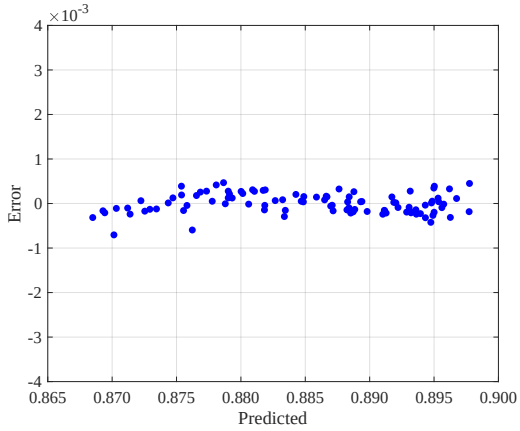


(c) Error-by-predicted

Figure 120: $PR$ error metrics - 400 snapshots.

## *B.3* $FPR$

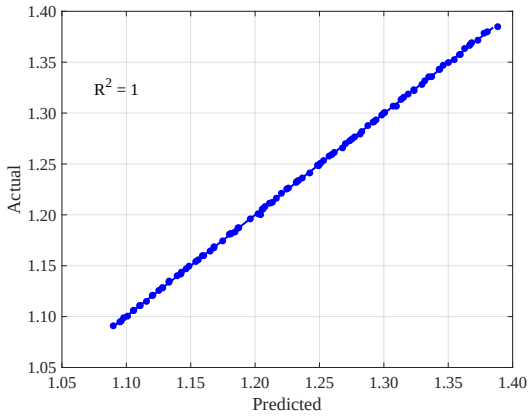


(a) Actual-by-predicted

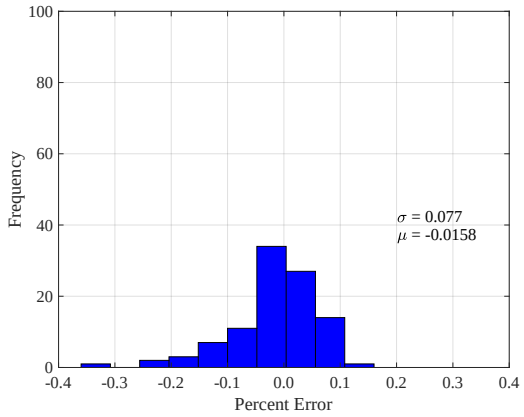


(b) Histogram

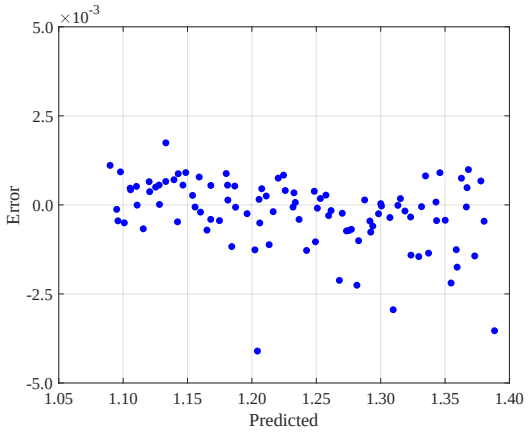


(c) Error-by-predicted

Figure 121: $FPR$ error metrics - 50 snapshots.

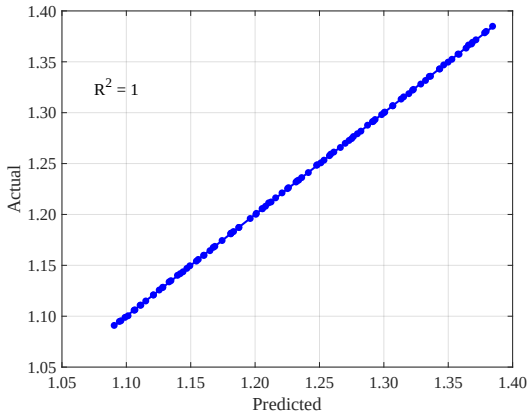


(a) Actual-by-predicted

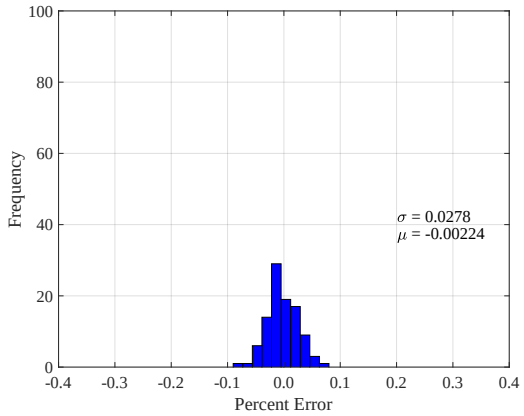


(b) Histogram

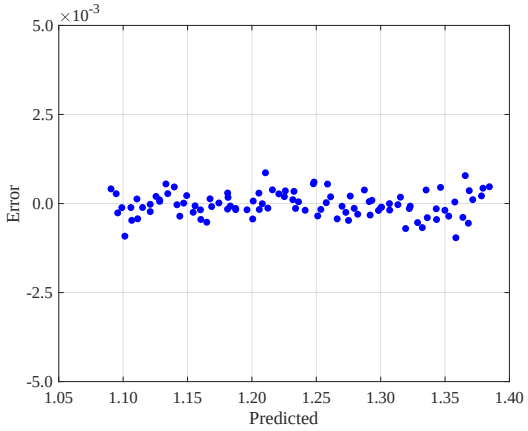


(c) Error-by-predicted

Figure 122: $FPR$ error metrics - 100 snapshots.

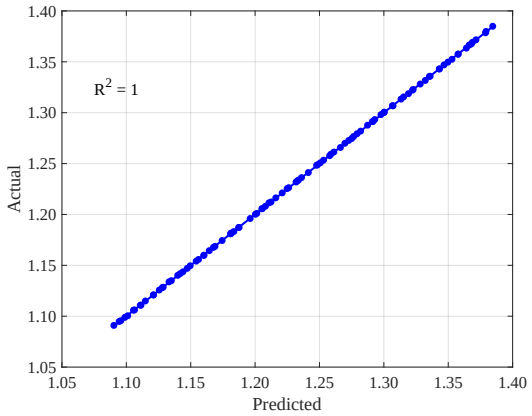


(a) Actual-by-predicted

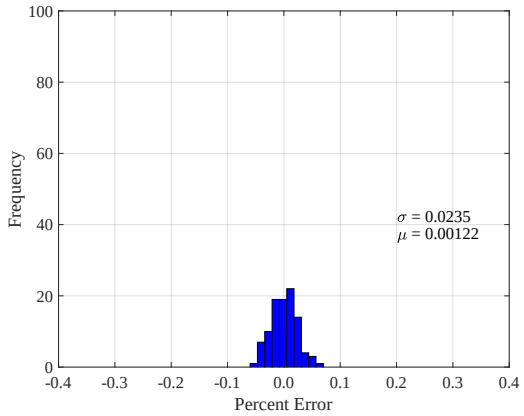


(b) Histogram

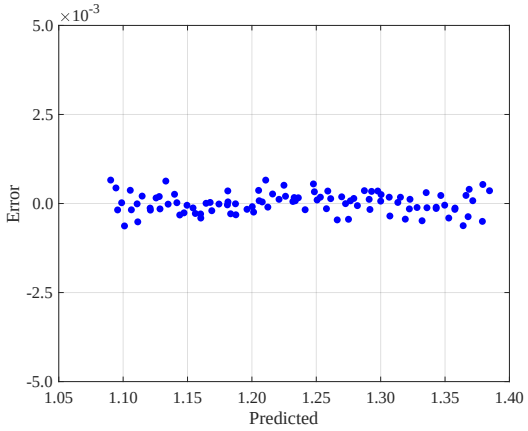


(c) Error-by-predicted

Figure 123: $FPR$ error metrics - 200 snapshots.

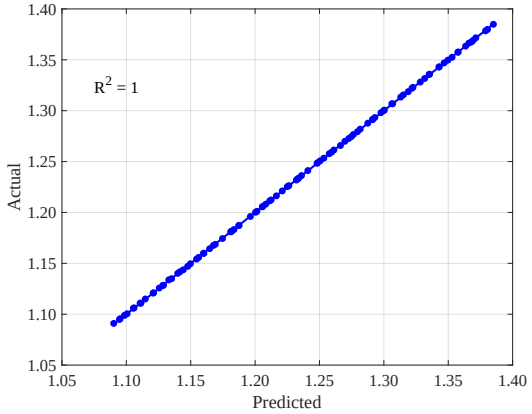


(a) Actual-by-predicted

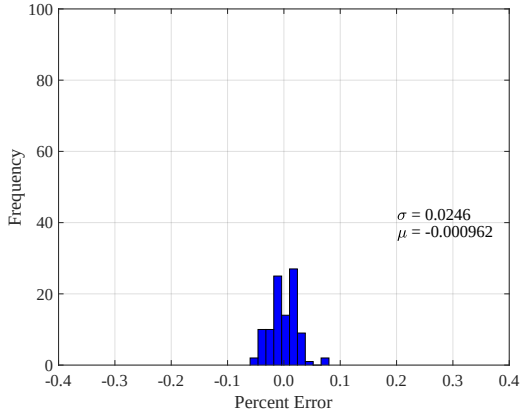


(b) Histogram

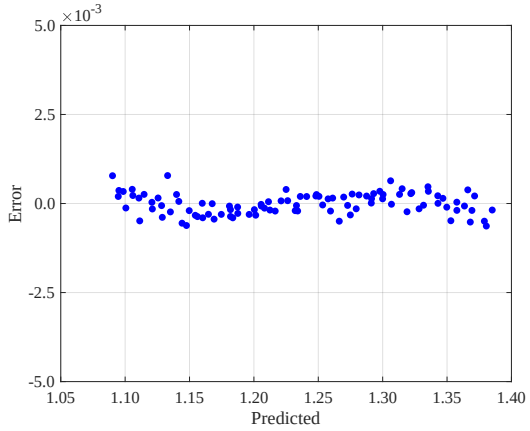


(c) Error-by-predicted

Figure 124: $FPR$ error metrics - 400 snapshots.

## *B.4* $P_{req}$

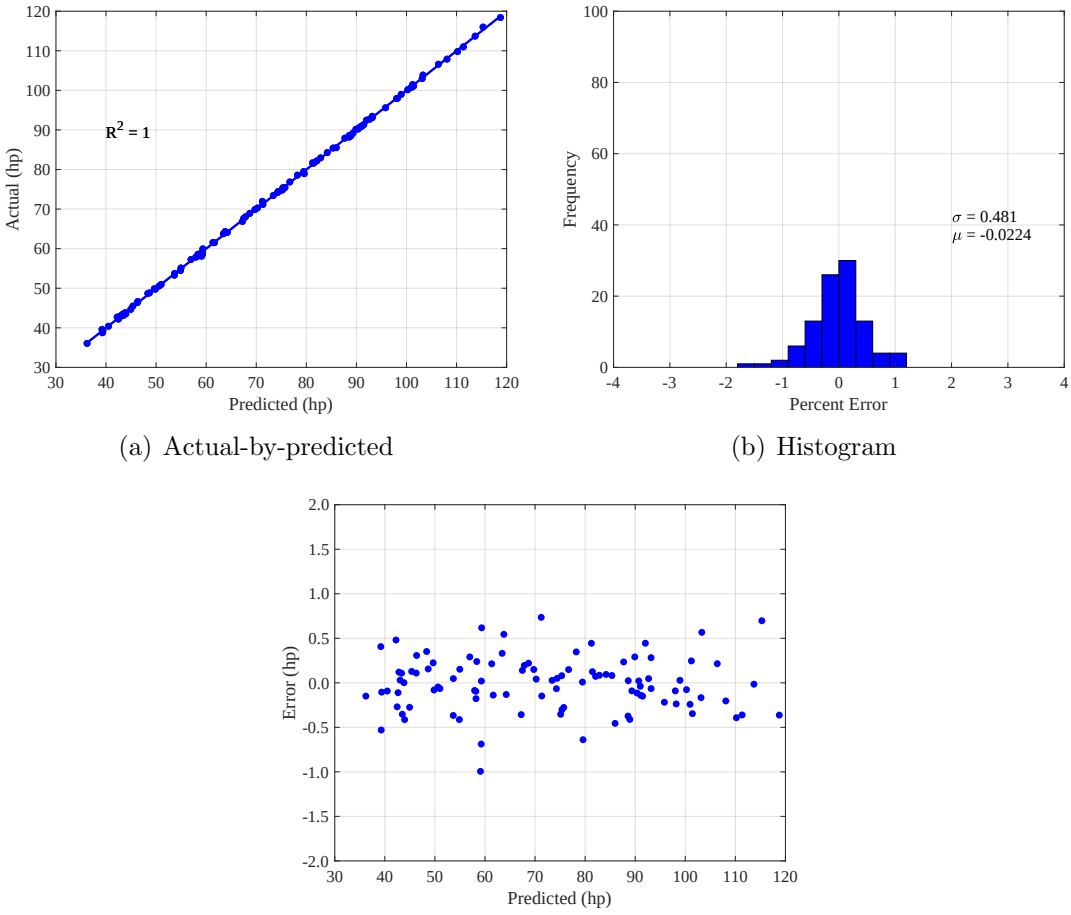


(a) Actual-by-predicted

(b) Histogram

(c) Error-by-predicted

Figure 125: $P_{req}$ error metrics - 50 snapshots.

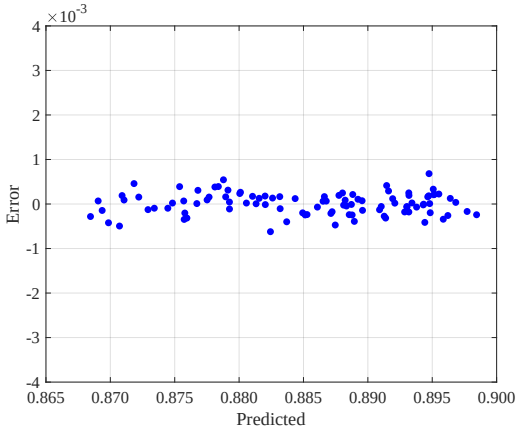


(a) Actual-by-predicted

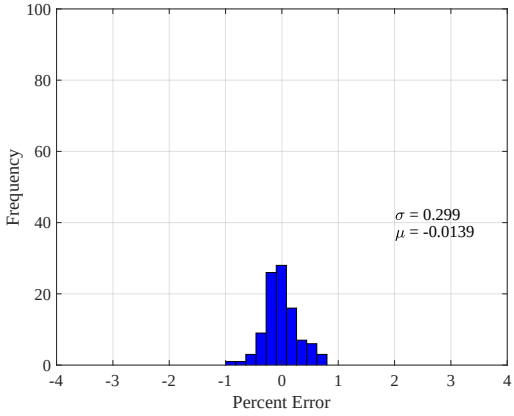


(b) Histogram

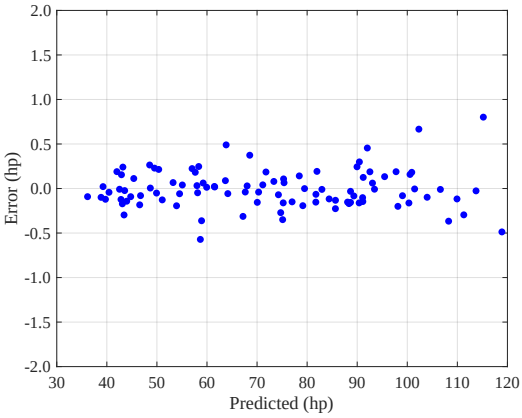


(c) Error-by-predicted

Figure 126: $P_{req}$ error metrics - 100 snapshots.

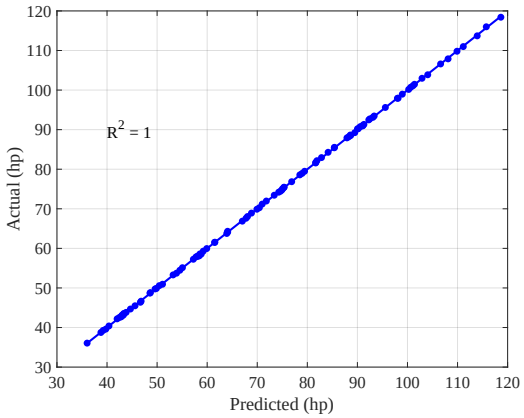


(a) Actual-by-predicted

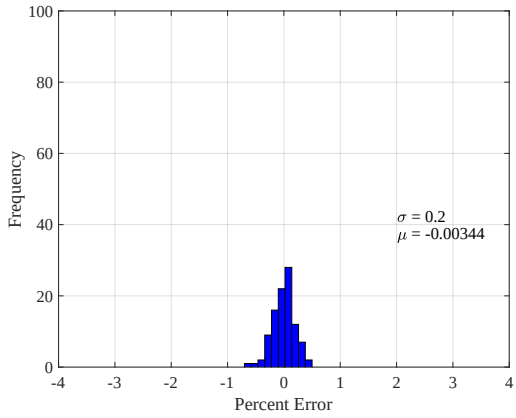


(b) Histogram

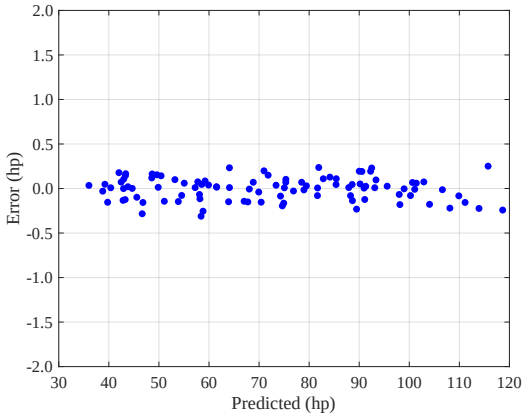


(c) Error-by-predicted

Figure 127: $P_{req}$ error metrics - 200 snapshots.

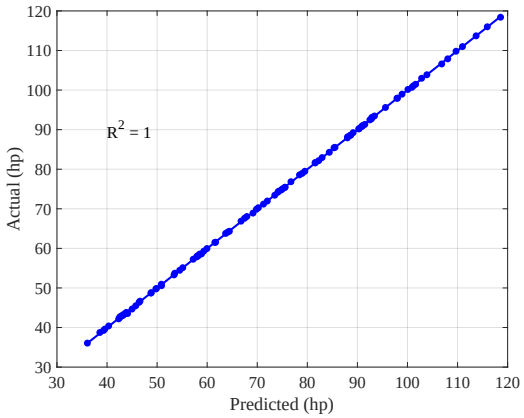


(a) Actual-by-predicted

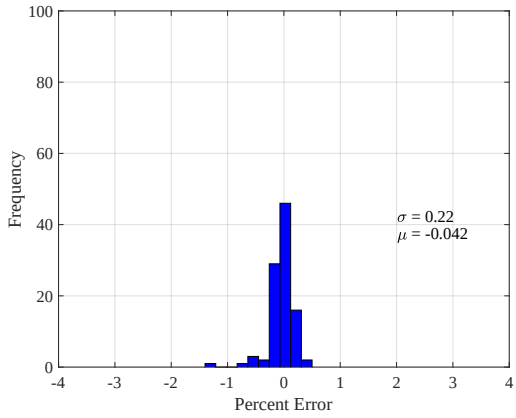


(b) Histogram

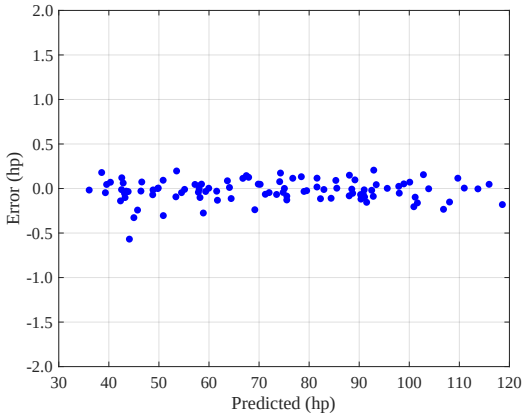


(c) Error-by-predicted

Figure 128: $P_{req}$ error metrics - 400 snapshots.

## *B.5* $F_x$

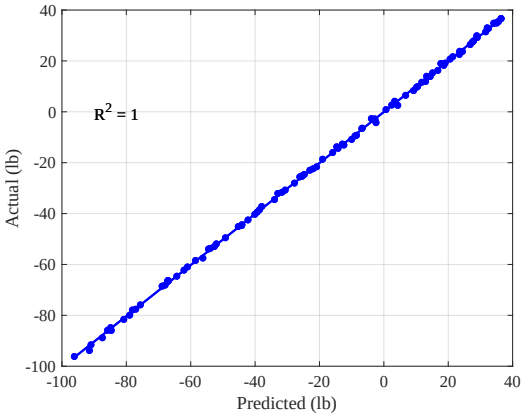


(a) Actual-by-predicted

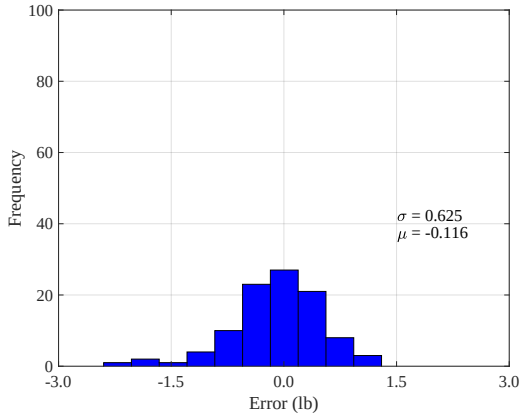


(b) Histogram

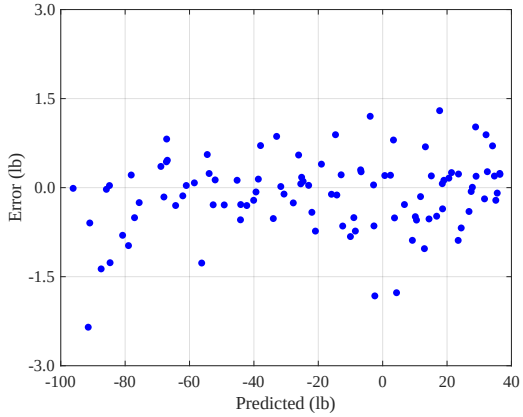


(c) Error-by-predicted

Figure 129: $F_x$ error metrics - 50 snapshots.

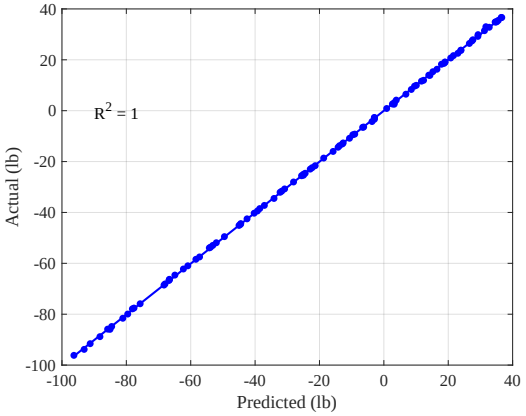


(a) Actual-by-predicted

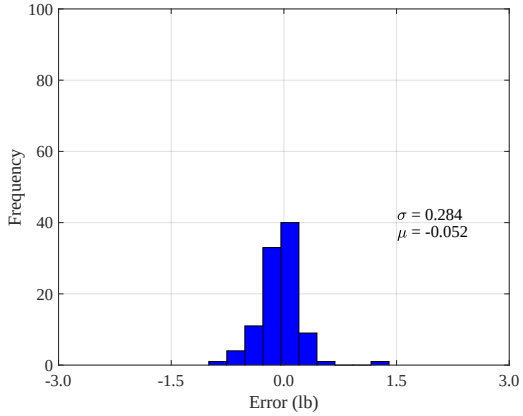


(b) Histogram

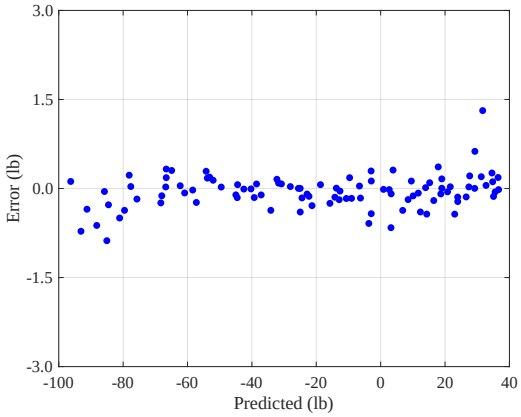


(c) Error-by-predicted

Figure 130: $F_x$ error metrics - 100 snapshots.

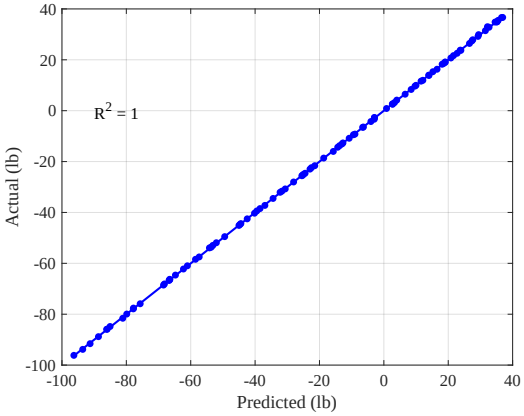


(a) Actual-by-predicted

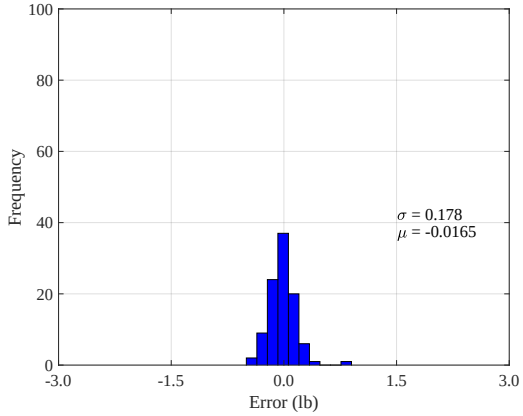


(b) Histogram

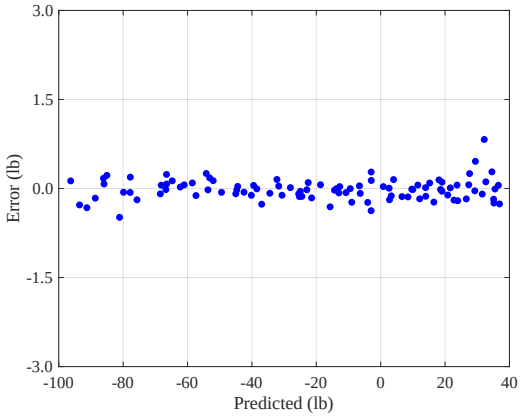


(c) Error-by-predicted

Figure 131: $F_x$ error metrics - 200 snapshots.

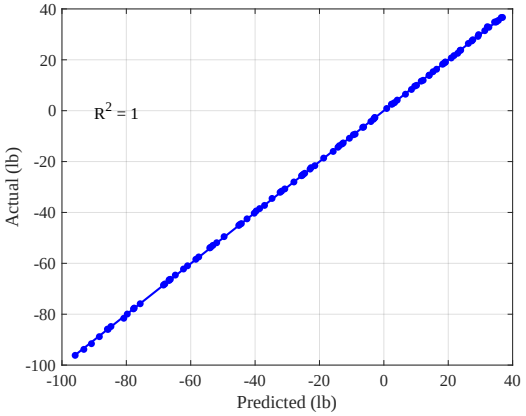


(a) Actual-by-predicted

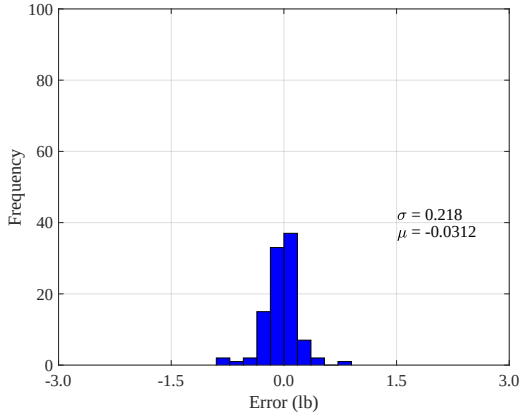


(b) Histogram

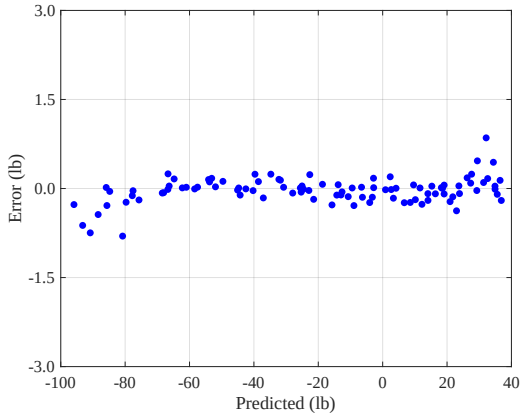


(c) Error-by-predicted

Figure 132: $F_x$ error metrics - 400 snapshots.

# REFERENCES


[1] "Strategic implementation plan 2017 update," *National Aeronautics and Space Administration, Washington, DC, NP-2017-01-2352-HQ*, 2017.

[2] Plas, A. A. P., *Performance of a boundary layer ingesting propulsion system*. PhD thesis, Massachusetts Institute of Technology, 2006. https://dspace.mit.edu/handle/1721.1/35568.

[3] Berguin, S. H., *A method for reducing dimensionality in large design problems with computationally expensive analyses*. PhD thesis, Georgia Institute of Technology, 2015. https://smartech.gatech.edu/handle/1853/53504.

[4] Renganathan, A., Berguin, S. H., Chen, M., Ahuja, J., Tai, J. C., Mavris, D. N., and Hills, D., "Sensitivity analysis of aero-propulsive coupling for over-wing-nacelle concepts," in *2018 AIAA Aerospace Sciences Meeting*, 2018. AIAA-2018-1757.

[5] Gray, J. S., Mader, C. A., Kenway, G. K., and Martins, J., "Approach to modeling boundary layer ingestion using a fully coupled propulsion-RANS model," in *58th AIAA/ASCE/AHS/ASC Structures, Structural Dynamics, and Materials Conference*, 2017. AIAA-2017-1753.

[6] Shi, M., Pokhrel, M., Gladin, J., Garcia, E., and Mavris, D. N., "Model fidelity requirements in boundary layer ingestion propulsion system conceptual design," in *2018 Aviation Technology, Integration, and Operations Conference*, 2018. AIAA-2018-3835.

[7] Blumenthal, B., Elmiligui, A. A., Geiselhart, K., Campbell, R. L., Maughmer, M. D., and Schmitz, S., "Computational investigation of a boundary layer ingestion propulsion system for the common research model," in *46th AIAA Fluid Dynamics Conference*, 2016. AIAA-2016-3812.

[8] Ripepi, M., Verveld, M., Karcher, N., Franz, T., Abu-Zurayk, M., Görtz, S., and Kier, T., "Reduced-order models for aerodynamic applications, loads and MDO," *CEAS Aeronautical Journal*, vol. 9, no. 1, pp. 171–193, 2018.

[9] Carlson, J.-R., "Inflow/outflow boundary conditions with application to FUN3D," 2011. NASA/TM-2011-217181.

[10] `https://fun3d.larc.nasa.gov`, 2019. Accessed: 2019-03-20.

[11] Samareh, J., "Aerodynamic shape optimization based on free-form deformation," in *10th AIAA/ISSMO Multidisciplinary Analysis and Optimization Conference*, 2004. AIAA-2004-4630.

[12] Budziszewski, N. and Friedrichs, J., "Modelling of a boundary layer ingesting propulsor," *Energies*, vol. 11, no. 4, p. 708, 2018.

[13] Jones, G. S., "Proposed transonic wind tunnel tests of a tailcone thruster fuselage," 2018. Invited Talk at 2018 AIAA Propulsion & Energy Forum.

[14] "Gas turbine engine inlet flow distortion," SAE ARP-1420, Society of Automotive Engineers, March 1978.

[15] Wislicenus, G. F., "Hydrodynamics and propulsion of submerged bodies," *ARS Journal*, vol. 30, no. 12, pp. 1140–1148, 1960.

[16] Gearhart, W. S. and Henderson, R. E., "Selection of a propulsor for a submersible system," *Journal of Aircraft*, vol. 3, no. 1, pp. 84–90, 1966.

[17] Smith, L. H., "Wake ingestion propulsion benefit," *Journal of Propulsion and Power*, vol. 9, no. 1, pp. 74–82, 1993.

[18] Welstead, J. and Felder, J. L., "Conceptual design of a single-aisle turboelectric commercial transport with fuselage boundary layer ingestion," in *54th AIAA Aerospace Sciences Meeting*, 2016. AIAA-2016-1027.

[19] Felder, J., Kim, H., Brown, G., and Kummer, J., "An examination of the effect of boundary layer ingestion on turboelectric distributed propulsion systems," in *49th AIAA Aerospace Sciences Meeting Including the New Horizons Forum and Aerospace Exposition*, 2011. AIAA-2011-300.

[20] Geiselhart, K. A., Daggett, D. L., Kawai, R., and Friedman, D., "Blended wing body systems studies: boundary layer ingestion inlets with active flow control," 2003. NASA/CR-2003-212670.

[21] Plas, A., Crichton, D., Sargeant, M., Hynes, T., Greitzer, E., Hall, C., and Madani, V., "Performance of a boundary layer ingesting (BLI) propulsion system," in *45th AIAA Aerospace Sciences Meeting and Exhibit*, 2007. AIAA-2007-450.

[22] Campbell, R., "Efficient viscous design of realistic aircraft configurations," in *29th AIAA Fluid Dynamics Conference*, 1998. AIAA-1998-2539.

[23] Hardin, L., Tillman, G., Sharma, O., Berton, J., and Arend, D., "Aircraft system study of boundary layer ingesting propulsion," in *48th AIAA/ASME/SAE/ASEE Joint Propulsion Conference & Exhibit*, 2012. AIAA-2012-3993.

[24] Claus, R. W., Evans, A., Lylte, J., and Nichols, L., "Numerical propulsion system simulation," *Computing Systems in Engineering*, vol. 2, no. 4, pp. 357–364, 1991.

[25] Gladin, J. C., *A sizing and vehicle matching methodology for boundary layer ingesting propulsion systems*. PhD thesis, Georgia Institute of Technology, 2015. https://smartech.gatech.edu/handle/1853/54408.

[26] Kawai, R. T., Friedman, D. M., and Serrano, L., "Blended wing body (BWB) boundary layer ingestion (BLI) inlet configuration and system studies," 2006. NASA/CR-2006-214534.

[27] Carter, M. B., Campbell, R. L., Pendergraft, O. C., Friedman, D. M., and Serrano, L., "Designing and testing a blended wing body with boundary-layer ingestion nacelles," *Journal of Aircraft*, vol. 43, no. 5, pp. 1479–1489, 2006.

[28] Carrier, G., Atinault, O., Grenon, R., and Verbecke, C., "Numerical and experimental aerodynamic investigations of boundary layer ingestion for improving propulsion efficiency of future air transport," in *31st AIAA Applied Aerodynamics Conference*, 2013. AIAA-2013-2406.

[29] Elmiligui, A. A., Fredericks, W. J., Guynn, M. D., and Campbell, R. L., "Numerical investigation of a fuselage boundary layer ingestion propulsion concept," 2013. AIAA-2013-4402.

[30] Sharma, A., "Design of inlet for boundary layer ingestion in a blended wing body aircraft," Master's thesis, Delft University of Technology, 2015.

[31] Kenway, G. K. and Kiris, C. C., "Aerodynamic shape optimization of the STARC-ABL concept for minimal inlet distortion," in *2018 AIAA/ASCE/AHS/ASC Structures, Structural Dynamics, and Materials Conference*, 2018. AIAA-2018-1912.

[32] Rodriguez, D. L., "Multidisciplinary optimization method for designing boundary-layer-ingesting inlets," *Journal of Aircraft*, vol. 46, no. 3, pp. 883–894, 2009.

[33] Gray, J. S., Kenway, G. K., Mader, C. A., and Martins, J., "Aeropropulsive design optimization of a turboelectric boundary layer ingestion propulsion system," in *2018 Aviation Technology, Integration, and Operations Conference*, 2018. AIAA-2018-3976.

[34] Ordaz, I., Rallabhandi, S. K., and Nielsen, E. J., "Adjoint-based design of a distributed propulsion concept with a power objective," in *AIAA Aviation 2019 Forum*, 2019. AIAA-2019-3681.

[35] Ordaz, I., Rallabhandi, S. K., Nielsen, E. J., and Diskin, B., "Mitigation of engine inlet distortion through adjoint-based design," in *35th AIAA Applied Aerodynamics Conference*, 2017. AIAA-2017-3410.

[36] LeGresley, P. and Alonso, J., "Airfoil design optimization using reduced order models based on proper orthogonal decomposition," in *Fluids 2000 Conference and Exhibit*, 2000. AIAA-2000-2545.

[37] LeGresley, P. and Alonso, J., "Investigation of non-linear projection for POD based reduced order models for aerodynamics," in *39th Aerospace Sciences Meeting and Exhibit*, 2001. AIAA-2001-926.

[38] Kroll, N., Abu-Zurayk, M., Dimitrov, D., Franz, T., Führer, T., Gerhold, T., Görtz, S., Heinrich, R., Ilic, C., Jepsen, J., and others, "DLR project Digital-X: towards virtual aircraft design and flight testing based on high-fidelity methods," *CEAS Aeronautical Journal*, vol. 7, no. 1, pp. 3–27, 2016.

[39] Eldred, M. and Dunlavy, D., "Formulations for surrogate-based optimization with data fit, multifidelity, and reduced-order models," in *11th AIAA/ISSMO Multidisciplinary Analysis and Optimization Conference*, 2006. AIAA-2006-7117.

[40] Berkooz, G., Holmes, P., and Lumley, J. L., "The proper orthogonal decomposition in the analysis of turbulent flows," *Annual Review of Fluid Mechanics*, vol. 25, no. 1, pp. 539–575, 1993.

[41] Bizon, K. and Continillo, G., "Reduced-order modelling of chemical reactors with recycle by means of pod-penalty method," *Computers & Chemical Engineering*, vol. 39, pp. 22–32, 2012.

[42] Chinesta, F., Ladeveze, P., and Cueto, E., "A short review on model order reduction based on proper generalized decomposition," *Archives of Computational Methods in Engineering*, vol. 18, no. 4, p. 395, 2011.

[43] Drohmann, M., Haasdonk, B., and Ohlberger, M., "Reduced basis method for finite volume approximation of evolution equations on parametrized geometries," in *Proceedings of ALGORITMY*, vol. 2008, pp. 111–120, 2009.

[44] Fletcher, C. A., *Computational Galerkin Methods*. Springer, 1984. p.

[45] Hesthaven, J. S., Rozza, G., Stamm, B., and others, *Certified reduced basis methods for parametrized partial differential equations*. Springer, 2016.

[46] Lassila, T. and Rozza, G., "Parametric free-form shape design with pde models and reduced basis method," *Computer Methods in Applied Mechanics and Engineering*, vol. 199, no. 23-24, pp. 1583–1592, 2010.

[47] Manzoni, A., Quarteroni, A., and Rozza, G., "Computational reduction for parametrized PDEs: strategies and applications," *Milan Journal of Mathematics*, vol. 80, no. 2, pp. 283–309, 2012.

[48] Prud Homme, C., Rovas, D. V., Veroy, K., Machiels, L., Maday, Y., Patera, A. T., and Turinici, G., "Reliable real-time solution of parametrized partial differential equations: reduced-basis output bound methods," *Journal of Fluids Engineering*, vol. 124, no. 1, pp. 70–80, 2002.

[49] Rheinboldt, W. C., "On the theory and error estimation of the reduced basis method for multi-parameter problems," *Nonlinear Analysis: Theory, Methods & Applications*, vol. 21, no. 11, pp. 849–858, 1993.

[50] Willcox, K., "Model reduction for large-scale applications in computational fluid dynamics," in *Real-Time PDE-Constrained Optimization*, pp. 217–232, SIAM, 2007.

[51] Bhattacharjee, S. and Matouš, K., "A nonlinear manifold-based reduced order model for multiscale analysis of heterogeneous hyperelastic materials," *Journal of Computational Physics*, vol. 313, pp. 635–653, 2016.

[52] Tenenbaum, J. B., De Silva, V., and Langford, J. C., "A global geometric framework for nonlinear dimensionality reduction," *Science*, vol. 290, no. 5500, pp. 2319–2323, 2000.

[53] Wu, Y. and Chan, K. L., "An extended isomap algorithm for learning multi-class manifold," in *Proceedings of 2004 International Conference on Machine Learning and Cybernetics, 2004*, vol. 6, pp. 3429–3433, IEEE, 2004.

[54] Franz, T., Zimmermann, R., Görtz, S., and Karcher, N., "Interpolation-based reduced-order modelling for steady transonic flows via manifold learning," *International Journal of Computational Fluid Dynamics*, vol. 28, no. 3-4, pp. 106–121, 2014.

[55] Volkwein, S., "Proper orthogonal decomposition: theory and reduced-order modelling," *Lecture Notes, University of Konstanz*, vol. 4, no. 4, 2013.

[56] Smith, T. R., Moehlis, J., and Holmes, P., "Low-dimensional modelling of turbulence using the proper orthogonal decomposition: a tutorial," *Nonlinear Dynamics*, vol. 41, no. 1-3, pp. 275–307, 2005.

[57] Qian, J., Wang, Y., Song, H., Pant, K., Peabody, H., Ku, J., and Butler, C. D., "Projection-based reduced-order modeling for spacecraft thermal analysis," *Journal of Spacecraft and Rockets*, vol. 52, no. 3, pp. 978–989, 2015.

[58] Amsallem, D., Zahr, M., Choi, Y., and Farhat, C., "Design optimization using hyper-reduced-order models," *Structural and Multidisciplinary Optimization*, vol. 51, no. 4, pp. 919–940, 2015.

[59] Zimmermann, R. and Görtz, S., "Non-linear reduced order models for steady aerodynamics," *Procedia Computer Science*, vol. 1, no. 1, pp. 165–174, 2010.

[60] Lin, Z., Xiao, D., Fang, F., Pain, C., and Navon, I. M., "Non-intrusive reduced order modelling with least squares fitting on a sparse grid," *International Journal for Numerical Methods in Fluids*, vol. 83, no. 3, pp. 291–306, 2017.

[61] Reed, J. A. and Afjeh, A. A., "A comparative study of high and low fidelity fan models for turbofan engine system simulation," 1991. GRC-E-DAA-TN38777.

[62] Curnock, B., Yin, J., Hales, R., and Pilidis, P., "High-bypass turbofan model using a fan radial-profile performance map," *Aircraft Design*, vol. 4, no. 2-3, pp. 115–126, 2001.

[63] Felder, J., Kim, H., and Brown, G., "Turboelectric distributed propulsion engine cycle analysis for hybrid-wing-body aircraft," in *47th AIAA Aerospace Sciences Meeting Including the New Horizons Forum and Aerospace Exposition*, 2009. AIAA-2009-1132.

[64] Biedron, R. T., Carlson, J.-R., Derlaga, J. M., Gnoffo, P. A., Hammond, D. P., Jones, W. T., Kleb, B., Lee-Rausch, E. M., Nielsen, E. J., Park, M. A., and others, "FUN3D manual: 13.3," 2018.

[65] Roe, P. L., "Approximate Riemann Solvers, Parameter Vectors, and Difference Schemes," *Journal Computational Physics*, vol. 43, pp. 357–372, 1981.

[66] Spalart, P. and Allmaras, S., "A one-equation turbulence model for aerodynamic flows," in *30th Aerospace Sciences Meeting and Exhibit*, 1992. AIAA-1992-439.

[67] White, J. and Morrison, J., "A pseudo-temporal multi-grid relaxation scheme for solving the parabolized Navier-Stokes equations," in *14th Computational Fluid Dynamics Conference*, 1999. AIAA-1999-3360.

[68] Biedron, R. and Thomas, J., "Recent enhancements to the FUN3D flow solver for moving-mesh applications," in *47th AIAA Aerospace Sciences Meeting including The New Horizons Forum and Aerospace Exposition*, 2009. AIAA-2009-1360.

[69] Sederberg, T. W. and Parry, S. R., "Free-form deformation of solid geometric models," *ACM SIGGRAPH Computer Graphics*, vol. 20, no. 4, pp. 151–160, 1986.

[70] Hahn, A., "Vehicle sketch pad: a parametric geometry modeler for conceptual aircraft design," in *48th AIAA Aerospace Sciences Meeting Including the New Horizons Forum and Aerospace Exposition*, 2010. AIAA-2010-657.

[71] Haimes, R. and Dannenhoffer, J., "The engineering sketch pad: A solid-modeling, feature-based, web-enabled system for building parametric geometry," in *21st AIAA Computational Fluid Dynamics Conference*, 2013. AIAA-2013-3073.

[72] Samareh, J., "Multidisciplinary aerodynamic-structural shape optimization using deformation (MASSOUD)," in *8th Symposium on Multidisciplinary Analysis and Optimization*, 2000. AIAA-2000-4911.

[73] Samareh-Abolhassani, J., "Triangulation of nurbs surfaces," *Numerical Grid Generation in Computational Fluid Dynamics and Related Fields*, pp. 377–388, 1994.

[74] Mathworks, "Statistics and machine learning toolbox: User's guide (r2018b)." `https://www.mathworks.com/help/stats/index.html`, 2018. Accessed: 2019-08-24.

[75] Lappo, V. and Habashi, W., "Reduced order POD/kriging modeling for real-time 3d CFD," 2009.

[76] Wang, C., Bai, J., Hesthaven, J. S., Qiu, Y., Qiao, L., and Han, X., "POD-kriging reduced method's application in tandem cylinders' flow," *Xibei Gongye Daxue Xuebao/Journal of Northwestern Polytechnical University*, vol. 36, no. 2, pp. 220–228, 2018.

[77] Lophaven, S. N., Nielsen, H. B., Søndergaard, J., and others, *DACE: a Matlab kriging toolbox*, vol. 2. Citeseer, 2002.

[78] Pointwise, R., "Release 18.2, Pointwise user manual, Pointwise," 2018.

[79] Dette, H. and Pepelyshev, A., "Generalized latin hypercube design for computer experiments," *Technometrics*, vol. 52, no. 4, pp. 421–429, 2010.

[80] Ferrar, A. and O'Brien, W., "Fan response to total pressure distortions produced by boundary layer ingesting serpentine inlets," in *48th AIAA/ASME/SAE/ASEE Joint Propulsion Conference & Exhibit*, 2012. AIAA-2012-3996.

[81] Lucas, J. R., *Effect of BLI-Type Inlet Distortion on Turbofan Engine Performance*. PhD thesis, Virginia Tech, 2013. https://vtechworks.lib.vt.edu/handle/10919/23272.

[82] Mitchell, M., *An introduction to genetic algorithms*. MIT Press, 1998.

[83] Koza, J. R., "Genetic programming," 1997.

[84] Diez, M. and Peri, D., "Robust optimization for ship conceptual design," *Ocean Engineering*, vol. 37, no. 11-12, pp. 966–977, 2010.

[85] Walton, S., Hassan, O., Morgan, K., and Brown, M., "Modified cuckoo search: a new gradient free optimisation algorithm," *Chaos, Solitons & Fractals*, vol. 44, no. 9, pp. 710–718, 2011.

[86] Deb, K., Agrawal, S., Pratap, A., and Meyarivan, T., "A fast elitist non-dominated sorting genetic algorithm for multi-objective optimization: NSGA-II," in *International Conference on Parallel Problem Solving from Nature*, pp. 849–858, Springer, 2000.

[87] Kenway, G. K., Kennedy, G. J., and Martins, J. R., "Scalable parallel approach for high-fidelity steady-state aeroelastic analysis and adjoint derivative computations," *AIAA Journal*, vol. 52, no. 5, pp. 935–951, 2014.

[88] Kenway, G. K. and Martins, J. R., "Multipoint high-fidelity aerostructural optimization of a transport aircraft configuration," *Journal of Aircraft*, vol. 51, no. 1, pp. 144–160, 2014.

[89] Liem, R. P., Kenway, G. K., and Martins, J. R., "Multimission aircraft fuel-burn minimization via multipoint aerostructural optimization," *AIAA Journal*, vol. 53, no. 1, pp. 104–122, 2014.